SUPERCOMPUTING IN SCIENCE AND ENGINEERING 2017–18

IT4Innovations National Supercomputing Center
Czech Republic

VSB TECHNICAL | IT4INNOVATIONS
UNIVERSITY | NATIONAL SUPERCOMPUTING
OF OSTRAVA | CENTER

SUPERCOMPUTING IN SCIENCE AND ENGINEERING 2017–18

IT4Innovations National Supercomputing Center
Czech Republic

MINISTRY OF EDUCATION,
YOUTH AND SPORTS

Table of contents

Dear readers,

We are proud to present to you the second edition of our publication "Supercomputing in Science and Engineering". Together with our users, we have selected over 50 scientific projects which were made possible thanks to the High Performance Computing (HPC) infrastructure of IT4Innovations National Supercomputing Center, in the years 2017-18.

During this period we have, through our open access grant competitions, distributed over 271,000,000 core hours across 245 projects. Those are significant numbers and I am pleased to see that the demand for HPC resources continues to grow. It shows that the Czech Republic's scientific community has adopted what is becoming the trend all over the world, enabling science in many domains through modelling, simulations, and data analytics.

We are committed to serving our users and continuously improving and extending our services. In 2019 we will increase our computing resources with a new cluster, and also a specialised system, NVIDIA DGX-2, the world's most powerful supercomputer for artificial intelligence and data science computations. In 2020 a new supercomputer with approximately 10 Petaflops will be installed, which will be a five-fold more powerful system than our current top cluster, Salomon.

In addition, through a high-class HPC and HPDA training programme, we are helping the community from the Czech Republic and abroad to develop their skills and learn about the latest HPC architectures, programming models, and performance and energy optimisations of selected applications.. Recently we have also been focusing on artificial intelligence, particularly on how to use tools for machine and deep learning efficiently on our infrastructure.

Enjoy the read.

Vít Vondrák
Managing director

THE INFRASTRUCTURE OF IT4INNOVATIONS

IT4Innovations operates the largest supercomputing facility in the Czech Republic in the public sphere, currently two X86 clusters named Salomon and Anselm. The supercomputer infrastructure was installed in several stages. The first cluster, Anselm, was installed in temporary mobile units in May 2013. The Salomon supercomputer became operational in September 2015 and was one of the most powerful supercomputers in the world. Both clusters are now permanently located in the new IT4Innovations building, which has a 500 m^2 server room.

The construction of the IT4Innovations building started in December 2012, the administrative section being completed in March 2014. The physical infrastructure supporting the supercomputers is fully redundant in power and cooling, using direct hot water cooling (2 x 600 kW), cold water cooling (200, 400 and 600 kW) and heat recovery (up to 380 kW) for building heating to lower the operational costs. The backup power is provided through diesel rotary UPSs, each with a capacity of 2.5 MVA. The Internet connection is 2x40 Gb/s connected to two different endpoints of CESNET network.

The Anselm Cluster

The Anselm cluster consists of 209 computational nodes. Each node is equipped with 16 cores (two eight-core Intel Sandy Bridge processors). There are four types of compute node: 180 regular compute nodes without any accelerator, with 2.4 GHz CPUs and 64 GB of RAM; 23 compute nodes with GPU accelerators (NVIDIA Tesla Kepler K20), with 2.3 GHz CPUs and 96 GB of RAM; 4 compute nodes with MIC accelerators (Intel Xeon Phi 5110P), with 2.3 GHz CPUs and 96 GB of RAM; and 2 fat nodes with a larger RAM (2.4 GHz CPUs, 512 GB RAM). InfiniBand (QDR) and Ethernet networks interconnect the nodes.

The theoretical peak performance of the Anselm cluster is 94 TFlop/s with a maximal aggregated LINPACK performance of 73 TFlop/s. All computing nodes share a 320 TiB /home disk storage to store user files. The 146 TiB shared /scratch storage is available for scratch data. These file systems are provided by a Lustre parallel file system. There is also a local hard drive (330 GiB available) on all compute nodes.

The Salomon Cluster

The Salomon cluster consists of 1008 computational nodes. Each node is equipped with 24 cores (two twelve-core Intel Haswell processors). All compute and login nodes are interconnected through a 7D Enhanced hypercube Infiniband network (see Figure 1). There are two types of compute nodes: 576 compute nodes without any accelerator and 432 compute nodes with MIC accelerators (two Intel Xeon Phi 7120P per node). Each node is equipped with two 2.5 GHz processors and 128 GB of RAM.

The theoretical peak performance of Salomon exceeds 2 PFlop/s with an aggregated LINPACK performance of over 1.5 PFlop/s earning the system 213th place in the TOP500 list of most powerful supercomputers (November 2018). All computing nodes share a 500 TiB /home disk storage to store user files. The 1.6 PiB shared storage is available for scratch and project data. In addition to the cluster nodes an SMP/NUMA machine is incorporated into the system with 112 CPU cores and 3.25 TB of RAM.

The operating system on Anselm is Redhat Linux and on the supercomputer Salomon it is CentOS. State of the art programs and tools to develop, profile and debug HPC codes, such as Intel Parallel Studio XE Cluster Edition, Allinea Forge and RougeWave Totalview are also available. The clusters provide several implementations of the MPI library. A large amount of application software, both open source and from ISVs is available, including numerical libraries and software packages from many domains of science.
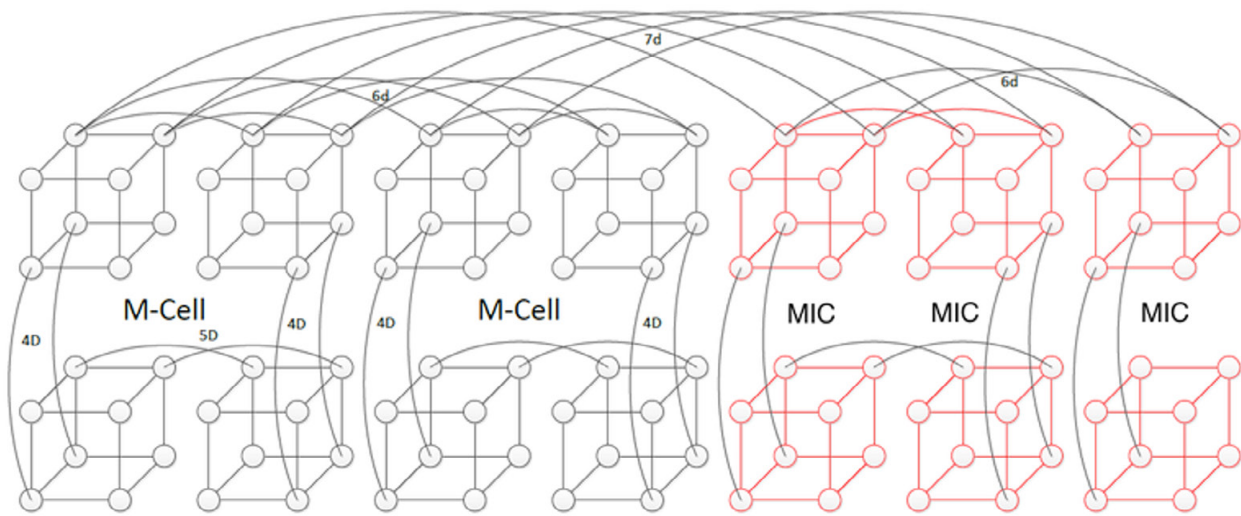
Figure 1.
A simplified view of the 7D Enhanced Hypercube topology of the Salomon supercomputer.
M-Cell denotes nodes without acceleration, MIC denotes the accelerated nodes interconnection.

	ANSELM CLUSTER	SALOMON CLUSTER
Put into operation	Spring 2013	Summer 2015
		213th at TOP500 world supercomputers (November 2018)
Peak performance	94 TFlop/s	2011 TFlop/s
Operating system	RedHat Linux 64bit 6.x	RedHat Linux 64bit 6.x
		CentOS 64bit 6.x
Nodes	209	1008
CPU	2x Intel SandyBridge 8 core 2.3/2.4 GHz	2x Intel Haswell 12 core 2.5 GHz
	3344 cores in total	24192 cores in total
RAM per computing node	64 GB / 96 GB / 512 GB	128 GB / 3.25 TB (UV node)
GPU accelerators	23x NVIDIA Tesla Kepler K20	N/A
MIC accelerators	4x Intel Xeon Phi 5110P	864x Intel Xeon Phi 7120P
		61 cores each
		52704 cores in total
Storage	320 TiB / home (2 GB/s speed)	500 TiB / home (6 GB/s speed)
	146 TiB / scratch (6 GB/s speed)	1638 TiB / scratch (30 GB/s speed)
Interconnection	Infiniband QDR 40 Gb/s	Infiniband FDR 56 Gb/s

Table 1.
Technical data

Acknowledgements

01 | ASTROPHYSICS

EVOLUTION OF ELECTRON DISTRIBUTION FUNCTIONS IN SOLAR RADIO ZEBRAS

Research institutions:	Principal investigator:	Researcher:	Project ID:
Masaryk University, The Astronomical Institute of the Czech Academy of Sciences	Jan Benáček	Marian Karlický	OPEN-13-34

Introduction

The most energetic processes in the solar atmosphere are solar flares. During the flare, the energy accumulated in the magnetic field and electric currents in the current sheet are explosively transformed into the acceleration of particles, plasma heating, and several types of plasma waves and motions. Electromagnetic waves in the range of radio waves to gamma-rays are radiated from the active region. Radio observations are highly important for understanding plasma waves and kinetic instabilities. A special type of radio observation, radio zebras, are used for precise measurements of electron densities and magnetic fields in solar magnetic loops.

In the present project, using a 3D particle-in-cell model, we study the internal processes of radio zebra regions, associated instabilities, changes in distribution function of accelerated electrons and their implications to radio zebra creation, and density and magnetic field estimations.

There are many theories describing the zebra pattern from radio observations (e.g. [1]). The most promising seems to be the double plasma resonance instability, which suggests the generated upper-hybrid waves are transformed into electromagnetic waves. They are then radiated into a narrow cone towards the observer [2].

Results and Methods

For understanding electron velocity distribution during double plasma resonance instability we use the 3-dimensional PIC model. Its two dimensional version was used in several of our previous studies of plasmoids in magnetic reconnection [3, 4]. This model describes plasma on the kinetic level of the plasma description: in a prescribed numerical box there are hundreds of millions of charged superparticles (each representing a bunch of particles of the same type) which self-consistently electromagnetically interact through Maxwell equations. Thus, this PIC model requires very powerful computers, especially when modelling larger spatial solar structures in three dimensions. We successfully used its small version in the study of Benáček and Karlický [5]. Now we use an extended version of this PIC model to compute the internal processes in the double plasma resonance region.

In this project we extend the previous works [5, 6] with several new unstable distributions which potentially generate the zebra pattern. The project is still in progress, but our preliminary results show that while the typical loss-cone Maxwellian or kappa distributions do not generate significant differences between minima and maxima, the kappa cut-off and delta distributions
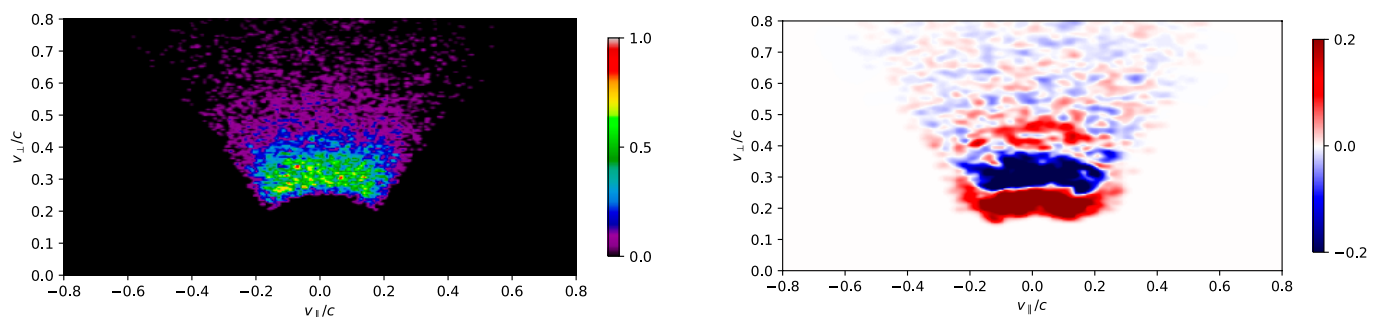
Figure 1.
Left: The initial distribution function of hot electrons. In this model the delta distribution for δ=5.
Right: The change of velocity distribution function between end time (ωpet = 2,000) and initial time (ωpet = 0). Blue indicates a decrease, red an increase.

(which is by cut-off by definition) generate significant peaks. Figure 1 illustrates the changes in velocity distribution function in the area of cut-off. The electrons lose its kinetic energy, which is converted to energy of the electrostatic field.

We also analyze waves generated in the model by the dispersion diagrams. In the dispersion diagram each generated wave is represented by a curve, or series of curves. In Figure 2 Left, you can see the dispersion diagram of transverse magnetic waves along a magnetic field and in Figure 2 Right, the longitudinal electric field is perpendicular to the magnetic field. There are not only the upper-hybrid and electromagnetic waves proposed by the theory, but also Whistler waves and Bernstein waves.

On-going Research / Outlook

For the rest of the project we will focus on analyses of the saturation energies of electrostatic waves for different distribution functions and their comparison with the initial energy of hot electrons. We also want to fully analyze the creation of waves in dispersion diagrams.

Conclusion

In our research we study the influence of upper-hybrid wave growth-rates with different distribution functions of hot electrons generated in solar flares. For the study we use the 3D electromagnetic relativistic Particle-in-Cell code. Preliminary results show that the cut-off type of distribution function is creating a significant peak growth rate. We found that during the double plasma instability are generated upper-hybrid, electromagnetic, and Whistler and Bernstein waves.

Figure 2.
Dispersion diagrams of the double plasma resonance instability.
Left: Transverse waves along the magnetic field.
Right: Longitudinal waves perpendicular to the magnetic field.

References

[1] Chernov, G. P. Fine Structure of Solar Radio Bursts. Berlin, Heidelberg: Springer Berlin Heidelberg, 2011. Astrophysics and Space Science Library. ISBN 978-3-642-20014-4. DOI: 10.1007/978-3-642-20015-1.

[2] Melrose, D. B., and G. A. Dulk. Electron-cyclotron masers as the source of certain solar and stellar radio bursts. The Astrophysical Journal. 1982, 259, 844. DOI: 10.1086/160219.

[3] Karlický, M., M. Bárta, and D. Nickeler. Fragmentation during merging of plasmoids in the magnetic field reconnection. Astronomy & Astrophysics. 2012, 541, A86. DOI: 10.1051/0004-6361/201218781.

[4] Karlický, M., and M. Bárta. Successive Merging of Plasmoids and Fragmentation in a Flare Current Sheet and Their X-Ray and Radio Signatures. The Astrophysical Journal. 2011, 733(2), 107. DOI: 10.1088/0004-637X/733/2/107.

[5] Benáček, J., M. Karlický, and L. V. Yasnov. Temperature dependent growth rates of the upper-hybrid waves and solar radio zebra patterns. Astronomy & Astrophysics. 2017, 598. DOI: 10.1051/0004-6361/201629717.

[6] Benáček, J., and M. Karlický. Double plasma resonance instability as a source of solar zebra emission. Astronomy & Astrophysics. 2018, 611. DOI: 10.1051/0004-6361/201731424.

Publication

EXPLORING THE ORIGIN OF OPTICALLY DARK CLOUDS IN THE VIRGO CLUSTER OF GALAXIES

Research institution:	Principal investigator:	Researcher:	Project ID:
The Astronomical Institute of the Czech Academy of Sciences	Richard Wünsch	Rhys Taylor	OPEN-9-25

Introduction

The "missing satellite problem" is a long-standing disagreement between cosmological models of galaxy formation and observational reality. The models (e.g. [1]) have generally only used dark matter, partly because it is computationally cheap, but also because it's thought to dominate the mass of galaxies. This means that the much more complex gas and stellar physics should not have a significant effect on the kinematics of galaxies (i.e. how fast they rotate) or on their distribution. Indeed, these models are extremely successful at reproducing the large-scale distribution of galaxy structures, e.g. the "cosmic web" of filaments and voids, but fail on the scale of individual galaxies. In particular, models generally predict around a factor of ten more dark matter "halos" than observed satellite galaxies around the Milky Way.

One suggestion is that most of the dark matter halos found in simulations do exist in reality, but not all of them accumulate enough gas for star formation to occur. The conditions under which gas is converted into stars are poorly understood, but most galaxies are known to possess a gas disc significantly more extended than their stellar component [2]. Davies et al. [3] suggested that it might be possible for a dark halo to accumulate enough gas to be detectable with radio surveys without triggering star formation. However, it is known that galaxy-galaxy encounters can tear off gas from the outer parts of galaxies, leaving a trail of optically dark gas clouds (tidal debris) that could potentially be mistaken for these proposed "dark galaxies".

Surveys such as AGES [4] use radio telescopes to search for neutral atomic hydrogen (HI) gas independently of optical emission. Taylor et al. [5] discovered eight HI clouds with particularly intriguing properties: they have high spectral line widths (180 km/s), no optical counterparts, and are relatively isolated. Taylor et al. [6] showed that such objects are extremely difficult to produce in galaxy-galaxy encounters. While streaming motions can produce high line widths, such features are highly transient - implying that tidal debris should be found close to its parent galaxy, which is not the case for these clouds. In contrast, if the clouds are rotating, this would imply a high dark matter content, which would allow them to remain stable and move freely.

Burkhart and Loeb [7] proposed a new mechanism to stabilise the clouds. The idea is that the internal outward pressure of the clouds is balanced by the confining pressure of the hot, thin, external gas found throughout most galaxy clusters (the intracluster medium, ICM). This internal pressure would have to be dynamic (bulk internal motions), not thermal, as the line width of the clouds would imply a temperature (>100,000 K) which would rapidly ionise the gas in the clouds. The model predicts the size of the clouds, which is important as our observations can only set an upper size limit and not a direct measurement of the true size. In this project we tested how long clouds in this pressure equilibrium could survive and resemble the features we detected in the Virgo cluster.

Results and Methods

We investigated this model on the Salomon cluster using 3D hydrodynamic simulations in FLASH [7]. FLASH is an MPI-parallel adaptive mesh refinement code that solves hydrodynamic equations using the piecewise parabolic method (PPM) [8]. Radiative cooling of the gas is calculated using a cooling function given by Schure et al. [9] for a variable chemical composition. Gravity forces are calculated by our own tree-solver [10], and heating by external UV radiation and cosmic rays by the radiation transport code TreeRay, also developed within our group. The whole code scales well up to at least 1,500 cores. Most calculations were run on 200–400 cores. Approximately 500,000 corehours were used for the whole project.

The HI is modelled as a Gaussian-density sphere with a turbulent velocity field, with properties that match the AGES clouds, embedded in a hot, thin ICM with properties based on X-ray observations. The exact structure of the HI velocity field is a free parameter, which we vary in a variety of ways under the constraint that the corresponding overall line width matches the observations. We set the size of the clouds initially based on the Burkhart and Loeb [11] calculation, but also tried varying this.

We found [12] that such clouds evolve rapidly and resemble the observed clouds for < 100 Myr. The clouds in this model
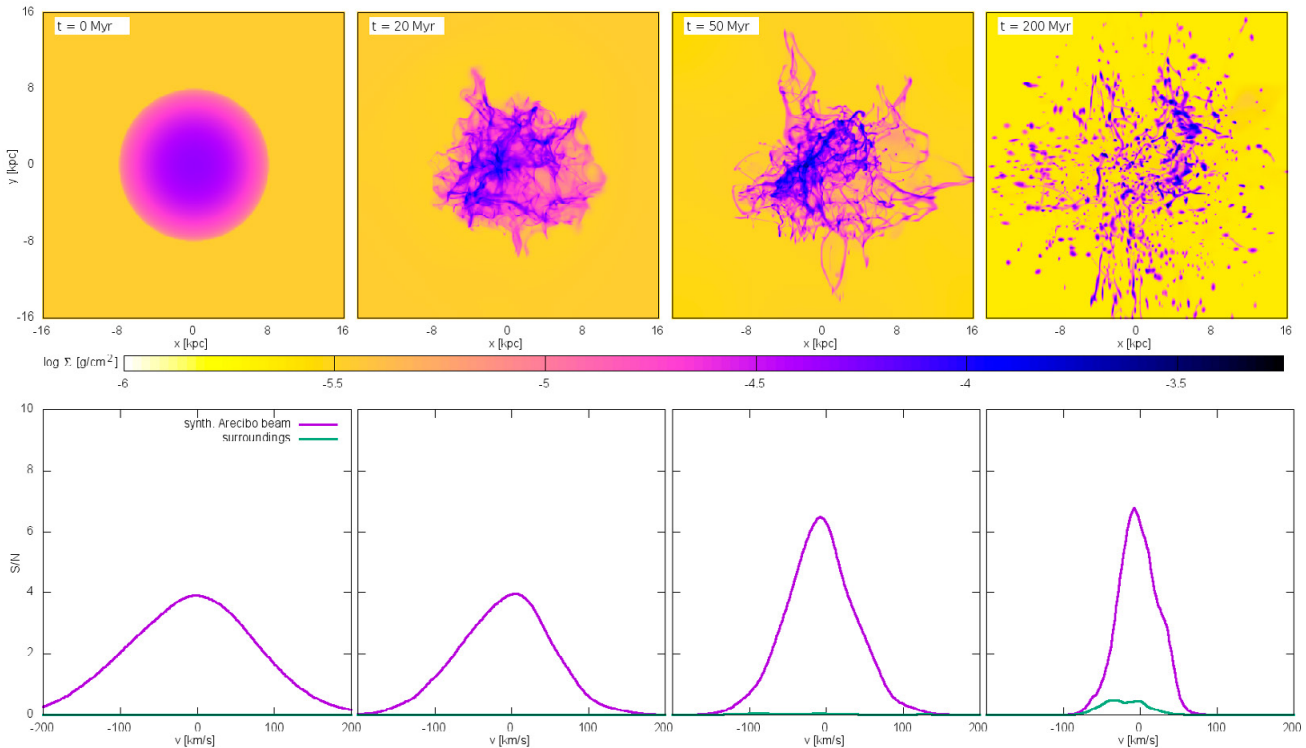
Figure 1.
Typical evolution of cloud surface density (top) and line profile (bottom)

are inherently unstable: their internal motions are essentially acting (against their negligible self-gravity) to tear them apart, while the confining pressure of the ICM is acting to crush them. The result is that the clouds fragment into a collection of dispersing filaments. No stable equilibrium state exists; it is not a matter of more careful adjustments to the initial conditions. While the clouds would remain detectable by HI surveys for up to ~400 Myr, their line drops rapidly, falling below 100 km/s in under 100 Myr. Thus, if this model does explain the AGES clouds, it would require us to have detected eight clouds in a very brief stage of their evolution, whereas in the dark galaxy hypothesis they are stable and long-lived.

On-going Research / Outlook

We are testing the behaviour of dark galaxies evolving inside the cluster. The gas density of these objects is lower than in typical galaxies in order to prevent star formation, making them especially vulnerable to the environment of the cluster: motion through the ICM causes ram pressure stripping, and tidal encounters with other galaxies could also disrupt the objects. We will also explore the effect of the ICM on the tidal debris hypothesis.

Conclusion

Currently the most successful interpretation of the clouds appears to be the dark galaxy hypothesis. This is the most natural way to explain the high line width and is consistent with cosmological theories. The tidal debris scenario cannot produce similar objects and the turbulent sphere models are too unstable. However, the full impact of the ICM on both the tidal debris and dark galaxy hypotheses requires more detailed numerical modelling, which we are beginning to implement.

References

[1] Moore, B., S. Ghigna, F. Governato, G. Lake, T. Quinn, J. Stadel and P. Tozzi. Dark Matter Substructure within Galactic Halos. The Astrophysical Journal. 1999, 524(1), L19-L22. DOI: 10.1086/312287.

[2] Broeils A. H., M. H. Rhee. Short 21-cm WSRT observations of spiral and irregular galaxies, HI properties. Astronomy and Astrophysics. 1997, 324, p. 877-887. ISSN: 1432-0746.

[3] Davies, J., R. Minchin, S. Sabatini, et al. A multibeam HI survey of the Virgo cluster - two isolated HI clouds? Monthly Notices of the Royal Astronomical Society. 2004, 349(3), 922-932. DOI: 10.1111/j.1365-2966.2004.07568.x.

[4] Auld, R., R. F. Minchin, J. I. Davies, et al. The Arecibo Galaxy Environment Survey: Precursor observations of the NGC 628 group. Monthly Notices of the Royal Astronomical Society. 2006, 371(4), 1617-1640. DOI: 10.1111/j.1365-2966.2006.10761.x.

[5] Taylor, R., J. I. Davies, R. Auld a R. F. Minchin. The Arecibo Galaxy Environment Survey - V. The Virgo cluster (l). Monthly Notices of the Royal Astronomical Society. 2012, 423(1), 787-810. DOI: 10.1111/j.1365-2966.2012.20914.x.

[6] Taylor R., J. I. Davies, P. Jáchym, O. Keenan, R. F. Minchin, J. Palouš, R. Smith, R. Wünsch. Kinematic clues to the origins of starless HI clouds: Dark galaxies or tidal debris? Monthly Notices of the Royal Astronomical Society. 2017, 467, 3648. DOI: 10.1093/mnras/stx187.

[7] Fryxell, B., K. Olson, P. Ricker, et al. FLASH: An Adaptive Mesh Hydrodynamics Code for Modeling Astrophysical Thermonuclear Flashes. The Astrophysical Journal Supplement Series. 2000, 131(1), 273-334. DOI: 10.1086/317361.

[8] Colella, P., and P. R. Woodward. The Piecewise Parabolic Method (PPM) for gas-dynamical simulations. Journal of Computational Physics. 1984, 54(1), 174-201. DOI: 10.1016/0021-9991(84)90143-8.

[9] Schure, K. M., D. Kosenko, J. S. Kaastra, R. Keppens, J. Vink. A new radiative cooling curve based on an up-to-date plasma emission code. Astronomy & Astrophysics. 2009, 508(2), 751-757. DOI: 10.1051/0004-6361/200912495.

[10] Wünsch, R., S. Walch, F. Dinnbier, A. Whitworth. Tree-based solvers for adaptive mesh refinement code FLASH - I: Gravity and optical depths. Monthly Notices of the Royal Astronomical Society. 2018, 475(3), 3393-3418. DOI: 10.1093/mnras/sty015.

[11] Burkhart, B., and A. Loeb. Predicted sizes of pressure-supported HI clouds in the outskirts of the virgo cluster. The Astrophysical Journal. 2016, 824(1), 7. DOI: 10.3847/2041-8205/824/1/L7.

Publication

[12] Taylor R., R. Wünsch, J. Palouš. Simulating the evolution of optically dark HI clouds in the Virgo cluster: Will no-one rid me of this turbulent sphere? Monthly Notices of the Royal Astronomical Society. 2018, 479, 377. DOI: 10.1093/mnras/sty1237.

DUSTY SUPERNOVAE INTERACTING WITH STAR CLUSTER WINDS

Research institution:
The Astronomical
Institute of the Czech
Academy of Sciences

Principal investigator:
Sergio Martínez
González

Researcher:
Richard Wünsch

Project ID:
OPEN-12-44

Introduction

Galaxies contain massive amounts of dust a few 100 million years after the Big Bang. One can mention A2744-YD4, the current record-holder for the oldest dust-rich galaxy, which ~100 million years after the Big Bang harbours around 6 million solar masses of dust. This has been interpreted as evidence of a rapid enrichment of the interstellar medium with dust produced in the ejecta of core-collapse supernovae (SNe) as observed in nearby supernova remnants (SNRs) like SN 1987A and Cassiopeia A.

However, based on the study of isolated SNRs, it has been argued that only 1–8% of the dust condensed in SN ejecta will be injected into the interstellar medium. The reason is that the material ejected with the explosion will eventually be processed by a shock resulting from the interaction of the SN ejecta with interstellar gas, and the shock will destroy the majority of grains as they collide with gas particles.

In order to help answer the question on how the Universe gets "too dusty too early", we have simulated the injection and destruction of the dust condensed out of the ejecta of SNe occurring in large clusters of young stars, where hundreds or even thousands of supernova explosions can occur in a relatively small region (a few dozen light years).

Results and Methods

We used IT4Innovations' facilities to perform a series of 3D hydrodynamic simulations using the publicly available hydrodynamic code FLASH [1] and modules developed by our team: tree-solver [2], WIND [3] and CINDER [8], with the last one created specifically to carry out this project. FLASH is an MPI-parallel adaptive mesh refinement code, and together with the used modules it scales well, up to at least 1,500 cores. The simulations were running typically on 200–400 cores. Approximately 500,000 corehours were used for the whole project.

Supernova explosions within coeval star clusters start to occur after 3 million years and last for about 40 Myr. Before the occurrence of any supernova explosion, the medium within the star cluster is already dense and hot as the winds from individual massive stars, distributed non-uniformly, have collided and merged to form a star cluster wind [3]. With each explosion, a certain mass (gas and dust grains), and kinetic energy were inserted into the simulation in a small spherical region and centered at an arbitrary position.

The grain size distribution was logarithmically-sampled into 10 bins with equal mass fractions of silicate and graphite grains. CINDER traces the dust-to-gas mass ratio of every grid-cell in the simulation as an advecting mass scalar associated to a characteristic grain size. It has enabled us to follow the evolution of the dust mass injected by SNe and subjected to multiple shock processing. To the best of our knowledge, it provides the first implementation of the cooling induced by dust in a hot plasma suitable for time-dependent three-dimensional hydrodynamical simulations.

The main input parameters of our model are the mass and size of the cluster, the location, ejecta mass and kinetic energy of the SN explosion, the initial ejecta mass density and velocity distributions, and the initial grain size distribution.

As discussed by Tenorio-Tagle et al. [4], off-centered SNRs facing a steep density gradient experience a blowout phase: they elongate in a preferential direction, become Rayleigh-Taylor unstable, and the SN ejecta suffers a rapid decline in density and temperature. The evolution of these SNRs is somewhat analogous to the growth of mushroom clouds formed by supervolcanoes here on Earth, which are capable of covering whole continents with pyroclasts and ashes. Therefore, our model was named the "pyroclastic blowout model".

The main result obtained by this study is that, regardless of the input parameters and contrary to previous expectations (e.g. Temim et al. [5]), clustered SN explosions are likely to cause a net increase in the amount of dust in the surroundings of young massive stellar clusters (see Figure 1) as 15–50% of the dust produced by SNe is not destroyed by the multiple shock waves that traverse the star cluster [8].

On-going Research / Outlook

The results already published suggest a bimodal scenario in which surviving grains accumulate in the vicinity of the clusters and manifest as a persistent mid- to far-infrared excess; whereas those smalls grains that are destroyed manifest as a transient near- to mid-infrared excess [6, 7]. We are currently working on the post-processing of our simulations in order to characterize this emission and compare it to observations of nearby young star clusters.

We have also produced a set of simulations to test if young massive clusters are able to retain a non-negligible fraction of SN ejecta under the influence of a strong gravity and fast radiative cooling. This is an interesting problem as only the most massive clusters, like Omega Cen, show enhanced Fe abundances in secondary stellar generations. The results of this analysis will be presented in the next year.

Conclusion

We have followed the evolution of SN remnants to derive the amount of dust that is capable of surviving from multiple shock processing within young massive star clusters. We found that clustered SNe are net enrichers of the ISM. This is a particularly interesting result as even the galaxies of the early Universe show evidence of dust enrichment, even though they are too young for other sources, like old stars, to have begun to produce the dust. This could have great implications given that dust is a key ingredient in the formation of stars, planets and complex molecules. These models can be contrasted directly to observations of nearby young massive stellar clusters; a task that we are already carrying out.
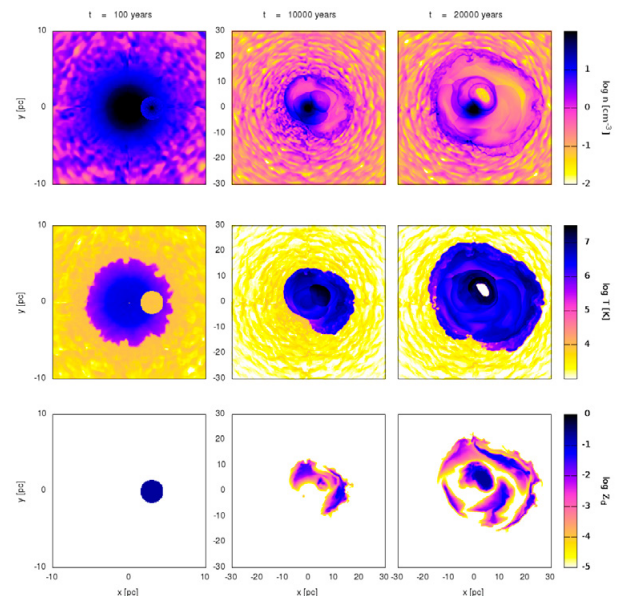
Figure 1.
High resolution (512)³ hydrodynamical simulation of the evolution of multiple SNe within a young massive cluster. Left: the upper, middle and bottom panels show gas number density, gas temperature, and dust-to-gas mass ratio, each displayed at three different times measured from the first explosion (left: 200 years, center: 3,000 years, right: 5,000 years).

References

[1] Fryxell, B., K. Olson, P. Ricker, et al. FLASH: An Adaptive Mesh Hydrodynamics Code for Modeling Astrophysical Thermonuclear Flashes.
The Astrophysical Journal Supplement Series. 2000, 131(1), 273-334. DOI: 10.1086/317361.

[2] Wünsch, R., S. Walch, F. Dinnbier, A. Whitworth. Tree-based solvers for adaptive mesh refinement code FLASH - I: Gravity and optical depths.
Monthly Notices of the Royal Astronomical Society. 2018, 475(3), 3393-3418. DOI: 10.1093/mnras/sty015.

[3] Wünsch, R., J. Palouš, G. Tenorio-Tagle, S. Ehlerová. The Formation of Secondary Stellar Generations in Massive Young Star Clusters from Rapidly Cooling Shocked Stellar Winds. The Astrophysical Journal. 2017, 835(1), 60. DOI: 10.3847/1538-4357/835/1/60.

[4] Tenorio-Tagle, G., C. Muñoz-Tuñón, S. Silich, S. Cassisi. Supernovae and Their Expanding Blast Waves during the Early Evolution of Galactic Globular Clusters. The Astrophysical Journal. 2015, 814(1), L8. DOI: 10.1088/2041-8205/814/1/L8.

[5] Temim, T., E. Dwek, K. Tchernyshyov, M. L. Boyer, et al. Dust Destruction Rates and Lifetimes in the Magellanic Clouds. The Astrophysical Journal. 2015, 799(2), 158. DOI: 10.1088/0004-637X/799/2/158.

[6] Martínez-González, S., G. Tenorio-Tagle, S. Silich. Infrared Observational Manifestations of Young Dusty Super Star Clusters. The Astrophysical Journal. 2016, 816(1), 39. DOI: 10.3847/0004-637X/816/1/39.

[7] Martínez-González, S., R. Wünsch, J. Palouš. Can Dust Injected by SNe Explain the NIR–MIR Excess in Young Massive Stellar Clusters?
The Astrophysical Journal. 2017, 843(2), 95. DOI: 10.3847/1538-4357/aa7510.

Publication

[8] Martínez-González, S., R. Wünsch, J. Palouš, C. Muñoz-Tuñón, S. Silich, and G. Tenorio-Tagle. Pyroclastic Blowout:
Dust Survival in Isolated versus Clustered Supernovae. The Astrophysical Journal. 2018, 866(1), 40. DOI: 10.3847/1538-4357/aadb88.

Press release in Czech: https://www.astro.cz/clanky/vzdaleny-vesmir/vyzkumy-v-asu-av-cr-123-prasny-vulkanismus-supernov.html
Press release in English: http://www.iac.es/divulgacion.php?op1=16&id=1481&lang=en

02 | COMPUTATIONAL SCIENCES
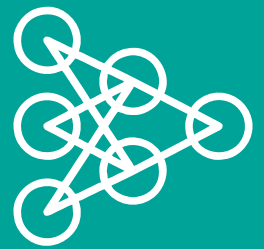
HYPERLOOM: A PLATFORM FOR DEFINING AND EXECUTING SCIENTIFIC PIPELINES IN DISTRIBUTED ENVIRONMENTS

Research institution:	Principal investigators:	Researchers:	Project partners:	Project IDs:
IT4Innovations National Supercomputing Center	Stanislav Böhm, Jan Martinovič	Vojtěch Cima, Vladimir Chupakhin	Janssen Pharmaceutica NV, IMEC, IdeaConsult	OPEN-11-36, OPEN-11-45, DD-15-31, OPEN-11-23

Introduction

Many scientific workloads for supercomputing machines or clusters can be described as interconnected tasks, often with various properties. For example, machine learning pipelines often contain preprocessing, folding for cross-validation, model training, and evaluations. Setting up such a pipeline may be nontrivial for non-experts in HPC. For example, elements to take into consideration include data layout, balance communication costs, and CPU utilization for efficient utilization of the machine.
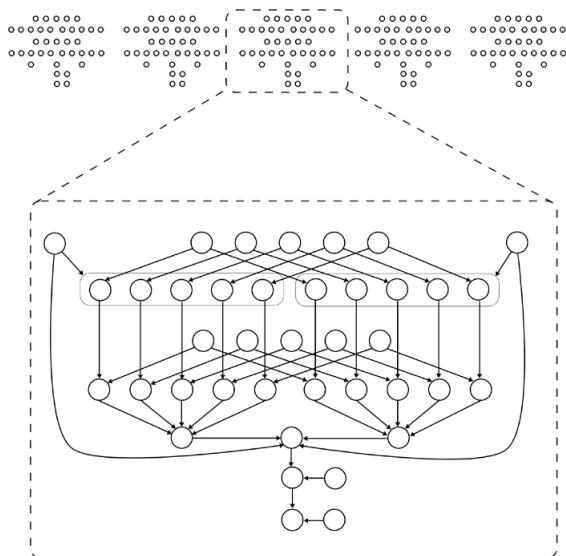
Figure 1. Pipeline

Tool

HyperLoom users can easily define dependencies between computational tasks and create a pipeline which can then be executed on HPC systems. The high-performance core of HyperLoom dynamically orchestrates the tasks over available resources, respecting task requirements. The entire system was designed to have minimal overhead and to efficiently deal with varying computational times of the tasks. HyperLoom allows the execution of pipelines that contain millions of tasks, ranging from basic built-in tasks, through user-defined Python tasks, to relatively large tasks wrapping third-party applications, or a combination of those.

We list the main pipeline properties which define the problem that HyperLoom aims to tackle:

- Task execution time - task execution time may vary from milliseconds (short running tasks) to days (long running tasks) and is difficult to estimate in advance.
- Task output size - the size of the output generated by a task is not known before task finishes. Program Matrix multiplication (MM) – implements the well-known Cannon's algorithm for a distributed matrix multiplication using systolic arrays. Verification was performed with rectangular input matrices and both were divided to sub-matrices with sizes 3x3.
- Plan heterogeneity - a plan may contain tasks of various types.
- Plan size - a plan may contain up to millions of tasks.
- Plan shape - a plan can have the shape of any directed acyclic graph.
- Cluster size - distributed environments, namely HPC clusters, may contain thousands of computational nodes.
- Cluster heterogeneity - different computational nodes may provide various resources with different capacities.

Many existing solutions expect that intermediate results are stored on a shared distributed file system; however, some of our use cases cover many short-living tasks that may produce a large number of intermediate results. This would lead to a high pressure on the file system that could easily become a large bottle-neck in the whole computation process. For this reason, HyperLoom is designed in a way that it does not use a file system for communication. The data are exchanged directly between worker processes on each computational node. However, as it still convenient to work with files for users, we provide an abstraction above this concept. Applications may read and generate files, but they actually live locally in the node and HyperLoom transports them as necessary.

Within the ExCAPE project, HyperLoom has already been used on large-scale machine learning pipelines for the pharmaceutical industry [3], and even by pharma partners themselves together with scalable matrix factorization framework SMURFF developed by Imec Leuven [2]. We also use HyperLoom in other domains represented for example by civil engineering (H2020 ExaQUte project). We provide easy access for non-HPC specialists for execution of HyperLoom pipelines on supercomputer infrastructure through the specialized HPC-as-a-Service framework [4].
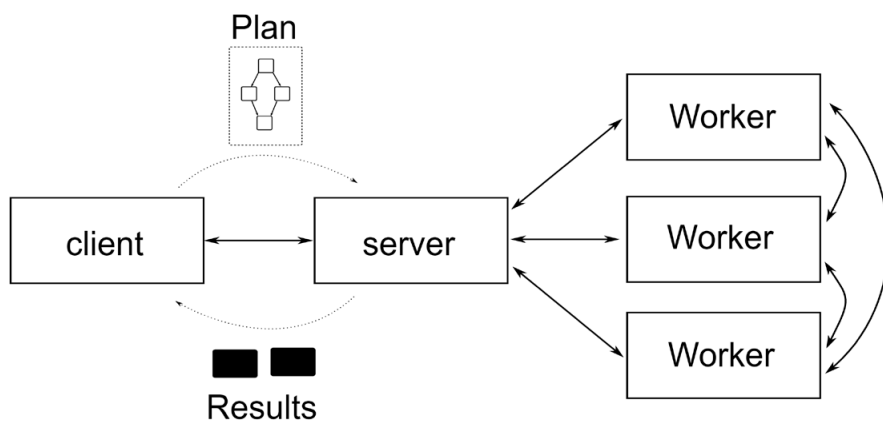
Figure 2.
Architecture

References

[1] The ExCAPE Consortium. ExCAPE: Exascale Compound Activity Prediction Engine. Available at http://excape-h2020.eu/. Retrieved: June 2017.

[2] Vander Aa, T., I. Chakroun, and T. Haber. Distributed Bayesian probabilistic matrix factorization. Procedia Computer Science. 2017, 108, 1030-1039. DOI: 10.1016/j.procs.2017.05.009.

[3] Vander Aa, T., T. Ashby, Y. Vandriessche, V. Cima, S. Böhm, and J. Martinovic. Machine Learning for Chemogenomics on HPC in the ExCAPE Project. INFOCOMP 2017: The Seventh International Conference on Advanced Communications and Computation. June 2017, p. 72–74. ISBN: 978-1-61208-567-8.

[4] Svatoň V., J. Martinovič, N. Jeliazkova, V. Chupakhin, P. Tomančák, Petr Vojta. HPC-as-a-Service for Life Sciences. Poster at Supercomputing Conference 2018. Available at https://sc18.supercomputing.org/proceedings/tech_poster/tech_poster_pages/post192.html

Publication

HyperLoom: http://hyperloom.eu

ESPRESO FEM – HEAT TRANSFER MODULE

Research institution:	Principal investigator:	Researchers:	Project ID:
IT4Innovations National Supercomputing Center	Tomáš Brzobohatý	Ondřej Meca, Lubomír Říha	OPEN-10-15

Introduction

The latest technological advances in computing have brought a significant change in the concept of new product design, production control, and autonomous systems. In the last few years we have been witnessing a considerable transition to virtual prototyping, and gradual pressure to integrate large parts of the industrial sector into the fourth industrial revolution, or Industry 4.0.

The main objective of the project is to create a robust open-source package applicable for a wide range of complex engineering simulations in areas such as mechanical engineering, civil engineering, biomechanics and the energy industry. Our development contributes to the needs of industry, focusing on the smooth implementation of new digital technologies applicable in Industry 4.0. The free licence for the developed package allows automatized simulation chains, based on HPC as a service, such as automatized systems for shape or topological optimization to be created on top of the ESPRESO framework. ESPRESO is a massively parallel framework based on the Finite Element Method for Engineering Application. The added value of this package is a highly scalable solver based on the methods of domain decomposition, which allows the computational capacity of state-of-the-art supercomputers to be fully utilized and thus solve problems with billions of unknowns. In addition, the advantage of this package is also its simple interface for the configuration of implemented solvers.

The ESPRESO framework contains several logical units which can be combined to match the requirements for a specific problem. These units include pre-processing input data, computational mesh processing, FEM/BEM object builders, solution of specific physical problems using massively parallel sparse linear solvers, and finally output data preparation for visualization of the results.

The ESPRESO project was initiated within the FP7 EXA2CT project as an open-source ExaScale PaRallel FETI (a numerical method - Finite Element Tearing and Interconnect) Solver library focused on solution of problems from engineering mechanics. By the end of the project, ESPRESO contained several FETI based domain decomposition algorithms. The most advanced is the Hybrid Total FETI method suitable for parallel machines with tens or hundreds of thousands of cores. The solver is based on a highly efficient communication layer on top of MPI. Its scalability has been tested up to 18,000 compute nodes on the ORNL Titan supercomputer. ESPRESO can also be accelerated by both Nvidia GPU and Intel Xeon Phi accelerators to achieve up to 5x higher performance improvements over general purpose CPUs. In addition, by dynamically tuning several key hardware parameters ESPRESO saves over 20% of its energy consumption. With all these properties, it has real potential to efficiently utilize future exascale systems where both performance and energy efficiency matter.
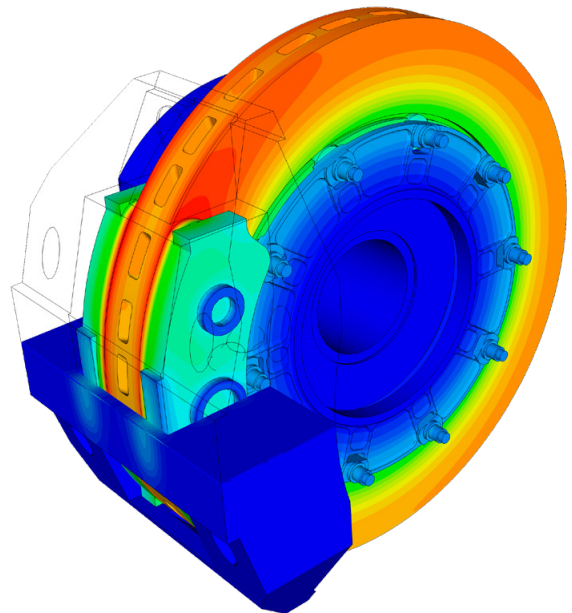
Figure 1.
Simulation of disc brake heating during the braking process

Results and Methods

The ESPRESO team is focusing on development of a complex framework, which will be ready to provide a whole toolchain for solving challenging engineering problems. In Q2 2018, a module for solution of the heat transfer problems via the ESPRESO framework was completed.

The capability list of this module contains many options for the solution of complex heat transfer problems. This list includes nonlinear and transient solvers with automatized time stepping and robust stabilization techniques, complex material models with phase change, linear and nonlinear boundary conditions, mesh morphing based on radial basis functions, translation motion with SUPG and CAU stabilization, asynchronous parallel I/O, input from popular open source and commercial packages like OpenFOAM and ANSYS, result monitoring, output to commonly used post-processing formats like VTK and EnSight, an in-house highly parallel multilevel FETI domain decomposition based solver for billions of unknowns, connection to third party algebraic multigrid solver BoomerAMG [1], adaptive precision control for linear solvers, and many others.

On-going Research / Outlook

A new module for structural mechanics including contact problems will be developed. To provide the possibility to execute simulations on HPC infrastructure using the ESPRESO framework for external non-experienced HPC users, and for custom-made solutions, we will create an online interface with a connection to the HPC as a Service framework developed at IT4I in the ADAS Laboratory. This framework enables integration of HPC computations with internal and external applications. The framework incorporates ideas from cloud infrastructures to high performance computing. The online interface will be split into three main parts: (i) uploading input database files containing computational mesh with the ECF espresso configuration file, which controls all of the solver parameters (the ESPRESO team is developing an offline graphical user interface for simplified setting of all parameters in the ECF), (ii) execution and control of the simulation process, (iii) online results monitoring and reporting.

Conclusion

The open source ESPRESO solver is a massively parallel sparse linear solver designed to take full advantage of today's most powerful petascale supercomputers and improves utilization of HPC systems with emphasis on productivity and efficiency. Effective utilization of HPC systems has a significant impact on the validity of allocating financial resources to HPC infrastructures from a global point of view. Through their research activities, the research laboratories at IT4Innovations collaborate with industrial partners, helping to efficiently solve the numerous problems associated with heat transfer.

Continuous development of new modules for the ESPRESO framework allows potential users from the commercial sector to solve a wider portfolio of physical problems such as highly nonlinear multiphysical problems, mechanical vibration, contact problems, and time dependent problems.
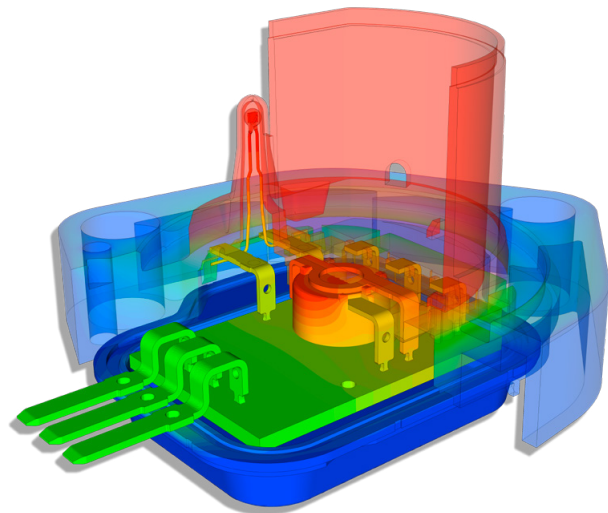
Figure 2.
Thermal simulation of the USL sensor – Continental Automotive

Reference

[1] Lawrence Livermore National Laboratory: HYPRE: Scalable Linear Solvers and Multigrid Methods. Available at http://www.llnl.gov/casc/hypre/

Publications

Říha, L., M. Merta, R. Vavřík, T. Brzobohatý, A. Markopoulos, O. Meca, T. Kozubek, V. Vondrák. Massively parallel and memory efficient FEM toolbox with Hybrid Total FETI solver with accelerator support. The International Journal of High Performance Computing Applications. 2018, SAGE Publications. DOI: 10.1177/1094342018798452.

Říha, L., T. Brzobohatý, A. Markopoulos, O. Meca, and T. Kozubek. Massively parallel hybrid total FETI (HTFETI) solver. In: Proceedings of the Platform for Advanced Scientific Computing Conference on - PASC '16. New York, USA: ACM Press, 2016, p. 7:1–7:11. DOI: 10.1145/2929908.2929909.

Project website: http://espreso.it4i.cz/

PARALLEL PROCESSING OF SEQUENTIAL MESH DATABASES

Research institution:	Principal investigator:	Researchers:	Project ID:
IT4Innovations National Supercomputing Center	Tomáš Brzobohatý	Ondřej Meca, Lubomír Říha	OPEN-12-63

Introduction

A wide range of engineers from industrial practice use numerical methods to simulate physical processes. The process of simulation can be divided into two parts (i) creation of a numerical model (finite element mesh, definition of boundary conditions, contact interfaces, etc.) and (ii) its solution. Since the solution quality is dependent on the numerical model, it is necessary to use an efficient and robust tool for its creation. A typical example is problems arising from structural mechanics, where the creation of a high-quality numerical model is one of the most complicated, and the most important parts of the simulation process. This is especially true for complex geometries of real-world problems.

In general, high-quality models are usually provided by commercial tools that produce sequential mesh databases (ANSYS, ABAQUS, HYPERMESH, ANSA), which can be defined as a database that is not assumed to be read efficiently in parallel. Hence, well known parallel open source tools must be able to convert external sequential database files into their own parallel database structures. For example, in the case of OpenFOAM, users have to convert the external database to the OpenFOAM format sequentially, and then use the *decomposePar* utility [1] for sequential creation of an initial decomposition that can later be redistributed in parallel. Similarly, Elmer FEM contains an ElmerGrid [2] tool that prepares meshes for ElmerSolver. This sequential conversion process greatly slows down, and in some cases even inhibits the connection between tools that generate sequential data and parallel solvers. This is one of the key factors that contributes to the low interest in HPC resources of the mainstream engineering community, who desire to use commercial tools for the pre-processing stage.

Our motivation is to connect tools for creation of complex engineering models and open source parallel solvers to allow broader usage of HPC by the engineering community. Through this direct connection, we achieve robust pre-processing together with the possibility to use various highly parallel solvers that are able to solve non-standard problems.

# of nodes	8	16	32	64	128	256	512
MPI I/O	8.45	6.76	6.76	6.76	6.76	6.76	6.76
Parse	7.96	3.99	2.05	1.11	0.64	0.5	0.46
Clusterization	61.8	33.1	17.6	9.47	5.54	3.33	2.57
ParMETIS	12.3	5.53	2.67	1.46	1.19	1.42	1.65
Pre-Processing	82.1	37.7	17.6	8.62	4.6	3.68	2.25
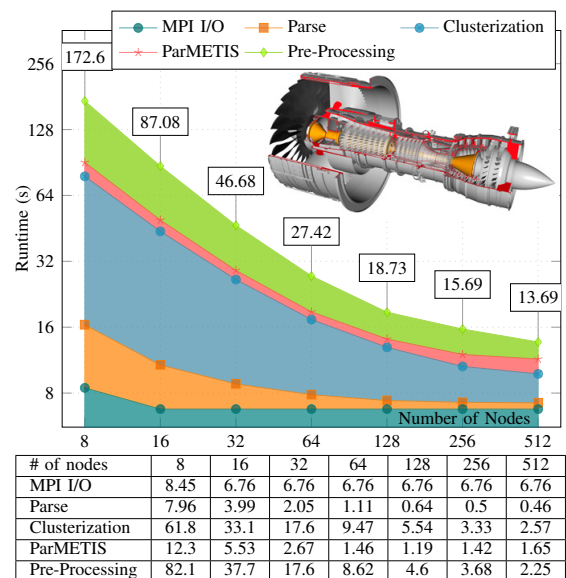
Figure 1.
Strong scalability for the Jet Engine benchmark including values for all points in the chart

Results and Methods

In this project we developed a novel approach for parallel loading of unstructured meshes that was implemented in the open source library ESPRESO [3]. The algorithm can be used for both (i) converting the input sequential mesh file to a parallel one, and (ii) as a direct loader and pre-processor of massively parallel solvers. The key challenge is that the database file stores elements in a spatially scattered fashion. The reason is that the file was not stored with the expectation of being read in parallel. The algorithm has two stages: in the first stage, the

input file is read in parallel by MPI I/O to the main memory of all compute nodes. It efficiently utilizes the I/O performance of the cluster storage. Then each MPI process parses its own portion of data simultaneously. Since individual MPI processes have no information about data loaded by other MPI processes, the purpose of the second step is to link data together in a way that it is suitable for later processing based on Domain Decomposition Methods (DDM).

Figure 1 shows an evaluation of the developed approach for the jet engine benchmark (mesh generated by the widely used commercial Ansys Workbench tool and stored in its native ascii solver format) with 12 MPI processes per node and 2 OpenMP threads. This configuration represents the optimal setting for the Salomon cluster from the workflow point of view. The processing time and scalability for a given benchmark depends on the mesh size rather than its geometry. This allows optimal parallelization based on the known mesh size only. Despite the fact that not every step of the algorithm is fully optimized in our implementation, the scalability tests show very promising results. The jet engine benchmark, which contains about 800 million nodes and 500 million elements, can be processed in 6.9s using 6144 MPI processes on 512 nodes of the Salomon supercomputer. An additional 6.8s is needed for MPI I/O to load and distribute the 142GB (21 GB/s throughput) file from the Lustre storage to compute nodes' memory. If this file were read sequentially, the I/O itself would take approximately 5 minutes (500MB/s throughput) and the whole workflow would take approximately at least 2 hours.
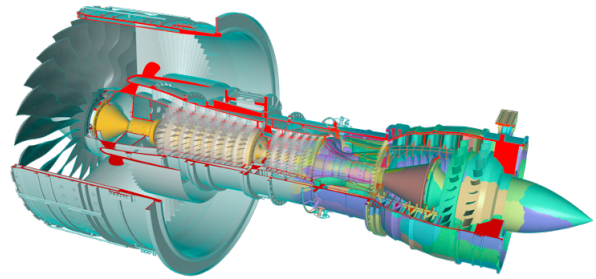
Figure 2.
Jet engine before and after domain decomposition

On-going Research / Outlook

We plan to implement loading of other formats and further optimize particular steps of the workflow. In some cases, it is possible to combine multiple steps, and overlap communication with processing. We will also investigate techniques to hide processing behind the MPI I/O, and other scalable decomposition techniques. Finally, our goal is to develop a standalone converter that performs fast conversion between sequential meshes, and native parallel formats of selected solvers.

Conclusion

In the project we developed a workflow that can be used for parallel loading of sequential mesh databases. It has been shown that despite the sequential nature of input data, they can be effectively parsed in parallel. The workflow was implemented in the ESPRESO library as a proof of concept. In the future, we will provide a library with this algorithm for other researchers.

References

[1] OpenFOAM documentation [online]: Running applications in parallel. Available at https://www.openfoam.com/documentation/user-guide/running-applications-parallel.php

[2] Raback, P. ElmerGrid manual. CSC – IT Center for Science, Tech. Rep., 2015. Available at http://www.nic.funet.fi/pub/sci/physics/elmer/doc/ElmerGridManual.pdf

[3] Říha, L., T. Brzobohatý, A. Markopoulos, O. Meca, and T. Kozubek. Massively Parallel Hybrid Total FETI (HTFETI) Solver. In: Proceedings of the Platform for Advanced Scientific Computing Conference on - PASC '16. New York, USA: ACM Press, 2016, p. 7:1–7:11. DOI: 10.1145/2929908.2929909.

BAYESIAN INVERSION IN PDEs ACCELERATED USING SURROGATE MODELS

Research institution:	Principal investigator:	Researcher:	Project partner:	Project ID:
IT4Innovations National Supercomputing Center	Simona Domesová	Michal Béreš	The Institute of Geonics of the Czech Academy of Sciences	OPEN-12-45

Introduction

Mathematical modeling of complex problems arising in various engineering fields usually involves intensive computations, including solution of partial differential equations (PDEs) and their systems. Engineers are often interested in evaluating the mathematical model for various values of input parameters that control the behavior of the model.

A specific need of repetitive solutions of complex models arises in the case of solving identification problems: Measurements that correspond to an unknown combination of input parameters are given, and the aim is to determine or to describe mathematically the unknown parameters. They represent e.g. boundary conditions, source, or material in a domain of interest.

For the deterministic approach, the result is a point estimate of the parameters that fits best to the observations. Therefore, the solution may not be unique. For the Bayesian approach, the vector of input parameters is treated as a random vector, and the aim is to describe its joint probability distribution (called posterior distribution). The Bayesian approach expects that measurements are distorted by noise, which is an important advantage compared to standard deterministic methods that do not take inaccuracies in the observed data into consideration. Furthermore, the Bayesian approach incorporates information about the unknown parameters available from experiences in the form of a prior distribution of the random vector.

The main aim of this project was the development and testing of efficient procedures for sampling the posterior distribution, which is particularly suitable when identification problems are governed by computationally expensive forward models.

Results and Methods

Since the resulting probability distribution depends on a complex mathematical model, it cannot be expressed analytically or sampled directly. Instead, the Metropolis-Hastings (MH) algorithm and its modifications can be used, see [1]. This algorithm is based on sequential proposing of samples from a chosen proposal distribution, each proposed sample is either accepted or rejected. This way, a Markov chain of correlated samples from the posterior distribution is created. In each step, the forward model has to be evaluated for a proposed vector of parameters. Therefore, the standard MH algorithm is com-

scatter real

-4.5e-02   -0.02   0   0.02   4.0e-02
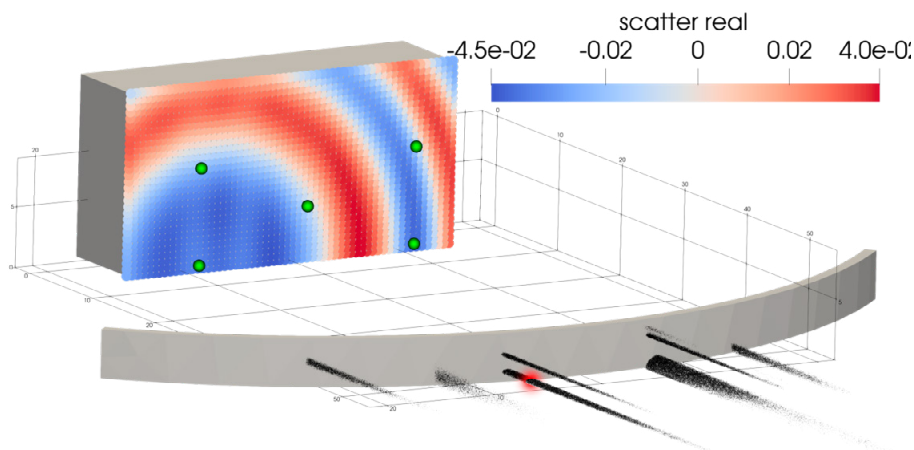
Figure 1.
Visualization of posterior samples (Source position identification)

putationally intensive. To reduce the number of evaluations, we focus on sampling methods based on the delayed acceptance MH (DAMH) algorithm, see [2]. In the resulting sampling framework, some of the evaluations of G are replaced by significantly cheaper evaluations of a surrogate model. For the construction of the surrogate model, we tested two non-intrusive approaches: radial basis functions (RBF) interpolation, and the stochastic collocation method (SCM).

In the first identification problem, the forward model is given by the solution of a half-space sound scattering problem modeled by the Helmholtz equation, see [3] and Figure 1. The prior distribution is N(0;10) in x, Exp(5) in y and Exp(1) in z coordinate (we know that the source is behind the barrier and above the ground). Green points are the locations of 5 noisy measurements (a real part of the complex wave). The red point represents the real position of the source that was chosen for the simulation. Posterior samples (visualized as black dots) were generated using 102 instances of the DAMH algorithm running in parallel. In all tests, Gaussian random walk was used as the proposal distribution. Its standard deviation (std) can be found in Table 1. To compare the quality of several sampling processes, autocorrelation time (AT) was also estimated (distance between samples in a Markov chain that can be treated as almost uncorrelated). Based on this quantity, cost per one almost uncorrelated sample (CpUS) was calculated.

	proposal std	AT	CpUS
DAMH RBF	$0.1 \cdot$ prior std	2333	**79.8947**
DAMH RBF	prior std	4199	**4.7006**

Table 1.
Sampling efficiency (Source position identification)

The second model problem is governed by the Darcy flow equation. The domain consists of two materials with different hydraulic conductivity parameters. Their structure is given (see Figure 2), but their values are unknown. The measurement is total flow through the left part of the boundary.

It was expected a priori that the first of the materials is highly pervious and the second is moderately pervious (represented by a Gaussian prior distribution with a mean of $\mu 0 = (8.0, 5.0)$. For the posterior pdf see Figure 3. The use of both RBF and SCM surrogate models was tested, see Table 2.

	proposal std	AT	CpUS
MH	0.1	1127.3	**1127.3**
DAMH RBF	1.2	427.1	**3.7**
DAMH SCM	1.2	432.6	**4.5**

Table 2.
Sampling efficiency (Hydraulic conductivity identification)
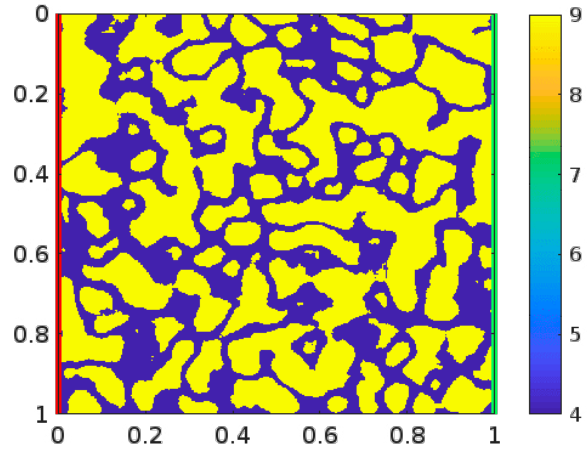
Figure 2.
Structure of materials
(Hydraulic conductivity identification)
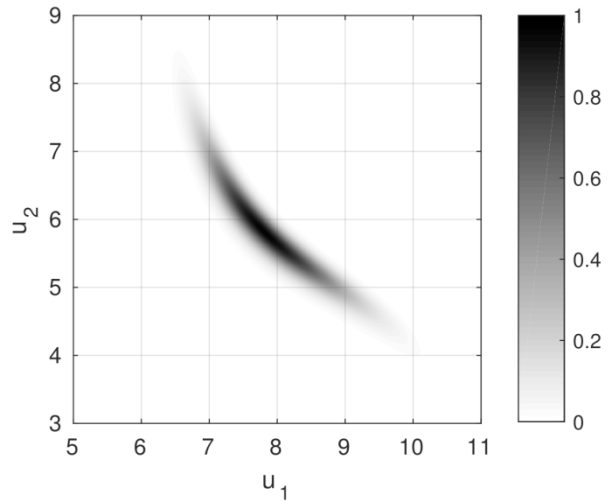
Figure 3.
Posterior pdf (highly pervious parameter u_1, medium pervious parameter u_2)

On-going Research / Outlook

Our current work focuses on further development of the current framework for efficient sampling of posterior distributions. The framework is implemented in Python using mpi4py, and several Markov chains that are constructed in parallel processes (samplers) and share one iteratively updated surrogate model. The solvers for forward problems are assumed as black box parallel libraries running on MPI sub-communicators provided by the Python framework. Future research directions also include combining the current approach with the parallel tempering method.

Conclusion

The numerical experiments showed that surrogate models can be successfully used to accelerate the process of posterior sampling. Due to the non-intrusive character of all the used methods, various identification problems can be solved. To use this sampling framework, only a solver using the forward mathematical model is required.

In the case of the first model problem, the cost of the forward model evaluation did not allow the use of the standard MH algorithm; however, using surrogate models, posterior samples were successfully provided. In the second model problem, the sampling cost was reduced by a factor of 300 in comparison to the standard MH algorithm, see Table 2.

References

[1] Robert, C. P. The Bayesian choice: From decision-theoretic foundations to computational implementation. 2nd ed. New York: Springer, c2007. ISBN 9780387715988.

[2] Christen, J. A., and C. Fox. Markov chain Monte Carlo Using an Approximation. Journal of Computational and Graphical Statistics. 2005, 14(4), 795-810. DOI: 10.1198/106186005X76983.

[3] Kravčenko, M., M. Merta, and J. Zapletal. A massively parallel ACA BEM for Helmholtz problems. SIAM Journal on Scientific Computing. Submitted (2018).

Publications

Blaheta, R., M. Béreš, S. Domesová, and P. Pan. A comparison of deterministic and Bayesian inverse with application in micromechanics. Applications of Mathematics. 2018, 63(6), 665-686. DOI: 10.21136/AM.2018.0195-18.

Domesová, S. The use of radial basis function surrogate models for sampling process acceleration in Bayesian inversion. The 5th International conference on Advanced engineering – Theory and Applications (AETA 2018), 11–13 September 2018, Ostrava, Czech Republic.

Domesová, S., and M. Béreš. Inverse Problem Solution using Bayesian Approach with Application to Darcy Flow Material Parameters Estimation. Advances in Electrical and Electronic Engineering. 2017, 15(2), 258 - 266. DOI: 10.15598/aeee.v15i2.2236.

Domesová, S., and M. Béreš. A Bayesian Approach to the Identification Problem with Given Material Interfaces in the Darcy Flow. Kozubek, T., M. Čermák, P. Tichý, R. Blaheta, J. Šístek, D. Lukáš, and J. Jaroš, ed. High Performance Computing in Science and Engineering. Cham: Springer International Publishing, 2018, 2018-07-17, p. 203-216. Lecture Notes in Computer Science. DOI: 10.1007/978-3-319-97136-0_15.

ADAPTATION OF HEURISTIC ALGORITHMS FOR DIFFERENT INSTANCES OF THE VEHICLE ROUTING PROBLEM, AND DEVELOPMENT AND OPTIMIZATION OF SOLVERS FOR THE VEHICLE ROUTING PROBLEM

Research institution:
IT4Innovations
National
Supercomputing
Center

Principal investigators:
Kateřina Slaninová,
Ekaterina Grakova

Researchers:
Matteo Salani,
Roberto
Montemanni,
Jan Martinovič,
Radim Sojka

Project partners:
The Dalle Molle
Institute for Artificial
Intelligence,
The University
of Applied Sciences
of Southern
Switzerland

Project IDs:
OPEN-12-36,
OPEN-12-38

Introduction

The first project was focused on testing and adaptation of heuristic algorithms for different instances of the Routing Problem on a real use case using IT4Innovations infrastructure. The second project was focused on the development of optimized parallel solvers for several variants of the Vehicle Routing Problem (VRP). It included an extension of our current implementation of the heuristic method and metaheuristic method. Furthermore, we intended to search for optimal parameter settings for the algorithms we created using the hyperparameter search method. Algorithms were tested on a real data set from waste collection, on the Solomon benchmarks, and on a real data set from oil collection. We also prepared a specific use case based on real data for testing algorithms on HPC infrastructure.

VRP are tasks which resolve the most efficient delivery route of goods from the distribution centre to individual customers. The requirements of an individual customer will not fill capacity of the vehicle, i.e. during one journey we can service more customers. Nowadays, there exists a large number of variants to the Routing Problem based on the limiting conditions. In these projects we used Periodic VRP, and the Sequential Ordering Problem (SOP). There are many algorithms to solve VRP and SOP. In the projects, we focused on exact algorithms, heuristic algorithms, and metaheuristic algorithms.

One of the tools used for testing the algorithms was Hyper-Loom [1]. HyperLoom is a platform for defining and executing pipelines in a distributed environment. This platform aims to be a highly scalable framework that is able to efficiently execute millions of interconnected tasks on hundreds of computational nodes. We used HyperLoom to define and execute the VRP hyperparameters sweep pipeline.

Results and Methods

Exact method

We used the Branch-and-Bound method for the experiments. The Branch and Bound method is one of the basic exact methods for solving optimization problems. In this method, the search tree is created dynamically. The initial tree is formed only by the root node. In the case of a minimization problem, the algorithm holds lower and upper bounds. The upper bound represents the cost of the best-found solution so far. The lower bound is estimated based on the relaxation of the origin problem. In each iteration of the algorithm, one node is selected for searching. The corresponding relaxation is solved, and the solution is compared with the bounds. If the relaxation solution is greater than the upper bound, then the node is discarded. If we have found an integral solution, we will compare it with the best-known solution so far. If the new solution is better, the upper bound is updated. If we get a non-integral solution with a cost lower than the upper bound, the node is branched, so the solution subspace is divided into smaller solution subspaces, the lower bound is updated, and the next node is selected. The algorithm is terminated if there are no nodes to be searched [2].

An OpenMP Parallel implementation of the exact algorithm was prepared, and the three different benchmark suites TSPLIB [5], SOPLIB [4], and COMPILERS [3] were used to test the parallelization of the algorithm on IT4Innovations HPC infrastructure.

Heuristic method

The heuristic method was tested on a specific use case situated in Ostrava, the Czech Republic (Figure 1). We prepared a set of 1,008 different locations for the oil collection problem where the amount of oil for each location was known. Travel time between any of the two locations was set and also metric distances between the locations were created. The vehicles start at the central depot. We used a two-level approach similar to the first assigned strategy used for PVRP [6]. The assignment of customers to vehicles and working days were managed on the first level of the heuristic and explored using a local search. The second level optimized the single routes of the different vehicles on different days. The changes imposed by the first level local search algorithm affected a portion of the solution (two routes). Therefore, only two routes were re-optimized, and usually the starting solution was already of a good quality.

A HyperLoom pipeline for this type of problem was prepared. We leveraged the possibilities and benefits of using the hyperparameter search for solving the Periodic Vehicle Routing Problem for exhausted oil collection by execution on the supercomputing infrastructure using the HyperLoom platform. The quality of results for the heuristic algorithm depended on the adjustment of the configuration parameters of the algorithm. For eight input parameters: number of vehicles, depot number, weight, random seed, horizon days, vehicle capacity, location per day, and liter per day, we created 6,000 combinations of configuration parameters.

During the experiments the execution time of the algorithm was monitored, with results between 62.999 sec. and 201.839 sec. for different configurations of the input parameters. A histogram of execution time is given in Figure 2.

The execution time of the algorithm is dependent on the input parameters. We also assessed the dependence of execution time on the input parameter values and the importance of parameter values for total execution time.

As can be seen from the results (Figure 3), the total execution time is dependent on only two input parameters: liter per day and number of vehicles.

Metaheuristic method

Swarm Intelligence algorithms are inspired by the real-life behaviour of multi-agent systems organised for instance by ants, bats and bees [7]. These Optimization algorithms are commonly used for optimization problems, such as TSP and VRP. We used Ant Colony Optimization (ACO) [8] in the pro-

THE VEHICLE ROUTING PROBLEM
DEPOT (ORIGIN/DESTINATION) AND CUSTOMERS (STOPS)

○ Depot · Customers
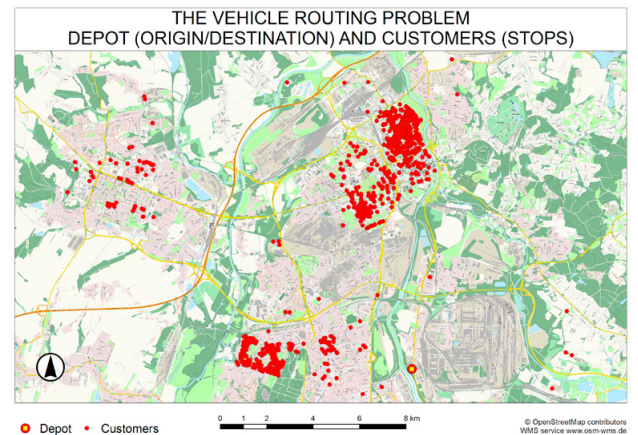
Figure 1.
GPS locations in Ostrava
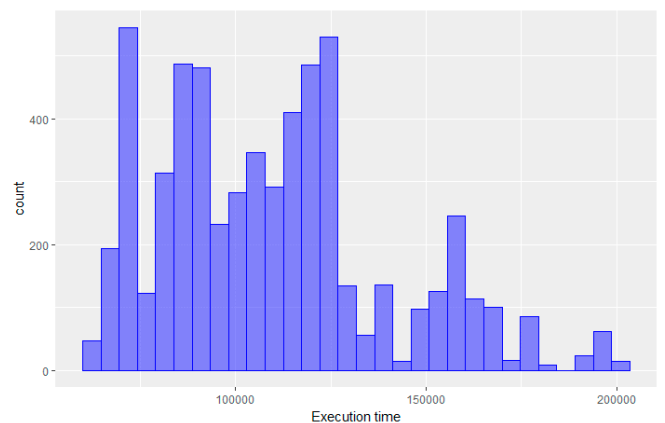
Figure 2.
Histogram of execution time

ject. This metaheuristic technique is based on the observations of the behaviour of real ant colonies looking for food. Though some ants are completely blind, they are nevertheless still able to find food. When ants are looking for food, they just go straight forward till they find some. To find a path back, they lay down a substance called pheromone. The amount of pheromone used in the path determines the quality of the path.

Ant Colony Optimization was tested on a real data set from waste collection. We used different combinations of input parameters to improve the quality of the result of the ACO algorithm. We used 25 different combination parameters in experiments for testing of the appropriate parameters settings for the ACO algorithm.
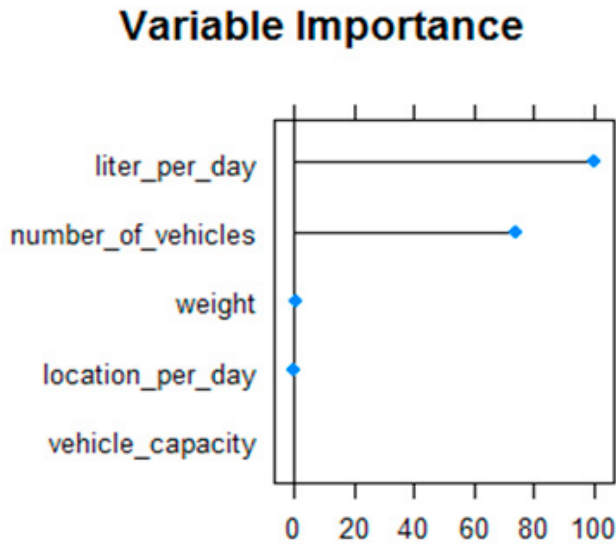
Figure 3.
Parameters' importance

On-going Research / Outlook

We are currently working on the development of a new type of parallelization for the exact algorithm. We are preparing new test sets for optimization algorithms. The HyperLoom platform will be used for the definition of a new hyperparameter search pipeline for the ACO algorithm. We will research more complicated but still unexplored models for optimization algorithms.

Conclusion

In these projects, we demonstrated the possibilities and benefits of using the hyperparameter search for solving the Periodic Vehicle Routing Problem for exhausted oil collection. We have observed the dependence of the total execution time values on the number of nodes. We also assessed the dependence of execution time on the input parameter values, and the importance of parameter values for total execution time for the heuristic algorithm. Using the HyperLoom platform for our problem, we showed that HPC infrastructure is very useful for the optimal setting of the input parameters (hyperparameter search) for Periodic Vehicle Routing Problem algorithms using larger instances. We used different benchmarks (TSPLIB, SOPLIB, COMPILERS, Solomon benchmarks, and real date) for the testing of the developed algorithms.

References

[1] Cima, V., S. Böhm, J. Martinovič, J. Dvorský, J. T. Ashby, V. Chupakhin. HyperLoom possibilities for executing scientific workflows on the cloud. Barolli, L., and O. Terzo, eds. Complex, Intelligent, and Software Intensive Systems. Cham: Springer International Publishing, 2018, 2018-07-05, p. 397-406. Advances in Intelligent Systems and Computing. DOI: 10.1007/978-3-319-61566-0_36.

[2] Jamal, J., G. Shobaki, V. Papapanagiotou, L. M. Gambardella, R. Montemanni. Solving the Sequential Ordering Problem using Branch and Bound. In: 2017 IEEE Symposium Series on Computational Intelligence (SSCI). IEEE, 2017. DOI: 10.1109/SSCI.2017.8280805.

[3] Shobaki, G., J. Jamal. An exact algorithm for the sequential ordering problem and its application to switching energy minimization in compilers. Computational Optimization and Applications. 2015, 61(2), 343-372. DOI: 10.1007/s10589-015-9725-9.

[4] Montemanni, R., D. H. Smith, L. M. Gambardella. A heuristic manipulation technique for the sequential ordering problem. Computers & Operations Research. 2008, 35(12), 3931-3944. DOI: 10.1016/j.cor.2007.05.003.

[5] Reinelt, G. TSPLIB: a library of sample instances for the TSP (and related problems) from various sources and of various types. Available at http://comopt.lfi. uniheidelberg.de/software/TSPLIB95.

[6] Baptista, S., R. C. Oliveira, E. Zuquete. A period vehicle routing case study. European Journal of Operational Research. 2002, 139(2), 220–229. DOI: 10.1016/S0377-2217(01)00363-0.

[7] Yang, X., M. Karamanoglu. Swarm intelligence and bio-inspired computation: An Overview. Swarm intelligence and bio-inspired computation. Elsevier, 2013, p. 3-23. DOI: 10.1016/B978-0-12-405163-8.00001-6.

[8] Dorigo, M., V. Maniezzo, A. Colorni. The ant system: An autocatalytic optimizing process. Technical Report, 91-016, 1991. Dipartimento di Elettronica, Politecnico di Milano, Milano, Italy. Available at http://citeseerx.ist.psu.edu/viewdoc/download?doi=10.1.1.51.4214&rep=rep1&type=pdf

Publication

TIME SERIES QUALITATIVE CHARACTERISTICS OF COMPLEX SYSTEMS USING HPC

Research institution:
IT4Innovations National Supercomputing Center, VŠB – Technical University of Ostrava

Principal investigator:
Marek Lampart

Researchers:
Tomáš Martinovič, Jaroslav Zapoměl

Project IDs:
OPEN-9-6, OPEN-10-8

Introduction

In general, systems show regular as well as chaotic patterns. The regularity corresponds to the periodic (or quasi-periodic) movements that are related to the equilibrium – stable attractor. On the other hand, irregularity detects chaotic paragons, so called strange attractors. Both the above stated situations have attracted researchers for decades, and many experimental tools, like the 0-1 test for chaos, approximate entropy, RQA analysis etc., have been rapidly developed for the detection of chaos. The main aim of the project was to compute values that detect chaotic or periodic movements using classical tools e.g. recurrent matrices, approximate entropies, and the newly established 0-1 test for chaos.

Results and Methods

The main outputs, supported by two OPEN projects 9-6 and 10-8, can be characterized as quantification and qualification of the dynamical properties of complex systems using HPC.

The main aim of the research activity supported by the OPEN-9-6 project is to extend knowledge of the behaviour of the given coupled map lattice (CML) models. There are detected regions of parameters where these systems are showing regular movement, regions of parameters where chaos appears, and regions of parameters where a period doubling effect is observable. These results will enhance the understanding of the underlying dynamics of CML models that are related to many real problems, such as the spatial profile of a chemical concentration, a population density, a velocity field etc. [1]. For this purpose, the 0-1 test for chaos was utilized, see Figure 1, and implemented in R, and subsequently was published as software output [2], and auxiliary one-dimensional results were reached [3].

The research in [4, 5], supported by the OPEN-10-8 project, was motivated by the real technological problem of vibrations of bodies hanging on chains or ropes in tubes or spaces limited by walls or other bodies. The studied system has two degrees of
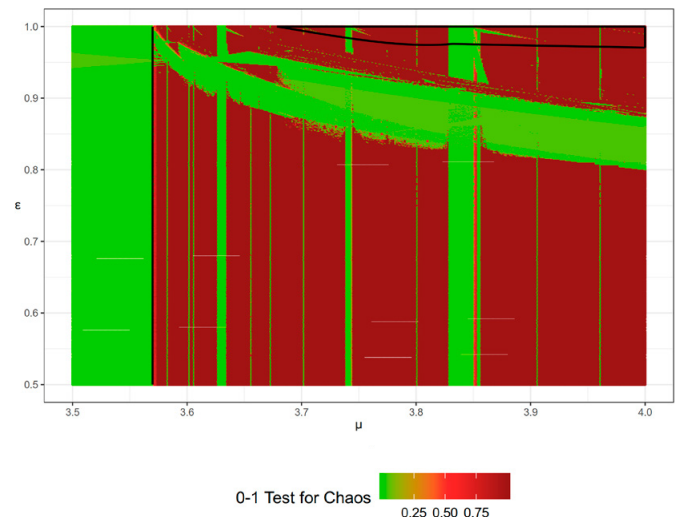
Figure 1.
Output of the 0-1 test for chaos of the CML model studied in [1]

freedom. It is formed by two pendulums moving between two walls, see Figure 2. Its movement is governed by a set of non-linear ordinary differential equations. The results of the simulations showed that the system exhibits regular, see Figure 3, and chaotic movement. The simulations were performed for three excitation amplitudes, and a range of excitation frequencies. The aim of the investigations was to determine the character of the pendulums' motions, and to identify their collisions with the sided walls.
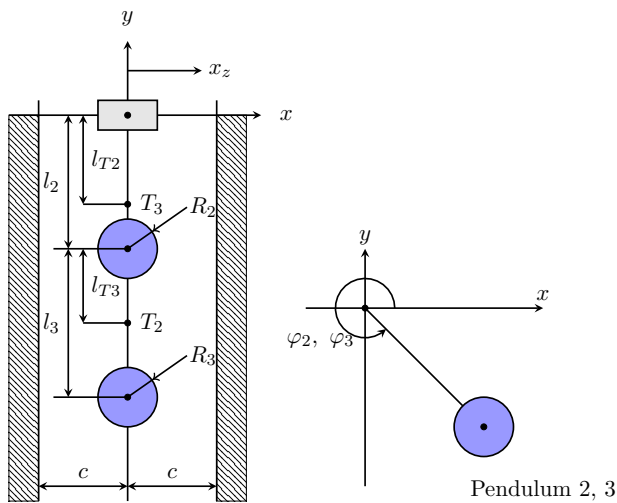
Figure 2.
Model of the double-pendulum mechanical system introduced in [4]

Figure 3.
Phase diagram of the model investigated in [4] showing high period movement

The main aim of [6, 7], supported by the OPEN-10-8 project, is to study the evolution of the transmembrane potential of cardiac cells under different rates and amplitudes of stimulation. For modelling this potential, a modification of the Fenton-Karma model was applied. It is a phenomenological model with three degrees of freedom that corresponds to non-dimensional transmembrane potential and gating variables for regulation of inward and outward ion currents which can better reproduce the shape of the transmembrane potential than the original Fenton-Karma model. The model was newly forced by a stimulus with the shape of the half-sine period. As the main goal of the paper is to show that this model is showing regular as well as irregular motion, periodic as well as chaotic patterns are detected using bifurcation diagrams, the Fourier spectra, and the 0-1 test for chaos.

On-going Research / Outlook

Currently, the team of Dynamical systems analysis is developing and improving tools for dynamical property detection tools; classical as well as newly established. This research is driven by real technological device problems that are well simulated, and also by real data problems.

Conclusion

Due to the support of the IT4Innovations OPEN projects 9-6 and 10-8 we were able to obtain very interesting results from chaos testing using classical tools e.g. recurrent matrices, approximate entropies, and the newly established 0-1 test for chaos. All the topics discussed here are being developed widely, and are attracting much interest from researches.

References

[1] Lampart, M., and T. Martinovič. Chaotic behaviour of the CML model with respect to the state and coupling parameters. Journal of Mathematical Chemistry. Submitted.

[2] Martinovič, T. 2016. Chaos01: 0-1 Test for Chaos. R package version 1.1.1. https://CRAN.R-project.org/package=Chaos01 (R).

[3] Lampart, M., and T. Martinovič. A survey of tools detecting the dynamical properties of one-dimensional families. Advances in Electrical and Electronic Engineering. 2017, 15(2), 304–313. DOI: 10.15598/aeee.v15i2.2314.

[4] Lampart, M., and J. Zapoměl, Double-pendulum with both-sided stops simulation analysis. In: J. Vigo-Aguiar et al. (edts.). In Proceedings of the 17th International Conference on Computational and Mathematical Methods in Science and Engeneering (CMMSE). Rota, Cadiz, España, 2017, p. 1230-1236.

[5] Lampart, M., and J. Zapoměl. Dynamical properties of a nonautonomous double pendulum model. Mathematical Methods in the Applied Sciences. 2018, 41(17), 7106-7114. DOI: 10.1002/mma.4650.

[6] Halfar, R. Dynamics of the FK3V cardiac cell model. In: J. Vigo-Aguiar et al. (edts.). In Proceedings of the 17th International Conference on Computational and Mathematical Methods in Science and Engeneering (CMMSE). Rota, Cadiz, España, 2017, p. 1022-1029;

[7] Halfar, R., and M. Lampart. Dynamical properties of the improved FK3V heart cell model. Mathematical Methods in the Applied Sciences. 2018, 41(17), 7472-7480. DOI: 10.1002/mma.5060.

ADVANCED TIME SERIES ANALYSIS USING HPC COMPUTING

Research institution:	Principal investigator:	Researchers:	Project partners:	Project ID:
IT4Innovations National Supercomputing Center	Tomáš Martinovič	Kateřina Slaninová, Kateřina Janurová, Lukáš Rapant, Martin Rusek	Charles University, The University of Bordeaux	OPEN-11-50

Introduction

This project was focused on the analysis of time series in several domains. The possibility of cover song identification (matching cover songs to their respective originals) was studied in collaboration with Charles University and the University of Bordeaux. New inputs, such as different representation of chords, notes changes, tempo, number of voices etc. were used together with the algorithms for clustering of the time series. These algorithms can discern similarities between songs, even there is a different tempo, or even different keys in the song. Ultimately we were able to match, and sometimes slightly outperform the best algorithms in the field.

Additionally, time series clustering in the problem of inventory optimization based on sales forecasts was tested. In this case, groups of products with similar historic sales were found and used to set different levels of optimal inventory for individual products. Instead of finding the optimal settings for each product individually it is possible to use the optimal settings for groups of products. In this way, a great deal of computational time was saved with negligible impact on the results.

Finally, the application of probabilistic graphical models on traffic time series was used for the generation of synthetic uncertain traffic time series of speed (called probabilistic speed profiles) for the purpose of realistic testing of routing algorithms developed in the H2020 ANTAREX project.

Results and Methods

Three main areas of time series analysis were studied.

One was the clustering of the time series, which was used for cover song identification and inventory optimization problems. It was shown that dynamic time warping can be used effectively in the cover song identification problem and can improve the correct matching of songs and cover songs based on different input data [1, 2]. New data inputs, such as different representation of chords, notes changes, tempo, number of voices, etc. were tested. The tested algorithms could discern similar songs,
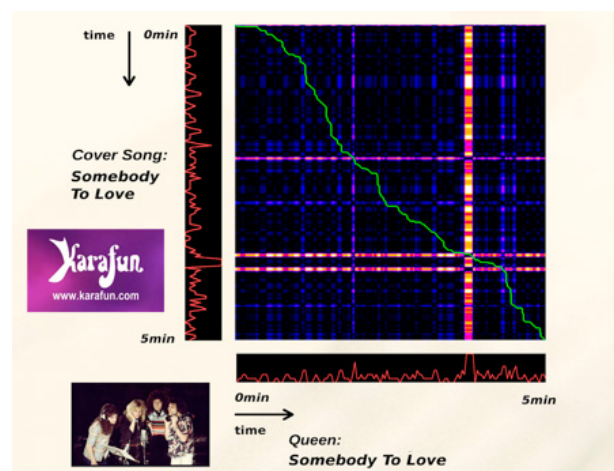
Figure 1.
Cover Song Identification

even when songs had different tempos, and were played in a different key. Ultimately, we were able to match and sometimes slightly outperform the best algorithms in the field. In Figure 1. is shown warping path of "Somebody To Love" cover song and its original.

Recurrence quantitative analysis was used to extract features from the time series, and partitioning around medoids was used to group the time series of product consumption. Optimal parameter settings for the inventory control algorithm were found for the central members of the groups. Figure 2. shows the cluster on two dataset and their silhouettes, which visualize how much is the object similar to its cluster compared to the other clusters. These settings were used for all members

of the group, greatly reducing the computational time necessary to find the optimal parameters for individual time series. The results for the proposed approach were compared against the optimal results for each individual time series and it was shown that there is a negligible effect on the inventory optimization results. [3]

Additionally, the application of probabilistic graphical models on traffic time series was investigated. We utilized several Markov models with a focus on various versions of Markov chains. The main task of these models was the generation of a synthetic uncertain traffic time series of speed (called probabilistic speed profiles) for the purpose of realistic testing of routing algorithms developed in the NPU II project. These profiles were generated by Markov chain models based on the spatial and temporal properties of each part of the road network (i.e. time series for each segment of the network were generated by a succession of Markov chains which were determined by the type of road and current period of the day and week). Figure 3. shows heatmap of probability of traffic incident for D1 motorway during one weak generated by our model (axis x represents segments of D1 and axis y 15 minute time intervals).

On-going Research / Outlook

We plan to further study time series clustering algorithms and test new approaches of time series feature extraction to further improve the clustering performance. Additionally, different clustering methods will be studied and possibilities for combining the results of different clustering methods will be analyzed.

Conclusion

We investigated time series clustering in two different settings, a cover song identification, and inventory optimization. For song identification we were able to leverage new inputs, and outperform some of the best algorithms in the field. For inventory optimization we were able to greatly reduce the computational time necessary for finding the near optimal parameter settings for the time series. We also used the Markov chains and hidden Markov models to create synthetic probabilistic speed profiles which were used for the testing of algorithms developed in the H2020 ANTAREX project.
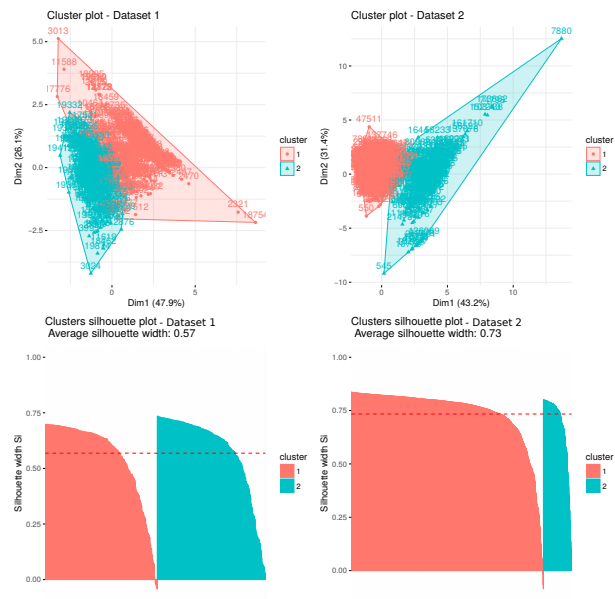
Figure 2.
Inventory Optimization
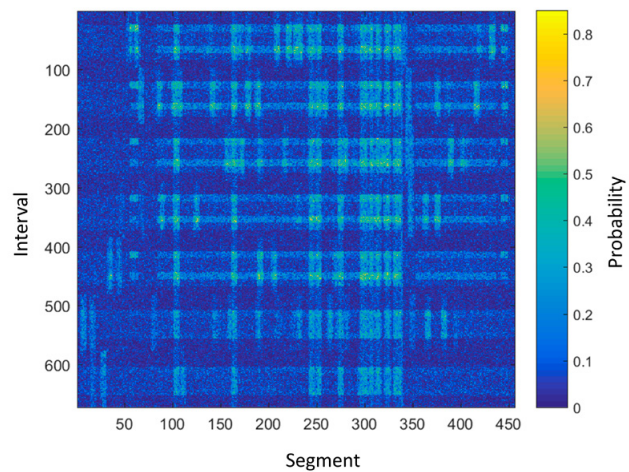
Figure 3.
Probability of traffic incidents

References

[1] Bayle, Y., L. Maršík, M. Rusek, M. Robine, P. Hanna, K. Slaninová, J. Martinovič, and J. Pokorný. Kara1k: A Karaoke Dataset for Cover Song Identification and Singing Voice Analysis. In: 2017 IEEE International Symposium on Multimedia (ISM). IEEE, 2017, 177-184. DOI: 10.1109/ISM.2017.32.

[2] Maršík, L., M. Rusek, K. Slaninová, J. Martinovič, and J. Pokorný. Evaluation of Chord and Chroma Features and Dynamic Time Warping Scores on Cover Song Identification Task. SAEED, Khalid, Władysław HOMENDA a Rituparna CHAKI, ed. Computer Information Systems and Industrial Management. Cham: Springer International Publishing, 2017, 2017-05-17, p. 205-217. Lecture Notes in Computer Science. DOI: 10.1007/978-3-319-59105-6_18.

[3] Martinovič, T., K. Janurová, J. Martinovič, and K. Slaninová. Inventory Optimization Model Parameter Search Speed-up Through Similarity Reduction. Proceedings - 8th International Workshop on Soft Computing Applications, SOFA 2018. Accepted.

BEM4I — DEVELOPMENT OF THE PARALLEL BOUNDARY ELEMENT LIBRARY III

Research institution:	Principal investigator:	Researchers:	Project partner:	Project ID:
IT4Innovations National Supercomputing Center	Michal Merta	Jan Zapletal, Stefan Dohr	Graz University of Technology	OPEN-11-3

Introduction

Natural phenomena occurring in the real world can be modelled by several numerical methods such as the finite element method, and the finite volume method. In our projects, we focus on the development of parallel solvers based on the boundary element method (BEM) not only in the in-house BEM4I library, but also in our partners' software. The main features of BEM make it well suited for problems stated in unbounded domains (such as sound or electromagnetic wave scattering) and shape optimization problems, and so it may be used for instance for development of sound barriers, electromagnets, and the optimization of various components. So far, the boundary element method has mainly been used to solve stationary problems. Due to the increasing performance of supercomputers, the development of boundary element solvers for time-dependent problems is currently a hot topic among mathematicians and scientific software developers since it will enable solution of more complex problems while fully utilizing computers' resources. Within this project we have also focused on optimization and parallelization of time-domain boundary element methods for the modelling of heat propagation in two spatial dimensions, which was developed jointly with our partners at Graz University of Technology.

Results and Methods

To discretize the space-time boundary integral operators associated with the heat equation one can use the Galerkin method [1, 2]. The spatial boundary of a 2D domain is discretized using planar elements and the given time interval is decomposed into subintervals. To construct a space-time mesh, we use a tensor product of the spatial and temporal discretizations. The resulting system matrices are dense, with dimensions growing proportionally to the product of number of time-steps and surface elements. Assembly of such matrices as well as the solution of the linear system is very demanding from the computational and memory point of view. Therefore, parallelization is necessary in order to be able to solve large real-world problems. Although some of the existing codes are parallelized in shared memory, to the best of our knowledge, distributed memory implementation of the BEM solver for the time-dependent heat equation has not yet been introduced. In our work we focus on all levels of parallelization, from SIMD vectorization within a single core, through shared memory parallelization using OpenMP, to distributed memory parallelization using MPI.

Our approach is based on a method originally presented in [3] where a new approach for the distribution of low-rank approximation of BEM system matrices for stationary problems among compute nodes is described. After the tensor product discretization of the space-time boundary we decompose the boundary into a given number of submeshes (see Figure 1). The decomposition defines the block structure of the system matrices. Distribution of the blocks among MPI processes is based on a modification of the scheme presented in [3, 4]. To ensure load balance among processes, each is assigned one diagonal block and P – 1 nondiagonal blocks, where P is the total number of processes. To find nearly optimal decompositions we rely on an algorithm based on a cyclic decomposition of directed graphs.
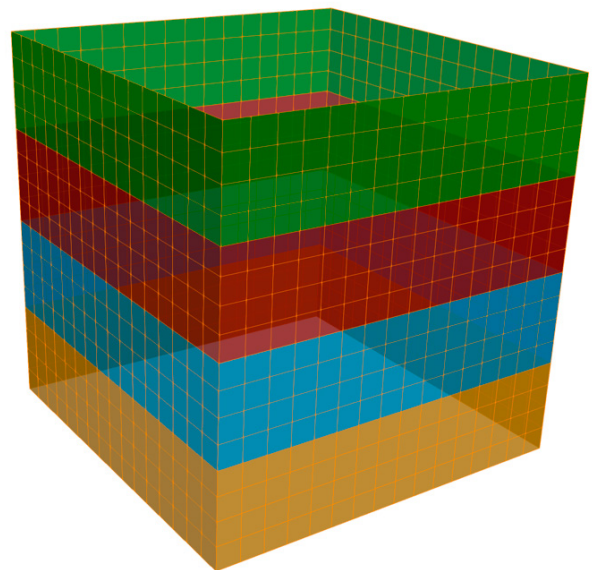
Figure 1.
Decomposition of the surface of a space-time tensor-product mesh into four submeshes
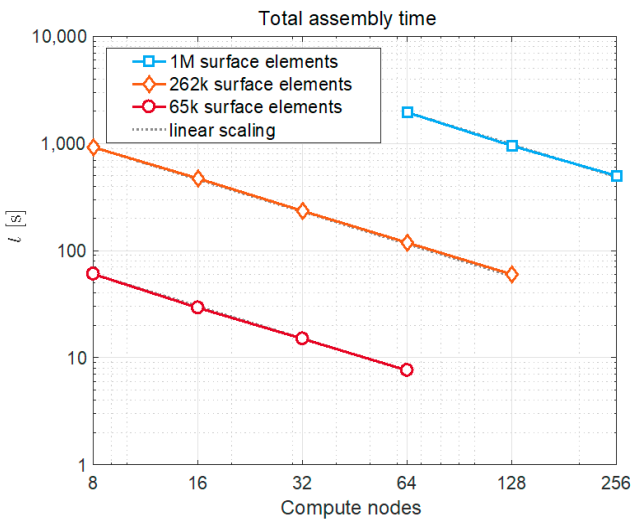
Figure 2.
Total time of assembly of system matrices
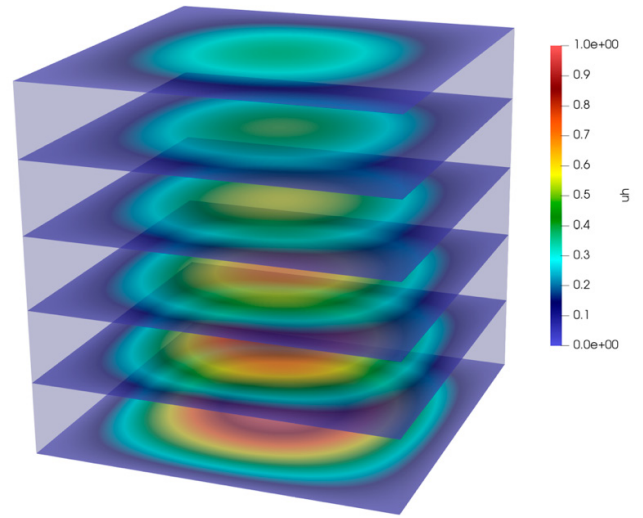
Figure 3.
Evolution of heat distribution computed using
the space-time boundary element method

Since the assembly of the system matrices is computationally the most demanding part of the BEM computation, in addition to the distributed memory parallelization, special attention must be paid to its optimization and shared memory parallelization. The high computational intensity of BEM makes it well suited for current multi- and many-core processors with wide SIMD registers. To assist the compiler with vectorization and enable utilization of SIMD instruction set extensions (SSE, AVX2, AVX512), we use OpenMP simd clauses. Currently, this enables concurrent operations on up to eight double precision operands. Similarly, we use OpenMP to parallelize the local computation and distribute the workload among available CPU cores. The approach is described in more details in [5, 6].

In Figure 2 the scalability of the total assembly time of all necessary time-domainBEM matrices (single-layer, double-layer, and initial matrices) is depicted for problems with various numbers of space-time surface elements. For given meshes, we reach the optimal scalability during the assembly phase. Similarly, very good scalability is obtained for the matrix-vector multiplication during the solution phase. See Table 1, where the efficiency in the case of a problem with 1 million surface space-time elements is 99.0 % on 256 nodes. Solution in individual time-steps (evaluated inside the space-time domain using the representation formula) is depicted in Figure 3.

Nodes → / Mesh size	1	2	4	8	16	32	64	128	256
65k	41.9	22.4	11.3	5.6	2.8	1.5	0.9		
262k				89.8	45.8	22.5	11.5	6.5	
1M							182.2	96.8	46.0

Table 1.
Scalability of the matrix-vector multiplication

On-going Research / Outlook

The presented research has opportunities for further development. Since the individual blocks in system matrices are dense, their sparsification using low rank approximation techniques (such as adaptive cross approximation or the fast multipole method) is desirable when solving large problems. Moreover, extension into spatially 3D problems is planned as well.

Conclusion

We have presented an approach for parallel solution of time dependent heat equations using the boundary element method. Blocks of the system matrices are distributed among compute nodes based on a scheme designed using cyclic decomposition of undirected graphs. Moreover, within each node the assembly of local matrices is parallelized and vectorized using OpenMP. Due to the high computational intensity of the boundary element code, this enables us to fully utilize the capabilities of the modern HPC environment.

References

[1] Costabel, M. Boundary integral operators for the heat equation. Integral Equations and Operator Theory. 1990, 13(4), 498-552. DOI: 10.1007/BF01210400.

[2] Messner, M., M. Schanz, and J. Tausch. A fast Galerkin method for parabolic space–time boundary integral equations. Journal of Computational Physics. 2014, 258, 15-30. DOI: 10.1016/j.jcp.2013.10.029.

[3] Lukáš, D., P. Kovář, T. Kovářová, and M. Merta. A parallel fast boundary element method using cyclic graph decompositions. Numerical Algorithms. 2015, 70(4), 807-824. DOI: 10.1007/s11075-015-9974-9.

Publications

[4] Kravčenko, M., M. Merta, J. Zapletal. Distributed fast boundary element methods for Helmholtz problems. Submitted (2018).

[5] Dohr, S., J. Zapletal, G. Of, M. Merta, M. Kravčenko. A parallel space-time boundary element method for the heat equation. Submitted (2018).

[6] Dohr, S., M. Merta, G. Of, O. Steinbach, J. Zapletal. A parallel solver for a preconditioned space-time boundary element method for the heat equation. Submitted (2018).

03 | EARTH AND
PLANETARY
SCIENCES

CONVECTION IN THE MANTLE OF EUROPA

Research institution:	Principal investigator:	Project ID:
Charles University	Marie Běhounková	OPEN-10-20

Introduction

Icy moons of giant planets are one of the most intriguing and the most intensively studied bodies in the Solar System. Some icy moons are very active, with a young surface, tectonic features, and active cryovolcanism (Enceladus and Europa) whereas others are inactive with an old and dusty surface (e.g. Callisto, Iapetus). Inside some of them (e.g. Europa, Ganymede, Enceladus), vast subsurface oceans have been detected, and they are therefore the center of attention of astrobiological research. Here, we have focused on the thermal evolution of the silicate mantle in Europa, a moon of Jupiter. Depending on the amount of radiogenic elements and orbital parameters, we have study conditions for the initiation of volcanism (melting) in the mantle. The possible presence of hydrothermal vents at the bottom of Europa's ocean, induced by such a volcanism as is in the silicate mantle, have been hypothesized as crucial ingredients for habitability.

Results and Methods

The thermal evolution and internal dynamics of Europa's silicate mantle represent necessary ingredients of global evolutionary models, as the processes within the deep interior, in particular the resulting heat flux, directly influence the dynamics of both the ocean and the outer shell [1]. The thermal state of the deep interior is controlled primarily by the efficiency of heat transfer (presence of convection/melting) and by the available heat sources (radiogenic heating controlled by the composition, and tidal heating controlled mainly by the orbit's eccentricity and the viscosity in the mantle). Here, we have investigated the thermal state of the silicate mantle of Europa and heat flux from the silicate mantle to water/ice shell. Especially, we have addressed conditions for the initiation and possible sustainability of melting in the silicate mantle of Europa leading to increased heat flux from the mantle.

To reach our goal, we have employed the numerical tool *Oedipus/Antigone* (e.g. [2, 3]) – a numerical model of the thermo-mechanical evolution of 3d planetary shells that couples: (i) long-term evolution of the silicate mantle governed by the mass, momentum, and energy equations for viscous material in the extended Boussinesq approximation and (ii) the short-term (tidal) deformation and associated tidal dissipation [4, 5] of the shell with Andrade-like rheology. The long-term component of *Antigone* employs the finite-volume technique with Godunov-like high resolution treatment of the advection terms. The tidal component of *Antigone* employs a spectral approach. By coupling the short-term and long-term components *Antigone* computes the thermal evolution of the shell while self-consistently adopting the temperature changes of tidal heating during the shell's evolution. The model allows the prescribing of temperature dependent viscosity and incorporates partial melting with instantaneous melt extraction. Furthermore, we have introduced a parameterized evolution of the core which controls the temperature at the bottom boundary of the mantle. Figure 1 shows the evolution of the radiogenic heating (left), the tidal heating (center) and melting rate (right).

In our preliminary study, we have mainly concentrated on the influence of three parameters: the viscosity of peridotite at its melting point (η_{melt}), core size (r_{core}), and the value of constant eccentricity (e). Evolution of the radiogenic heating, the tidal heating and the melting rate is shown in Figure 1. The simulations start shortly after the moon's formation, and differentiation where the temperature reaches the melting temperature except for the uppermost layer. After the initial stage of the evolution, the onset of convection occurs. Shortly after the onset (Figure 2, first row), the melting rate and positive temperature anomalies
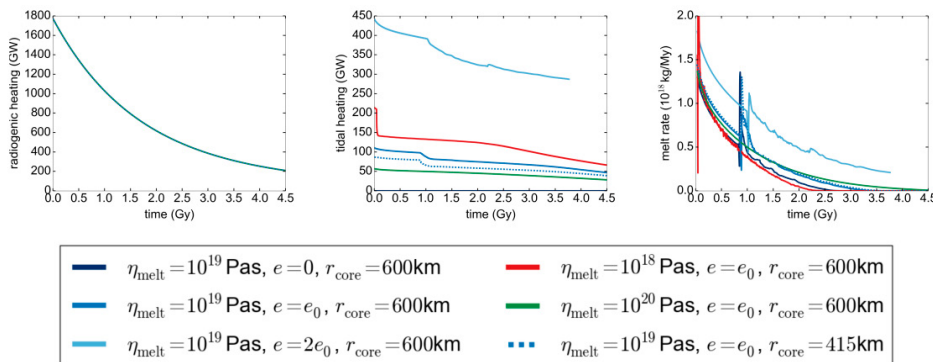
Figure 1.
Evolution of the radiogenic heating (left), the tidal heating (center) and melting rate (right).

Legend:
- $\eta_{melt} = 10^{19}$ Pas, $e = 0$, $r_{core} = 600$km
- $\eta_{melt} = 10^{19}$ Pas, $e = e_0$, $r_{core} = 600$km
- $\eta_{melt} = 10^{19}$ Pas, $e = 2e_0$, $r_{core} = 600$km
- $\eta_{melt} = 10^{18}$ Pas, $e = e_0$, $r_{core} = 600$km
- $\eta_{melt} = 10^{20}$ Pas, $e = e_0$, $r_{core} = 600$km
- $\eta_{melt} = 10^{19}$ Pas, $e = e_0$, $r_{core} = 415$km
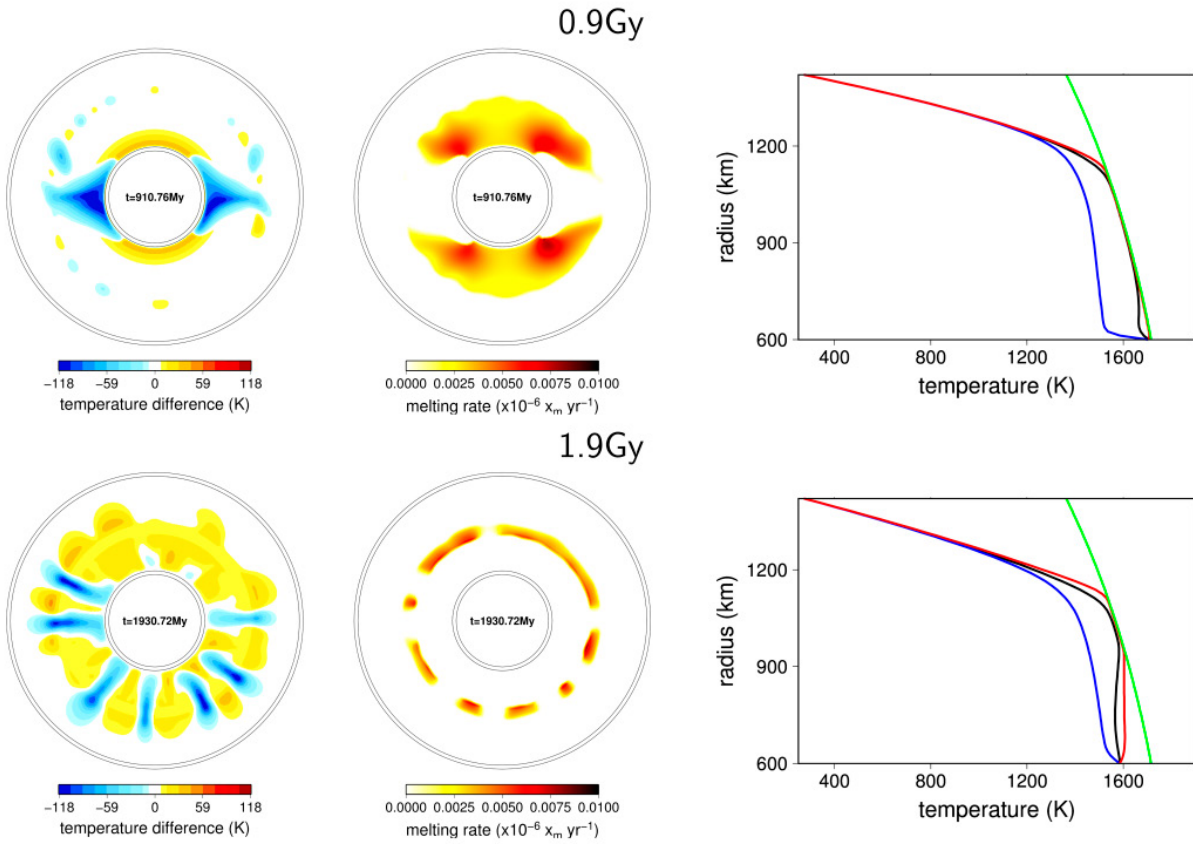
Figure 2.
Snapshots after the onset of convection (first row) and during the convective stage (second row) for model
$\eta_{melt} = 10^{19}Pas$, *tidal dissipation for the present-day value of eccentricity ($e=e_o$) and the core size 600km.*
Left: temperature anomaly; center: melting rate; right: temperature profile of minimum (blue),
averaged (black) and maximum (red) temperature compared to melting temperature (green).

occur in the polar region, where the tidal dissipation is the largest. We also observe a peak in the melting rate during this stage, of which the amplitude depends strongly on the melting viscosity (Figure 1, left). During the convective stage of the evolution, the temperature decreases rapidly. We therefore predict a significant decrease in the tidal dissipation due to the strong dependence of the tidal heating on the temperature. During this stage, the melting is mainly observed beneath the stagnant lid (Figure 2, second row). We observe that the tidal dissipation is significantly lower than the radiogenic heating shortly after the formation (Figure 1, first and second columns). Nevertheless, the radiogenic heating decreases fast due to the radiogenic decay. We predict that the two energy sources are currently comparable for some models. For viscosity $\eta_{melt}=10^{19}Pas$ (Figure 1, blue line), our results sug-

gest the occurence of melting can be prolonged by ~0.5Gy if the tidal dissipation for the present-day value of the eccentricity is included, and significant melting can be sustained for 3Gy. If the eccentricity was twofold greater in the past, the melting could persist until the present day. For viscosity $\eta_{melt}=10^{18}Pas$, (Figure 1, red line) the tidal dissipation is larger due to lower viscosity. On the other hand, the heat transfer is more effective. The increase in the tidal dissipation cannot compensate the augmented heat lost, and we predict that the melting can be sustained for 2Gy. For viscosity $\eta_{melt}=10^{20}Pas$ (Figure 1, green line), the onset of convection does not occur within the 4.5Gy, and even though the tidal dissipation is rather small, the melting can persist until the present day.

On-going Research / Outlook

In our preliminary results, we concentrated mainly on the effect of the viscosity at the melting temperature, the size of the core, and the eccentricity value. In future studies we will address the effect of parameterized orbital evolution, and different compositions (radiogenic heating). We will also further develop our code in order to take into account the effect of the ice shell on the tidal deformation within the core.

Conclusion

The possible presence of volcanism and induced hydrothermal vents supporting Europa's habitability can be sustained at least up to 3Gy by tidal dissipation when viscosity at the melting point is 10^{19}Pas and has present-day eccentricity. The volcanism can persist up to the present day if the eccentricity was twofold higher in the past and/or viscosity is higher than 10^{19}Pas.

References

[1] Soderlund, K. M., B. E. Schmidt, J. Wicht a D. D. Blankenship. Ocean-driven heating of Europa's icy shell at low latitudes. Nature Geoscience. 2013, 7(1), 16-19. DOI: 10.1038/ngeo2021.

[2] Choblet, G., O. Čadek, F. Couturier and C. Dumoulin. ŒDIPUS: A new tool to study the dynamics of planetary interiors. Geophysical Journal International. 2007, 170(1), 9-30. DOI: 10.1111/j.1365-246X.2007.03419.x.

[3] Běhounková, M., G. Tobie, G. Choblet and O. Čadek. Coupling mantle convection and tidal dissipation: Applications to Enceladus and Earth-like planets. Journal of Geophysical Research. 2010, 115(E9). DOI: 10.1029/2009JE003564.

[4] Tobie, G., O. Čadek a C. Sotin. Solid tidal friction above a liquid water reservoir as the origin of the south pole hotspot on Enceladus. Icarus. 2008, 196(2), 642-652. DOI: 10.1016/j.icarus.2008.03.008.

[5] Běhounková, M., G. Tobie, O. Čadek, G. Choblet, C. Porco and F. Nimmo. Timing of water plume eruptions on Enceladus explained by interior viscosity structure. Nature Geoscience. 2015, 8(8), 601-604. DOI: 10.1038/ngeo2475.

Publications

Tobie, G., M. Běhounková et al. Tidal dissipation in Europa's silicate mantle: Implications for seafloor activities and potential observations by Europa clipper. COSPAR 2018, 14–22 July 2018, Pasadena, USA. B5.3-0009-18. Available at http://cospar2018.org/wp-content/uploads/2018/07/COSPAR-2018-Abstract-Book.pdf

Tobie, G., L. Harel, K. Kalousová, J. Kvorka, M. Běhounková et al. Core-ocean-ice exchange processes in Europa, Ganymede and Callisto. European Planetary Science Congress 2018, 16-21 September 2018, TU Berlin, Germany, id.EPSC2018-894. Available at https://meetingorganizer.copernicus.org/EPSC2018/EPSC2018-894-1.pdf

CONVECTION-PERMITTING CLIMATE SIMULATIONS

Research institution:	Principal investigator:	Researcher:	Project ID:
Charles University	Michal Belda	Tomáš Halenka	OPEN-11-30

Introduction

So far only a limited number of climate models have been used with a horizontal resolution fine enough to allow direct, local scale application of model results without some form of statistical post-processing. Models required for this kind of application are generally limited area models with grid spacing in the order of kilometers or less. Another important factor is that models with such a high resolution allow for explicit representation of convection processes. These so-called convection permitting climate models [1] have only recently been made possible through advances in computational technologies. Climate models are very complex systems and have become even more complex with ongoing development, driven by the needs of the users of model results. However, simply increasing the resolution may not necessarily improve the results; in fact, without proper evaluation and tuning, the models may be less accurate.

In the year 2016 a flagship pilot study (FPS, [2]) was started under the auspices of the World Climate Research Program's (WCRP) Coordinated Regional Downscaling Experiments Flagship Pilot Studies programme (CORDEX-FPS, [3]). The FPS employs regional models in non-hydrostatic mode with a 3 km resolution to study the effect of a convection permitting mode. Creating this kind of ensemble of simulations will facilitate research in this area that is very promising, however, being still very cutting-edge, it needs much research.

Results and Methods

For the purposes of the FPS, three short term case studies were planned in a weather-like mode (initializing the simulation just before the event) and a climate mode (with a one month spin-up period before the event). Next, a two year simulation was designed, testing the capability of the model for long-term climate simulations. With the computational resources of IT4I supercomputers, Charles University contributed several simulations with the regional climate model RegCM [4] for the study. The RegCM model is capable of running in a massive parallel configuration using the MPI standard. Preliminary tests indicated performance scaling for up to hundreds of cores for the task at hand. In our case, the simulations were run on 16 nodes of the Salomon computer (384 cores) to best utilize allocated computational resources.

Short term case studies were analyzed within the context of a large ensemble of simulations (18–21 members representing six different modeling systems with different physics and modeling chain options). Results indicate that in the weather-like mode the model is able to capture the event quite well, whereas in climate mode the skill is dependent on the large-scale flow of the event (Figure 1 and 2). Long-term simulation shows an overall large dependence on the physics parameterizations chosen, showing a generally large precipitation bias with the Nogherotto/Tompkins scheme. The shape of the diurnal cycle of precipitation is captured well in some regions, although it is still skewed toward higher values.

On-going Research / Outlook

The present project was instrumental in testing the latest convection permitting version of the RegCM model within the framework of a larger ensemble of simulations performed by various institutions involved in the EURO-CORDEX initiative. These simulations were a first step that in future should allow the use of the RegCM model for producing high-resolution climate scenarios. With the help of IT4I infrastructure, we hope to be able to participate in these activities in the future. In the near future an evaluation simulation, present-climate simulation and future scenario simulation are planned, all for a period of 10 years (with a one year spin-up period) selected according to a consensus among the FPS contributors.

Conclusion

In this project, the regional climate model RegCM was employed in a so-called convection permitting mode (ie. resolution high enough to allow explicit representation of convection). The simulations produced by the model served as one of the members of a large ensemble of regional climate models in a Flagship Pilot Study on convection permitting climate modeling within the CORDEX initiative of the World Climate Research Program. Results of the first phase of the study indicate a good level of accuracy of the regional models in the weather-like mode, and a large dependence of the model performance on large-scale flow, and also on other parameterizations chosen in the climate mode.
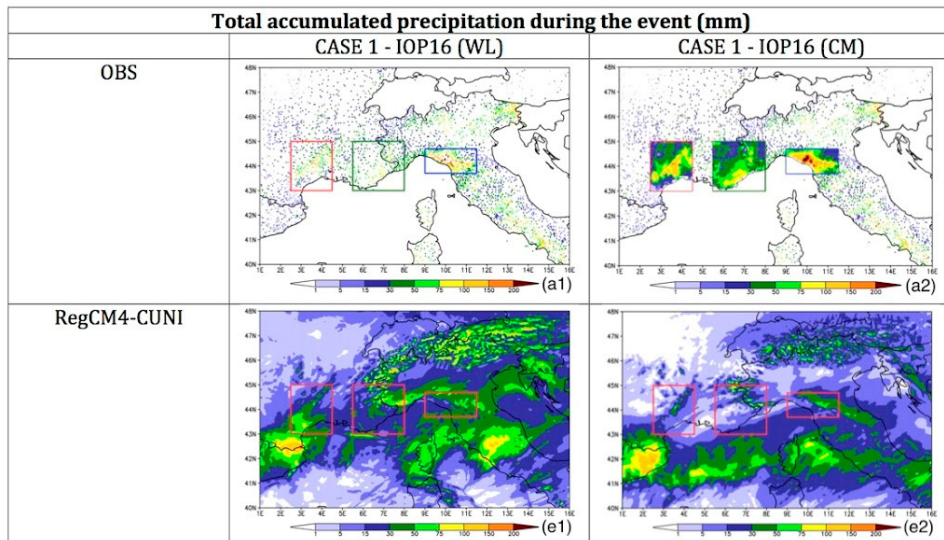
Figure 1.
Comparison of observed and modeled precipitation during the IOP16 event in the weather-like (left), and climate modes (right).
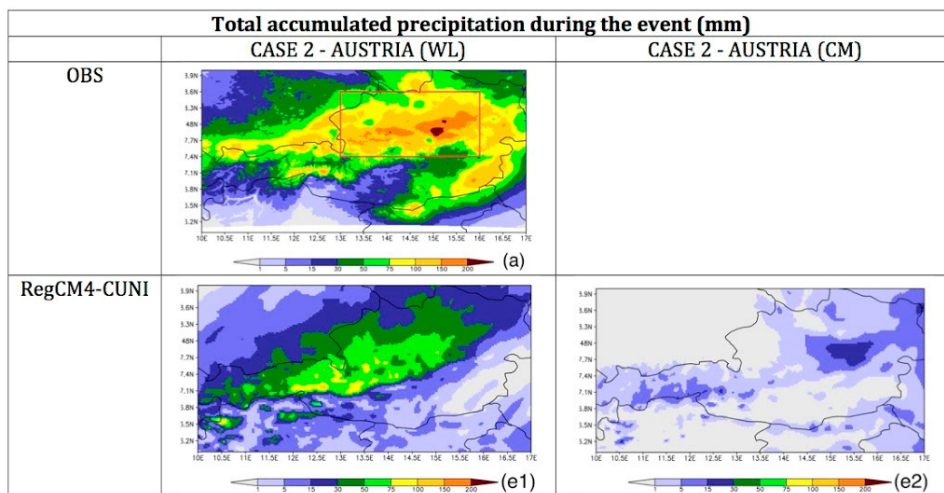
Figure 2.
Comparison of observed and modeled precipitation during the Austria event in the weather-like (left), and climate modes (right).

References

[1] Prein, A. F., W. Langhans, G. Fosser, et al. A review on regional convection-permitting climate modeling: Demonstrations, prospects, and challenges. Reviews of Geophysics. 2015, 53(2), 323-361. DOI: 10.1002/2014RG000475.

[2] Gutowski, W. J. Jr., F. Giorgi, B. Timbal. WCRP COordinated Regional Downscaling EXperiment (CORDEX): A diagnostic MIP for CMIP6. Geoscientific Model Development. 2016, 9(11), 4087-4095. DOI: 10.5194/gmd-9-4087-2016.

[3] Giorgi, F., C. Jones, G. R. Asrar. Addressing climate information needs at the regional level: The CORDEX framework. Bulletin - World Meteorological Organization. 2009, 58(3), 175-183. ISSN: 0042-9767.

[4] Giorgi, F., E. Coppola, F. Solmon, et al. RegCM4: Model description and preliminary tests over multiple CORDEX domains. Climate Research. 2012, 52, 7-29. DOI: 10.3354/cr01018. ISSN 0936-577X.

Publication

Coppola, E., S. Sobolowski, E. Pichelli, F. Raffaele, B. Ahrens, I. Anders, N. Ban, S. Bastin, M. Belda, et al. A first-of-its-kind multi-model convection permitting ensemble for investigating convective phenomena over Europe and the Mediterranean. Climate Dynamics. 2018. DOI: 10.1007/s00382-018-4521-8.

TRANSPORT PROCESSES IN THE DEEP ICE LAYERS OF OCEAN WORLDS

Research institution:	Principal investigator:	Researcher:	Project IDs:
Charles University	Klára Kalousová	Christophe Sotin	OPEN-10-1, OPEN-11-21, OPEN-12-15

Introduction

The exploration of icy ocean worlds – planets or moons that harbour deep oceans locked beneath a shell of ice – is driven by the question of the emergence of life in places where liquid water has been present. A lot of attention is given to Europa and Enceladus where the ocean is in a direct contact with the silicate core – such conditions are similar to those at terrestrial sea floors where life develops. Ganymede and Titan, the largest moons in the solar system, possess large amounts of H_2O so that a layer of high-pressure (HP) ice is predicted between the ocean and the silicates that seems to prevent exchange between the two layers. These moons are similar in mass and radius but their radial mass distribution is different, with Ganymede being the more differentiated. Titan is the only known moon that has its own dense atmosphere, composed mainly of nitrogen. The measured abundance of atmospheric methane and argon can only be explained by endogenic sources, which indicates that some exchange processes may be ongoing in the interior of Titan.

Results and Methods

The goal of this project was to investigate the transport processes through the HP ice layers of large moons where melting has been predicted for a broad range of parameters [1]. To model the generation and transport of liquid water in a convecting ice layer, we treat the layer material as a mixture of two phases – solid ice and liquid water. The dynamics of such mixtures is described by the equations derived in [2], and we extended the formulation to capture the effect of solid ice phase changes (ice VI-ice V and ice V-ice III) that are relevant for Titan. The governing equations combine the compressible Stokes system with the advection-diffusion equation for temperature and the advection-reaction equation for water content. The code [3] is implemented in the open source FEM software FEniCS [4].

We performed simulations tailored to the conditions within the HP ice layers of Ganymede and Titan. Our results show that water can be generated at the bottom interface of HP ice and silicates and, being less dense than HP ice, it can be transported through the layer by hot upwelling plumes (Figure 1). Melting also occurs within the warm layer below the ocean interface and water is then extracted into the ocean. By this process, volatiles that may have been leached by water at the silicates interface can be transported through the HP ice into the ocean. Substantial melting is occurs when there is a large incoming heat flux and a not too thick HP ice layer (Figure 2). As the moons cool, their HP ice layers thicken and become less permeable. Combined with the present-day thickness estimates, our results indicate that transport of volatiles was possible in earlier stages of Ganymede's evolution, when its HP ice layer was thinner, but has already ceased. On the other hand, in the case of Titan, the volatiles transport from silicates to the ocean may be ongoing, which can help explain the presence of argon and methane in Titan's atmosphere.
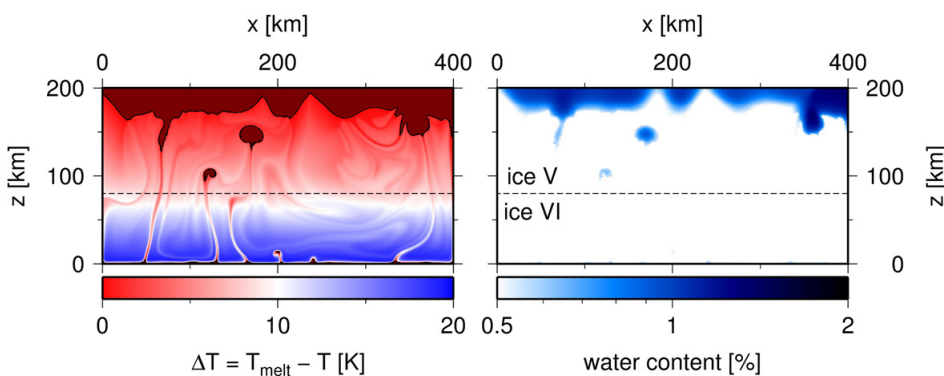

Figure 1.
(Left) Temperature difference from the melting temperature. Dark red marks the ice where $T=T_{melt}$. (Right) Water content. Dashed lines mark the phase transition between ice VI and ice V.
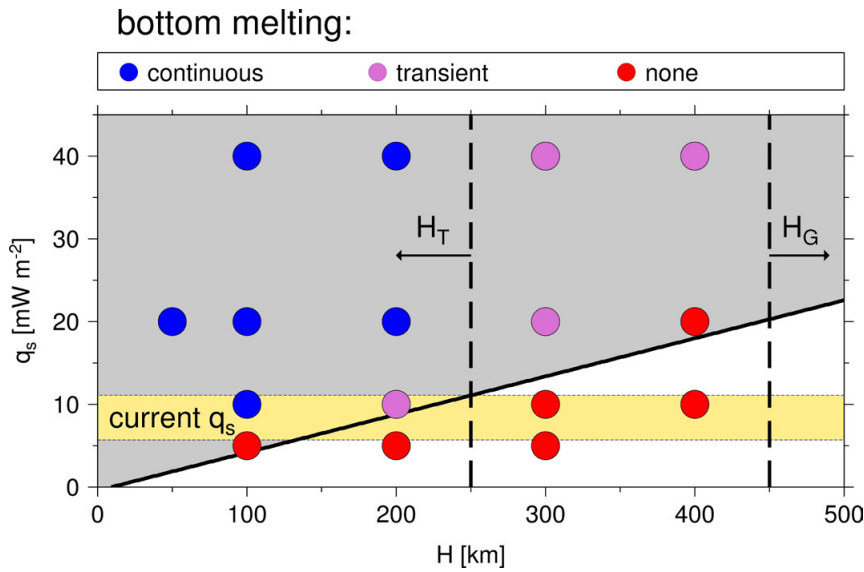
Figure 2.
Degree of bottom melting (colored circles)
for different ice thicknesses H and heat flux
q_s. The scaling law for critical q_s
(full line) divides the parameter's space
into a region with (gray) and without (white)
bottom melting, and corresponds well
with the simulations results. Estimate
of present-day heat flux q_s is indicated
(yellow) as well as estimates of ice thickness
(dashed lines) for Ganymede (H_G>450 km)
and Titan (H_T<250 km).

We have also derived scaling laws to predict: (1) the critical value of silicates heat flux that leads to bottom melting (Figure 2), (2) the amount of generated melt, (3) the thermal profile within the HP ice layer, and (4) the velocity of water flowing from the HP ice into the ocean. The derived scaling laws will be implemented into a 1d model that will simulate the global thermo-chemical evolution of large ocean worlds.

On-going Research / Outlook

The presence of salts in the oceans of Ganymede and Titan has been inferred from the electro-magnetic measurements made the Galileo and Cassini-Huygens missions. Salts such as NaCl or $MgSO_4$ modify the melting curve as well as the relative densities between water and ice. To include these effects, the code will be extended through modification of the melting process and buoyancy, and by adding a new advection equation. The implementation is currently ongoing.

The derived scaling laws, extended by the effect of salts, will be used in models of the global thermo-chemical evolution of Ga-

nymede and Titan as well as of extrasolar ocean worlds. Such models will provide estimates on the timing of exchange processes, and their results can be compared with the amount of argon in Titan's atmosphere. The results will also be relevant for the future exploration of Ganymede by the ESA's JUICE mission [5].

Conclusion

Using a numerical code of two-phase convection, we investigated melting and water transport in the HP ice layers of Ganymede and Titan. We found that melting may occur in these layers and that it can play an important role in the exchange of volatiles between the silicate core and the ocean. This exchange has probably already ceased in the interior of Ganymede, while it may be ongoing in the interior of Titan, which could explain the presence of argon and methane in Titan's atmosphere. We derived scaling laws that will be implemented in the thermo-chemical evolution models of Ganymede and Titan as well as extrasolar ocean worlds.

References

[1] Choblet, G., et al. Heat transport in the high-pressure ice mantle of large icy moons. Icarus. 2017, 285, 252-262. DOI: 10.1016/j.icarus.2016.12.002.

[2] Souček, O., K. Kalousová, and O. Čadek. Water transport in planetary ice shells by two-phase flow – a parametric study. Geophysical & Astrophysical Fluid Dynamics. 2014, 108(6), 639-666. DOI: 10.1080/03091929.2014.969251.

[3] Kalousová, K., et al. Two-phase convection in Ganymede's high-pressure ice layer — Implications for its geological evolution. Icarus. 2018, 299, 133-147. DOI: 10.1016/j.icarus.2017.07.018.

[4] Logg, A., K. A. Mardal, and G. N. Wells (editors). Automated Solution of Differential Equations by the Finite Element Method. The FEniCS Book, 84, Springer-Verlag, Berlin Heidelberg, 2012. ISBN 978-3-642-23098-1.

[5] Grasset, O., et al. JUpiter ICy moons Explorer (JUICE): An ESA mission to orbit Ganymede and to characterise the Jupiter system. Planetary and Space Science. 2013, 78, 1-21. DOI: 10.1016/j.pss.2012.12.002.

Publications

Kalousová, K., and C. Sotin (2018). Melting in high-pressure ice layers of large ocean worlds – Implications for volatiles transport. Geophysical Research Letters. DOI: 10.1029/2018GL078889.

Kalousová, K., and C. Sotin, Dynamics of Titan's high-pressure ice layer. Earth and Planetary Science Letters (submitted)

AUTOMATIZED SENTINEL-1 MONITORING SYSTEM

Research institution:
IT4Innovations
National
Supercomputing
Center

Principal investigator:
Milan Lazecký

Researchers:
Ivana Hlaváčová,
Matúš Bakoň,
Antonio Miguel-Ruiz
Armenteros

Project partners:
CESNET,
insar.cz,
Universidad
de Jaen

Project ID:
OPEN-11-37

Introduction

The preparation of a database of pre-processed satellite Synthetic Aperture Radar (SAR) images is a prerequisite for effective analyses using SAR interferometry (InSAR), intensity and polarimetry analyses. InSAR techniques are able to observe terrain and structure displacements with a very high sensitivity (reaching 1 mm/year for vertical motion rates). Intensity analyses including polarimetry are able to identify deforestation, flooded, and burnt areas, with the advantage of the cloud penetration abilities of the radar, and prepare soil moisture maps etc. Our database is connected to the Czech Collaborative Copernicus Ground Segment (CollGS) maintained by CESNET, and contains bursts of Copernicus programme's Sentinel-1 SAR satellite that have been preprocessed to the state of a consistent well-coregistered dataset by an open-source NASA/JPL software ISCE [1]. Further processing time is significantly reduced in order to achieve displacements velocity maps based on so-called Persistent Scatterers (PS) [2] or other techniques, e.g. Small Baseline (SB) [3], as demonstrated using open-source STAMPS multitemporal InSAR processor [4]. Our approach (named IT4S1) has several advantages over similar works, namely a processing speed and a preparedness for inclusion of various advanced techniques, for example a warning system for dangerous motion of landslides or infrastructure.

Results and Methods

Sentinel-1 data are delivered in a format called Single Look Complex (SLC). It is almost raw data, which requires specific calibration steps. We have identified the general steps needed for any InSAR type of processing and implemented it into a system storing Sentinel-1 data after their calibration (SLC-C data). After the arrival of new Sentinel-1 SLC image to CollGS, a Sentinel-1 specific metadata database system [5] ensures the proper identification of its image sub-units called bursts (covering around 40x100 km), including information about their geographic location. When activated, the system loads the SLC image with the latest available ephemeris data and splits it into bursts, radiometrically calibrated by an SLC preprocessor server that sends the output to the SLC-C preprocessing High Performance Computing (HPC) facility at IT4Innovations.

At the SLC-C processing HPC facility, a custom solution prepares coherent burst combinations in order to perform a critical computation and correction of Enhanced Spectral Diversity (ESD) [6]. This ensures precise coregistration of images at the level of 0.001 pixel needed for InSAR processing of this acquisition type of Sentinel-1 (TOPS mode [7]). A digital elevation model (DEM) from SRTM in 1 arcsecond resolution was applied for computing terrain offset fields that are removed from the bursts, inducing InSAR-ready burst SLC-C images that are well coregistered towards the same framework and do not contain topography-related signals. The whole process is parallelized and one new burst is computed on average in 2.2 minutes using a 24-core node.

The precisely coregistered and basically calibrated bursts are saved into a SLC-C storage for further use. For multitemporal processing, currently STAMPS and SALSIT [8] InSAR tools are implemented in the system. The full processing of one burst by a custom parallelized STAMPS (PS+SB) takes around 24 core-hours. Our tests using small subset reprocessing show that on-demand requests to process areas around 8 km in radius finish within 15 minutes for PS and another 30 minutes for SB on a 24-core node. STAMPS PS burst-wide processing has been performed over all bursts within the Czech Republic. A full map is shown in Figure 1 together with the basic information.

On-going Research / Outlook

The coregistered Sentinel-1 images can also be used for polarimetric analyses. Experiments to identify forest segments affected by the hurricane in March 2018 over the Jeseniky mountains showed the potential for practical usage, see Figure 2. For this, cross-polarized images should also be converted to the SLC-C format, and additional corrections should be performed (radiometric calibration and terrain flattening). With this outlook, we are evolving towards establishing full Sentinel-1 exploitation tools for fast analyses over the Czech Republic. It will be also necessary to introduce advanced methods for storage and visualization of the resultant products and optimization of the processing tools.
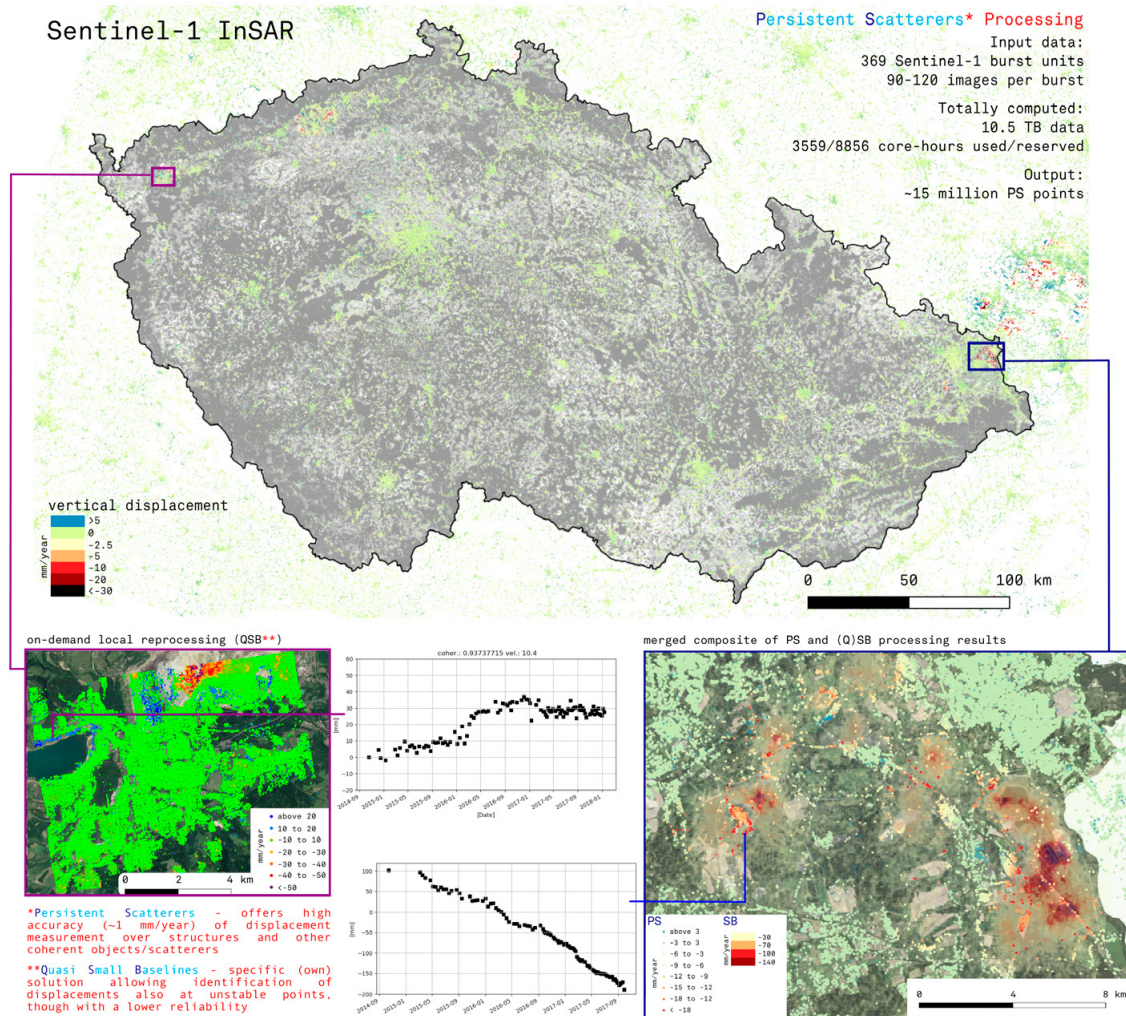
Figure 1.
A Persistent Scatterers InSAR result using Sentinel-1 SLC-C data (2015-2018) from all tracks available over the Czech Republic, processed by STAMPS algorithms. Experimental on-demand InSAR processing algorithms show additionally identified moving points.

Finally, it is possible to establish a time series update using every new pre-processed burst automatically in order to detect unexpected changes in an InSAR time series that can be used as a trigger for early warning against suspicious occurrences of potentially dangerous displacements. Using other open-source tools such as the ESA's SNAP the system can be upgraded to deliver other advanced products such as soil moisture change maps or forest change maps over Czech areas.

Conclusion

While common HPC approaches of utilizing Sentinel-1 images for InSAR start their processing chain from either original SLC data or raw non-coregistered data, e.g. [9], the IT4S1 system allows a faster and more flexible multitemporal processing thanks to generation of pre-prepared SLC-C images. A large spatial coverage of processed data can lead to significant economic savings instead of e.g. installation of in-situ measurement tools such as GPS or other geodetic instruments for monitoring generally large areas of interest. It is expected that the heavy computational load needed for nation-wide SLC-C data generation will be valorized in non-commercial applications for national geologic, urban planning, forestry, and risk management spheres.
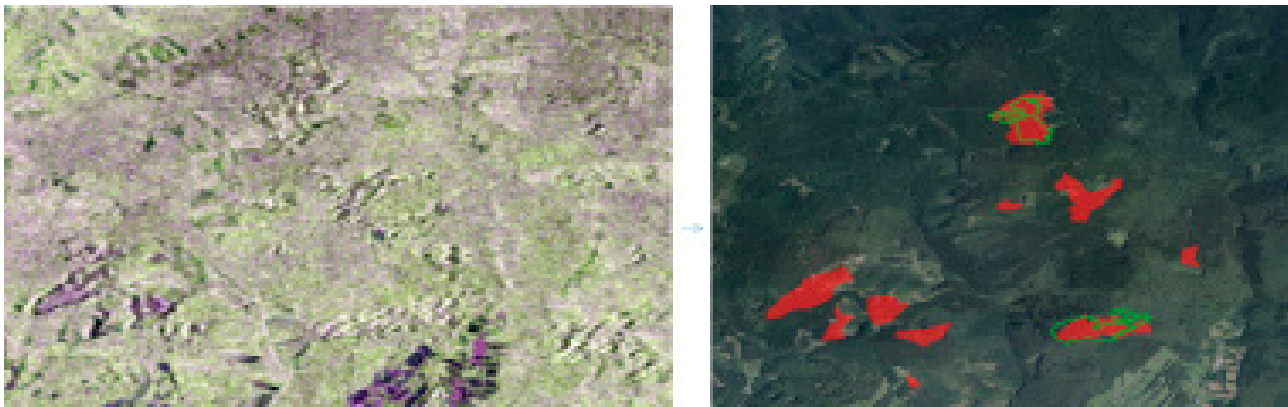
Figure 2.
Identification of change polygons after a hurricane over the Jeseniky mountains' forests: left: RGB
composite of average image created from 20 radiometrically corrected images after the disaster
(VV, VH, VH/VV) overlaid by a PCA-based difference image using post- and pre-disaster sets of images.
Right: Identified change polygons (red) and results from a selective terrain mapping (green).

References

[1] Zebker, H. A., S. Hensley, P. Shanker, and C. Wortham. Geodetically Accurate InSAR Data Processor. IEEE Transactions on Geoscience and Remote Sensing. 2010, 48(12), 4309-4321. DOI: 10.1109/TGRS.2010.2051333.

[2] Ferretti, A., C. Prati and F. Rocca. Nonlinear subsidence rate estimation using permanent scatterers in differential SAR interferometry. IEEE Transactions on Geoscience and Remote Sensing. 2000, 38(5), 2202-2212. DOI: 10.1109/36.868878.

[3] Berardino, P., G. Fornaro, R. Lanari, and E. Sansosti. A new algorithm for surface deformation monitoring based on small baseline differential SAR interferograms. IEEE Transactions on Geoscience and Remote Sensing. 2002, 40(11), 2375-2383. DOI: 10.1109/TGRS.2002.803792.

[4] Hooper, A. A multi-temporal InSAR method incorporating both persistent scatterer and small baseline approaches. Geophysical Research Letters. 2008, 35(16). DOI: 10.1029/2008GL034654.

[5] Li, Z., T. Wright, A. Hooper, et al. Towards InSAR everywhere, all the time, with Sentinel-1. ISPRS – International Archives of the Photogrammetry, Remote Sensing and Spatial Information Sciences. 2016, XLI-B4, 763-766. DOI: 10.5194/isprs-archives-XLI-B4-763-2016.

[6] De Zan, F., and A. Monti Guarnieri. TOPSAR: Terrain Observation by Progressive Scans. IEEE Transactions on Geoscience and Remote Sensing. 2006, 44(9), 2352-2360. DOI: 10.1109/TGRS.2006.873853.

[7] Yague-Martinez, N., P. Prats-Iraola, F. Rodriguez Gonzales, et al. Interferometric Processing of Sentinel-1 TOPS Data. IEEE Transactions on Geoscience and Remote Sensing. 2016, 54(4), 2220-2234. DOI: 10.1109/TGRS.2015.2497902.

[8] Lazecký, M., I. Hlaváčová, J. Martinovič, and A. Miguel Ruiz-Armenteros. Accuracy of Sentinel-1 Interferometry Monitoring System based on Topography-free Phase Images. Procedia Computer Science. 2018, 138, 310-317. DOI: 10.1016/j.procs.2018.10.044.

[9] De Luca, C., I. Zinno, M. Manunta, R. Lanari, and F. Casu. Large areas surface deformation analysis through a cloud computing P-SBAS approach for massive processing of DInSAR time series. Remote Sensing of Environment. 2017, 202, 3-17. DOI: 10.1016/j.rse.2017.05.022.

Publications

Ruiz-Armenteros, A. M., M. Lazecký, I. Hlaváčová, et al. Deformation monitoring of dam infrastructures via spaceborne MT-InSAR. The case of La Viñuela (Málaga, southern Spain). Procedia Computer Science. 2018, 138, 346-353. DOI: 10.1016/j.procs.2018.10.049.

Ruiz-Armenteros, A. M., M. Lazecký, A. Ruiz-Constán, et al. Monitoring continuous subsidence in the Costa del Sol (Málaga province, southern Spanish coast) using ERS-1/2, Envisat, and Sentinel-1A/B SAR interferometry. Procedia Computer Science. 2018, 138, 354-361. DOI: 10.1016/j.procs.2018.10.050.

Lazecký, M., I. Hlaváčová, J. Martinovič and A. M. Ruiz-Armenteros. Accuracy of Sentinel-1 Interferometry Monitoring System based on Topography-free Phase Images. Procedia Computer Science. 2018, 138, 310-317. DOI: 10.1016/j.procs.2018.10.044.

Lazecký, M., 2018: Identification of active slope motion in Czech environment using Sentinel-1 interferometry. In: GIS Ostrava 2018, 21-23 Mar 2018, Springer Lecture Notes in Geoinformation and Cartography, 7 p.

Lazecký, M. System for Automatized Sentinel-1 Interferometric Monitoring. Soille, P., and P.G. Marchetti, eds. Proceedings of the 2017 conference on Big Data from Space. BIDS' 2017, EUR 28783 EN, Publications Office of the European Union, Luxembourg, 2017. ISBN 978-92-79-73527-1, DOI:10.2760/383579, JRC108361.

THE GLOBAL TOROIDAL MAGNETIC FIELD GENERATED IN THE EARTH'S OCEANS

Research institution:
Charles University

Principal investigator:
Jakub Velímský

Researchers:
**Zdeněk Martinec,
Libor Šachl**

Project ID:
OPEN-10-13

Introduction

The movement of the oceans through the Earth's main magnetic field generates a secondary, motionally induced magnetic field [1]. Besides a well known class of tidally forced ocean flows, which are not considered here, the global ocean circulation system involves water movements driven by wind stresses and heat fluxes on the ocean surface and by the temperature- and salinity-dependent buoyancy force. Such flows are capable of generating both the poloidal and toroidal magnetic fields. The toroidal field is invisible on the ocean surface. However, lateral variations of the ocean electrical conductivity allow for energy exchange between poloidal and toroidal fields. The toroidal field can thus significantly influence the observable poloidal field, both in terms of its amplitude, and seasonal variations. In our project, we concentrate on the calculation of the global toroidal magnetic field in the ocean interior, and the phenomenon of mutual interaction of the poloidal and toroidal fields by the comparison of full and decoupled (no energy exchange) solutions.

Results and Methods

We use the recently developed 3D z-coordinate baroclinic ocean model LSOMG to calculate the ocean flows forced by the wind stresses and heat fluxes derived from ERA-Interim data [2]. We run the model with 1° horizontal resolution and for 11 vertical layers. The model reaches a quasi-equilibrium after a spin-up period of 20 years. We use the predictions of the ocean flows for the year 2014.

In order to calculate the magnetic field induced by the ocean flow model LSOMG, we employ the time-domain, spherical harmonic-finite element approach to the EM induction equation with a 3-D distribution of electrical conductivity [3] that has been recently modified to include internal sources. The use of the vector spherical harmonic base [4] to represent the magnetic field vector B implicitly comprises the separation of the poloidal and toroidal components.

The 3D electrical conductivity of the oceans is assembled from the temperatures and salinities provided by the World Ocean Atlas 2013 [5, 6], using an empirical formula [7]. For continental conductivity, we have combined the thicknesses of continental and oceanic sediments, and igneous rocks, with a priori fixed conductivity values. In the Earth's mantle, we have used a global 1D conductivity model of [8]. The Earth's core conductivity is set to 105 S/m.

Figure 1 shows a snapshot of the predicted ocean-induced magnetic field from 31 December 2014 at the Earth's surface, at the depth of 1,840 m, where the amplitude of the toroidal field is at its peak, and at the depth of 3,530 m, corresponding to the average ocean depth. The columns from left to right display respectively the radial, poloidal meridional, poloidal zonal, toroidal meridional, and toroidal zonal components. At the Earth's surface, the toroidal field vanishes, as required by the boundary condition. However, in the deep ocean, the amplitude of the
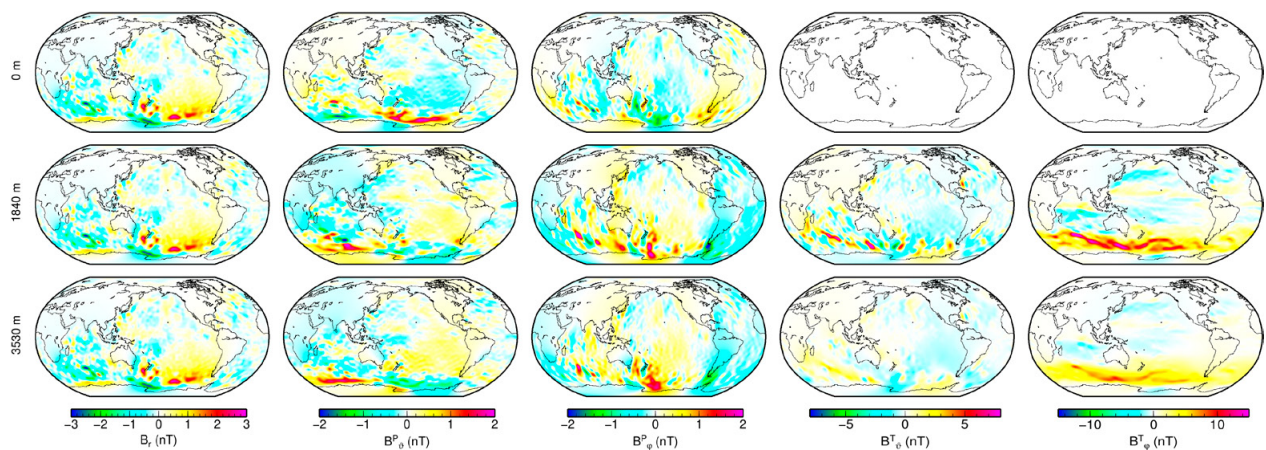

Figure 1.
Snapshots of the induced magnetic field on December 31, 2014 for the full solution.

toroidal field, especially its zonal component is almost one order of magnitude larger, than that of the poloidal field. The most pronounced feature is the eastward ACC signature. The toroidal meridional component points mostly to the north in the Atlantic and Pacific oceans. In the Southern Ocean, its spatial variations are influenced by the small-scale variations of the zonal field through the divergence-free condition. The radial magnetic field is almost invariable with depth. It is dominated by the ACC signature, with the largest signals present in the Southern Ocean, Southern Pacific, and Southern Indian Oceans. On the other hand, the poloidal horizontal field reverses its sign between the surface and the 1,840 m depth. This is a direct consequence of the concentration of horizontal fluxes and corresponding horizontal electric currents in the shallower parts of the ocean.

Figure 2 shows the power spectra of the poloidal magnetic field at the Earth's surface. In the left-hand panel, the annual geometric means for the full and decoupled runs are shown respectively by crosses and triangles. The geometric standard deviation intervals are marked by the red and blue bands. The full solution has approximately three times larger total energy of the observable field at the Earth's surface than the decoupled solution. The time variations of the full model are more pronounced, as shown in the right-hand panel of Figure 2 for spherical harmonic degree 3.

On-going Research / Outlook

The direct observability of the toroidal magnetic field at sea-bottom observatories remains an open question. We predict seasonal variations in the toroidal field in the order of units of nT, a value possibly detectable by current modern sea-bottom equipment. However, to our knowledge, no such observatory has yet been deployed in the area of ACC, where maximum amplitudes can be expected.
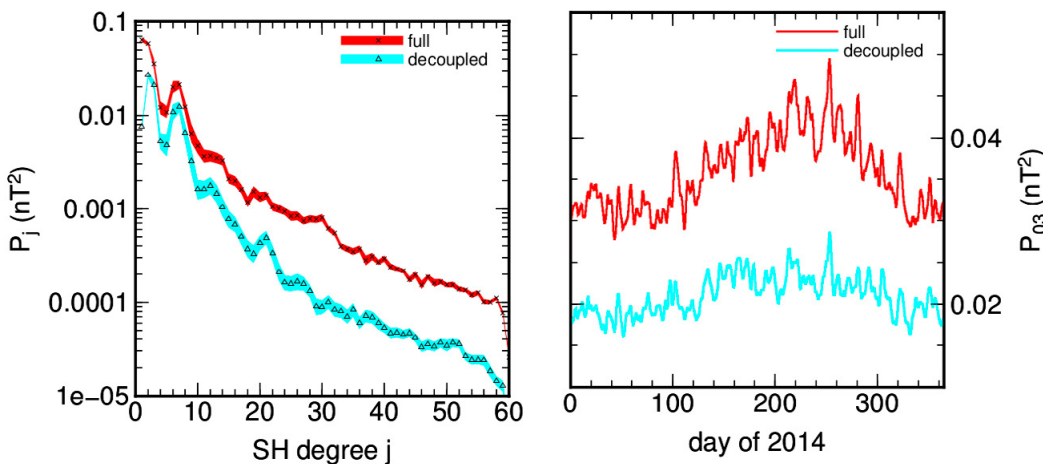
Figure 2.
The power spectra
of the observable poloidal
magnetic field
at the Earth's surface.

Conclusion

We have calculated one year of the magnetic signatures of Earth's oceans by solving the 3D electromagnetic induction (EMI) equation with a realistic conductivity distribution of the Earth's oceans, lithosphere, and underlying mantle, and using vertically stratified 3D ocean flows predicted by a state-of-the-art baroclinic ocean model LSOMG. In particular, we have demonstrated that the global toroidal field induced by differential zonal velocities reaches values of up to 15 nT at the depth of 1,800 m and in the vicinity of the ACC. This is almost one order of magnitude larger than the poloidal field.

We have also quantified the effect of the energy exchange between the toroidal and poloidal fields through lateral conductivity variations. The toroidal field, while invisible on the Earth's surface, has a substantial effect on the observable poloidal component. When the toroidal field is omitted, the power of the poloidal field is about three times smaller with reduced spatial and temporal variability.

In general, in the case of global ocean circulation the 3D models incorporating the full physics of the EMI equation should be used for the accurate prediction of the motionally induced magnetic field within the oceans.

References

[1] Sanford, T. B. Motionally induced electric and magnetic fields in the sea. Journal of Geophysical Research. 1971, 76 (15), 3476–3492. DOI: 10.1029/JC076i015p03476.

[2] Dee, D. P., S. M. Uppala, A. J. Simmons, et al. The ERA-Interim reanalysis: Configuration and performance of the data assimilation system. Quarterly Journal of the Royal Meteorological Society. 2011, 137(656), 553-597. DOI: 10.1002/qj.828.

[3] Velímský, J., Z. Martinec. 2005. Time-domain, spherical harmonic-finite element approach to transient three-dimensional geomagnetic induction in a spherical heterogeneous Earth. Geophysical Journal International. 2005, 161(1), 81-101. DOI: 10.1111/j.1365-246X.2005.02546.x.

[4] Varshalovich, D. A., A. N. Moskalev, V. K. Khersonskii. Quantum Theory of Angular Momentum. 1989, World Scientific, Singapore. ISBN 978-9971-5-0107-5.

[5] Locarnini, R. A., A. V. Mishonov, J. I. Antonov, et al. World Ocean Atlas 2013. Vol. 1: Temperature. S. Levitus, ed.; A. Mishonov, technical ed. NOAA Atlas NESDIS 73, 40 pp.

[6] Zweng, M., J. Reagan, J. Antonov, et al. World Ocean Atlas 2013. Vol. 2: Salinity. S. Levitus, ed., A. Mishonov, technical ed. NOAA Atlas NESDIS 74, 39 pp.

[7] APEL, John R. Principles of ocean physics. Orlando: Academic Press, 1987. ISBN 0-12-058865-x.

[8] Püthe, C., A. Kuvshinov, A. Khan and N. Olsen. A new model of Earth's radial conductivity structure derived from over 10 yr of satellite and observatory magnetic data. Geophysical Journal International. 2015, 203(3), 1864-1872. DOI: 10.1093/gji/ggv407.

Publication

Velímský, J., L. Šachl, Z. Martinec. The global toroidal magnetic field generated in the Earth's oceans. Earth and Planetary Science Letters (2018). In review.

HEAT AND WATER GENERATION IN THE VICINITY OF EUROPA'S STRIKE-SLIP FAULTS

Research institution:	Principal investigator:	Researchers:	Project ID:
Charles University	Kateřina Sládková	Ondřej Souček, Marie Běhounková, Klára Kalousová	OPEN-12-21

Introduction

Europa is the smallest of the four Galilean moons of Jupiter with a radius of approximately 1,560 kilometres. Its interior consists of an iron-rich core, a silicate mantle and an outer water-ice layer, which is further divided into an ocean and an icy outer shell (probably 10–40 kilometres thick). Europa's surface is very young (in a geological timescale) which may be an indication of ongoing activity within Europa's interior, recent observation of vapour plumes above its south pole also support this idea.

Apart from a global subsurface ocean, confirmed by magnetic data, several morphological features, in particular so-called "chaos terrain" and "double ridges", indicate that near-surface meltwater may also be present. Two mechanisms for the production of subsurface meltwater have been introduced: the hot plumes scenario and the strike-slip fault heating scenario. Here we explore the latter one by means of numerical modelling.

A strike-slip fault is a vertical rupture facilitating horizontal displacement of the two geological blocks in contact, see Figure 1. Nimmo and Gaidos [1] presented a first numerical study of frictional and shear heating on and in the vicinity of Europa's strike-slip faults, and they argued that such a mechanism might produce meltwater. Their study used simplified rheology, describing ice as purely viscous material. In this project, we revisit the strike-slip fault configuration on Europa, considering a more realistic visco-elastic model for ice rheology. The numerical simulations are carried out using the finite element library FEniCS [2].

Results and Methods

Our model simulates the behaviour of a section of Europa's icy shell in the vicinity of a generic strike-slip fault. Assuming small variations along the fault, we only study the 2D projection (perpendicular to the surface), see Figure 1. Furthermore, thanks to the symmetry of the problem we can restrict the computations to just half of the domain.

To calculate the evolution of the fault's vicinity with frictional and shear heating produced, we apply two computational modules coupled together. One solves for tidally induced deformation and associated heating within a viscoelastic body with a prescribed fault; the second employs computed heating in a long-term thermomechanical evolution of the fault's vicinity described as a convecting compressible two-phase material composed of ice and melt, as in [3].

Concerning the first part, we describe the ice as a visco-elastic Maxwell medium deformed due to periodic forcing (imposed by prescribed velocity on the top boundary). The fault (represented by the left edge of the square in Figure 1) is treated as a visco-plastic contact surface, captured through a suitable boundary condition. Effective surface viscosity, mimicking the surface friction coefficient, has a high background value for small slip velocities and decays for increasing slip rates in a manner that guarantees that stress does not exceed the prescribed yield stress. Consequently, rupture of the fault occurs whenever the stress reaches the yield value. As the yield stress is proportional to the hydrostatic pressure, the rupture depth varies during the tidal period.

The second component (the two-phase model) calculates the time evolution of temperature, pressure, porosity, and velocity for a two-phase ice-water mixture [3]. We do not consider porous flow, assuming that water is advected along with the ice. Ice rheology in this module is described by the composite temperature-dependent constitutive law as presented in [4] taking into account weakening of the ice by the presence of melt. The two modules are coupled through viscosity and heating, see the flowchart for calculation in Figure 2.
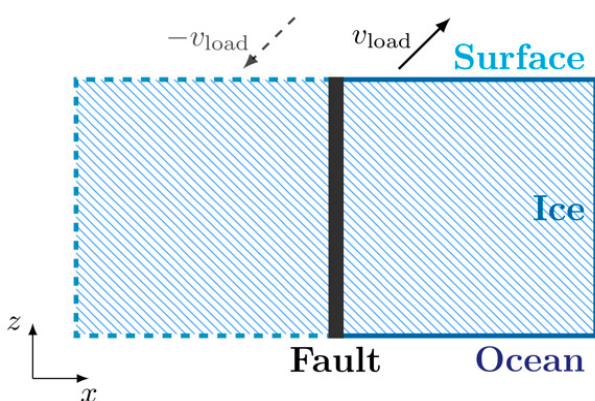

Figure 1.
A sketch of the vicinity of the strike-slip fault,
computational domain is in full lines,
dashed lines simulate the whole
2D cut of the faults surrounding.
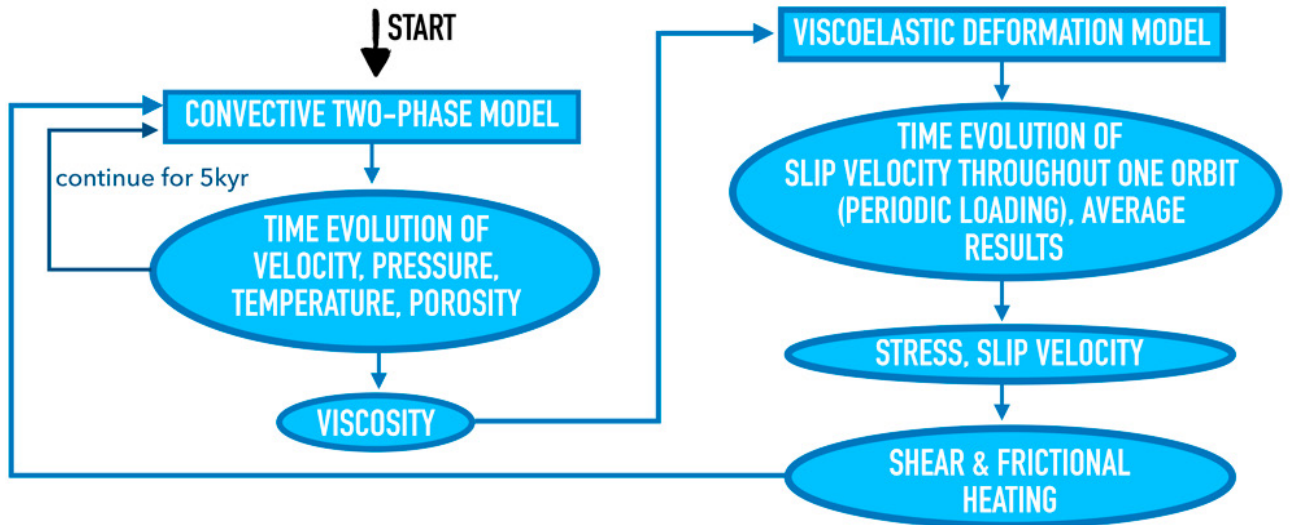
Figure 2. The flow of the computation: First, the convective two-phase model calculates the time evolution of four variables for five thousand years, then viscosity is sent to the viscoelastic deformation model, where the evolution of slip velocity throughout one orbit of Europa (~3.5 days) is computed. Finally, heating is expressed from stress and slip velocity and sent back to the convective two-phase model.

Preliminary results of our model show an increase in temperature in the fault's vicinity, but not enough for the production of melt. Moreover, to achieve at least significant warming of the fault (by approx. 40 K) one order of magnitude higher loading velocities are needed than reported in [1], see Figure 3, suggesting that the concept relating double ridges with meltwater may be incorrect.

Conclusion

Preliminary results of our model show that it is not possible to produce meltwater by frictional and shear heating near the strike-slip faults. Possible improvements of our model include adding the effect of salts, and changing the constant coefficient of friction for a rate and state friction model, which may facilitate melting at lower temperatures.
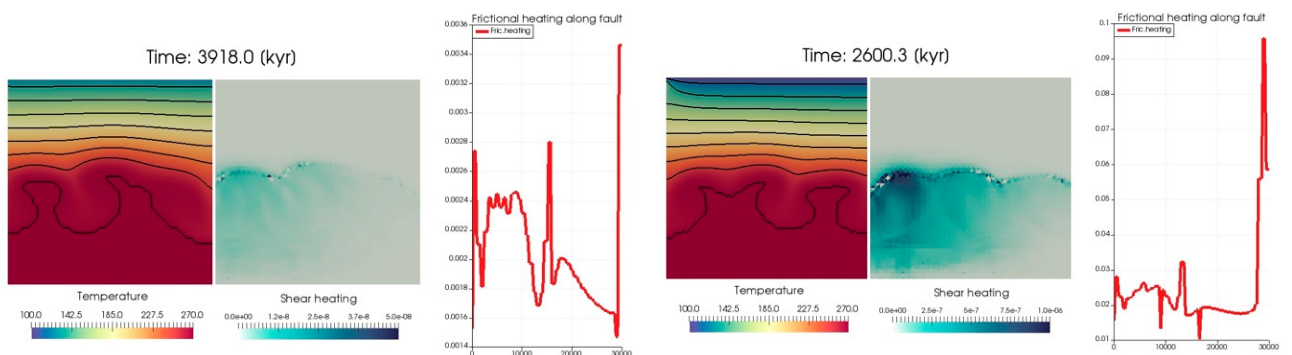
Figure 3.
Results from our model for values from [1] (on the left) and with the amplitude of loading velocity one magnitude higher than in [1] (on the right). In each of the figures: from the left: temperature, shear heating and frictional heating along the fault.

References

[1] Nimmo, F., and E. Gaidos. Strike-slip motion and double ridge formation on Europa. Journal of Geophysical Research. 2002, 107(E4). DOI: 10.1029/2000JE001476.

[2] Alnæs M. S., et al. The FEniCS Project Version 1.5. Archive of Numerical Software. 2015, 3(100), 9-23. DOI: 10.11588/ans.2015.100.20553.

[3] Kalousová, K., O. Souček, G. Tobie, G. Choblet, and O. Čadek. Water generation and transport below Europa's strike-slip faults. Journal of Geophysical Research: Planets. 2016, 121(12), 2444-2462. DOI: 10.1002/2016JE005188.

[4] Goldsby, D. L., D. L. Kohlstedt. Superplastic deformation of ice: Experimental observations. Journal of Geophysical Research: Solid Earth. 2001, 106(B6), 11017-11030. DOI: 10.1029/2000JB900336.

TIDALLY INDUCED DEFORMATION OF THE ICY SHELL OF ENCELADUS

Research institution:	Principal investigator:	Researchers:	Project IDs:
Charles University	Ondřej Souček	Jaroslav Hron, Marie Běhounková	OPEN-7-32, OPEN-10-12, OPEN-12-21, OPEN-14-29

Introduction

The goal of the project is the investigation of tidal deformation of planetary outer shells of icy moons in the Solar system, with a particular emphasis on Saturn's moon Enceladus. Enceladus is a relatively small planetary body (approximately 250 km in radius) differentiated by an outer water-ice layer of thickness varying between a few up to tens of km, a global underlying liquid water ocean, and a silicate core. Cassini mission flybys revealed ongoing surface activity, in particular active jets of water emanating from the surface fissures ("tiger stripes") around the south pole [1], which may be connected to a global subsurface water ocean. This makes Enceladus, together with the Jovian moon Europa, one of the more promising candidates for the presence of extra-terrestrial life, and one of the most geologically active bodies in the Solar system.

In the study, we have investigated the effect of the presence of the faults in Enceladus south polar region and variable ice shell thickness, and we have attempted to quantify the impact these two features might have on the deformation of, and associated dissipation within the outer icy shell when subjected to tidal potential loading in the gravitational field of Saturn.

Results and Methods

Our current methodology has been described in papers [2] and [4]. To summarize, we model the spherical layer as a three dimensional linear elastic or Maxwell viscoelastic body by the method of finite elements using an open-source finite element software package FeniCS [3]. Realistic viscosity variations require many orders of magnitude difference across the shell, leading to severe requirements on mesh quality and vertical resolution. The model incorporates the faults in the south polar region (SPR), which are implemented as narrow, approximately 2 km wide zones passing vertically through the ice shell, in which the elastic moduli are artificially reduced by several orders of magnitude. In the first approximation, our approach is equivalent to modeling the faults as narrow open slots which do not transmit stress, and the walls of which can be treated as free boundaries. Ice shell thickness is either prescribed analytically or represented in terms of spherical harmonic expansion, obtained in the case of Enceladus from recent topography, gravity, and libration inversion data [5]. Along with the mechanical equations, the stationary heat transport
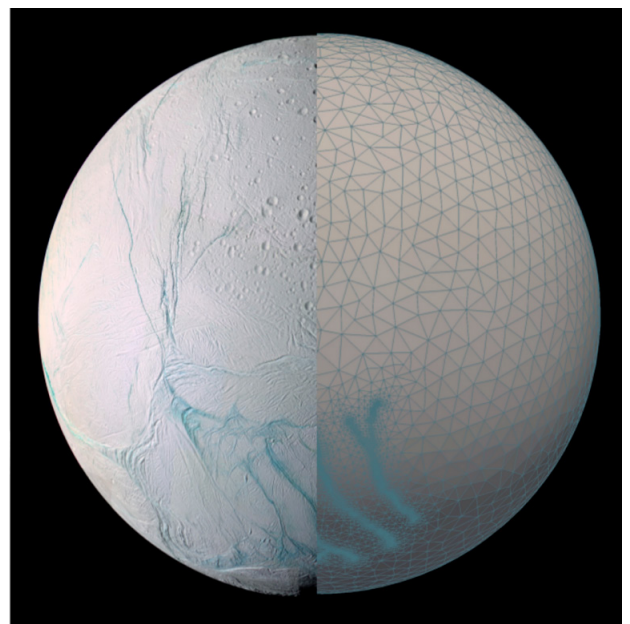
Figure 1.
Enceladus - reality and model (modified from nasa.gov)

equation is solved for the temperature, with prescribed Dirichlet data on the top and bottom surfaces, and with internal heating sources arising due to the tidally-induced deformation and associated dissipation within the shell. The mechanical and thermal equations are solved separately and iterated until convergence is reached.

Results of our numerical simulations indicate that the combination of thinning in the polar region and the presence of faults has a synergistic effect that leads to an increase of both the displacement and stress in the south polar terrain by an order of magnitude compared to that of the traditional model with a uniform shell thickness and without faults.

The presence of faults results in large spatial and temporal heterogeneity of displacement, stress, and predicted geysering activity compared to the traditional models without faults. Our

Figure 2.
Amplitude of tidal displacement of the outer shell
of Enceladus in 3 different time snapshots
for model without faults (left panels)
and with faults (right panels).

about 1/10 of the local ice thickness, and the associated volumetric heating is less than 10^{-6} W/m^3, corresponding to less than 1.5 GW of dissipated power. In the SPR, the tidal effects are enhanced by the combined action of faults and ice shell thinning. Although the volumetric heating in this relatively small region may reach values larger than 10^{-4} W/m^3, the total heat production does not exceed 2.1 GW. Our computations show that tidal heating in the ice shell can explain only a small fraction of Enceladus hea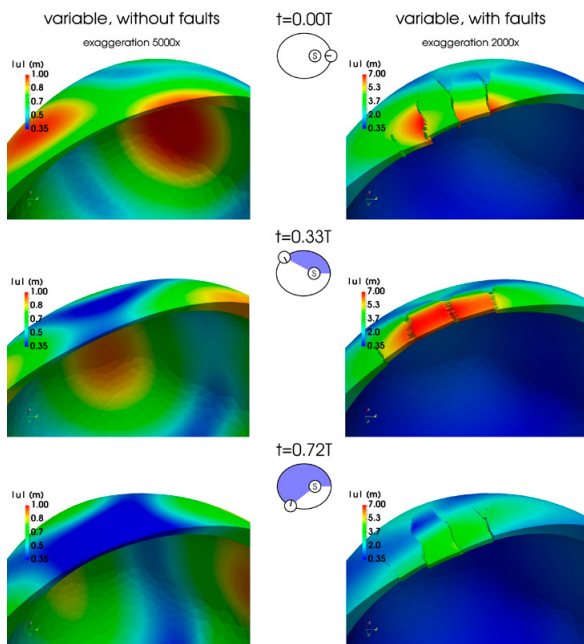t production derived from astrometric observations, implying that Enceladus heat engine is powered by dissipation in the core or in the ocean.

On-going Research / Outlook

Currently, we are investigating the possibility of validating our results through future dedicated space missions by predicting the observable variations in gravity field and other measurable quantities. Concerning the numerical model, we have been developing a more advanced description of the south polar fault zones in an attempt to mimic realistic friction behavior of an ice-ice frictional contact and we plan to incorporate this model into the existing large scale ice shell model described above.

Conclusion

We have successfully implemented the model of viscoelastic tidal deformation and heat transfer of planetary ice shell of variable thickness with a predefined system of fractures modeled as mechanically weak zones. We have demonstrated through numerical simulations the synergistic effect of ice shell thickness variations and the presence of faults, which leads to significant enhancement of both deformation and associated dissipation in the south polar region. This localized heat source is however not powerful enough to ensure the long-term stability of Enceladus global ocean, indicating the importance of deeper heat sources, either tidal dissipation in a highly deformable core and/or in the global ocean.

model contributes to the understanding of the physical mechanisms that control the fault activity, and it provides potentially useful information for future missions that will sample the plume for evidence of life.

Our results further indicate that tidal heating is concentrated in a narrow low viscosity zone near the base of the ice shell and along faults. Outside the SPR, the thickness of this zone is

References

[1] Porco, C. C., et al. Cassini Observes the Active South Pole of Enceladus. Science. 2006, 311(5766), 1393-1401. DOI: 10.1126/science.

[2] Souček, O., Hron, J., Běhounková, M., and O. Čadek. Effect of the tiger stripes on the deformation of Saturn's moon Enceladus. Geophysical Research Letters. 2016, 43(14), 7417-7423. DOI: 10.1002/2016GL069415.

[3] Alnæs M. S., J. Blechta, J. Hake, A. Johansson, B. Kehlet, A. Logg, C. Richardson, J. Ring, M. E. Rognes and G. N. Wells. The FEniCS Project Version 1.5. Archive of Numerical Software. 2015, 3(100), 9-23. DOI: 10.11588/ans.2015.100.20553.

Publications

[4] Běhounková, M., O. Souček, J. Hron, and O. Čadek. Plume Activity and Tidal Deformation on Enceladus Influenced by Faults and Variable Ice Shell Thickness. Astrobiology. 2017, 17(9), 941-954. DOI: 10.1089/ast.2016.1629.

[5] Čadek, O., O. Souček, M. Běhounková, G. Choblet, G. Tobie, and J. Hron. Long-term stability of Enceladus' uneven ice shell. Icarus. 2019, 319, 476-484. DOI: 10.1016/j.icarus.2018.10.003.

04 | CHEMISTRY AND MATERIAL SCIENCES
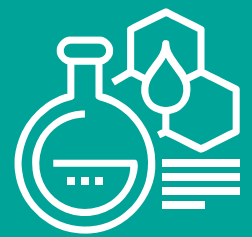
MAGNETIC PROPERTIES OF TOPOLOGICAL INSULATORS AND ANTIFERROMAGNETS

Research institution:	Principal investigator:	Researchers:	Project partner:	Project ID:
IT4Innovations National Supercomputing Center	Pavel Baláž	Karel Carva, Jakub Šebesta, František Máca, Josef Kudrnovský, Václav Drchal	Charles University	OPEN-11-31

Introduction

New classes of materials, featuring spin-orbital interactions acting on itinerant electrons, appear to have a strong potential to replace old-fashioned components of magnetic memories and data processing units. To this group of novel materials, topological insulators as well as tetragonal antiferromagnets (AFMs) can be assigned. Thanks to their unique features, new concepts of manipulating with magnetic moments were developed in the past years, opening a direct highway towards new electronic devices. However, to successfully reach the desired goals, the fundamental physical properties of these materials on the atomistic and subatomic level need to be studied. Therefore, in our research we have applied both ab initio calculations, based on the density functional theory, and atomistic spin dynamics simulations to study the basic magnetic properties of most promising materials.

Here, we shall focus on AFM alloy CuMnAs. This material can be prepared under special conditions in a tetragonal phase, which cannot be observed in nature. However, special physical properties of tetragonal CuMnAs, make this alloy a promising material for AFM spintronics. Namely, by means of ab initio calculations, it has been shown that electric current can induce staggered spin orbit fields acting on localized magnetic moments [1, 2], which allows an efficient manipulation with the AFM ordering parameter. The current magnetic state of AFM can be checked using anisotropic magnetoresistance. The main advantage of including AFM elements in spintronics is their operational frequency, which is typically in the terahertz range, which significantly exceeds the gigahertz frequencies of standard ferromagnet based devices.

However, during the fabrication of tetragonal CuMnAs a number of defects might appear. The presence of defects has been predicted by resistance measurements. Particularly, vacancies on Mn and Cu sublattices have been confirmed by ab initio calculations [3]. Moreover, there is a high chance that atoms in the Cu sublattice can be substituted by Mn (Mn_{Cu} antisite) or vice versa (Cu_{Mn} antisite). All these defects might substantially influence the band structure, which also affects the macroscopic properties of the sample, such as resistivity, saturated magnetization, and Neel temperature. Therefore, we theoretically studied how these defects can influence the basic magnetic properties of CuMnAs.
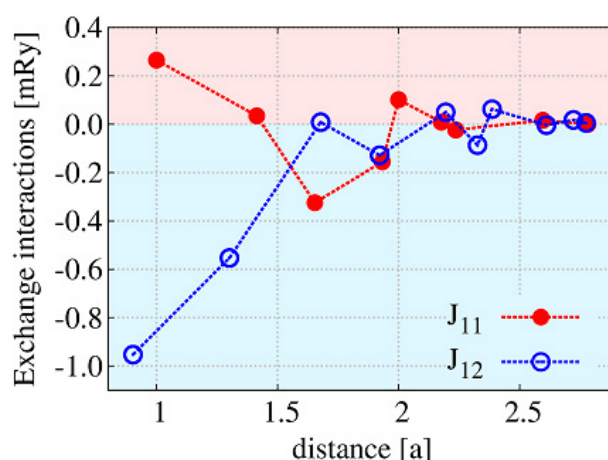
Figure 1.
Exchange interactions in defect-free CuMnAs between the Mn atoms belonging to the same sublattice (J_{11}) and different sublattices (J_{12}) as a function of the distance (in the units of lattice constant); see Ref. 3.

Results and Methods

The quantities that determine the magnetic ordering and critical temperature, are the exchange interactions between the atomic moments. These can be calculated by ab initio calculations based on the Green function formulation of the tight-binding linear muffin-tin orbitals (TB-LMTO) method with disorder effects treated in the coherent potential approximation (CPA) [4].

The exchange interactions were determined by the Liechtenstein formula generalized to random alloys [5] in the disordered local moment (DLM) reference state.

Figure 1 shows the exchange interactions in defect-free CuMnAs acting between the Mn moments inside the same sublattice, J_{11}, and between Mn moments belonging to different sublattices, J_{12}, as a function of their distance. A dominant contribution of negative (AFM) interactions between the sublattices can be noticed.
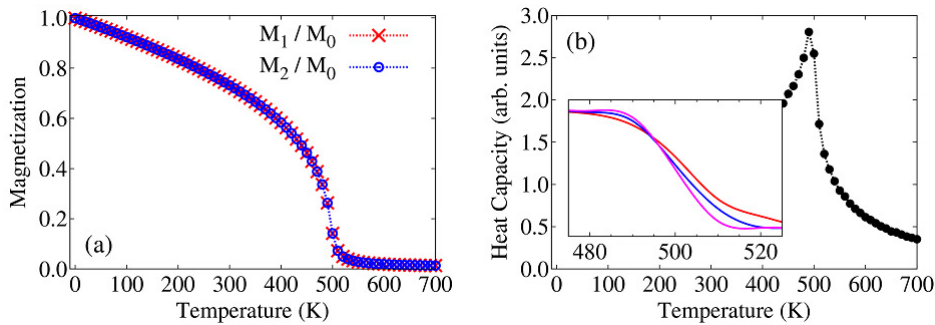
Figure 2.
(Left) Temperature dependence
of sublattice magnetizations (normalized
to zero-temperature saturated magnetization,
M_0). (Right) Temperature dependence
of the heat capacity with a peak at 495 K.
The inset shows intersection of three Binder
cumulants calculated for superlattices
of sizes N=16, 20, and 24; see Ref. 6.

In turn, to study the thermodynamic properties of CuMnAs we used the previously calculated exchange interactions in classical Heisenberg Hamiltonian. Using classical Monte Carlo (MC) simulations based on the Metropolis algorithm we estimated the Neel temperature from the specific heat as well as from the Binder cumulants calculated separately for each Mn sublattice.

Figure 2 (left) depicts the temperature dependence of the Mn sublattice magnetizations. Although the sublattice magnetizations are antiparallel (thus total magnetization is zero) the magnetic moments are feromagnetically oriented inside the sublattices. Figure 2 (right) shows the calculated heat capacity for the defect-free CuMnAs. In addition the inset of Figure 2 (right) depicts three Binder cumulants calculated for three different sizes of the supercell. Both the peak in the heat capacity as well as the intersection of the Binder cumulants indicate the Neel temperature T_N=495 K.

In the same way, calculating exchange interactions and employing classical MC simulations, one can obtain Neel temperatures for CuMnAs superlattices including various kind of defects. A comprehensive study of this problem can be found in Ref. 6. Here, we mention two cases including antisites on Cu and vacations. First, we assumed CuMnAs includes 5% Mn_{Cu} an-

tisites. The Neel temperature decreased to T_N=465K. Second, 10% of vacations on the Mn sublattices together with 10% of vacations on the Cu sublattices lead to a lowering of the Neel temperature to T_N=446K.

On-going Research / Outlook

Our calculations indicate that various lattice defects can significantly influence important material parameters of CuMnAs including Neel temperature, magnetic moments, and electric conductivity [6]. This open new possibilities for the engineering of materials with desirable properties for spintronic devices.

Conclusion

In summary, we used Monte Carlo simulations to predict the critical temperature of CuMnAs. Particularly, we focused on various defects, which might occur in the crystal lattices, and studied how they can influence the material properties. First, we studied how the defects affect the exchange interactions between the magnetic moments. Second, the Neel temperatures were determined using the Binder cumulants of the Mn sublattices.

References

[1] Železný, J., H. Gao, K. Výborný, et al. Relativistic Néel-Order Fields Induced by Electrical Current in Antiferromagnets. Physical Review Letters. 2014, 113(15). DOI: 10.1103/PhysRevLett.113.157201.

[2] Wadley P., B. Howells, J. Železný, et al. Electrical switching of an antiferromagnet. Science. 2016, 351(6273), 587-590. DOI: 10.1126/science.aab1031.

[3] Máca, F., J. Kudrnovský, V. Drchal. Physical properties of the tetragonal CuMnAs: A first-principles study. Physical Review B. 2017, 96(9). DOI: 10.1103/PhysRevB.96.094406.

[4] Turek, I., et al. Electronic Structure of Disordered Alloys, Surfaces and Interfaces. Boston, MA: Springer US, 1997. ISBN 978-0-7923-9798-4.

[5] Turek, I., J. Kudrnovský, V. Drchal, and P. Bruno. Exchange interactions, spin waves, and transition temperatures in itinerant magnets. Philosophical Magazine. 2006, 86(12), 1713-1752. DOI: 10.1080/14786430500504048.

[6] Máca, F., et al. Tetragonal CuMnAs alloy: Role of defects. Journal of Magnetism and Magnetic Materials. 2019, 474, 467-471. DOI: 10.1016/j.jmmm.2018.10.145.

CONTRAST AGENTS FOR MAGNETIC RESONANCE IMAGING UNDER THE SCOPE OF AB-INITIO METHODS

Research institution:
Charles University

Principal investigator:
Jan Blahut

Researchers:
**Jan Kotek,
Daniel Hollas,
Danuta Kruk,
Petr Hermann**

Project ID:
OPEN-9-5

Introduction

Nowadays, magnetic resonance imaging is one of the most commonly used methods for diagnosis in clinical practice as well as in medicinal research. The increasing performance of available tomographs enables the application of conceptually different contrast agents than the Gd^{3+}-H_2O based system [1]. One promising methodology is based on the detection of ^{19}F nuclei, which are directly bound to a paramagnetic complex and administered to the patient [2, 3]. A sufficient amount of experimental data for comparison is not available yet. Therefore, the possibility of a comparison with a simulation is highly appreciated.

Molecular dynamic (MD) simulations in synergy with efficient implementation of post-Hartee-Fock methods for transition metal complexes enable simulation of relaxation processes that determine the efficiency of developed contrast agent [4–7].

The target molecule of this project is a nickel(II) complex with a macrocyclic ligand decorated by a CF_3 group (see Figure 1).

This complex was already identified as a contrast agent for high efficiency cell labelling and tracing, but its usage is limited [8, 9]. Proper description of the effects responsible for fast ^{19}F nuclear relaxation in nuclear magnetic resonance (NMR), especially electronic relaxation of the proximate paramagnetic center, can help to rationalize design of novel, better systems.

Results and Methods

Transient, time dependent modulation of zero-field splitting (ZFS) by molecular fluctuation is expected to be the dominant mechanism of nickel(II) electronic relaxation in octahedral complexes. Therefore, the static values of ZFS do not provide sufficient description of the system for comparison with experimental data.

In this project we have focused on the application of methodology described by Pollet and Platas-Iglesias [7, 10]. This
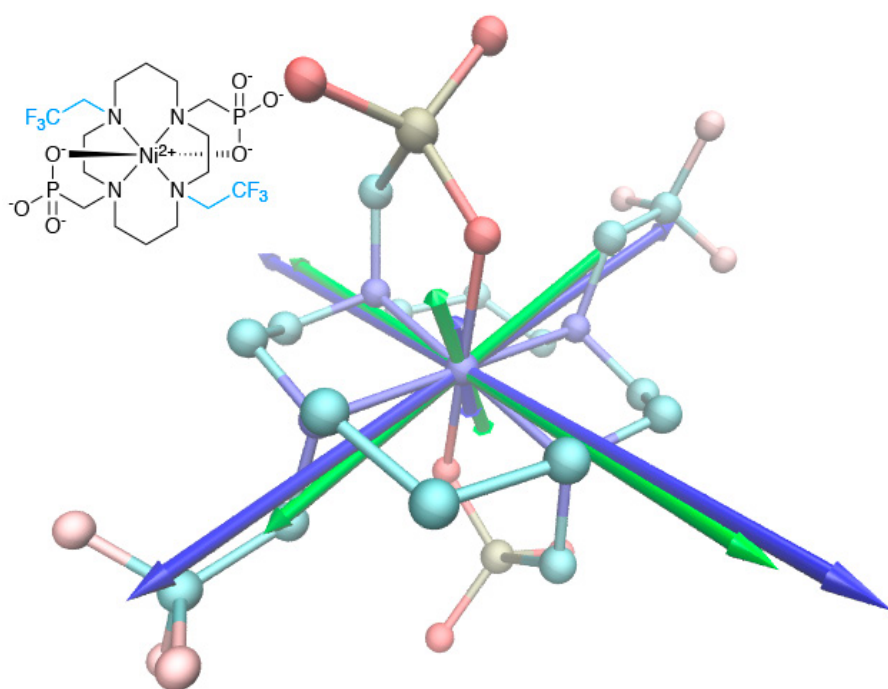
Figure 1.
Formula of the complex
[Ni(te2f2p)]²⁻ and its 3D representation
(geometry optimized on the TPPSh/
TZVP level) with indication of
traceless ZFS tensor principal
components obtained
from static structure (green arrows)
and from traceless ZFS tensor
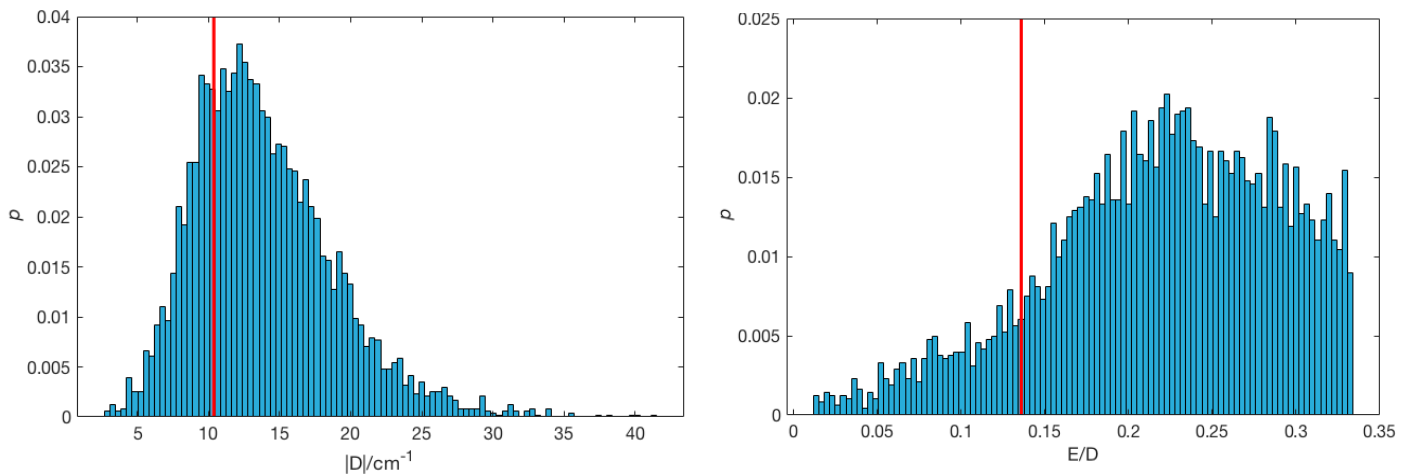*average NVT MD (blue arrow)*

Figure 2.
Distribution of axial |D^{MD}| (left) and rhombic (E/D)^{MD} (right) ZFS parameters obtained by NVT simulation of complex
[Ni(te2f2p)]$^{2-}$ (blue bars), and values for complex [Ni(te2f2p)]$^{2-}$ in minimalized geometry (red lines).

approach is based on the calculation of ZFS parameters for geometry snapshots taken from a MD run, and subsequent calculation of electronic relaxation time from time modulation of ZFS tensor D.

Ab-initio NVT molecular dynamic simulations (23 ps) of a [Ni(te-2f2p)]$^{2-}$ ion were used in this study. Snapshots were taken every 4.8 fs and the D^{MD} tensor was calculated using the CASS-CF+NEVPT2/TZVP wave function employing the "effective Hamiltonian spin-orbit coupling method" as implement in ORCA 4.0. For each snapshot, the axial and rhombic parameters D^{MD} and E^{MD} were calculated, see Figure 2. The principal components of D^{static}, obtained from the minimal-energy structure, and those from the time average D^{MD} are compared in Figure 1 as well. While the orientation of the ZFS tensor is similar, the overall size of ZFS is higher in dynamic-simulation. This is caused by fluctuations in the nickel(II) coordination environment.

The strength Δ_T^{MD} of the transient ZFS was estimated from the standard deviation of D^{MD} and E^{MD} distribution as $(\Delta_T^{MD})^2 = \frac{2}{3}(D_T^{MD})^2 + 2(E_T^{MD})^2 = 4.6$ cm^{-1}. This value is in excellent agreement with experimental data $\Delta_T^{MD} = 4.6(2)$ cm^{-1} [11].

Every element d_{ij} of the D^{MD} tensor was then divided into static, time average, contribution d_{ij}^S, and transition contribution d_{ij}^T, which has a zero time-average.

A time autocorrelation function was calculated for each d_{ij}^T. By nonlinear regression analysis of the overall, normalised, autocorrelation function $C(t)$ with exponential decay, the transient ZFS correlation time was calculated. In our case the single exponential fit does not describe $C(t)$ well, and another exponential function must be added. It indicates two processes of electronic relaxation. The resulting values of transient ZFS correlation time are $\tau_v = 0.103(6)$ ps and $3.22(14)$ ps. The higher value of ZFS correlation time is in reasonable agreement with the experimental value, $\tau_v = 7.0(2)$ fs. The contribution of the faster process is not fully understood.

On-going Research / Outlook

The following step in the presented project is a detailed analysis of Experimental data obtained recently using a field-cycling relaxometer. The existing analysis is based on rough estimations and is probably insufficient for comparison with a simulation. The obtained dynamical description of nickel(II)'s electronic structure could also be used for spin-dynamic simulation as described for example by Vaara [12].
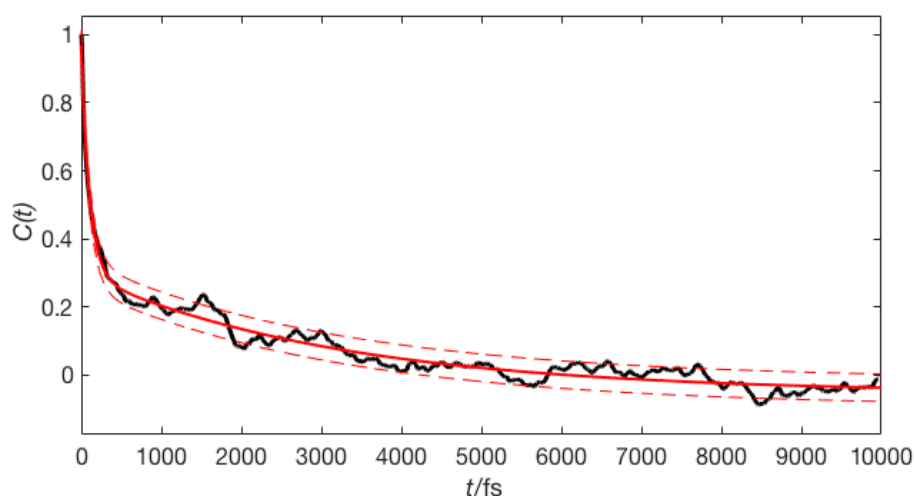
Figure 3.
Normalized time autocorrelation
functions of the transient part of ZFS
for [Ni(te2f2p)]²⁻(black), fitted with double
exponential functions with 90% prediction
bonds (red solid and dashed line
respectively).

Conclusion

The 23 ps long simulations of nickel(II)'s electronic structure development in complex [Ni(te2f2p)]²⁻ has shown a substantial effect on the size of zero-filed-splitting compared to static minimal energy structure. Obtained dynamical characteristics are in partial agreement with experimental relaxometric values.

References

[1] Viswanathan, S., Z. Kovacs, K. N. Green, S. J. Ratnakar, and A. D. Sherry. Alternatives to Gadolinium-Based Metal Chelates for Magnetic Resonance Imaging †. Chemical Reviews. 2010, 110(5), 2960-3018. DOI: 10.1021/cr900284a.

[2] Tirotta, Ilaria, et al. ¹⁹F Magnetic Resonance Imaging (MRI): From Design of Materials to Clinical Applications. Chemical Reviews. 2014, 115(2), 1106-1129. DOI: 10.1021/cr500286d.

[3] Chalmers, K., et al. Design Principles and Theory of Paramagnetic Fluorine-Labelled Lanthanide Complexes as Probes for ¹⁹F Magnetic Resonance: A Proof-of-Concept Study. Chemistry – A European Journal. 2010, 16(1), 134-148. DOI: 10.1002/chem.200902300.

[4] Lasaroski, A., R. Vuilleumier and R. Pollet. Vibrational dynamics of zero-field-splitting hamiltonian in gadolinium-based MRI contrast agents from ab initio molecular dynamics. The Journal of Chemical Physics. 2014, 141(1). DOI: 10.1063/1.4885848.

[5] Kowalewski, J., et al. Extensive NMRD studies of Ni(II) salt solutions in water and water-glycerol mixtures. Journal of Magnetic Resonance. 2008, 195(1), 103-111. DOI: 10.1016/j.jmr.2008.08.011.

[6] Liimatainen, H. T. O. Pennanen, and J. Vaara. Magnetic Properties of Ni²⁺ (aq) from First Principles. Journal of Chemical Theory and Computation. 2011, 7(10), 3248-3260. DOI: 10.1021/ct200336c.

[7] Platas-Iglesias, C., et al. Transient versus Static Electron Spin Relaxation in Mn²⁺ Complexes Relevant as MRI Contrast Agents. The Journal of Physical Chemistry A. 2016, 120(32), 6467-6476. DOI: 10.1021/acs.jpca.6b05423.

[8] Blahut, J., K. Bernášek, A. Gálisová, et al. Paramagnetic ¹⁹F Relaxation Enhancement in Nickel(II) Complexes of N -Trifluoroethyl Cyclam Derivatives and Cell Labeling for ¹⁹F MRI. Inorganic Chemistry. 2017, 56(21), 13337-13348. DOI: 10.1021/acs.inorgchem.7b02119.

[9] Blahut, J., et al. Nickel(ii) complexes of N-CH₂CF₃ cyclam derivatives as contrast agents for ¹⁹F magnetic resonance imaging. Dalton Transactions. 2016, 45(2), 474-478. DOI: 10.1039/C5DT04138D.

[10] Lasaroski, A., R. Vuilleumier and R. Pollet. Vibrational dynamics of zero-field-splitting hamiltonian in gadolinium-based MRI contrast agents from ab initio molecular dynamics. The Journal of Chemical Physics. 2014, 141(1). DOI: 10.1063/1.4885848.

[11] Blahut, J. Dynamics of paramagnetic complexes observed by Nuclear Magnetic Resonance. (Dissertation, Charles University, 2017). Publication in preparation.

[12] Rantaharju, J., J. Mareš and J. Vaara. Spin dynamics simulation of electron spin relaxation in Ni²⁺ (aq). The Journal of Chemical Physics. 2014, 141(1). DOI: 10.1063/1.4885050.

UNFEASIBLE MOLECULAR FRAMEWORKS: PROPERTIES AND APPLICATIONS

Research institution:
The Institute of Organic Chemistry and Biochemistry of the Czech Academy of Sciences

Principal investigator:
Ota Bludský

Researchers:
Miroslav Rubeš, Michal Trachta

Project ID:
OPEN-12-6

Introduction

Recent progress in advanced synthesis of molecular sieves opens up the possibility of preparing novel materials that have not been accessible by traditional synthetic pathways [1]. These new materials do not obey the criteria based on correlation between framework energy and density, and therefore they have not been considered as feasible synthesis targets [2]. It has been shown that the limitation of solvothermal synthesis of zeolites, known as the 'zeolite conundrum', can be overcome by new synthetic pathways using 2D zeolites as nanoscale building blocks [3]. Expanding the diversity of zeolite structures is certainly helpful for the improvement of performance in current technological applications. More importantly, unique features of the corresponding 'unfeasible' molecular frameworks might also be the key to novel functions and new applications.

The number of hypothetical zeolite topologies is enormous. Computer enumeration predicts the existence of millions of zeolite structures, and the recent breakthrough in the synthesis of unfeasible zeolites suggests that many of them can actually be prepared [4, 5]. Given the number of possible candidates, it is certainly worthwhile to develop a methodology for the evaluation of their properties computationally prior to their synthesis. The synthesis of zeolites from lamellar precursors using the ADOR (Assembly–Disassembly–Organization–Reassembly) protocol can lead to a large number of new materials with topologically unique molecular frameworks. For each application (adsorption, separation, catalysis), an optimal synthesis target can thus be searched for. To achieve this goal, we have employed state-of-the-art methods of contemporary computational chemistry combined with experiments tailored to improve our understanding of the underlying physico-chemical processes.

Results and Methods

The ADOR nanomaterials have been described within the periodic dispersion-corrected DFT model using unit cells with the chemical composition representing the experimentally studied material. Periodic DFT calculations were carried out using the Vienna Ab initio Simulation Package (VASP) [6].
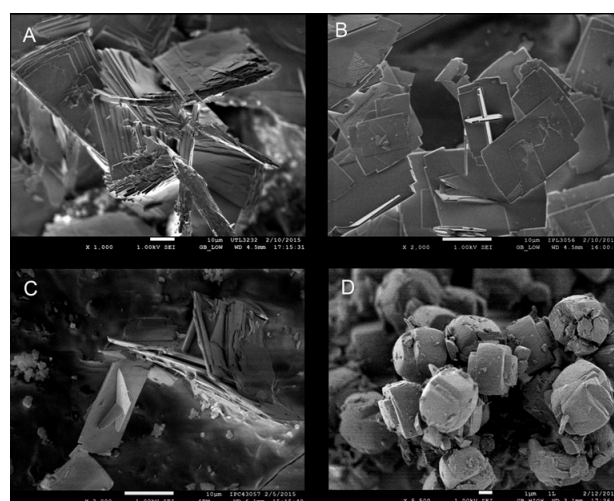
Figure 1.
SEM images of the zeolites:
A – UTL, B – OKO, C – PCR, D – MFI.

DFT functionals do not properly account for non-local correlation (dispersion) effects. The dispersion energy contribution is important for all extended systems, and therefore DFT (GGA, Generalized Gradient Approximation) calculations must be corrected for the dispersion effects. We have employed the DFT/CC correction scheme developed to overcome the well-known deficiency of local (LDA, Local Density Approximation) and semi-local (GGA) density functionals [7]. This method has been extensively tested on zeolite systems and shown to provide results in excellent agreement with experimental data [8]. The DFT/CC method has been implemented as an extension of the VASP code.

To fully capture the details of the adsorption and separation processes in 'unfeasible' zeolites synthesized via the ADOR protocol, MD (molecular dynamics) and MC (Monte Carlo) simulations have been performed. First, empirical potential energy functions have been parameterized using the high-level ab initio calculations described above. We used our recently developed approach for the automatic generation of ab initio force fields (AIFF) from

combined DFT/CC and MD calculations. The resulting AIFFs are system-specific (nontransferable) interatomic potentials which closely resemble the DFT/CC potential energy function for geometries sampled by the MD simulation. Second, standard MD and GCMC (Grand Canonical Monte Carlo) simulation packages were used for predicting isosteric heats and diffusivities.

Molecular sieves prepared by a recently discovered synthetic pathway using 2D zeolites as nanoscale building blocks were investigated by means of combined experimental and theoretical approaches. These materials may or may not obey criteria for traditional solvothermal synthesis based on the correlation between framework energy and density. The research effort was mainly focused on unique properties of 'unfeasible' molecular frameworks leading to novel functions and new technological applications. The main results of this project are (i) development of a precise and reliable methodology for evaluating the properties of these materials and (ii) determination of properties that can be utilized in technologically important processes such as adsorption, gas separation and catalytic applications.

On-going Research / Outlook

In this project, the issue of in-silico determination of the properties of the hypothetical molecular sieves has been addressed. The synthesis of new molecular sieves with improved adsorp-tion and catalytic properties has the potential to result in large economic or environmental gains. About 20 different structural types of zeolites are currently used in the large-scale chemical processes representing several billion of USD. There is no doubt about huge economic and environmental benefits from the introduction of novel zeolitic materials or other molecular sieves with improved adsorption and catalytic properties (and the reviewer should know that). In the future, we plan to focus on diffusion processes in catalytic applications.

Conclusion

A recently published discovery of a new synthesis pathway has opened up the possibility of a step increase in the number of zeolite frameworks available, many of them with uncommon features. We have examined the properties of selected ADOR zeolites of the UTL family, both theoretically and experimentally. Although all investigated materials share the same layer topology, their channel structure and diffusion characteristics are significantly different. Some of the investigated zeolites possess small window openings, and therefore the diffusion limitations through 7-, 8-, and 9-membered rings were determined for several probe molecules (CH_4, N_2, CO_2, CO, C2 and C3 hydrocarbons). These findings may lead to optimal design and improved functions for future catalytic applications.

References

[1] Eliášová, P., M. Opanasenko, P. S. Wheatley, et al. The ADOR mechanism for the synthesis of new zeolites. Chemical Society Reviews. 2015, 44(20), 7177-7206. DOI: 10.1039/C5CS00045A.

[2] Majda, D., F. A. A. Paz, O. D. Friedrichs, M. D. Foster, A. Simperler, R. G. Bell and J. Klinowski. Hypothetical Zeolitic Frameworks: In Search of Potential Heterogeneous Catalysts. The Journal of Physical Chemistry C. 2008, 112(4), 1040-1047. DOI: 10.1021/jp0760354.

[3] Mazur, M., P. S. Wheatley, M. Navarro, W. J. Roth, M. Polozij, A. Mayoral, P. Eliasova, P. Nachtigall, J. Cejka, R. E. Morris. Synthesis of 'unfeasible' zeolites. Nature Chemistry. 2016, 8(1), 58-62. DOI: 10.1038/nchem.2374.

[4] Pophale, R.; P. A. Cheeseman, M. W. Deem. A database of new zeolite-like materials. Physical Chemistry Chemical Physics. 2011, 13(27). DOI: 10.1039/c0cp02255a.

[5] Akporiaye, D. E. and G. D. Price. Systematic enumeration of zeolite frameworks. Zeolites 1989, 9(1), 23-32. DOI: 10.1016/0144-2449(89)90005-5.

[6] Kresse, G., and J. Hafner. Ab initio molecular dynamics for open-shell transition metals. Physical Review B. 1993, 48, 13115. DOI: 10.1103/PhysRevB.48.13115.

[7] Bludský O., M. Rubeš, P. Soldán, and P. Nachtigall. Investigation of the benzene-dimer potential energy surface: DFT/CCSD(T) correction scheme. The Journal of Chemical Physics. 2008, 128, 114102. DOI: 10.1063/1.2890968.

[8] Rubeš M., M. Trachta, E. Koudelková, R. Bulánek, J. Klimeš, P. Nachtigall, O. Bludský. Temperature Dependence of Carbon Monoxide Adsorption on a High-Silica H-FER Zeolite. Journal of Physical Chemistry C. 2018, 122, 26088. DOI: 10.1021/acs.jpcc.8b08935.

Publications

Rubeš, M., E. Koudelková, F. Solanea de Oliveira Ramos, M. Trachta, O. Bludský, R. Bulánek. Experimental and Theoretical Study of Propene Adsorption on K-FER Zeolites: New Evidence of Bridged Complex Formation. The Journal of Physical Chemistry C. 2018, 122(11), 6128-6136. DOI: 10.1021/acs.jpcc.7b12706.

Rubeš, M., M. Trachta, E. Koudelková, R. Bulánek, J. Klimeš, P. Nachtigall, O. Bludský. Temperature Dependence of Carbon Monoxide Adsorption on a High-Silica H-FER Zeolite. The Journal of Physical Chemistry C. 2018, 122(45), 26088-26095. DOI: 10.1021/acs.jpcc.8b08935.

Trachta M., O. Bludský, M. Rubeš. The interaction of proteins with silica surfaces. Part II: Free energies of capped amino acids. Comput. Theor. Chem. 1148 (2019) 38-43. DOI: 10.1016/j.comptc.2018.12.013.

Bulánek, R., E. Koudelková, F. S. de Oliveira Ramos, M. Trachta, O. Bludský, M. Rubeš, J. Čejka. Experimental and theoretical study of propene adsorption on alkalimetal exchanged FER zeolites. Microporous Mesoporous Mat. Submitted (2019).

ATOMIC SCALE STRATEGIES FOR FACILE TRANSITION METAL DICHALCOGENIDES EXFOLIATION (FATRADEX)

Research institution:
The Czech Technical University in Prague

Principal investigators:
Antonio Cammarata, Benjamin Irving, Paolo Nicolini

Project ID:
OPEN-8-2

Introduction

Transition metal dichalcogenides (TMDs) are perhaps the most promising substitute for graphene for building the next generation of low-dimensional functional materials. They offer an unprecedented array of physicochemical properties, allowing for wide applicability in fields as diverse as photovoltaics, lithium ion batteries, hydrogen evolution catalysis, transistors, photodetectors, DNA detection, memory devices and tribological applications [1–4]. In addition to the versatile chemical composition and stoichiometry, dimensionality plays a key role in determining the characteristics of TMDs. Like graphene and other van der Waals solids, bulk TMDs can be exfoliated into single- or few-layered structures by physical or chemical routes, such as the scotch-tape technique [5], solvent assisted exfoliation [6], and chemical exfoliation via ion intercalation [7–9]. Exfoliation of these materials into mono or few-layers thin films leads to additional exciting properties due to confinement effects not seen in the bulk counterparts [10–15]. The present project investigates the microscopic mechanisms functioning at the atomic scale that govern the exfoliation of transition metal dichalcogenides, individuating feasible experimental routes to produce mono- and few-layer TMD films on a large scale. The project thus establishes guidelines that will narrow the experimental exploration to only the most favorable conditions for layer exfoliation, and to formulate protocols to design new exfoliation strategies for high-efficiency production of 2D layered TMD-based materials.

Results and Methods

Density functional calculations have been used to investigate the sliding properties and associated phenomena of six members of the TMD family of materials [21]. The compounds selected for investigation have stoichiometry MX2, where M=Mo, W, and X = S, Se, Te. Potential energy and charge transfer profiles were calculated in order to highlight the dependence of important nanomechanical properties such as shear strength on chemical composition and bilayer orientation (sliding direction). Our results also underline the intrinsic relationship between incommensurate crystals and the well-known superlubric behaviour of molybdenum disulfide.

By exploiting accidental angular commensuration, we have been able to perform calculations on three different incommensurate configurations, giving an estimation of the roughness of the potential energy landscape with respect to the sliding coordinate (Figure 1). The results reveal that a decrease in friction of two to four orders of magnitude is expected when one moves from the commensurate configuration to an incommensurate one. This is particularly interesting if one considers that such a rotationally disordered configuration has recently been synthesised for WSe_2 via annealing of amorphous precursors, suggesting that progress is being made regarding fabrication of interfaces with non-random rotational angles.

We also developed a new approach to look for possible sliding paths, named Normal-Modes Transition Approximation (NMTA)
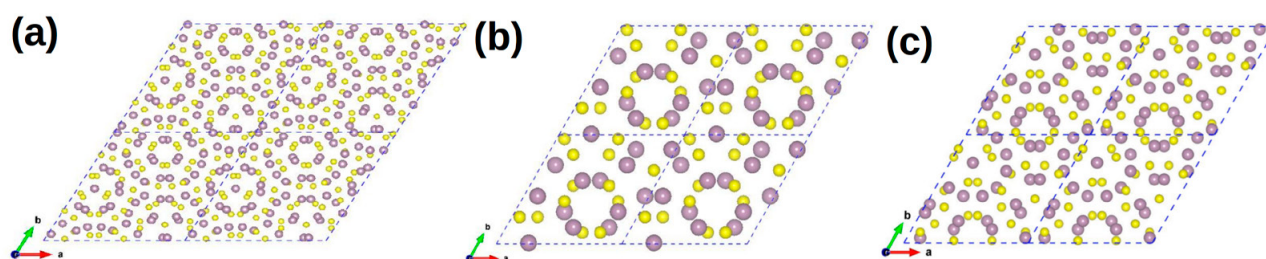

Figure 1.
Renderings of 4x4 supercells for MoS_2 bilayers with incommensuration angles of (a) 17.9, (b) 38.2 and (c) 92.2 degrees; space group = P312 (No. 149) [21]. A decrease in friction of two to four orders of magnitude is expected when one moves from the commensurate configuration to an incommensurate one.
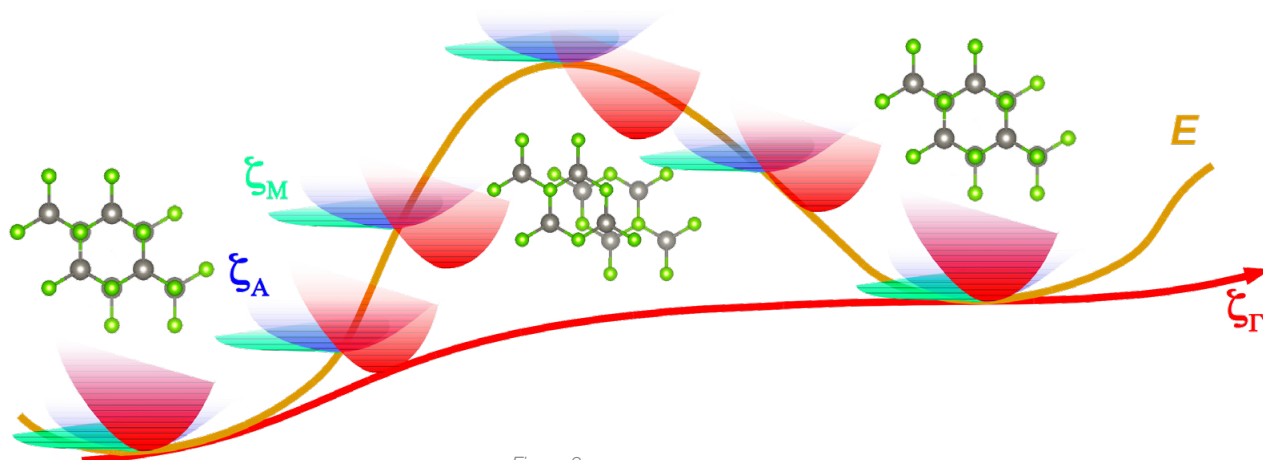
Figure 2.
Our developed Normal-modes Transition Approximation method allowed us to identify possible sliding paths from the analysis of the phonon modes of the stable geometry [22]. The potential energy barrier E to overcome along the selected configurational coordinate ζ_Γ (sliding path) is found to be smallest for the Ti:MoS$_2$ system.

(Figure 2) [22]. In this framework, we individuate possible sliding paths from the analysis of the phonon modes of the stable geometry. In particular, we considered those modes the atom displacement pattern of which represents relative layer shifts of adjacent MX_2 layers. Using such modes, we built a sliding path consisting of relative layers shift along the M-X bond direction.

Besides the aforementioned MX_2 compounds, we also considered the Ti:MoS$_2$ system which we recently individuated as promising material with enhanced frictional properties [16]. We find that the potential energy barrier to overcome along the selected sliding path is smallest for the Ti:MoS$_2$ system, further supporting our previous findings on such a Ti-doped MoS$_2$ phase. Following the NMTA prescription, we also analysed two case studies, namely the inversion of the ammonia molecule and the isomerization mechanism of the HCN molecule. We find that the NMTA method is also able to individuate which are the phonon mode contributions to transition rates, allowing for the adjustment of the transition rate and barrier. Such case studies enabled us to show that the NMTA method can be easily applied to study materials other than MX_2 TMDs, thanks to its general formulation being independent of the chemistry and the atomic topology of the considered system.

Vibrational contributions to intrinsic friction have been studied at different charge content [23]. We find that any deviation from charge neutrality produces complex rearrangements of atomic positions and electronic distribution, and consequent phase transitions. Upon charge injection, cell volume expansion is observed, due to charge accumulation along an axis orthogonal to the layer planes. Such accumulation is accounted for by the d_{z^2} orbital of the transition metal and it is regulated by the t_{2g}-e_g orbital polarization [17]. The latter, in turn, determines the frequency of the phonon modes related to the intrinsic friction through non-trivial electro-vibrational coupling. The bond covalency [18] and atom pair cophonicity [17] can be exploited as a knob to control such coupling, ruling subtle charge flows through atomic orbitals, hence determining vibrational frequencies at specific charge content. The results can be exploited to finely tune vibrational contributions to intrinsic friction in TMD structures, in order to facilitate assembly and operation of nano-electromechanical systems and, ultimately, to govern electronic charge distribution in TMD-based devices for applications beyond nanoscale tribology.

We then performed non-equilibrium molecular dynamics simulations with reactive many-body interaction potential [19]. We systematically studied the effect of the reaction parameters (i.e., the system temperature, the normal load, the imposed sliding speed and the density of the initial amorphous state) on the layer dynamics. We find that the formation of MoS$_2$ layers from an amorphous phase can be explained in the framework of classical nucleation theory as it predicts the conditions for their nucleation and growth. These results are part of a larger computational investigation published in [20].

On-going Research / Outlook

Results obtained from additional density functional calculations performed within the present project have extended the discourse to van der Waals heterostructures, i.e., layered structures comprising two (or more) chemically distinct TMDs stacked vertically atop one another. The purpose of these calculations is two-fold: firstly, we are able to better understand how fundamental quantum chemical parameters of the constituent elements within each TMD layer influence the nanomechanical

properties of these hybrid systems; secondly, such heterostructures also offer promising electronic properties, rendering them suitable candidate materials for the next generation of thin film photovoltaics. Complementary calculations will also consider the assembly and properties of lateral heterostructures for use in solar cell assemblies. Finally, the results obtained studying the accidentally commensurate structures stimulated the research that is currently carried out by some of us on amending the known necessary conditions for achieving superlubricity. Preliminary results show that, in addition to the pure structural commensuration, the sliding direction also greatly affects the dissipative properties of TMDs, enabling one to foresee practical applications of the frictional anisotropy of molybdenum disulfide and other 2D materials.

Conclusion

We used computational methods in order to study the effect of the chemical composition and structural commensurability on the intrinsic friction of TMDs, the latter affecting the exfoliation process. Results from our ab initio simulations deepen our understanding of the energetics of the sliding process. We have also proposed a new approach, named Normal-Modes Transition Approximation, aimed at finding possible sliding paths from the analysis of the vibrational behavior of the system at the stable geometry. We further studied which are the electro-structural features governing layer sliding after removal of charge neutrality, and propose how to control them to harness layer gliding and separation. Finally, we performed non-equilibrium molecular dynamics simulations with reactive many-body interaction potential, showing the mechanism of layer formation in tribological conditions.

References

[1] LI, H., J. Wu, Z. Yin, and H. Zhang. Preparation and Applications of Mechanically Exfoliated Single-Layer and Multilayer MoS_2 and WSe_2 Nanosheets. Accounts of Chemical Research. 2014, 47(4), 1067-1075. DOI: 10.1021/ar4002312.

[2] Chhowalla, M., H. S. Shin, G. Eda, L.-J. Li, K. P. Loh, and H. Zhang. The chemistry of two-dimensional layered transition metal dichalcogenide nanosheets. Nature Chemistry. 2013, 5(4), 263-275. DOI: 10.1038/nchem.1589.

[3] Geim, A. K., and I. V. Grigorieva. Van der Waals heterostructures. Nature. 2013, 499(7459), 419-425. DOI: 10.1038/nature12385.

[4] Vanossi, A., N. Manini, M. Urbakh, S. Zapperi, E. Tosatti. Colloquium: Modeling friction. Reviews of Modern Physics. 2013, 85(2), 529-552. DOI: 10.1103/RevModPhys.85.529.

[5] Frindt, R. F. Single Crystals of MoS_2 Several Molecular Layers Thick. Journal of Applied Physics. 1966, 37(4), 1928-1929. DOI: 10.1063/1.1708627.

[6] Nicolosi V., et al. Liquid Exfoliation of Layered Materials. Science. 2013, 340(6139), 1226419-1226419. DOI: 10.1126/science.1226419.

[7] Joensen, P., et al. Single-layer MoS_2. Materials Research Bulletin. 1986, 21(4), 457-461. DOI: 10.1016/0025-5408(86)90011-5.

[8] Zeng, Z., et al. Single-Layer Semiconducting Nanosheets: High-Yield Preparation and Device Fabrication. Angewandte Chemie International Edition. 2011, 50(47), 11093-11097. DOI: 10.1002/anie.201106004.

[9] Zeng, Z., et al. An Effective Method for the Fabrication of Few-Layer-Thick Inorganic Nanosheets. Angewandte Chemie International Edition. 2012, 51(36), 9052-9056. DOI: 10.1002/anie.201204208.

[10] Cao, T., et al. Valley-selective circular dichroism of monolayer molybdenum disulphide. Nature Communications. 2012, 3(1). DOI: 10.1038/ncomms1882.

[11] Zeng, H., et al. Valley polarization in MoS_2 monolayers by optical pumping. Nature Nanotechnology. 2012, 7(8), 490-493. DOI: 10.1038/nnano.2012.95.

[12] Mak, K. F., et al. Control of valley polarization in monolayer MoS_2 by optical helicity. Nature Nanotechnology. 2012, 7(8), 494-498. DOI: 10.1038/nnano.2012.96.

[13] K. F. Mak et al. Atomically Thin MoS_2: A New Direct-Gap Semiconductor. Physical Review Letters. 2010, 105(13). DOI: 10.1103/PhysRevLett.105.136805.

[14] Gutierrez, H. R. et al. Extraordinary Room-Temperature Photoluminescence in Triangular WS 2 Monolayers. Nano Letters. 2013, 13(8), 3447-3454. DOI: 10.1021/nl3026357.

[15] Yin, X. et al. Edge Nonlinear Optics on a MoS_2 Atomic Monolayer. Science. 2014, 344(6183), 488-490. DOI: 10.1126/science.1250564.

[16] Cammarata, A., and T. Polcar. Tailoring Nanoscale Friction in MX_2 Transition Metal Dichalcogenides. Inorganic Chemistry. 2015, 54(12), 5739-5744. DOI: 10.1021/acs.inorgchem.5b00431.

[17] Cammarata, A., and J. M. Rondinelli. Octahedral engineering of orbital polarizations in charge transfer oxides. Physical Review B. 2013, 87(15). DOI: 10.1103/PhysRevB.87.155135.

[18] Cammarata, A., and J. Rondinelli. Covalent dependence of octahedral rotations in orthorhombic perovskite oxides. The Journal of Chemical Physics. 2014, 141(11). DOI: 10.1063/1.4895967.

[19] Liang, T., S. R. Phillpot, S. B. Sinniott. Parametrization of a reactive many-body potential for Mo–S systems. Physical Review B. 2009, 79(24). DOI: 10.1103/PhysRevB.79.245110.

[20] Nicolini, P., et al. Structural Ordering of Molybdenum Disulfide Studied via Reactive Molecular Dynamics Simulations. ACS Applied Materials & Interfaces. 2018, 10(10), 8937-8946. DOI: 10.1021/acsami.7b17960.

Publications

[21] Irving, B., P. Nicolini, T. Polcar. On the lubricity of transition metal dichalcogenides: an ab initio study. Nanoscale. 2017, 9(17), 5597-5607. DOI: 10.1039/C7NR00925A.

[22] Cammarata, A., and T. Polcar. Overcoming nanoscale friction barriers in transition metal dichalcogenides. Physical Review B. 2017, 96(8). DOI: 10.1103/PhysRevB.96.085406.

[23] Cammarata, A., and T. Polcar. Vibrational contributions to intrinsic friction in charged transition metal dichalcogenides. Nanoscale. 2017, 9(32), 11488-11497. DOI: 10.1039/C7NR04034B

CLEAVAGE PROPERTIES OF NITRIDE MULTILAYERS FROM FIRST PRINCIPLES

Research institution:
The Central
European Institute
of Technology,
Brno University
of Technology

Principal investigator:
Miroslav Černý

Researchers:
Petr Šesták,
Petr Řehák,
David Nezval,
Mojmír Šob,
David Holec

Project partners:
The Institute
of Physics
of Materials of the
Czech Academy
of Sciences,
Montanuniversität
Leoben

Project ID:
OPEN-8-17

Introduction

Computer aided materials design is a powerful tool for the development of new materials with desired properties. One can use it within many strategies such as developing new materials (alloying, doping) or tuning the microstructure (e.g., multilayer design, residual stress design, grain boundary design).

Protective coatings are a class of materials applied to protect tool and component surfaces as well as whole devices in either harsh environments or demanding application conditions. In the case of cutting tools, hard protective layers can extend their operational lifetime, thus reducing production costs, saving energy, etc. TiN with hardness reaching 34 GPa has been shown to be of special practical value. When Al is added to form a metastable solid solution, the hardness slightly increases to 37 GPa for a 0.66 fraction of Al on the metal sublattice [1, 2]. More importantly, the TiAlN coatings exhibit a hardness increase under thermal loads as a spinodal decomposition takes place [1].

In our research, however, we focus on the option to enhance and adopt the functionality of a particular system by applying a careful structural design. Even in the simplest possible case of super-

lattices, i.e. systems with two different alternating (semi)coherent materials with small periodic length, interfaces become the crucial building elements since the interface area-to-bulk volume ratio of each component rapidly increases as compared with monolithic design. Helmersson et al. [3] showed that by setting the bi-layer period of the TiN/VN superlattice to 5.2 nm, hardness values of about 55 GPa can be obtained, which is more than a 100% increase as compared with single-phase TiN or VN.

The main aim of the proposed research was to perform computer-aided design of selected nitride multilayers that can serve as a protective coating for cutting tools. Namely, we studied TiN/VN, TiN/AlN and AlN/VN systems. At the atomic level, one can compute quantities such as the cleavage energy and critical stress, which can be used as a measure of mechanical durability of the modeled systems. For this purpose we calculated these quantities for a number of possible cleavage planes in each model of multilayers and subsequently evaluated the multilayer parameters leading to its best performance.
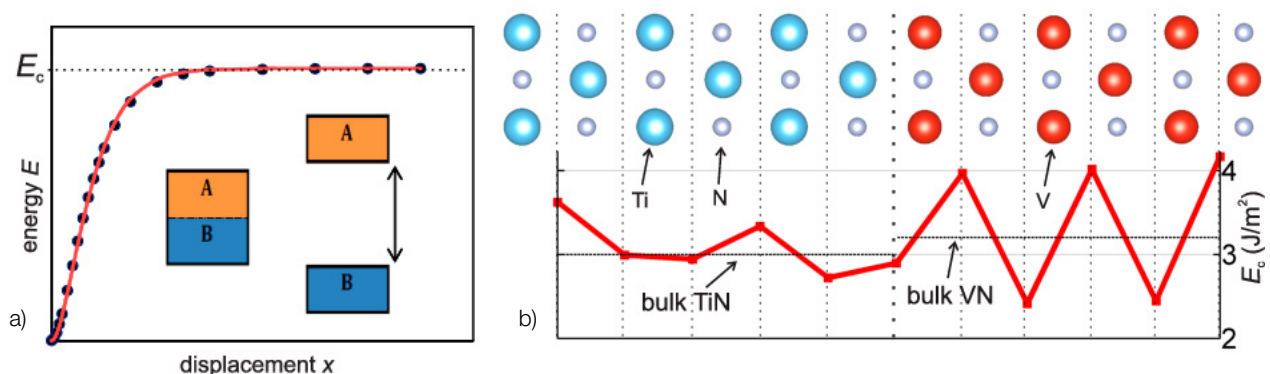

Figure 1.
(a) Determining the cleavage energy. (b) Computed cleavage energy E_c in the TiN/VN bilayer as a function of cleavage plane position.

Results and Methods

For studied systems we determined the total energy using a first-principles code VASP [4] as a function of separation of two rigid blocks (see Figure 1a) and found the cleavage energy E_c. In agreement with previous studies [5] we confirmed that the VN/TiN exhibits interface induced toughening of VN as compared to bulk values, and we predicted a similar effect in the VN/AlN system [6]. However, a more detailed insight revealed that the theoretical critical stress for brittle cleavage oscillates strongly (even below the critical stress for bulk) with the distance from the interface inside the VN layer (see Figure 1b), a phenomenon not present (or hugely reduced) in TiN and AlN layers.

The oscillating values for critical stress correlate well with the same behavior of interplanar distances and charge density. An explanation for this phenomenon [6] can be based on the structural instability of cubic VN at zero temperature which, along with the Friedel oscillations of a charge density due to the presence of the interface, result in a modulation of the lattice along the [100] direction and subsequent periodic changes of E_c from plane to plane.

On-going Research / Outlook

Since our calculations did not reveal any dynamic instability along the [111] direction, we decided to continue in our study focusing on the (111) interfaces between selected nitride layers.

Conclusion

We computed the cleavage characteristics of selected nitride multilayers. On the particular example of TiN/VN, TiN/AlN and AlN/VN bilayers and multilayers we demonstrated spatially oscillating values of the cleavage energy, particularly in the VN layers. The origin of these unexpected properties was pinpointed to low temperature structural instabilities of cubic VN.

References

[1] Mayrhofer, P. H., A. Hörling, L. Karlsson, et al. Self-organized nanostructures in the Ti–Al–N system. Applied Physics Letters. 2003, 83(10), 2049-2051. DOI: 10.1063/1.1608464.

[2] PalDey, S., and S. C. Deevi. Single layer and multilayer wear resistant coatings of (Ti,Al)N: A review. Materials Science and Engineering: A. 2003, 342(1-2), 58-79. DOI: 10.1016/S0921-5093(02)00259-9.

[3] Helmersson, U., S. Todorova, S. A. Barnett, et al. Growth of single-crystal TiN/VN strained-layer superlattices with extremely high mechanical hardness. Journal of Applied Physics. 1987, 62(2), 481-484. DOI: 10.1063/1.339770.

[4] [12] Kresse, G., and J. Furthmüller. Efficient iterative schemes for ab initio total-energy calculations using a plane-wave basis set. Physical Review B. 1996, 54(16), 11169-11186. DOI: 10.1103/PhysRevB.54.11169.

[5] Lazar, P., J. Redinger, and R. Podloucky. Density functional theory applied to VN ∕ TiN multilayers. Physical Review B. 2007, 76(17). DOI: 10.1103/PhysRevB.76.174112.

Publication

[6] Řehák, P., M. Černý and D. Holec. Interface-induced electronic structure toughening of nitride superlattices. Surface and Coatings Technology. 2017, 325, 410-416. DOI: 10.1016/j.surfcoat.2017.06.065.

FORCE FIELD DEVELOPMENT FOR THE THERMORESPONSIVE POLYMER PNIPAM

Research institution:	Principal investigator:	Researcher:	Project IDs:
The University of Chemistry and Technology, Prague	Jan Heyda	Vladimír Palivec	OPEN-7-50, OPEN-10-36

Introduction

Thermoresponsive polymers are prospective materials with number of applications, including artificial tissues, bio-compatible coatings, and smart sensors [1]. However, due to unusual physico-chemical behavior their further optimization is limited by the lack of theoretical description. Namely the sudden, but fully reversible collapse transition presents many challenges for model development. In this project we investigated a prominent role model poly-N-isopropylacrylamide (PNIPAM), which exhibits a lower critical solution temperature (LCST) at 33°C [2]. Owing to a uniquely balanced hydrophobic-hydrophilic character within only a few degree-window, PNIPAM changes from a dissolved swollen to a collapsed state, and forms a second phase. Interestingly the LCST is almost independent of the polymer chain length and concentration. Understanding of this process may be revealed by molecular dynamics simulation (MD) in pure water or osmolyte solutions [3, 4]. From early on, the simulations faced the issue of poor sampling of transition events. The investigation of coil and swollen states was still possible, but not their relative populations. Recently, the role of an initial conformation on the conformational ensemble of a PNIPAM 30mer chain was systematically studied in μs long simulations. It was found that tightly collapsed states do not re-swell in good solvent conditions on the simulation timescale [5]. To bypass this issue it was suggested to perform thousands of short (ns-long) independent MD simulations initiated from a large pool of polymer states. Such an approach allows very detailed knowledge of the two states, but cannot provide insight into transition thermodynamics. In this project, we have employed extensive MD simulations in order to develop an improved PNIPAM force-field and determine transition thermodynamics.

Results and Methods

The development of a polymer model must respect that macroscopic thermodynamics relies on large scale replica-exchange MD simulations (REMD). This is an established tool to collect an equilibrium ensemble over a broad range of temperatures, which is necessary for the determination of thermodynamics. In our case 76 replicas of the system in the temperature range of 250–420 K were simulated in parallel, each on a single node with 24
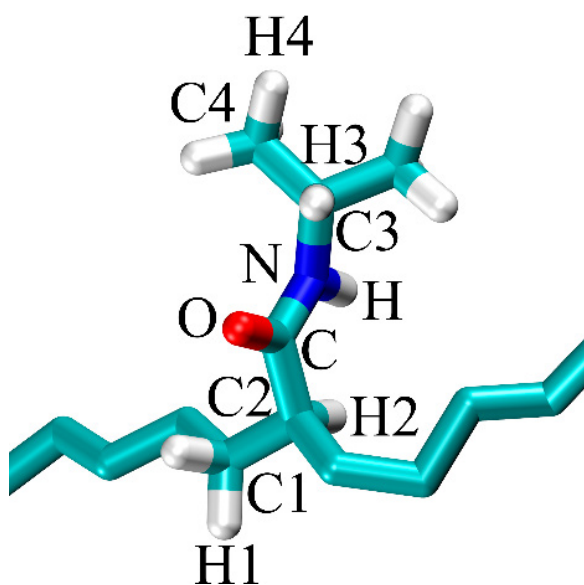

Figure 1.
Labeling of atom type names in the monomer unit of PNIPAM. Their partial charges are presented in Table 1.

cores. With this setup, a typical 100 ns simulation required about 45 kCPUhr and was completed in 1 day. The structure of the monomer unit of PNIPAM, atom names, and their partial charges for the originally proposed OPLS force field parameterization which is abundant in the literature are presented in Figure 1 and Table 1 [3]. This description, however, fails to populate swollen states at any temperature, and does not reproduce the equilibrium between collapsed and swollen PNIPAM states (Figure 2, top). We varied partial charge distribution within the monomer NIPAM unit and tested a number of PNIPAM models [7]. Upon mild increase of the polarity of the peptide bond and charge distribution within isopropyl moiety, both collapsed and swollen states are populated, see Figure 2. New parameterization leads to much better agreement with the experimental data as presented in Table 1.

	C1	H1	C2	H2	C	O	N	H	C3	H3	C4	H4	T_0 [K]	ΔH [kJ/mol]	ΔS [J/mol/K]
OPLS	-0.12	0.06	-0.06	0.06	0.5	-0.5	-0.5	0.3	0.14	0.06	-0.18	0.06	<250	--	--
QM2	-0.18	0.09	0	0.05	0.5	-0.57	-0.57	0.33	0.36	0.06	-0.32	0.08	303	-20	-65
exp.	--	--	--	--	--	--	--	--	--	--	--	--	307	-125	-400

Table 1.
Partial charges in the PNIPAM monomer unit in the original OPLS and refined QM2 force field.
The atom labeling is shown in Figure 1. Experimental (~100 mer) and simulated (30 mer) thermodynamic
parameters of PNIPAM are included.

On-going Research / Outlook

Two main challenges remain. First, the salt-specific action of PNI-PAM in aqueous solutions, known experimentally and qualitatively captured already with the original OPLS force-field, must be put on solid thermodynamics grounds [4, 6]. We will employ the developed PNIPAM model in combination with established salt force-fields and perform quantitative thermodynamic analysis.

The second challenge is to build a relation between the single chain collapse transition and aggregation process, which is experimentally difficult since they largely overlap in temperature. In order to provide a quantitative microscopic insight and relate the single chain collapse with aggregation process we plan, by means of REMD, to investigate PNIPAM solutions at a finite
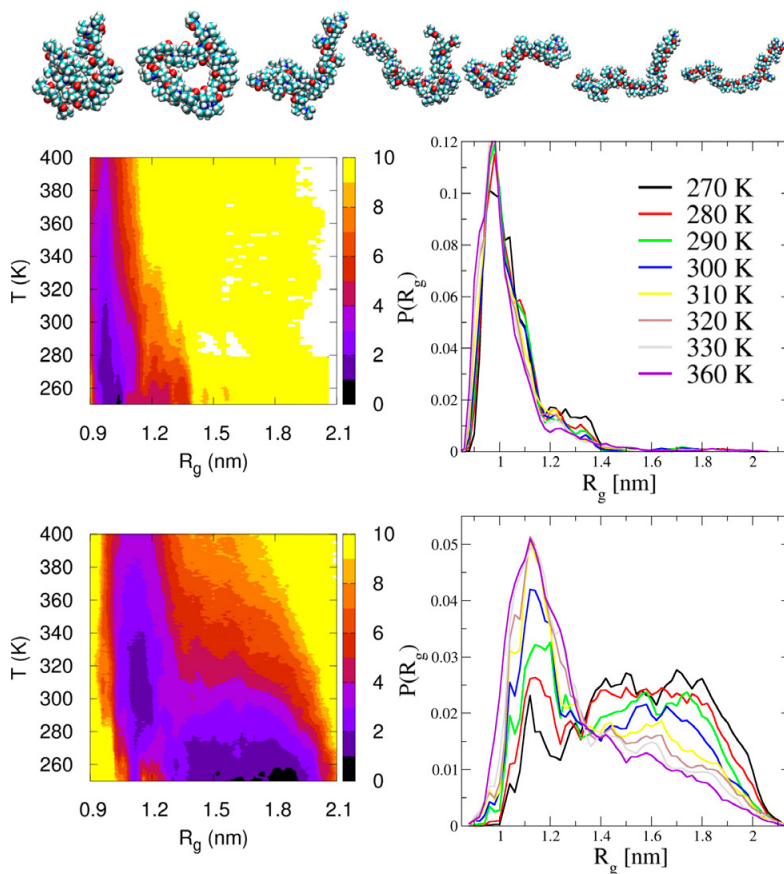

Figure 2.
Distribution of the radius of gyration of PNIPAM 30mer over the whole investigated temperature range as sampled in REMD simulations comparing the OPLS (top row), and QM2 (bottom row) force fields. The 2-dimensional free energy landscape (color-coded in kJ/mol) is presented on the left and the polymer size distribution at selected temperatures around the LCST (303 K) are presented on the right. At the very top of the figure, we present seven polymer chain conformations which are equally spaced in the explored range of radius of gyration, i.e. 0.9-2.1 nm.

polymer concentration (10 wt%) in temperatures around LCST. These computationally demanding calculations may provide microscopic and thermodynamic insight in the PNIPAM chain dehydration and phase transition.

Conclusion

Employing large scale REMD simulations we have proved that the original parameterization of the thermoresponsive polymer PNIPAM, based on the OPLS force field, describes poorly its thermodynamic properties in aqueous solutions. Thanks to the IT4I infrastructure, a significant amount of computational resources was dedicated to the development of an improved PNIPAM force field, the so called QM2. The new force-field reproduces the equilibrium between the collapsed ↔ swollen equilibrium, critical temperature, and semi-quantitatively also the underlying transition thermodynamics.

References

[1] Stuart, M. A. C., et al. Emerging applications of stimuli-responsive polymer materials. Nature Materials. 2010, 9(2), 101-113. DOI: 10.1038/nmat2614.

[2] Halperin, A., M. Kröger, F. M. Winnik. Poly(N -isopropylacrylamide) Phase Diagrams: Fifty Years of Research. Angewandte Chemie International Edition. 2015, 54(51), 15342-15367. DOI: 10.1002/anie.201506663.

[3] Walter, J., V. Ermatchkov, J. Vrabec, H. Hasse. Molecular dynamics and experimental study of conformation change of poly(N-isopropylacrylamide) hydrogels in water. Fluid Phase Equilibria. 2010, 296(2), 164-172. DOI: 10.1016/j.fluid.2010.03.025.

[4] Algaer, E. A., N. F. A. Van Der Vegt. Hofmeister Ion Interactions with Model Amide Compounds. The Journal of Physical Chemistry B. 2011, 115(46), 13781-13787. DOI: 10.1021/jp208583w.

[5] Kang, Y., H. Joo, J. S. Kim. Collapse–Swelling Transitions of a Thermoresponsive, Single Poly(N -isopropylacrylamide) Chain in Water. The Journal of Physical Chemistry B. 2016, 120(51), 13184-13192. DOI: 10.1021/acs.jpcb.6b09165.

[6] Zhang, Y. J., et al. Specific Ion Effects on the Water Solubility of Macromolecules: PNIPAM and the Hofmeister Series. Journal of the American Chemical Society. 2005, 127(41), 14505-14510. DOI: 10.1021/ja0546424.

Publication

[7] Palivec, V., D. Zadražil, J. Heyda. All-atom REMD simulation of poly-N-isopropylacrylamide thermodynamics in water: A model with a distinct 2-state behavior. 2018, arXiv:1806.05592.

FROM SINGLE PNIPAM CHAIN COLLAPSE TO PHASE SEPARATION

Research institution:
The University
of Chemistry
and Technology,
Prague

Principal investigator:
Jan Heyda

Researchers:
Vladimír Palivec,
Denis Zadražil

Project IDs:
OPEN-10-36,
OPEN-12-27

Introduction

Smart devices rely on fast and reversible response, which does not degrade over time. This sets physico-chemical and mechanical requirements for suitable responsive materials. Since temperature is a widely available stimulus, development and utilization of thermoresponsive materials has attracted much attention. Linear polymer structures, surfaces, and gels can be found already in use in numerous applications, including artificial tissues, bio-compatible coatings, and smart sensors [1]. The majority of applications take place in solutions, where these materials undergo macroscopic volume phase transition, 'shrinking', when crossing their characteristic transition temperature. This abrupt fully reversible transition, illustrated in Figure 1, which happens typically within 1-2 K originates from the temperature-sensitive interplay between polymer-solvent and polymer-polymer interactions [2, 3]. The temperature and

Figure 1.
Illustration of the equilibrium between the swollen and collapsed states at infinite dilution (top) and between the dissolved and aggregated states at the finite polymer concentration (bottom). Both processes originate from the complex chemistry of the polymer, and competition between hydrophobic and hydrophilic interactions.

quality of the response depends not only on the chemistry of the polymer and solvent, but also on polymer topology and concentration. While macroscopic thermodynamics is well established, the microscopic insight has become available only recently, thanks to neutron scattering and MCR-Raman experiments [4, 5].

In order to characterize the volume phase transition of a role-model thermoresponsive (polymer poly-N-isopropylacrylamide, PNIPAM) with atomistic detail, we have employed large-scale all-atom molecular dynamics simulations of concentrated polymer solutions. This is a necessary step towards a unified interpretation of thermodynamic and spectroscopic observations.

Results and Methods

In order to closely reproduce experimental conditions we performed large scale replica-exchange molecular dynamics (REMD) simulations of concentrated aqueous solutions of PNIPAM (10 wt%) and investigated the thermodynamics of the phase separation process. We employed our recently developed force-field, which was shown to accurately reproduce conformation ensembles and thermodynamics of a single PNIPAM chain over a broad range of temperatures, including the LCST (lower critical solution temperature) region [6]. Efficient sampling of the dissolved ⇌ aggregate state equilibrium was performed via simulation of 16 PNIPAM chains of 20mer length (and about 10k SPC/E water molecules). This is a valid approach, as experimental observations are independent of PNIPAM chain length when longer than ~15mer. The system was employed on 76 replicas in the temperature range of 250–400 K. Equilibration of the system required 200 ns, and was followed by the 300 ns production period, which was used for data collection and analysis.

The progress of chain association and aggregate formation was measured by the number of water molecules in the polymer hydration layer. The direct simulation results include the degree of hydration vs. temperature, which is presented in the left panel of Figure 2. A monotonic function in temperature is obtained with a strong dehydration region between 280–310 K, where about 1/3 of hydration water is released.

Interestingly, recent hydration water sensitive MCR-Raman experiments show time-evolution of the spectra above LCST, al-
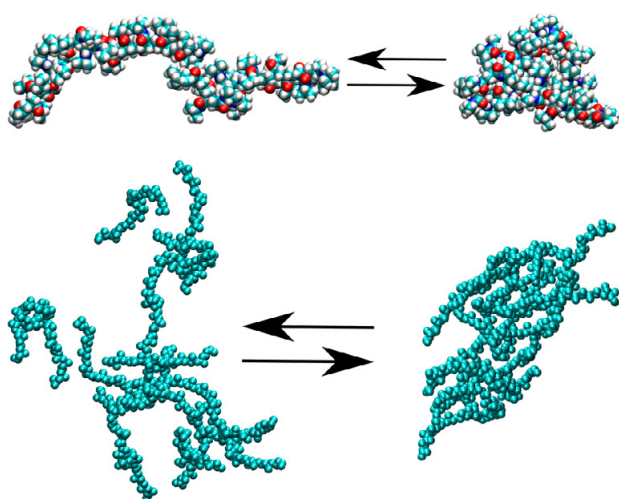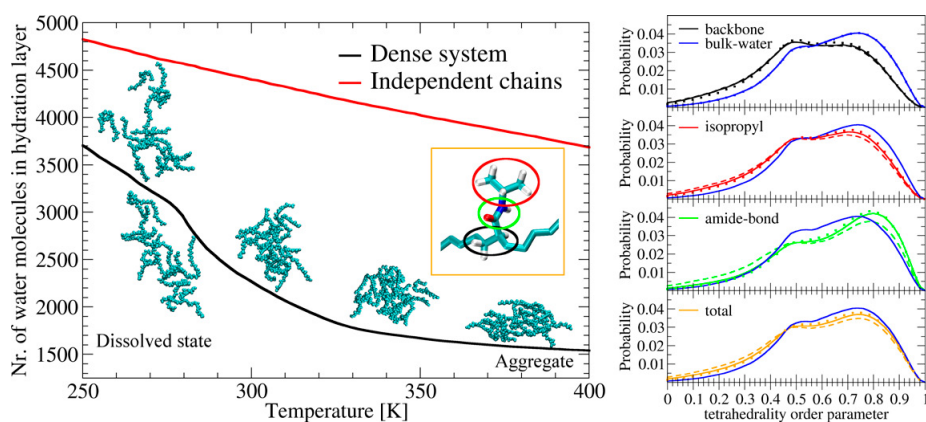
Figure 2.
Left: Hydration of 20mer PNIPAM chains at 10 wt% concentration (black line) and at infinite dilution (red) over a broad range of temperatures. Right: Water structure in terms of tetrahedrality order parameter at 298 K around chemically different parts of the PNIPAM chain, see the monomer inset. Results for a single polymer chain (dotted) in a dissolved state (full line) and a dehydrated aggregate (dashed) are compared.

though clouding itself is a rapid (sub second) process. This points to rather slow progress of solvent expulsion from the newly formed aggregate core [4]. This was mimicked at the simulation level in short (20 ns) MD simulations at 298 K, initiated from polymer states of a different level of hydration. The quality of hydration water was measured by means of the tetrahedral order parameter. We probed the vicinity of chemically different parts of the PNIPAM chain, namely hydrophobic and hydrophilic regions, with results presented in the right panel of Figure 2.

We confirmed that the water is more ordered, (peak at $P(q\sim0.8)$), near the hydrophilic regions and more disordered (shoulder at $P(q\sim0.3)$) near the hydrophobic regions compared to the bulk water. More importantly, we have observed only a marginal effect of polymer concentration on hydration structure, when the polymer is in dissolved state (compare full and dotted lines in Figure 2). A significant decrease of water order near the amide-bond is observed, when the aggregation proceeds (full and dashed lines in Figure 2).

On-going Research / Outlook

So far, we have connected our simulations to the MCR-Raman experiments at LCST [4]. In future, we plan to investigate interfacial water behavior in relation to polymer conformation also below and above the LCST temperature, where the dissolved and aggregated states dominate respectively. From REMD simulations the structure factor at different levels of dehydration can be determined and connected to the neutron scattering data [5].

Conclusion

Employing large scale REMD simulations, we have connected macroscopic dehydration processes and microscopic, yet global, changes in interfacial water structure. These observations were related to the time-evolution in MCR-Raman spectra. Our simulation results confirmed that our recently developed force-field allows for quantitative description of PNIPAM not only at infinite dilution, but also at finite concentrations.

References

[1] Stuart, M. A. C., et al. Emerging applications of stimuli-responsive polymer materials. Nature Materials. 2010, 9(2), 101-113. DOI: 10.1038/nmat2614.

[2] Halperin, A., M. Kröger, F. M. Winnik. Poly(N -isopropylacrylamide) Phase Diagrams: Fifty Years of Research. Angewandte Chemie International Edition. 2015, 54(51), 15342-15367. DOI: 10.1002/anie.201506663.

[3] Chudoba, R., J. Heyda, J. Dzubiella. Temperature-Dependent Implicit-Solvent Model of Polyethylene Glycol in Aqueous Solution. Journal of Chemical Theory and Computation. 2017, 13(12), 6317-6327. DOI: 10.1021/acs.jctc.7b00560.

[4] Mochizuki, K., et al. Hydration-Shell Transformation of Thermosensitive Aqueous Polymers. The Journal of Physical Chemistry Letters. 2017, 8(7), 1360-1364. DOI: 10.1021/acs.jpclett.7b00363.

[5] Philipp, M., et al. From Molecular Dehydration to Excess Volumes of Phase-Separating PNIPAM Solutions. The Journal of Physical Chemistry B. 2014, 118(15), 4253-4260. DOI: 10.1021/jp501539z.

[6] Palivec, V., D. Zadražil, J. Heyda. All-atom REMD simulation of poly-N-isopropylacrylamide thermodynamics in water: A model with a distinct 2-state behavior. 2018, arXiv:1806.05592.

NEW PREDICTED MAGNETIC STRUCTURES FOR RARE-EARTH FREE PERMANENT MAGNETS

Research institution:	Principal investigator:	Researchers:	Project partners:	Project ID:
IT4Innovations National Supercomputing Center	Dominik Legut	Sergiu Arapan, Pablo Nieves	ICCRAM, The University of Burgos	OPEN-11-33

Introduction

Permanent magnets (PM) are an indispensable part of modern technology. They are mainly used for data and energy conversion and are present in most of the devices we use in our everyday life, such as smartphones, laptops, audio and video devices, as well as in industrial applications, including electrical motors and green energy generators. With an increasing awareness of environmental issues, there has recently been a high demand for PMs that perform well at efficient renewable energy production and conversion. An efficient PM has the following physical properties: high saturation magnetization, $\mu_0 M_S > 1T$ (where μ0 is the vacuum permeability), magneto-crystalline anisotropy, $K_U > 1MJ/m^3$, and a Curie temperature of $T_C > 300K$. In particular, magnets with a hardness parameter of $\kappa = \sqrt{K_U/\mu_0 M_S^2} > 1$ (called "hard") are very desirable because they can be used to make efficient magnets of any shape [1]. At present, the efficiency of the PMs depends on the amount of Rare-Earth (RE) elements present in its composition. These elements became, however, critical raw materials, and their production and supply is limited and monopolized by China [2], which greatly influences the market of PMs. Recently, therefore, a great deal of attention within the materials science community is paid to manufacturing competitive RE free PMs. One possibility is trying to discover new magnetic materials without critical elements. The advance of computational methods makes possible the prediction of new structures by numerical simulations on a computer. In our study we have used genetic algorithms combined with first-principles calculations for the prediction of new magnetic materials suitable for PMs. We have performed an extensive search within the Fe-reach binary systems, and have identified some new structures with promising magnetic properties.
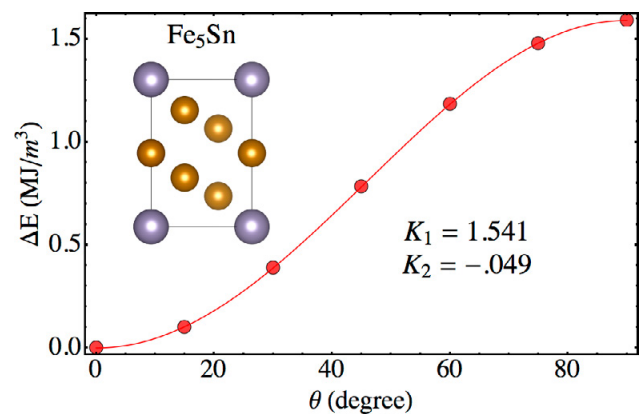

Figure 1.
The dependence of the magneto-crystalline anisotropy energy versus the angle between the spin direction and the [001] for the hexagonal Fe₅Sn structure.
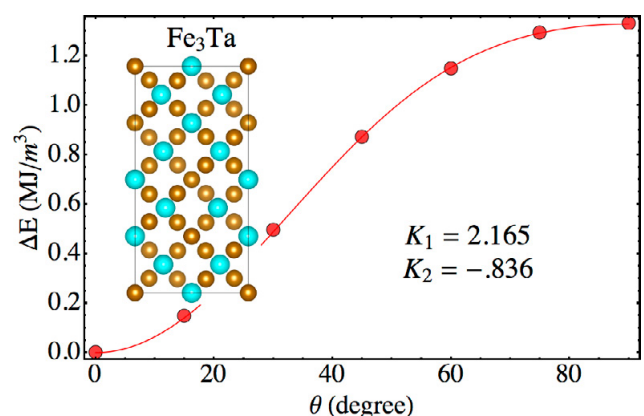

Figure 2.
The dependence of the magneto-crystalline anisotropy energy versus the angle between the spin direction and the [001] for the tetragonal Fe₃Ta structure.

Results and Methods

We have explored the phase space of binary structures by using the USPEX code [3, 4]. USPEX uses an evolutionary algorithm to generate different structures. It uses as an input the number and type of ions to be considered within the unit cell only. At the first step a set of structures is generated at random, by randomly choosing a crystal space group, corresponding lattice vectors, and ion positions. Structures generated in such a way are far from their equilibrium. Thus, performing a structure relaxation is required to accurately estimate the energy of a structure, which serves as a fitness criterion. A subset of fitted structures is selected to generate the next generation of structures by means of genetic operations (crossover and mutations). The process of random generation of structures is also performed at each step to provide a diversity of structures for each generation. The search for optimal structure is performed until no new best structures are generated for a certain number of generations, or the maximum number of generations is reached.

The efficiency of exploring a large number of structures with structure predicting methods depends strongly on the performance of the structural optimization. We used the versatile ab-initio code VASP [5, 6] to perform accurate structural optimization. Computationally, magnetic materials add an extra degree of complexity due to magnetic interaction. In the current study, we have designed our own scheme for VASP calculations [7]. First, it starts with non-spin-polarized calculation at a larger volume, performing shape and ion positions relaxations. Second, it switches to spin-polarized calculations, and adds volume relaxation with an increased energy cut-off. Finally, it obtains the equilibrium parameters via a series of shape and ion position optimizations at given volumes by fitting $E=E(V)$ to an equation of state (EOS). All VASP calculations where performed with the PAW PBE 5.4 potentials, with an energy cut-off of up to 1.4 of the default VASP energy cut-off, and an automatic k-points generating scheme with a scaling factor starting from 10 to 30.

We have obtained several new RE binary structures that show the potential for an efficient PM. Here we present two of them, the binary compounds Fe_5Sn and Fe_3Ta.

Both structures are uniaxial, and the dependence of the magneto-crystalline anisotropy energy as a function of the angle θ between the direction of spin and the [001] direction is shown in Figure 1 and Figure 2 for the Fe_5Sn and Fe_3Ta phases, respectively. Calculated values are shown as dots and the curves show the fitting:

$$E(\theta) = K_1 (\sin \theta)^2 + K_2 (\sin \theta)^4,$$

where K_1 and K_2 are given in MJ/m^3.

The Fe_5Sn structure is a hexagonal phase (a view along the [100] direction is shown in Figure 1, with Fe as smaller balls), with a saturation magnetization of 1.7T, and a magneto-crystalline anisotropy energy of 1.5MJ/m^3 (Figure 1). The phase is meta-stable, but has a negative enthalpy of formation and one may attempt to synthesize it in a similar manner to Fe_3Sn, which also shows a good saturation magnetization, but planar magneto-crystalline anisotropy.

The Fe_3Ta structure is tetragonal (a view along the [100] direction is shown in Figure 2, with Fe as smaller balls), with a saturation magnetization of 1.1T, and a magneto-crystalline anisotropy energy of 1.2MJ/m^3 (Figure 2). This structure is very close to the enthalpy hull of Fe-Ta binaries, and there are some instances of experimental evidence of a new binary phase for this composition.

On-going Research / Outlook

Many technologically relevant binary compounds are experimentally known and studied. However, the majority of these compounds have been obtained by metallurgical methods suitable for mass-production, so there may still exist other stable binary phases that can occur under certain experimental conditions. Structure predicting methods offer the possibility to find new phases through simulations, and guide the experiment towards their materialization. Even for the magnetic binary compounds that are constrained to have one binary element from a small set of magnetic elements, like Fe, Co, and Mn, the phase space of possible compounds is huge, and so we continue to explore it for new structures. Another direction of research is, within the set of predicted structures with large saturation magnetization, to search for prototype structures with large magneto-crystalline anisotropy energy. Finally, selected candidate structures should also exhibit a high Curie temperature, which will extend the current research to the study of magnetic exchange interactions and spin dynamics.

Conclusion

We have used structure prediction based on genetic/evolutionary algorithms combined with ab-initio calculations to search for new RE-free PMs. We have implemented a routine, which performs this search in a high-throughput manner, and is optimized for magnetic structures. We have identified several new binary compounds, which look promising for designing competitive RE-free PMs: they show a sufficiently high saturation magnetization and magneto-crystalline anisotropy energy.

References

[1] Skomski, R., and J. M. D. Coey. Magnetic anisotropy — How much is enough for a permanent magnet? Scripta Materialia. 2016, 112, 3-8. DOI: 10.1016/j.scriptamat.2015.09.021.

[2] Li, L. Z., and Yang, X. China's rare earth resources, mineralogy, and beneficiation. Rare Earths Industry. Elsevier, 2016, 139-150. DOI: 10.1016/B978-0-12-802328-0.00009-7.

[3] Oganov, Artem R., and C. W. Glass. Crystal structure prediction using ab initio evolutionary techniques: Principles and applications. The Journal of Chemical Physics. 2006, 124(24). DOI: 10.1063/1.2210932.

[4] Lyakhov, A. O., A. R. Oganov, H. T. Stokes, and Q. Zhu. New developments in evolutionary structure prediction algorithm USPEX. Computer Physics Communications. 2013, 184(4), 1172-1182. DOI: 10.1016/j.cpc.2012.12.009.

[5] Kresse, G., and J. Furthmüller. Efficient iterative schemes for ab initio total-energy calculations using a plane-wave basis set. Physical Review B. 1996, 54(16), 11169-11186. DOI: 10.1103/PhysRevB.54.11169.

[6] Kresse, G., and D. Joubert. From ultrasoft pseudopotentials to the projector augmented-wave method. Physical Review B. 1999, 59(3), 1758-1775. DOI: 10.1103/PhysRevB.59.1758.

Publication

[7] Arapan, S., P. Nieves, and S. Cuesta-López. A high-throughput exploration of magnetic materials by using structure predicting methods. Journal of Applied Physics. 2018, 123(8). DOI: 10.1063/1.5004979.

CONTROLLING THE TOPOLOGICAL SECTORS IN SHORT CHIRAL ANTIFERROMAGNETIC CHAINS WITH MAGNETIC FIELDS

Research institution:
IT4Innovations National Supercomputing Center

Principal investigator:
Dominik Legut

Researcher:
Jaroslav Chovan

Project ID:
OPEN-10-44

Introduction

Chiral Dzyaloshinskii-Moriya (DM) interaction [1, 2] in magnets with broken inversion symmetry stabilizes nontrivial spatially modulated spin textures. Such structures are currently of high interest. A commensurate-to-incommensurate (CI) phase transition was predicted a long time ago [3], but observed much later [4, 5]. In short, the shape of an incommensurate spin spiral becomes distorted with an applied magnetic field H, while its period grows. At strong fields, the spiral is significantly distorted, and can be viewed as a chiral soliton lattice, with large uniform magnetic domains separated by narrow topological soliton states – domain walls (DW). Above certain critical field H_c, the system becomes a uniform magnetic state. Some DM helimagnets display appealing magnetoelectric properties [6–8]. This enables the control of magnetic states by electric fields and vice versa, which is attractive for spintronics applications. In addition to one-dimensional textures, the ground states can form a vortex (skyrmion) lattice [9–10]. Recently such states were observed experimentally in several magnets [7, 11–13]. Finite-size systems and confinement effects were also studied. Confinement discretizes soliton density and make solitons countable. Counting can be accomplished e.g. electrically and utilized for data storage applications. In particular, the properties of finite chains with N spins can be controlled by manipulating the topological sector – the number n of domain walls (solitons) in the chain, which depends on N and the applied field H. Recent experiments on thin films in DM ferromagnets (FM) demonstrated field-induced discrete magnetization jumps whose number depends on system size [14–16]. Such jumps are absent in bulk systems, and originate in transitions between the topological sectors with a different number n of 2π-solitons [16–18]. For a given N, n decreases with the field in steps of 1; the CI transition occurs at the critical field which quickly approaches its bulk value H with N. Motivated by the above studies, we carried out a theoretical study of a finite classical Heisenberg antiferromagnetic chain with chiral DM interaction subject to a magnetic field.

Results and Methods

The system

We consider a short chain with N spins and free boundary conditions. The Hamiltonian is characterized by the three parameters; the Heisenberg exchange constant J with $J > 0$, the DM interaction strength D, and the magnetic field H. We also assume strong easy-plane anisotropy which, however, does not explicitly appear in the Hamiltonian. The chiral axis is taken to be perpendicular to the easy-plane.

Methods

We perform numerical calculations within the standard (classical) discrete spin model adapted to a finite open one-dimensional lattice. We look for the corresponding energy minimum, which is a static solution of the Landau-Lifshitz equations. This is achieved by first writing down the Landau-Lifshitz equations in their dissipative form for discrete spins of constant magnitude. One then chooses an initial trial spin configuration and lets the spins evolve in time. The presence of dissipation guarantees that initial configuration will eventually relax to a terminal state that is a local minimum of the energy. To accelerate the solution we suppress the precession terms. This fully dissipative algorithm rapidly leads to equilibrium. To find the true global minimum for any field H and chain length N, we use initial trial guesses from different topological sectors. Finally, for the ground state, we determine its topological sector n, the magnetization M, and monitor their evolution with N and H.

Results

Short chiral antiferromagnetic chains possess several novel features. In particular, the topological states display pronounced odd-even N-effects. For chains with even-N spins, evolution of topological sectors is virtually identical to that encountered in chiral ferromagnets. That is, the individual sectors again carry n 2π-solitons (or an even number of π-solitons), and the transition to the uniform state with $n=0$ occurs when the magnetic field reaches its bulk critical value H_c .
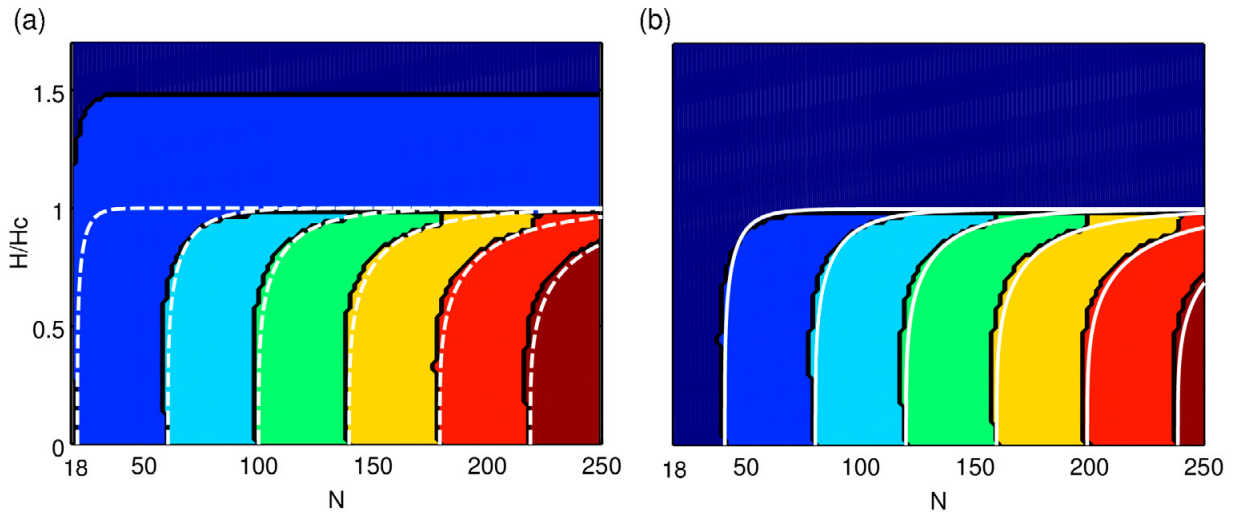
Figure 1.

Phase diagram of a finite DM AFM chain with N spins obtained from our numerics applied with D/J=0.16. The individual topological sectors n are distinguished by colors, from the lowest (dark blue) to the highest (dark red). For each N, the field-induced transition between the sectors is manifested by a discrete magnetization jump; within the sectors, the magnetization evolves continuously. The lines are the phase boundaries as predicted by the (bulk) continuum field theory. (a) Odd-N: higher sectors with n ≥1 carry (2n-1) π-solitons. At the bulk critical field H$_c$, the system enters the 'intermediate' state n=1 with one π-soliton which mediates the commensurate-to-incommensurate transition. Transition to the uniform AFM with n=0 occurs at the critical field H$_2$ ≈ 1.5 H$_c$. (b) Even-N: the chain carries n 2π-solitons. The transition to the uniform AFM state occurs at H$_c$.

Odd-N spins behave very differently. Higher topological sectors with $n \geq 1$ carry ($2n$ -1) π-solitons (odd number π-solitons!). The transition to the uniform antiferromagnetic state with $n=0$ is strongly modified, and occurs at the new critical field $H_2 \approx 1.5\,H_c \gg H_c$. At H_c the systems enter the sector $n=1$, with one π-soliton, which mediates the CI phase transition (Figure 1). All transitions between topological sectors are accompanied by discrete magnetization jumps. Upon the transition between the sectors $n=1$ and $n=0$ (in the limit of the vanishing field) the magnetization change is $\Delta M = \pm S$, where S is the value of classical spin. This is reminiscent of a surface spin-flop (SSF) transition in short easy-axis classical antiferromagnetic chains [19–22]. $H_c/H_2 \cong 1.5$ is not far from $\sqrt{2}$, which corresponds to the ratio of the bulk and surface spin-flop critical fields in the limit of vanishing easy-axis anisotropy. We thus speculate the link between the SSF transition and our findings.

Finally, our results are valid for weak and moderate values of the parameter $D/J \leq 0.2$, where D is the strength of the DM anisotropy, and J the isotropic exchange constant. For very strong DM interaction, the picture for even-N chains remains essentially intact, but the scenario for odd-N chains is spoiled. Specifically, the upper critical field H_2 appears to display periodic behavior with increasing chain length, and its value oscillates between H_c and $1.5\,H_c$. We believe that this is the manifestation of discrete lattice effects.

On-going Research / Outlook

For odd-N spin chains, it is highly desirable to clarify and confirm/rule out the speculated link between the CI transition and the SSF transition in classical antiferromagnetic chains. We note the systems are very different; the SSF transition occurs in *easy-axis* systems for even-N chains, whereas our effects occur in the *easy-plane* system and for odd-N chains; the roles of the bulk critical fields also appear reversed. Therefore, an unambiguous explanation of our findings requires additional theoretical effort. The firm explanation of the oscillatory behaviour of the upper critical field H_2 also deserves further attention.

Conclusion

We numerically studied topological states in short chiral antiferromagnetic chains and found several new features. The system displays pronounced odd-even effects. Even-N spin chains are similar to those in chiral ferromagnets: the individual sectors carry an even number of π-solitons, and the CI transition occurs at its bulk value. In odd-N spin chains, higher topological sectors carry an odd number of π-solitons. The transition to the uniform state is significantly modified, and is mediated by the intermediate phase with one of π-soliton, which exists in the region of $H_c < H < 1.5\,H_c$.

References

[1] Dzyaloshinskii, I. E. Thermodynamical Theory of "Weak" Ferromagnetism in Antiferromagnetic Substances. Soviet Physics Journal of Experimental and Theoretical Physics. 1957, 5 (6), 1259.

[2] Moriya, T. Anisotropic Superexchange Interaction and Weak Ferromagnetism. Physical Review. 1960, 120(1), 91–98. DOI: 10.1103/PhysRev.120.91.

[3] Dzyaloshinskii, I. E. The Theory of Helicoidal Structures in Antiferromagnets. II. Metals. Soviet Physics Journal of Experimental and Theoretical Physics. 1965, 20(1), 223.

[4] Zheludev, A., et al. Field-Induced Commensurate-Incommensurate Phase Transition in a Dzyaloshinskii-Moriya Spiral Antiferromagnet. Physical Review Letters. 1997, 78(25), 4857–4860. DOI: 10.1103/PhysRevLett.78.4857.

[5] Togawa, Y., T. Koyama, K. Takayanagi, et al. Chiral Magnetic Soliton Lattice on a Chiral Helimagnet. Physical Review Letters. 2012, 108(10). DOI: 10.1103/PhysRevLett.108.107202.

[6] Murakawa, H., Y. Onose, and Y. Tokura. Electric-Field Switching of a Magnetic Propagation Vector in a Helimagnet. Physical Review Letters. 2009, 103(14). DOI: 10.1103/PhysRevLett.103.147201.

[7] Seki, S., X. Z. Yu, S. Ishiwata, and Y. Tokura. Observation of Skyrmions in a Multiferroic Material. Science. 2012, 336(6078), 198–201. DOI: 10.1126/science.1214143.

[8] Seki, S., S. Ishiwata, and Y. Tokura. Magnetoelectric nature of skyrmions in a chiral magnetic insulator Cu_2OSeO_3. Physical Review B. 2012, 86(6). DOI: 10.1103/PhysRevB.86.060403.

[9] Bogdanov, A., and D. Yablonski. Thermodynamically stable "vortices" in magnetically ordered crystals. The mixed state of magnets. Soviet Physics Journal of Experimental and Theoretical Physics. 1989, 98(1), 178.

[10] Roßler, U. K., A. N. Bogdanov, and C. Pfleiderer. Spontaneous skyrmion ground states in magnetic metals. Nature. 2006, 442(7104), 797–801. DOI: 10.1038/nature05056.

[11] Muhlbauer, S., B. Binz, F. Jonietz, C. Pfleiderer, A. Rosch, A. Neubauer, R. Georgii, P. Boni. Skyrmion Lattice in a Chiral Magnet. Science. 2009, 323(5916), 915-919. DOI: 10.1126/science.1166767.

[12] Yu, X. Z., Y. Onose, N. Kanazawa, J. H. Park, J. H. Han, Y. Matsui, N. Nagaosa, Y. Tokura. Real-space observation of a two-dimensional skyrmion crystal. Nature. 2010, 465(7300), 901-904. DOI: 10.1038/nature09124.

[13] Yu, X. Z., N. Kanazawa, Y. Onose, K. Kimoto, W. Z. Zhang, S. Ishiwata, Y. Matsui, Y. Tokura. Near room-temperature formation of a skyrmion crystal in thin-films of the helimagnet FeGe. Nature Materials. 2011, 10(2), 106–109. DOI: 10.1038/nmat2916.

[14] Wilson, M. N., E. A. Karhu, D. P. Lake, et al. Discrete helicoidal states in chiral magnetic thin films. Physical Review B. 2013, 88(21). DOI: 10.1103/PhysRevB.88.214420.

[15] Togawa, Y., K. Koyama, Y. Nishimori, et al. Magnetic soliton confinement and discretization effects arising from macroscopic coherence in a chiral spin soliton lattice. Physical Review B. 2015, 92(22). DOI: 10.1103/PhysRevB.92.220412.

[16] Wang, W., N. Chepiga, D. K. Ki, et al. Controlling the Topological Sector of Magnetic Solitons in Exfoliated $Cr_{1/3}NbS_2$ Crystals. Physical Review Letters. 2017, 118(25). DOI: 10.1103/PhysRevLett.118.257203.

[17] Kishine, J., I. G. Bostrem, A.S. Ovchinnikov, V. E. Sinitsyn. Topological magnetization jumps in a confined chiral soliton lattice. Physical Review B. 2014, 89(1). DOI: 10.1103/PhysRevB.89.014419.

[18] Fishman, R. S., and S. Okamoto. Spiral spin state with open boundary conditions in a magnetic field. Physical Review B. 2017, 96(1). DOI: 10.1103/PhysRevB.96.014439.

[19] Papanicolaou, N. Low-frequency dynamics in an antiferromagnetic superlattice. Journal of Physics: Condensed Matter. 1999, 11(1), 59–79. DOI: 10.1088/0953-8984/11/1/006.

[20] Leese, R. A., M. Peyrard, and W. J. Zakrzewski. Soliton stability in the O(3) sigma -model in (2+1) dimensions. Nonlinearity. 1990, 3(2), 387–412. DOI: 10.1088/0951-7715/3/2/007.

[21] Wang, R. W., D. L. Mills, E. E. Fullerton, J. E. Watson, S. D. Bader. Surface spin-flop transition in Fe/Cr(211) superlattices: Experiment and theory. Physical Review Letters. 1994, 72(6), 920–923. DOI: 10.1103/PhysRevLett.72.920.

[22] Mills, D. L. Surface Spin-Flop State in a Simple Antiferromagnet. Physical Review Letters. 1968, 20(1), 18–21. DOI: 10.1103/PhysRevLett.20.18.

Publications

Chovan, J., and D. Legut. Topological jumps in a finite-size Dzyaloshinskii-Moriya antiferromagnetic chain. Verhandlungen der Deutschen Physikalischen Gesellschaft (DPG 2018), talk, 11–16 March 2018, Berlin.

Chovan, J., and D. Legut. Field evolution of topological sectors in a finite Dzyaloshinskii-Moriya antiferromagnetic chain. 21st International Conference on Magnetism (ICM2018), poster, 15–20 July 2018, San Francisco.

LATTICE VIBRATIONS IN THE POLAR ANTIFERROMAGNET Ni$_2$MnTeO$_6$

Research institution:	Principal investigator:	Researcher:	Project ID:
IT4Innovations National Supercomputing Center	Dominik Legut	Stella Skiadopoulou	OPEN-9-3

Introduction

Magnetoelectric (ME) multiferroics (MFs) are strong candidates for a wide range of novel hybrid technological applications, such as sensing, energy harvesting, photovoltaics, solid-state refrigeration, data storage, magnonics, and spintronics, to name a few [1]. Most importantly, the ability to manipulate the magnetization by electric fields leads to simple, cost-effective and energetically sustainable technological strategies.

In pursuit of multiferroic compounds resembling the polar antiferromagnet Ni$_3$TeO$_6$, exhibiting static (colossal) [2] and dynamic magnetoelectric coupling [3], Ni$_2$MnTeO$_6$ was synthesized, for the first time, in the form of single crystals and ceramics; their magnetic and dielectric properties were studied. Ni$_2$MnTeO$_6$ exhibits an antiferromagnetic (AFM) transition at $T_N \sim 70$ K, 20 K higher than the parent structure Ni$_3$TeO$_6$. Ab initio lattice dynamics calculations were performed and compared with IR, Raman and THz spectroscopy experiments, showing good agreement.

Results and Methods

Computational and experimental methods

Spin-polarized density functional theory calculations were conducted, implementing projector-augmented-wave formalism to describe the electron-ion interactions, and the generalized gradient approximation parametrized by Pedrew, Burke, and Ernzerhof (GGA-PBE) for the exchange-correlation potential [4, 5]. To account for the correct AFM order, the unit cell was doubled along the c-axis and sampled with a 5x5x2 grid. The lattice dynamics calculations were used within the Phonopy code [6], employing calculated Hellman Feynman forces, and using a 2x2x2 supercell with 60 displacements of 0.01 Å. Additional on-site Coulomb repulsion interactions were considered concurrently, within the rotationally invariant form of the GGA+U approach [7], where the localized 3d electrons experience a spin- and orbital-dependent potential (U) and an exchange interaction J, while the other orbitals are delocalized and treated with the conventional GGA approximation.
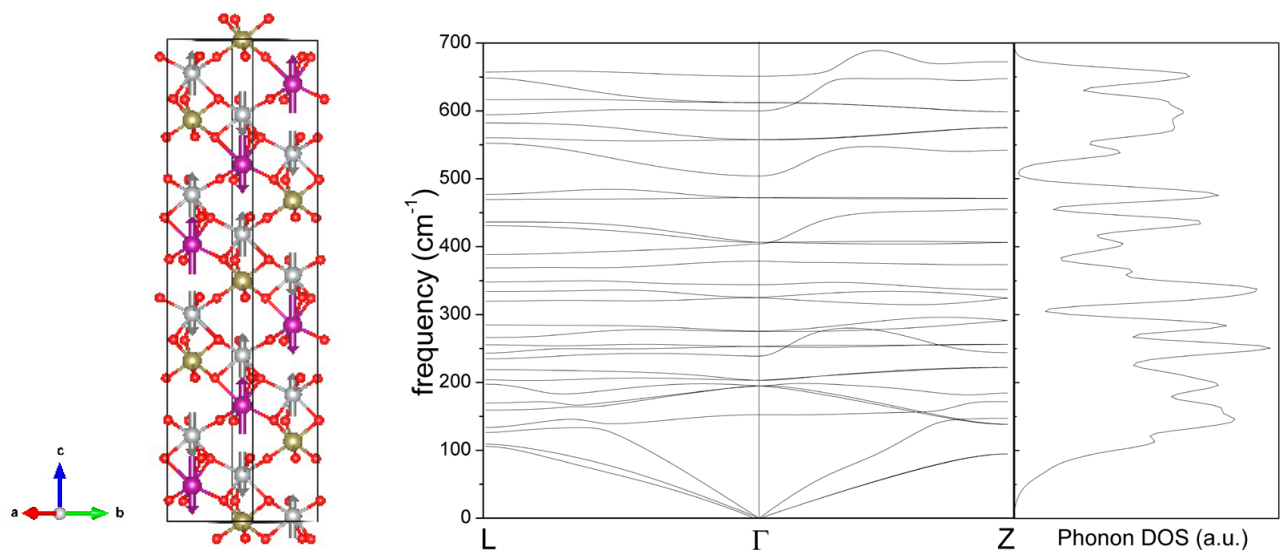

Figure 1.
Left: Schematic representation of a double hexagonal cell for Ni$_2$MnTeO$_6$ (60 atoms). Ni: grey, Mn: purple, Te: golden, O: red.
Right: Calculated phonon dispersion relation for the path L-Γ-Z, and total density of states for Ni$_2$MnTeO$_6$.

Near-normal incidence IR reflectivity spectra of the Ni_2MnTeO_6 ceramics were measured using Fourier-transform IR spectroscopy from 7–300 K in the frequency range of 20–3000 cm^{-1} (0.6 – 90 THz) at room temperature, and 20-650 cm^{-1} for the low-temperature measurements. THz measurements from 3 to 60 cm^{-1} (0.09 – 1.8 THz) were performed for the transmission geometry. For Raman studies of single crystals, the experiments were performed with backscattering geometry in the 5–1800 cm^{-1} range.

Results

Employing first-principles calculations, we determined the structural geometry with the AFM order as depicted in Figure 1(left). The calculated hexagonal lattice parameters of a=5.21386 Å and c=14.17241 Å correspond to a less than 1% high-

er volume value than the experimental one (a=5.1317(3) Å, c=13.9155(9) Å, V=317.37(3) Å^3) [8]. Within the GGA+U approach, the U_{eff}=U-J is only meaningful when U_{eff}=7 eV for both Ni and Mn sites, and yield the Ni^I/Ni^{II} and Mn magnetic moments 1.8 μB and 4.8 μB, respectively. These values lie close to the previously reported experimental ones for Ni (2 μ$_B$) and Mn (3–6 μ$_B$) in the Ni_3TeO_6 [9] and Mn_3TeO_6 [10] compounds, respectively.

As predicted by the factor-group analysis for the R3 structure, nine E(x,y,x^2-y^2,xy,xz,yz) and nine A(x^2+y^2,z^2,z) modes are expected, both IR and Raman active, analogously to the Ni_3TeO_6 case [3]. Lattice dynamics calculations, based on the computed Hellman Feynman forces were performed. The phonon dispersion relation for the reciprocal space path L-Γ-Z is depicted in Figure 1 (right), together with the total density of states. At the

Ni_3TeO_6 [3]	Ni_2MnTeO_6				
IR 7 K	Calculations	Raman 4 K	IR 10 K		
ω_{TO} (cm^{-1})	ω (cm^{-1})	ω (cm^{-1})	ω_{TO} (cm^{-1})	γ_{TO} (cm^{-1})	Δε
16.2			7.9	1.3	0.04
32.4					
	168.0 (A)	164.6	163.1	5.8	0.12
185.0	195.4 (E)	185.5$_w$	189.2	28.5	0.34
	206.8 (A)	211.2	205.4	5.4	0.85
219.3	220.8 (E)		214.8	6.4	0.16
232.1	243.6 (A)		240.9	23.9	0.23
259.2	265.6 (E)	266.0	262.8	14.5	0.83
279.3	284.9 (E)		284.2	17.3	0.74
303.1	319.4 (E)	300.0	293.6	8.7	0.07
313.2	352.8 (A)	354.1$_w$	345.8	18.1	0.50
345.2	368.7 (E)	369.7	369.8	7.2	0.10
361.7	408.1 (A)	403.2	397.2	33.4	0.25
380.0	440.0 (A)		431.4	9.8	1.17
406.6	443.7 (A)	436.5	435.7	6.3	0.21
454.2	507.7 (E)	475.6	509.3	14.4	0.29
466.1		484.3			
516.5	546.8 (E)	501.6	518.7	17.1	0.31
536.6	555.3 (E)	538.0	525.5	5.5	0.01
		570.8$_w$			
597.1	587.1 (A)	590.6	590.6	24.6	0.09
661.2		603.4$_w$			
	663.4 (A)	681.0$_w$	653.9	17.7	0.27
		693.6			
		720.0$_w$			

Table 1.
Comparison of the phonon modes as obtained by first-principles calculations, IR reflectivity and Raman spectroscopy measurements.

long-wavelength limit (Γ-point), the calculated phonon bands yield all expected 18 IR- and Raman-active phonon modes, as predicted by factor group analysis. The computed values are in good agreement with the experimental ones obtained by IR and Raman spectroscopies (see Table 1). The damping constants and dielectric strengths of the IR-active modes are also listed in Table 1. The modes observed as weak in Raman spectra are marked by w in subscript. All Raman modes which are not IR active correspond to longitudinal optic modes. The theoretical frequencies obtained by first-principles calculation are also included, together with the assigned symmetry for each mode in parentheses. The low-frequency mode in the first line was identified in the THz spectra as a magnon. The first column corresponds to the IR mode frequencies of Ni_3TeO_6 ceramics at 7 K from Skiadopoulou et al. [3].

On-going Research / Outlook

Our aim is to unveil the underlying mechanisms that lead to the enhancement of the ME MF properties, as well as possibly increase the critical temperatures in favour of the applications.

Further investigation of spin-lattice interactions and magnetic exchange interactions in the compound Ni_2MnTeO_6 is currently being taken into consideration. In order to account for the effect of the spin-order in the phonon modes, lattice dynamics calculations of different spin configurations will be performed.

Conclusion

Single crystals and polycrystalline ceramic samples of the new compound Ni_2MnTeO_6 were synthesized for the first time. The Mn-substitution of Ni in Ni_3TeO_6 leads to an increase in the AFM transition temperature by 20 K, thus reaching ~70 K, whereas the compound preserves the polar R3 space group. Ab initio lattice dynamics calculations are in good agreement with the experimental results obtained from IR and Raman spectroscopies, revealing all expected IR and Raman active modes of the R3 symmetry.

References

[1] Vopson, M. M. Fundamentals of Multiferroic Materials and Their Possible Applications. Critical Reviews in Solid State and Materials Sciences. 2015, 40(4), 223–250. DOI: 10.1080/10408436.2014.992584.

[2] Oh, Y. S., S. Artyukhin, J. J. Yang, V. Zapf, J. W. Kim, D. Vanderbilt, and S.–W. Cheong. Non-hysteretic colossal magnetoelectricity in a collinear antiferromagnet. Nature Communications. 2014, 5(1). DOI: 10.1038/ncomms4201.

[3] Skiadopoulou, S., F. Borodavka, Ch. Kadlec, F. Kadlec, M. Retuerto, Z. Deng, M. Greenblatt, and S. Kamba. Magnetoelectric excitations in multiferroic Ni_3TeO_6. Physical Review B. 2017, 95(18). DOI: 10.1103/PhysRevB.95.184435.

[4] Kresse, G., and J. Furthmüller. Efficient iterative schemes for ab initio total-energy calculations using a plane-wave basis set. Physical Review B. 1996, 54(16), 11169-11186. DOI: 10.1103/PhysRevB.54.11169.

[5] Perdew, J. P., K. Burke, and M. Ernzerhof. Generalized Gradient Approximation Made Simple. Physical Review Letters. 1996, 77(18), 3865-3868. DOI: 10.1103/PhysRevLett.77.3865.

[6] Togo, A., and I. Tanaka. Scripta Materialia. 2015, 108, 1-5. DOI: 10.1016/j.scriptamat.2015.07.021

[7] Dudarev, S. L., G. A. Botton, S. Y. Savrasov, C. J. Humphreys, and A. P. Sutton. Electron-energy-loss spectra and the structural stability of nickel oxide: An LSDA+U study. Physical Review B. 1998, 57(3), 1505–1509. DOI: 10.1103/PhysRevB.57.1505.

[8] Retuerto, M., S. Skiadopoulou, F. Borodavka, et al. Structural and spectroscopic properties of the polar antiferromagnet Ni_2MnTeO_6. Physical Review B. 2018, 97(14). DOI: 10.1103/PhysRevB.97.

[9] Živković, I., K. Prša, O. Zaharko, and H. Berger. Ni3TeO6 – a collinear antiferromagnet with ferromagnetic honeycomb planes. Journal of Physics: Condensed Matter. 2010, 22(5). DOI: 10.1088/0953-8984/22/5/056002.

[10] Ivanov, S. A., P. Nordblad, R. Mathieu, R. Tellgren, C. Ritter, N. V. Golubko, E. D. Politova, and M. Weil. New type of incommensurate magnetic ordering in Mn_3TeO_6. Materials Research Bulletin. 2011, 46(11), 1870-1877. DOI: 10.1016/j.materresbull.2011.07.041.

IMPACT OF MAGNETIC INTERACTIONS ON PHONONS IN 2D TI$_2$X (X=C,N) MXenes

Research institution:
IT4Innovations National Supercomputing Center

Principal investigator:
Dominik Legut

Researcher:
Urszula D. Wdowik

Project partner:
The Pedagogical University, Cracow

Project ID:
OPEN-12-35

Introduction

Two-dimensional (2D) solids with a thicknesses of a few atomic layers have attracted theoretical and experimental interest not only for their unique properties, which differ from those of their three-dimensional (3D) counterparts, but also for their potential applications in energy storage and electronic devices [1]. The most studied example of a two-dimensional system is graphene, but other graphene-like materials such as hexagonal BN (boron nitride), transition metal dichalcogenides (TMD's), and metal oxides and hydroxides have gained renewed attention [2–5]. Recently, a novel family of 2D early transition-metal carbides, nitrides and carbonitrides [6, 7], termed MXenes, have been synthesized from the MAX phases [8].
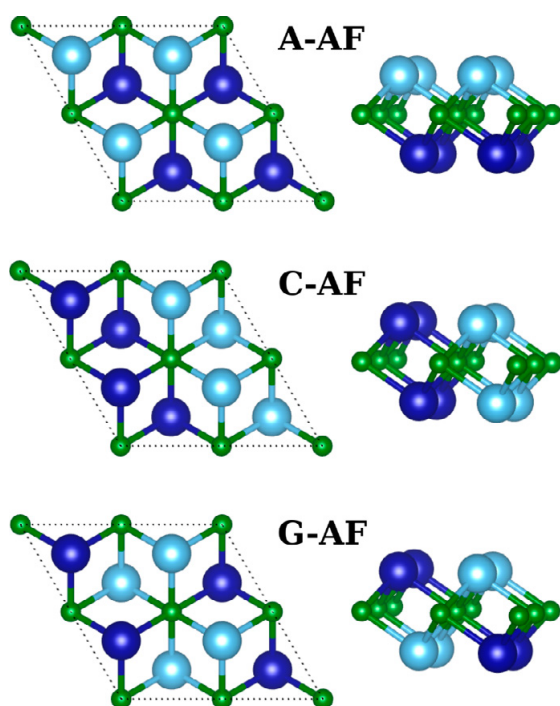

Figure 1.
Top and side views of AF configurations of Ti$_2$X monolayers. Light and dark blue balls represent Ti atoms with opposite spin directions. Small green balls indicate X=C/N atoms.
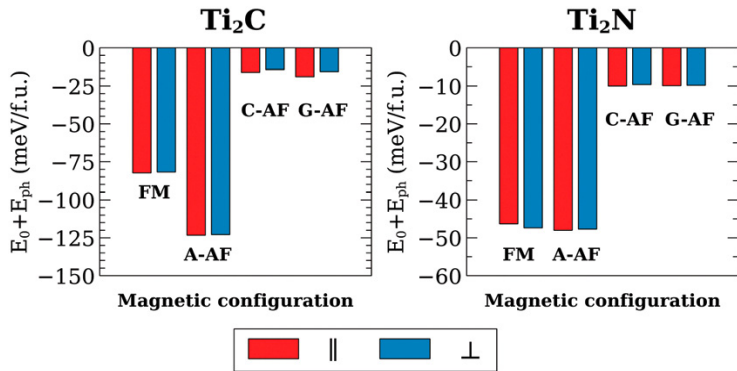
With the increased attention on 2D materials beyond graphene, and with MXenes representing a new large family extending the world of 2D materials, it is timely to obtain a deeper insight into their structural, electronic, magnetic and dynamical properties which determine to a large extent their potential applications. Therefore, comprehensive first-principles calculations using state-of-the-art density functional theory (DFT) have been undertaken [9] to explore the effect of magnetic interactions on the structural, electronic and dynamical properties of Ti$_2$X (X=C,N) monolayers belonging to the MXene family.

Results and Methods

The current research is based on a DFT method implementing the PAW (projected augmented wave) technique and the GGA-PBE (generalized gradient approximation as parametrized by Perdew-Burke-Ernzerhof) approximation for the exchange-correlation effects [10]. The wave functions are expanded in a plane-wave basis set with a cut-off energy of 520 eV. The semi-empirical corrections of Grimme et al. [11] (DFT-D3) are incorporated to account for van der Waals interactions. Reference configurations for valence electrons are as follows: Ti($3d^34s^1$), C($2s^22p^2$), and N($2s^22p^3$). The semi-empirical corrections of Grimme et al. [11] (DFT-D3) are incorporated to account for van der Waals interactions. Structural optimizations of Ti$_2$X (X=C,N) systems are performed on the 2x2x1 supercells. Phonon and Raman spectra were obtained within the harmonic approximation [12, 13].

To elucidate the influence of magnetic interactions on the fundamental properties of these systems, the nonmagnetic (NM), ferromagnetic (FM) and three distinct antiferromagnetic (AF) spin arrangements on the Ti sublattice have been considered (shown in Figure 1). Each magnetic configuration has also been studied at two directions of the spin magnetic moment with respect to the MXene layer.

The zero-point energy motion, following from the phonon calculations, has been taken into account while analyzing the energetic stability of the magnetic phases against the nonmagnetic solution. This contribution was found not to change any sequence of the energetic stability of the considered Ti$_2$X (X=C, N) magnetic structures. Both Ti$_2$X (X=C,N) systems are shown to prefer AF

arrangement of spins between Ti layers and FM order within each layer (see Figure 2). This energetically favoured phase is semiconducting for Ti$_2$C and metallic for Ti$_2$N.

Results of the present studies indicate that the type of magnetic order as well as the in-plane or out-of-plane spin polarizations have a relatively small impact on the structural parameters, Ti-X bonding length, force constants and phonon spectra of both Ti$_2$X systems, leading to observable differences only between the nonmagnetic and any other magnetic configuration. Nonetheless, a noticeable effect of the spin orientation on the degeneracy of the Ti-3d orbitals is encountered. By substituting C atoms with N atoms one can modify to a great extent the electronic bands near the Fermi energy of the A-AF magnetic configuration. Upon such a replacement the Ti$_2$X system transforms from a semiconducting to a metallic state. The magnetic interactions affect positions, and to a large extent intensities of the Raman-active modes, as schematically indicated in Figure 3. Hence, one could exploit this effect for experimental verification of the theoretically predicted magnetic state of Ti$_2$X monolayers. In addition, theoretical phonon spectra of the Ti$_2$X (X=C,N) MXenes exhibit linear dependence on energy in the long-wavelength limit, which is typical for a 2D system.
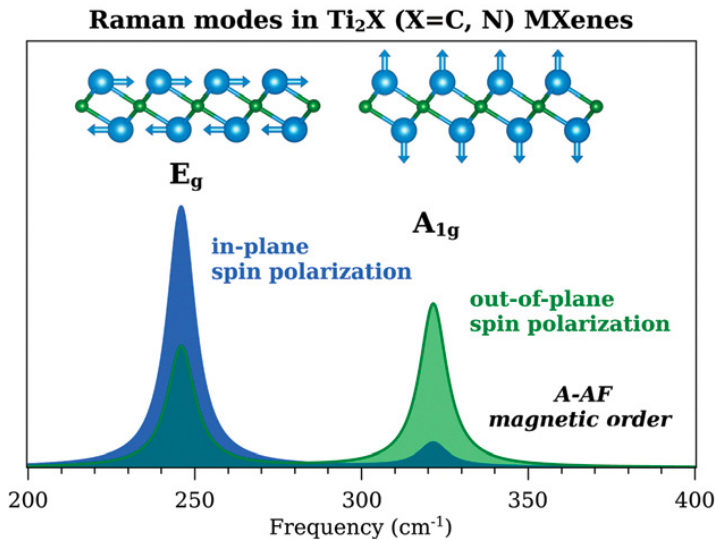
Conclusion

Comparative studies of the structural, electronic and dynamical properties of Ti_2X monolayers with X=C,N were performed with the DFT method to explore modifications of the fundamental properties of these 2D MXene materials upon (i) changing the magnetic order and spin polarization on the Ti atoms, (ii) enlarging the X-atom mass, and (iii) introducing an extra valence electron per formula unit by the atom X. The force constants which govern the dynamics of phonons remain practically insensitive to magneto-structural correlations. The magnetic interactions seem to play a more important role in the intensities of Raman-active phonon modes in Ti_2X (X = C, N) monolayers.

References

[1] S. Chen, Z.H. Fu, H. Zhang, D. Legut, T. C. Germann, Q. F. Zhang, S. Y. Du, J. S. Francisco, R. F. Zhang, Surface Electrochemical Stability and Strain-Tunable Lithium Storage of Highly Flexible 2D Transition Metal Carbides Adv. Func. Mater. 28, 1804867 (2018).

[2] Novoselov, K. S. Electric Field Effect in Atomically Thin Carbon Films. Science. 2004, 306(5696), 666–669. DOI: 10.1126/science.1102896.

[3] Pacilé, D., J. C. Meyer, Ç. Ö. Girit, and A. Zettl. The two-dimensional phase of boron nitride: Few-atomic-layer sheets and suspended membranes. Applied Physics Letters. 2008, 92(13). DOI: 10.1063/1.2903702.

[4] Ma, R., and T. Sasaki. Nanosheets of Oxides and Hydroxides: Ultimate 2D Charge-Bearing Functional Crystallites. Advanced Materials. 2010, 22(45), 5082-5104. DOI: 10.1002/adma.201001722.

[5] Coleman, J. N., M. Lotya, A. O'Neill, et al. Two-Dimensional Nanosheets Produced by Liquid Exfoliation of Layered Materials. Science. 2011, 331(6017), 568-571. DOI: 10.1126/science.1194975.

[6] Naguib, M., M. Kurtoglu, V. Presser, et al. Two-Dimensional Nanocrystals Produced by Exfoliation of Ti_3AlC_2. Advanced Materials. 2011, 23(37), 4248–4253. DOI: 10.1002/adma.201102306.

[7] Naguib, M., O. Mashtalir, J. Carle, V., et al. Two-Dimensional Transition Metal Carbides. ACS Nano. 2012, 6(2), 1322-1331. DOI: 10.1021/nn204153h.

[8] Barsoum, M. W. MAX phases: properties of machinable ternary carbides and nitrides. Weinheim, Germany: Wiley-VCH Verlag GmbH & Co., [2013]. ISBN: 978-3-527-33011-9.

[9] Sternik, M., and U. D. Wdowik. Probing the impact of magnetic interactions on the lattice dynamics of two-dimensional Ti_2X (X = C, N) MXenes. Physical Chemistry Chemical Physics. 2018, 20(11), 7754–7763. DOI: 10.1039/C7CP08270C.

[10] Kresse, G., and J. Furthmüller. Efficient iterative schemes for ab initio total-energy calculations using a plane-wave basis set. Physical Review B. 1996, 54(16), 11169–11186. DOI: 10.1103/PhysRevB.54.11169.

[11] Grimme, S., J. Antony, S. Ehrlich, and H. Krieg. A consistent and accurate ab initio parametrization of density functional dispersion correction (DFT-D) for the 94 elements H-Pu. The Journal of Chemical Physics. 2010, 132(15). DOI: 10.1063/1.3382344.

[12] Parlinski, K., Z. Q. Li, and Y. Kawazoe. First-Principles Determination of the Soft Mode in Cubic ZrO_2. Physical Review Letters. 1997, 78(21), 4063–4066. DOI: 10.1103/PhysRevLett.78.4063.

[13] Software PHONON ver. 6.15, Cracow, Poland, 2015.

DESIGN OF NOVEL Li-BASED BATTERIES — PROTECTION OF THE Li-METAL ANODE

Research institution:
IT4Innovations National Supercomputing Center

Principal investigator:
Dominik Legut

Researchers:
Qianfan Zhang, Ruifeng Zhang, Shihao Zhang

Project partner:
Beihang University, Beijing

Project ID:
OPEN-8-34

Introduction

Li metal is desirable as the anode material with the highest theoretical specific capacity and the lowest standard potential, to significantly increase the energy density in rechargeable Li-ion batteries. However, Li anode material carries with it many challenges such as the growth of Li dendrites and low coulombic efficiency. Therefore, further study of lithium electrode materials is needed. Many strategies have been carried out to modify the nano-scaled interphase between the Li metal anode and electrolytes, to improve the performance of Li metal anodes, including development of inorganic and organic molecules coatings, all-solid-state electrolytes, and alkaline ion additives [1–6]. These kinds of protection schemes can greatly improve the performance of metal anodes. However, they can also suffer from disadvantages such as low ionic conductivity at room temperature, large interfacial impedance, large thickness, etc. In the present project, we investigated the practicability of typical two-dimensional layer-structured materials such as hexagonal boron nitride (h-BN), graphene, silicene, germanene, stanene, phosphorene, SnS, and SnSe as protecting films (PFs) for Li metal anodes. The first major aim is to find the most suitable material considering both the electrical and mechanical properties derived from their electronic structure obtained by means of first-principles (quantum-mechanical) calculations. We focus on the relationship with the crystalline structure, defect feature, and metal's proximity effect. We will investigate various crystalline structures that can induce different Li$^+$ ion diffusion and stiffness features, the effect of defect presence at the metal/insulator interface on conductivity, and at the same time on the strength and stress vs. strain relations of the two-dimensional materials. Using the computed electronic structure we identify the electronic origin of the obtained theoretical results and try to describe the interaction picture of Li$^+$ and the PFs.

Results and Methods

First, the diffusion properties of Li$^+$ ions transferring through these PFs were explored, and the transfer barriers of a single Li$^+$ ion passing perpendicularly through various 2D layered materials were computed by the climbing-image nudged elastic band (CI-NEB) method [7]. Then, the barriers for Li$^+$ ions penetrating through various PF materials are computed as the energy profiles of Li$^+$ ion diffusion as a function of the diffusion coordinate. For the case of the pristine graphene, see Fig. 1, it amounts to 7.9 eV. After introducing defects, the situation is fundamentally different. For the graphene sheet with single vacancy (SV), double vacancy (DV), and Stone-Thrower-Wales (STW) defects the barriers lower to 3.60 eV, 1.31 eV, and 2.98 eV, respectively. The diffusion rates for Li+ are in the range of 10^{-18}–10^{-52} cm^{2}s^{-1}, more than 83 orders higher than that of pristine graphene. This is also the reason why defective graphene can do comparatively well as PF. As a stable interfacial layer to protect a Li metal anode, not only good diffusion properties but also excellent mechanical stability is required for 2D PFs. First, we calculate the Young's modulus of 985 GPa, 656 GPa, 914 GPa, and 940 GPa for pristine, SV, DV, and STW graphene, respectively. It indicates that all the materials we studied possess much higher Young's moduli than that of Li metal ($\approx$4.9 GPa), and also higher than or comparable with common inorganic components in native solid electrolyte interphase (SEI) (e.g., $\approx$68 GPa for Li$_2$CO$_3$) [8]. Also it shows that the Young moduli values of defected graphene are lower than those of pristine graphene.
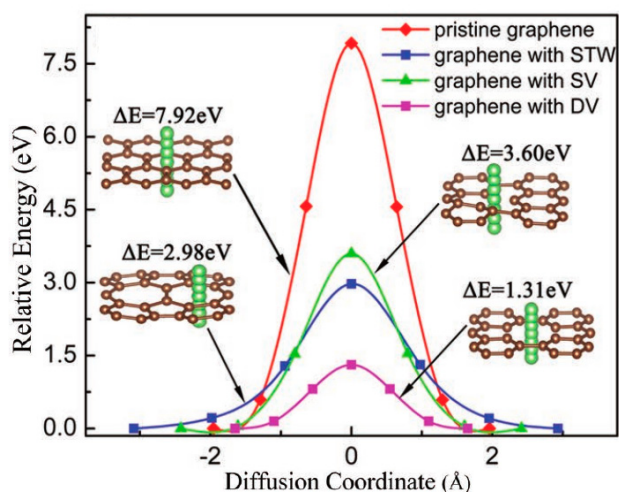
Figure 1.
Potential-energy curves of Li+ ion diffusion in the direction perpendicular to the sheet of graphene and defective graphene
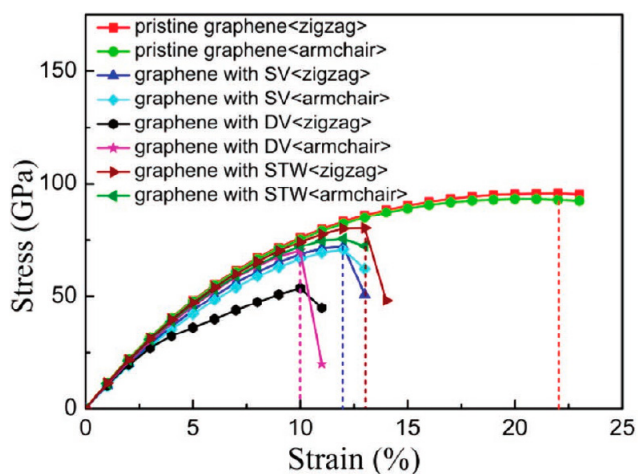

Figure 2.
Strain–stress relations for graphene and defected graphene

Second, the stiffness of 2D layered materials can be evaluated by critical strain (the strain at which ideal strength reaches). Equivalent tensile strains were simultaneously applied in the zigzag and armchair direction to investigate the critical biaxial strain. Such ideal strength sets the upper limit of the material in reality and can also be applied to many materials in experiments, especially in 2D materials [9, 10]. The applied strain is defined as $\varepsilon = (a-a_0)/a_0$, where a and a_0 are the lattice constants of strained and stable materials, respectively. Here, the strain–stress relations of these materials under equibiaxial loading were calculated, and are presented in Figure 2. For the graphene free from defect, the critical strain is approximately 22% and stress is 90 GPa. With the presence of defect, the situation can be quite different, and both the critical strain and the critical loading force dramatically decrease, especially for graphene, with drop to 10–13% and 50–80GPa. Therefore, the existence of defects can significantly impair the mechanical properties of these materials and should be avoided in PFs.

Concerning the methodology, each of the points along a stress-strain or diffusion barrier path (Climbing Image Nudged Elastic Band Method, CI-NEB) is based on the first-principles calculations using density functional theory [11] to solve Schroedinger/Dirac equations for the electronic states employing VASP code [12, 13] and performed with the projected augmented plane wave potentials as parametrized by Perdew-Burke-Ehrenzof [14]. The energy cut-off of 550 eV, k-point grid of 5x5x1, and vacuum space of 20 Å at the surface were used to model defect-free and defected graphene with a 5x3x1 supercell.

Conclusion and Outlook

We investigated the practicability of h-BN, graphene, silicene, germanene, stanene, phosphorene, SnS, and SnSe as PFs for Li(Na) anodes through first-principles calculations. Our theoretical calculations indicate that the defect pattern, crystalline structure, bond length and bond angle (or the ring size), and metal proximity effect play key roles on the protective effect of a PF. Introducing defect, increasing the size of the hollow ring and the proximity effect at PFs can improve the conductivity of Li+ ions, but all of them can decrease hardness and stiffness of the PFs against the suppression of lithium (sodium) dendrite growth. Therefore, it is important to design PFs that possess a compromise between the ion conductivity and stiffness against the lithium dendrites. For details and a more detailed analysis we refer the reader to [15], where this work was presented.

References

[1] Winter, M., and R. J. Brodd. What Are Batteries, Fuel Cells, and Supercapacitors? Chemical Reviews. 2004, 104(10), 4245-4270. DOI: 10.1021/cr020730k.

[2] Armand, M., and J.-M. Tarascon. Building better batteries. Nature. 2008, 451(7179), 652-657. DOI: 10.1038/451652a.

[3] Tarascon, J.-M., and M. Armand. Issues and challenges facing rechargeable lithium batteries. Nature. 2001, 414(6861), 359-367. DOI: 10.1038/35104644.

[4] Bruce, P. G., S. A. Freunberger, L. J. Hardwick, and J.-M. Tarascon. Li-O$_2$ and Li-S batteries with high energy storage. Nature Materials. 2012, 11(1), 19-29.
DOI: 10.1038/nmat3191.

[5] Chu, S., and A. Majumdar. Opportunities and challenges for a sustainable energy future. Nature. 2012, 488(7411), 294-303. DOI: 10.1038/nature11475.

[6] Mikhaylik, Y. V., and J. R. Akridge. Polysulfide Shuttle Study in the Li-S Battery System. Journal of The Electrochemical Society. 2004, 151(11).
DOI: 10.1149/1.1806394.

[7] Henkelman, G., B. P. Uberuaga, and H. Jónsson. A climbing image nudged elastic band method for finding saddle points and minimum energy paths.
The Journal of Chemical Physics. 2000, 113(22), 9901–9904. DOI: 10.1063/1.1329672.

[8] Yan, K., H.-W. Lee, T. Gao, et al. Ultrathin Two-Dimensional Atomic Crystals as Stable Interfacial Layer for Improvement of Lithium Metal Anode.
Nano Letters. 2014, 14(10), 6016-6022. DOI: 10.1021/nl503125u.

[9] Wei, Q., and X. Peng. Superior mechanical flexibility of phosphorene and few-layer black phosphorus. Applied Physics Letters. 2014, 104(25).
DOI: 10.1063/1.4885215.

[10] Hu, S., M. Lozada-Hidalgo, F. C. Wang, et al. Proton transport through one-atom-thick crystals. Nature. 2014, 516(7530), 227–230.
DOI: 10.1038/nature14015.

[11] Hohenberg, P., and W. Kohn. Inhomogeneous Electron Gas. Physical Review. 1964, 136(3B), B864–B871. DOI: 10.1103/PhysRev.136.B864.

[12] Kresse, G., and J. Furthmüller. Efficiency of ab-initio total energy calculations for metals and semiconductors using a plane-wave basis set.
Computational Materials Science. 1996, 6(1), 15–50. DOI: 10.1016/0927-0256(96)00008-0.

[13] Kresse, G., and J. Furthmüller. Efficient iterative schemes for ab initio total-energy calculations using a plane-wave basis set. Physical Review B.
1996, 54(16), 11169–11186. DOI: 10.1103/PhysRevB.54.11169.

[14] Perdew, J. P., K. Burke, and M. Ernzerhof. Generalized Gradient Approximation Made Simple. Physical Review Letters. 1996, 77(18), 3865–3868;
1997, 78(7), 1396. DOI: 10.1103/PhysRevLett.77.3865.

Publication

[15] Tian, H., Z. W. Seh, K. Yan, Z. Fu, P. Tang, Y. Lu, R. Zhang, D. Legut, Y. Cui, Q. Zhang. Theoretical Investigation of 2D Layered Materials as Protective Films
for Lithium and Sodium Metal Anodes. Advanced Energy Materials. 2017, 7(13). DOI: 10.1002/aenm.201602528

INTERACTION OF PROTEINS WITH SILICEOUS BASED SUPPORTS

Research institution:	Principal investigator:	Project ID:
The Institute of Organic Chemistry and Biochemistry of the Czech Academy of Sciences	Miroslav Rubeš	OPEN-11-2

Introduction

The interaction of proteins with silica-based surfaces is a very active area of research because of the application potential of protein anchoring, ranging from sensors, to wastewater treatment and bio-catalysis. Notwithstanding the tremendous progress that has been made in recent years to understand protein interaction with silica surfaces, some of the fundamentals are still not yet well understood. This mainly stems from the fact that most silica surfaces are experimentally not defined with atomistic resolution. As a result, it is necessary in computer simulations to rely on models that describe the silica surface with a high degree of uncertainty. The modelling is further complicated by the effect of pH, which causes surface charging and possible proton transfer between the adsorbed protein and surface siloxy groups either directly or via water.

In this project, we compared the binding free energies of capped amino acids (hydrophobic, aromatic, and polar) interacting with three different silica-based surfaces with varying silanol densities for two different generic force fields, and compared their performance against the force field parameterized on ab initio data (AIFF). It is important to mention that two of the selected surfaces are hypothetical materials (quartz - perfectly reconstructed (001) α-quartz without surface silanol groups, and quartzOH – fully hydroxylated (001) α-quartz) and one has been prepared experimentally (IPC-1P).

Results and Methods

The binding free energies of capped amino acids on various silica surfaces are summarized in Figure 1.
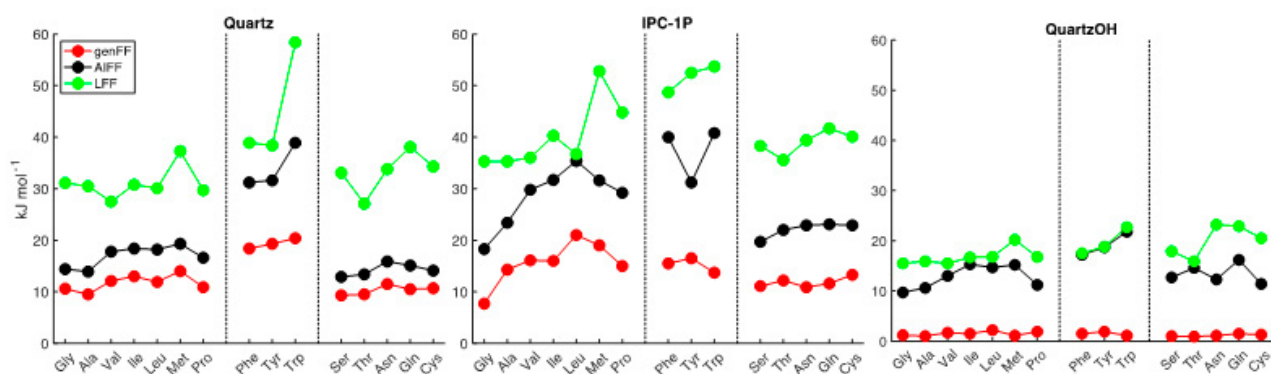

Figure 1.
Binding free energies for each investigated proteinogenic amino acid. The vertical dotted lines separate hydrophobic, aromatic, and polar amino acids. Two generic force fields (genFF and LFF) are compared against our parameterization based on ab initio data.

In general, the binding free energy increases in the order quartzOH < quartz < IPC-1P. The binding seems to be driven mainly by the affinity of amino acids to the hydrophobic surface (quartz). In the case of IPC-1P, the binding is stronger due to the heterogenous properties of the IPC-1P lamella. The large hydrophobic domains of IPC-1P allow for a similar adsorption
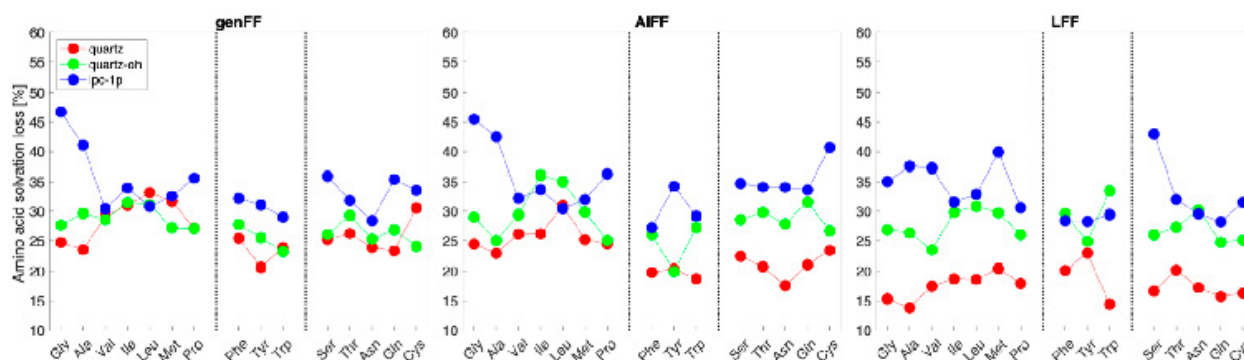
Figure 2.
The relative solvation loss of amino acids upon interaction with silica surfaces.

phenomenon to that on the quartz surface. At the same time, the sparse silanol groups enable the stabilization of amino-acid polar groups by forming hydrogen bonds. Such a strong interaction as on the IPC-1P lamella will probably not be observed on typical silica surfaces with higher and more homogeneous silanol densities. Both of these properties prevent the interaction of amino acids with the framework silicon and oxygen atoms in favour of the interaction with silanol groups, leading to a weaker adsorption due to surface solvation. This effect may be clearly illustrated on the quartzOH surface, where the amino acids interact directly only with silanol groups.

The MD simulations were performed using Gromacs 5.1.4 patched with the Plumed 2.3.0 library. The initial structures for the replica-exchange umbrella sampling (REUS) simulations were prepared by pulling towards the material; the perpendicular dimension of the box was at least 55 Å long. The reference periodic DFT calculations were performed using the VASP package employing a plane-wave basis set with an energy cutoff of 400 eV. The Brillouin-zone sampling was restricted to the Γ-point.

On-going Research / Outlook

The results of this project clearly indicated several open issues for addressing a protein interaction with silica supports. It is obvious that further development in force field parameterizations is necessary to obtain a reliable magnitude of the binding free energies. The natural next step is to address the role of pH, which leads to the interaction between the charges on the adsorbate (amino acids in zwitterionic form, or charged side chain species) and surface siloxy groups. The computational requirements to address these issues are going to be significantly greater than in case of this study due to the more complicated task of force field parameterization from ab initio reference data.

Conclusion

We have investigated the performance of three different force fields for fifteen capped proteinogenic amino acids on three different silica surfaces of increasing silanol density. The following conclusions can be made:

- predicted binding free energies differ significantly based on the force-field used
- reference calculations clearly indicate that the generic force field (genFF) fails to describe the interaction with silanol groups, and the force field proposed by Lopes et al. (LFF) overestimates the interaction with the silicon and oxygen atoms of silica layers
- the force field parameterized on ab initio data (AIFF) provides a more balanced description for peptide-silica interaction
- the surface heterogeneity and the local curvature (e.g. IPC-1P) enhances the binding free energy due to the decreased amino acid solvation (Figure 2) and in cases of hydrophobic amino acids there is an additionally cooperative interaction between IPC-1P surface and nonpolar and polar amino acids groups
- silica surfaces without silanol groups (quartz) provide a homogenous adsorption landscape, where propensity towards amino acids with aromatic side chains is observed
- fully hydroxylated silica surfaces (quartzOH) yield the weakest binding free energies due to significant surface solvation

Publication

RADIATION DAMAGE TOLERANT NANOMATERIALS: MODELLING INTERFACES WITH SELF-HEALING PROPERTIES (RATONMO)

Research institution:
The Czech Technical University in Prague

Principal investigator:
Huseyin Sener Sen

Researchers:
Benjamin Irving,
Antonio Cammarata,
Paolo Niccolini,
Alberto Fraile Garcia

Project ID:
OPEN-11-13

Introduction

A common goal for materials employed in nuclear environments is to exhibit the highest possible radiation tolerance. Radiation damage initially appears in the form of local intrinsic point defects within the material (i.e. vacancies and interstitials) [1]. The point defects agglomerate, interact with the underlying microstructure, and lead to undesirable effects such as blistering and radiation-induced embrittlement, which render the materials unsuitable for the desired application [2–4]. Another important factor is represented by helium (He) embrittlement. He originates from the transmutation of reactor elements which can release alpha particles that acquire electrons to become helium atoms. He is insoluble and mobile in most metals and migrates to grain boundaries and interfaces where it forms bubbles leading to embrittlement and mechanical property degradation [5–7]. In this project, we focused on understanding the reasons behind such behaviour of defects and He atoms, and how to minimize or if possible prevent the damage they cause. We used Zr-Nb multilayer nanocomposites since it is possible to create and control various interfaces that capture defects and He atoms. Ab initio and molecular dynamics simulations are employed to calculate mechanical properties and the 'defect-interface-helium' interaction microscopically.

Results and Methods

In the first stage of the project classical MD simulations on Zr, Nb and Zr-Nb multilayers were carried out using the LAMMPS code, where the main goal was to understand a variety of problems related to the mechanical properties of multi-layered systems. Firstly, we simulated the magnetron sputtering deposition process to understand the structures and properties of the Zr-Nb interfaces, and their dependence on the deposition parameters (adatom velocities, temperature, orientation of the substrate etc). An unexpected result was observed; namely, Zr growth in fcc phase is possible under some conditions. Apart from that, we conducted a series of simulations where an hcp to fcc phase transition took place. The transition is triggered by a small percent (5%) of vacancies [8]. Secondly, we focused on the real hardness of Zr-Nb multilayers at the atomic level. We conducted a comprehensive study of the response of pure, crystalline Zr and Nb at different orientations to indentation. Moreover, we carried out indentation simulations on larger layered systems in order to compare the response and behaviour of the layered systems to the pure constituents. A deep analysis of the dislocation dynamics in the Nb(bcc), Zr(hcp) and Zr-Nb systems, as well as the effect of defects and dislocations on the mechanical properties, was also carried out. The results, with a comparison to real experiments and theoretical & empirical laws, will be presented in [9].

In the second stage of the project we employed density functional calculations to investigate the mechanical properties of, and vacancy-interface-helium interaction within, the Zr-Nb multi-layer nanocomposite. An example of such a multi-layered structure can be seen in Figure 1a. We first calculated the elastic constants of Zr crystal, Nb crystal and Zr-Nb multi-layer systems with various numbers of layers. The results for crystals agreed with the experimental results in the literature perfectly, which validated our results for multi-layer systems. Using elastic constants we calculated the bulk modulus, shear modulus, Young's modulus, Poisson's ratio and universal anisotropy index of multi-layer systems. Some of the results are given in Table 1. Next, we analysed the charge density of the multi-layer systems revealing the charge transfer from the Zr side to the Nb side of the interface. Then, the vacancy-helium-interface interaction was analysed in terms of the energy change in the system. For both the vacancy and the He atom, the most energetically favourable position is to sit within the 1st Zr layer, which can be seen in Figure 1b, and c. When both the He atom and the vacancy are present in the system, the He atom will go inside the vacancy to fill the gap within the vacancy as if it is a substitution atom. All the ab-initio results are presented in [10].
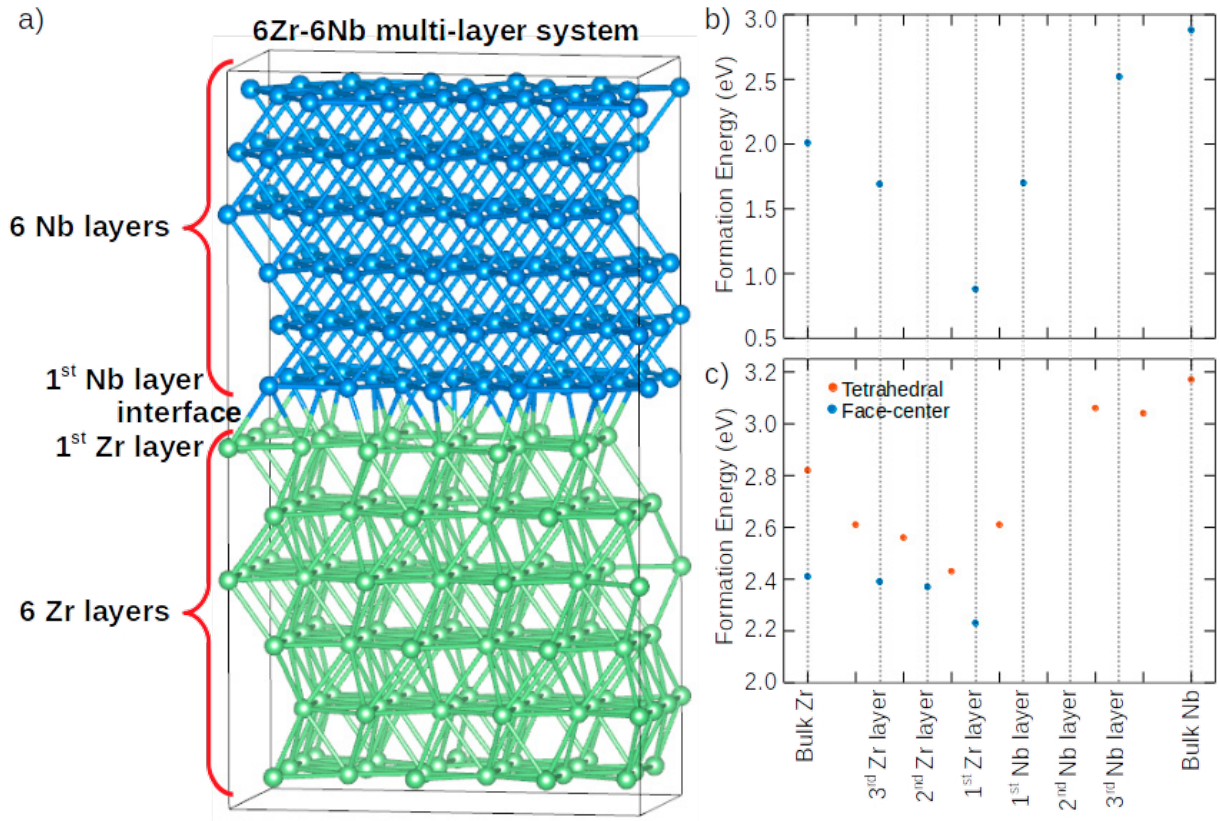
Figure 1.
a) 6Zr-6Nb multilayer system. Formation energy of b) the vacancy, c) He impurity with respect to its position.

System	c11	c12	c44	B (GPa)	G (GPa)	E (GPa)	v	A
bulk Zr	140.8	74.1	28.5	95.2	32.9	88.4	0.345	0.04
bulk Nb	247.2	132.1	27.3	170.4	37.0	103.6	0.399	0.7
6Zr-6Nb	164.1	91.3	17.7	125.5	27.1	75.7	0.400	1.56
2Zr-2Nb	174.1	96.0	12.6	130.3	26.8	75.3	0.404	2.14

Table 1.
Mechanical properties of Zr-Nb multi-layer nanocomposite systems

On-going Research / Outlook

The project is still ongoing and currently we are working on the migration process of He atoms and interstitials within the system. The migration energy barriers depend very much on the migration direction and the distance from the interface.

Conclusion

Mechanical properties and vacancy-helium-interface interactions of Zr-Nb multi-layer systems have been investigated. Phase transformation of Zr from hcp to fcc is observed at 5% of vacancy density. Furthermore, we found that the multi-layer retains most of the mechanical properties from its constituents in bulk form, except for the anisotropy index due to the change in lattice symmetry (it becomes orthorhombic – see Figure 1a). The Zr side of the interface acts as a sink for vacancies with a formation energy of 0.88 eV. When the layers come into contact, they exchange charge at the interface, creating a charge difference between the sides. When helium is at the face-center site of the positively charged 1st Zr layer, the system has its minimum energy with a formation energy of 2.24 eV. When both helium and a vacancy are present in the system, the He atom is positioned within the void of the vacancy.

References

[1] Beyerlein, I. J., A. Caro, M. J. Demkowicz, N. A. Mara, A. Misra, and B. P. Uberuaga. Radiation damage tolerant nanomaterials. Materials Today. 2013, 16(11), 443–449. DOI: 10.1016/j.mattod.2013.10.019.

[2] ONIMUS, F., and J. L. BÉCHADE. Radiation Effects in Zirconium Alloys. Comprehensive Nuclear Materials. Elsevier, 2012, p. 1–31. DOI: 10.1016/B978-0-08-056033-5.00064-1.

[3] CARPENTER, G. J. C, and J. F WATTERS. Vacancy precipitation in zirconium alloys. Acta Metallurgica. 1973, 21(9), 1207–1214. DOI: 10.1016/0001-6160(73)90161-2.

[4] Griffiths. M. A review of microstructure evolution in zirconium alloys during irradiation. Journal of Nuclear Materials. 1988, 159, 190–218. DOI: 10.1016/0022-3115(88)90093-1.

[5] Bloom, E. E. The challenge of developing structural materials for fusion power systems. Journal of Nuclear Materials. 1998, 258-263, 7–17. DOI: 10.1016/S0022-3115(98)00352-3.

[6] Maloy, S., M. James, W. Johnson, T. Byun, K. Farrell, and M. Toloczko. Comparison of fission neutron and proton/spallation neutron irradiation effects on the tensile behavior of type 316 and 304 stainless steel. Journal of Nuclear Materials. 2003, 318, 283-291. DOI: 10.1016/S0022-3115(03)00087-4.

[7] Becquart, C. S., and C. Domain. Migration Energy of He in W Revisited by Ab Initio Calculations. Physical Review Letters. 2006, 97(19). DOI: 10.1103/PhysRevLett.97.196402.

Publications

[8] Defects, Dislocations & hcp-fcc Phase Transition in Zr; Correlation with mechanical properties. (in preparation)

[9] Reaching the theoretical hardness limit in ZrNb nanolayered systems. (in preparation)

[10] H.S. Sen and T. Polcar, Vacancy-interface-helium interaction in Zr-Nb multi-layer system: a first-principles study, submitted to Journal of Nuclear Materials.

LOCAL STRUCTURE OF CATIONIC SITES IN DEHYDRATED ZEOLITES INFERRED FROM ^{27}AL MAGIC-ANGLE SPINNING NMR AND DENSITY FUNCTIONAL THEORY CALCULATIONS. A STUDY ON Li-, Na-, AND K-CHABAZITE

Research institution:
The J. Heyrovsky Institute of Physical Chemistry of the Czech Academy of Sciences

Principal investigator:
Štepán Sklenák

Researchers:
Petr Klein,
Veronika Pashkova,
Haunani M. Thomas,
Sarah R. Whittleton,
Jiří Brus,
Libor Kobera,
Jiří Dědeček

Project ID:
OPEN-8-9

Introduction

Zeolites are crystalline microporous alumosilicates industrially employed as catalysts and sorbents. Their three-dimensional frameworks are made of corner-sharing SiO_4 and AlO_4^- tetrahedra. The isomorphous substitutions of Al atoms into the silicate framework result in the introduction of negative charges of AlO_4^- tetrahedra that are balanced by either protons or extra-framework cationic species (metal cations and metal-oxo cations) which correspond to catalytic and sorption centres. Unique properties of the cationic species together with the variability of microporous channel systems of zeolites are responsible for the fact that zeolites represent a wide and very important group of heterogeneous catalysts [1].

High-resolution ^{27}Al magic-angle spinning (MAS) NMR spectroscopy of dehydrated Li-chabazite, Na-chabazite, and K-chabazite in tandem with density functional theory calculations are employed to study the quadrupolar interaction of ^{27}Al nuclei in dehydrated zeolites and to understand the corresponding high-resolution ^{27}Al MAS NMR spectra. Chabazite is a zeolite with a simple unit cell and serves as a model material to explore high-resolution ^{27}Al MAS NMR spectra of zeolites with more complex unit cells. High-resolution ^{27}Al MAS NMR spectroscopy is widely used to investigate zeolites which are very important heterogenous catalysts [2–4].

Results and Methods

The starting structure of the chabazite framework is generated from the X-ray structure of chabazite. Six models featuring one Al/Si substitution in the framework of the chabazite structure

and one Me^+ (Me^+ = Li^+, Na^+, and K^+) cation compensating the corresponding negative charge of AlO_4^- are employed. Three of the models, designated as Li^+-6-ring, Na^+-6-ring, and K^+-6-ring, feature the Li^+, Na^+, and K^+ cations, respectively, accommodated in the 6-ring while the other three, designated as Li^+-8-ring, Na^+-8-ring, and K^+-8-ring, respectively, are located in the 8-ring. The model includes neither cations nor water molecules, features one Al/Si substitution, and bears a formal charge of −1. It is adopted to calculate the local structure around the AlO_4^- tetrahedra and to predict the ^{27}Al NMR parameters in fully hydrated, cation-containing silicon-rich zeolites. The hybrid DFT method, employing the B3LYP functional was used. Subsequent to the structure determination, we calculated ^{27}Al NMR shielding tensors; nuclear quadrupolar coupling constants, C_Q; and asymmetry parameters, η, for the ^{27}Al atom by the gauge independent atomic orbital method (GIAO) using the B3LYP functional and the pcS basis sets of Jensen. The EFGShield program was employed to extract the C_Q and η values from the Gaussian output files. Moreover, the nuclear quadrupolar coupling product P_Q, which is defined as follows: $P_Q = CQ(1 + \eta^2/3)^{1/2}$, was calculated from the C_Q and η values. These P_Q values can be compared with those obtained from simulations of the measured ^{27}Al MAS NMR spectra.

^{27}Al 3Q MAS NMR spectra of the dehydrated Me-CHA samples were collected to investigate the mechanism of line broadening in dehydrated zeolites. Note that the collection of the ^{27}Al MQ MAS NMR spectrum of an enormously broad signal requires an acquisition time of several days.
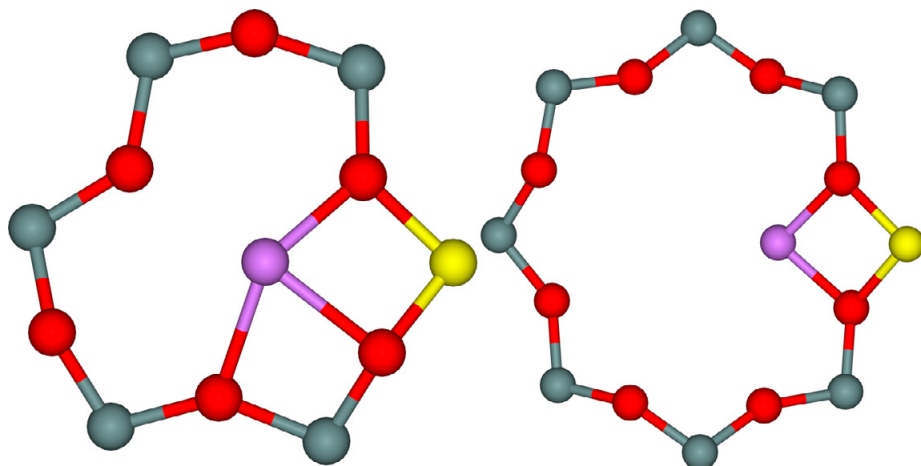
Figure 1.
Optimized structures of the cationic sites of Li+ accommodated in the 6-ring (left) and 8-ring (right). Silicon atoms are in grey, oxygen atoms in red, aluminium atoms in yellow, and lithium atoms in violet.
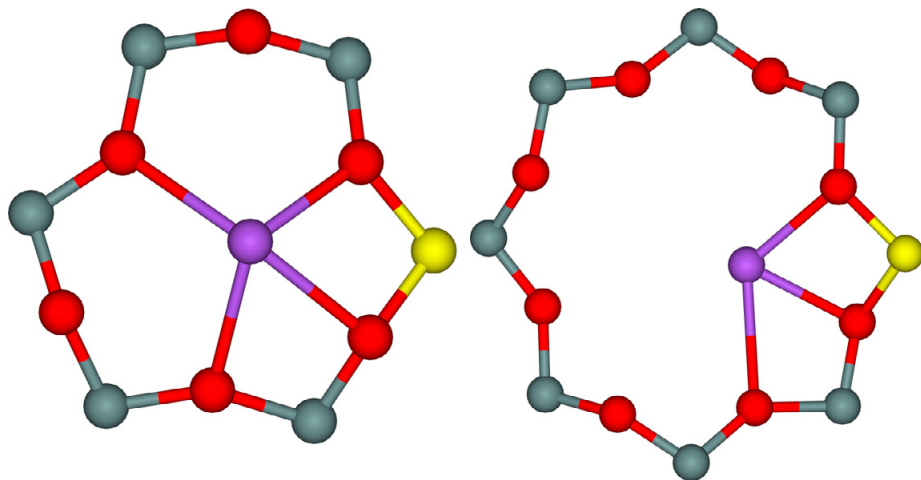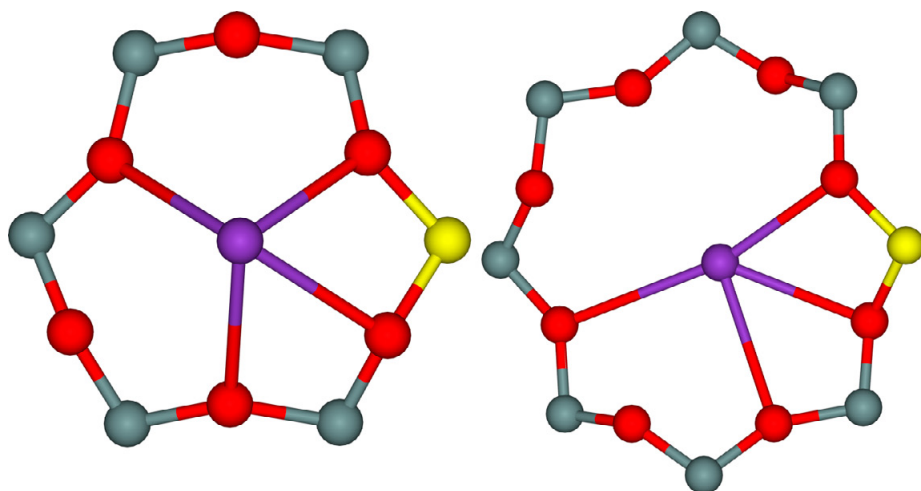

Figure 2.
Optimized structures of the cationic sites of Na+ accommodated in the 6-ring (left) and 8-ring (right). Silicon atoms are in grey, oxygen atoms in red, aluminium atoms in yellow, and sodium atoms in violet.

Figure 3.
Optimized structures of the cationic sites of K+ accommodated in the 6-ring (left) and 8-ring (right). Silicon atoms are in grey, oxygen atoms in red, aluminium atoms in yellow, and potassium atoms in violet.

Local Structure of Cationic Sites in Dehydrated Zeolites
Inferred from ^{27}Al Magic-Angle Spinning NMR and Density
Functional Theory Calculations.
A Study on Li-, Na-, and K-Chabazite

Our calculations of the six models of the cationic sites yielded the optimized structures and the corresponding relative energies of the two cationic sites (Me$^+$ accommodated in 6- and 8-rings), see Figures 1–3.

Our computational results show that all three Me$^+$ cations are coordinated to two O atoms of AlO$_4^-$ tetrahedra for both the sites. Furthermore, there is additional coordination to O atoms of SiO$_4$: one for Li$^+$-6-ring and Na$^+$-8-ring; two for Na$^+$-6-ring, K$^+$- 6-ring, and K$^+$-8-ring. The smaller Li$^+$ and Na$^+$ cations accommodated in the 6-ring are calculated to be more stable by 2 kcal/mol, while the largest K$^+$ cation prefers the 8-ring by 4 kcal/mol.

On-going Research / Outlook

In the future, we will further investigate effects of other cations.

Conclusion

Our study shows that the broadening of the ^{27}Al NMR signal in dehydrated zeolites occurs predominantly because of the deformation of the local structure of AlO$_4^-$ tetrahedra caused by the binding of Me$^+$ to the zeolite framework. This deformation increases with the decreasing diameter of the cations from K$^+$ to Li$^+$. The influence of water in hydrated zeolites is limited only to prevent a strong coordination of the Me$^+$ cation to O atoms of the AlO$_4^-$ tetrahedron, but there is no "averaging" effect concerning the local electrostatic field due to molecular motion of water molecules. Our results show that the ^{27}Al NMR parameters in dehydrated zeolites can be calculated accurately enough to allow the description of the local structure of AlO$_4^-$ tetrahedra in dehydrated zeolites and to infer the local structure of the sites accommodating the extra-framework Me$^+$ cations.

References

[1] Dědeček, J., Z. Sobalík, B. Wichterlová. Catal. Rev. Siting and Distribution of Framework Aluminium Atoms in Silicon-Rich Zeolites and Impact on Catalysis. Catalysis Reviews. 2012, 54(2), 135-223. DOI: 10.1080/01614940.2012.632662.

[2] Sklenák, S., J. Dědeček, C. Li, B. Wichterlová, V. Gábová, M. Sierka, J. Sauer. Aluminum Siting in Silicon-Rich Zeolite Frameworks: A Combined High-Resolution27Al NMR Spectroscopy and Quantum Mechanics/Molecular Mechanics Study of ZSM-5. Angewandte Chemie International Edition. 2007, 46(38), 7286–7289. DOI: 10.1002/anie.200702628.

[3] Sklenák, S., J. Dědeček, C. Li, B. Wichterlová, V. Gábová, M. Sierka, J. Sauer. Aluminium siting in the ZSM-5 framework by combination of high resolution 27Al NMR and DFT/MM calculations. Phys. Chem. Chem. Phys. 2009, 11(8), 1237–1247. DOI: 10.1039/B807755J.

[4] Dědeček, J., M. J. Lucero, C. Li, F. Gao, P. Klein, M. Urbanova, Z. Tvaruzkova, P. Sazama, S. Sklenák. Complex Analysis of the Aluminum Siting in the Framework of Silicon-Rich Zeolites. A Case Study on Ferrierites. The Journal of Physical Chemistry C. 2011, 115(22), 11056–11064. DOI: 10.1021/jp200310b.

Publication

TNU-9 ZEOLITE: ALUMINUM DISTRIBUTION AND EXTRA-FRAMEWORK SITES OF DIVALENT CATIONS

Research institution:

The J. Heyrovsky Institute of Physical Chemistry of the Czech Academy of Sciences

Principal investigator:

Štepán Sklenák

Researchers:

Robert Karcz, Jiří Dědeček, Barbara Supronowicz, Haunani M. Thomas, Petr Klein, Edyta Tabor, Petr Sazama, Veronika Pashkova

Project ID:

OPEN-9-17

Introduction

Periodic DFT calculations were carried out by employing the VASP code. The high-spin electron configuration cobalt d5(up)d2(down) was employed for the Co(II) accommodated in the zeolite. The Kohn–Sham equations were solved variationally in a plane-wave basis set using the projector-augmented wave (PAW) method. The exchange-correlation energy was described by the PW91 generalized gradient approximation (GGA) functional. Brillouin zone sampling was restricted to the Γ point. A plane-wave cut-off of 400eV was utilized for geometry optimizations and a smaller cut-off of 300 eV was used for the molecular dynamics simulations.

The TNU-9 zeolite (TUN framework) is one of the most complex zeolites known. It represents a highly promising matrix for both acid and redox catalytic reactions. We present here a newly developed approach involving the use of ^{29}Si and ^{27}Al (3Q) MAS NMR spectroscopy, Co(II) as probes monitored by UV/Vis and FTIR spectroscopy, and extensive periodic DFT calculations, including molecular dynamics, to investigating the aluminium distribution in the TUN framework and the location of aluminium pairs and divalent cations in extra-framework cationic positions. Unique properties of the cationic species together with the variability of microporous channel systems of zeolites are responsible for the fact that zeolites represent a wide and very important group of heterogeneous catalysts [1–5].
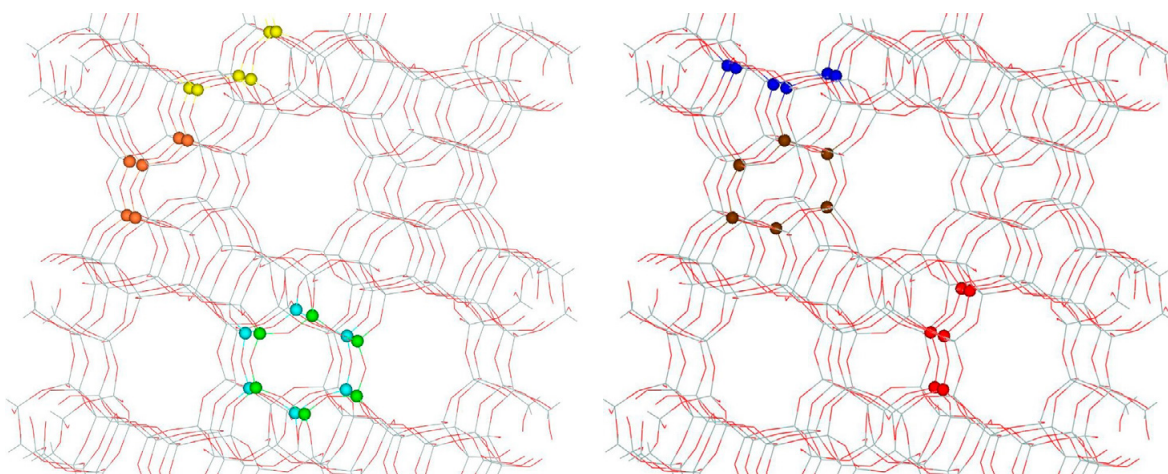

Figure 1.
Locations of the β *cationic site (• top), the* βT5T2T22 *(• top),* βT9T6T4 *(• top),* βT11T4T9 *(• bottom),* βT8T10T11 *(• bottom),* βT14T12T21
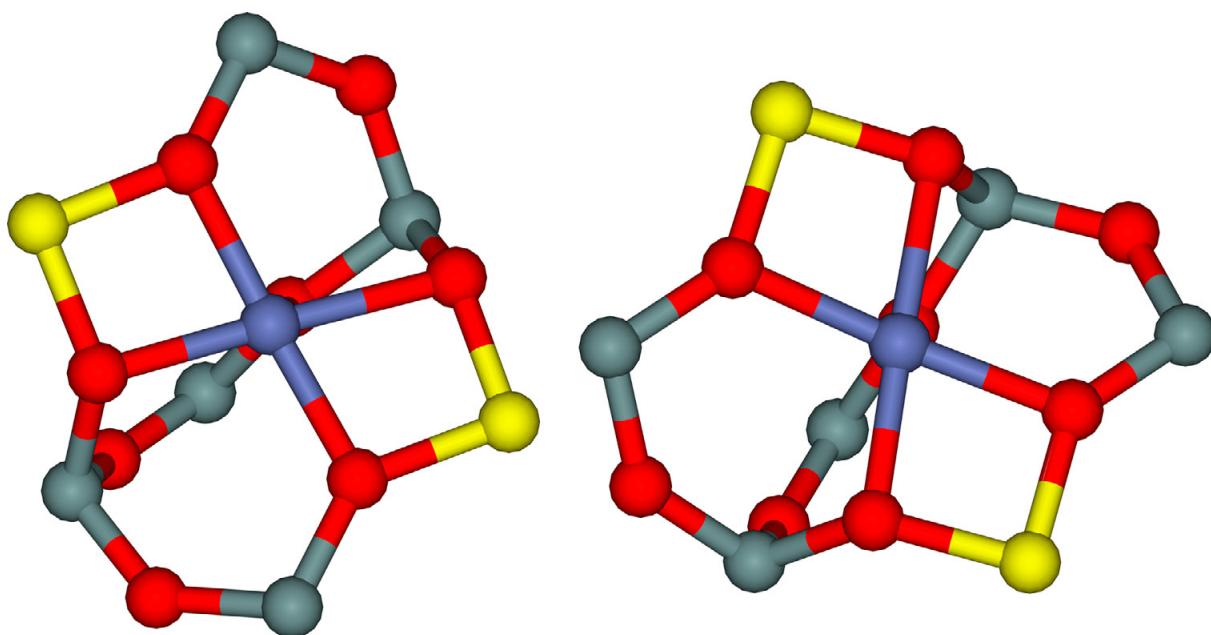*(• top), and* βT23T19T17 *(• bottom) sites in the TUN framework. View along the straight channel.*

Figure 2.
Optimized structures of the α(T4T24) (left) and α(T10T22) (right) models. Silicon atoms are in grey,
oxygen atoms in red, aluminium atoms in yellow, and the cobalt atom in blue.

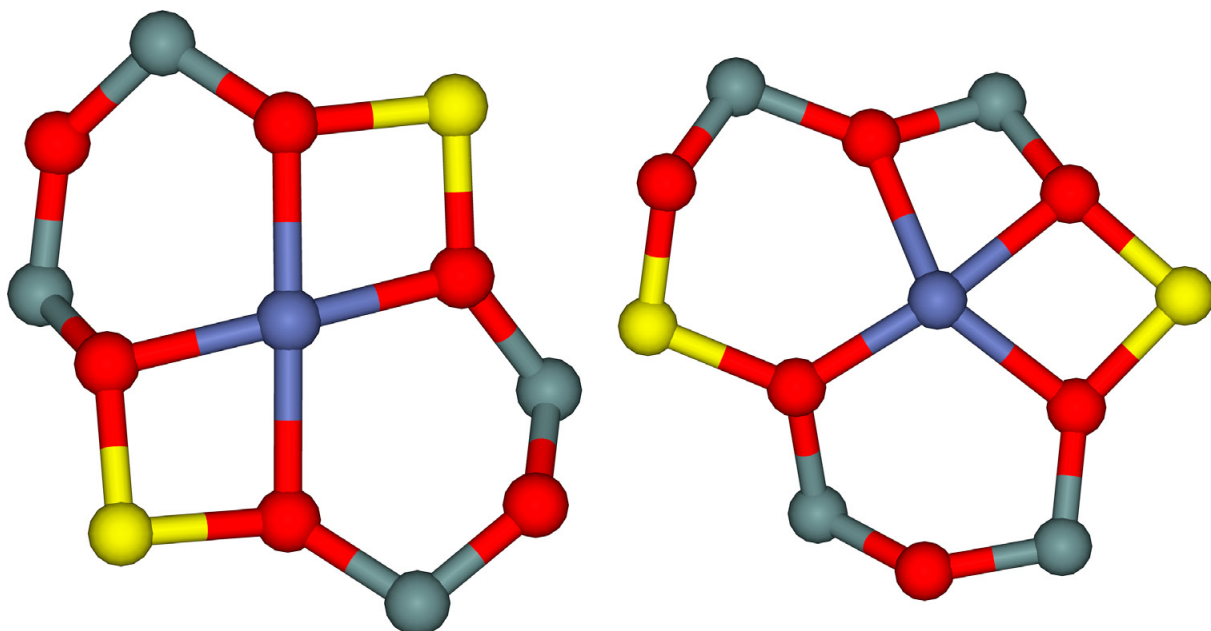Figure 3.
Optimized structures of the best candidate $\beta_{T11T4T9}$(T11T9) (left) and the second-best candidate $\beta_{T8T10T11}$(T11T8) (right)
models. Silicon atoms are in grey, oxygen atoms in red, aluminium atoms in yellow, and the cobalt atom in blue.

Results and Methods

Seventeen models were employed. They feature one unit cell of TUN with two Al/Si substitutions forming the cationic sites accommodating a Co(II).

Only eight models, selected on the basis of our ^{27}Al 3Q MAS NMR experiments, were optimized. The atomic positions were optimized at a constant volume by employing a conjugate-gradient algorithm minimization of energies and forces whereas the lattice parameters were fixed at their experimental values.

The molecular dynamics (MD) simulations were carried out on all 17 models. The time step for the integration of the equations of motion was 1 fs. The simulations were run for 4,000 fs at 400 K. Visual inspection of the structures along the MD trajectories showed that the duration of the MD simulations was long enough because it included both the rearrangements of the local structures of the TUN framework for some cationic sites (up to ca. 1,000 fs) as well as a long period (ca. 3,000 fs) when the system fluctuated around the equilibrium and "snapshots" were collected and optimized.

Our MD calculations of the 17 computational models revealed that the 6-ring forming the α cationic site as well as the six 6-rings creating six possible β cationic sites (Figure 1) with all the possible aluminium sitings in the 6-rings could accommodate bare Co(II).

The MD results showed the proper binding of Co(II) mainly to the oxygen atoms of the AlO_4^- tetrahedra and significant rearrangements of the local structures of the zeolite framework at some cationic sites.

The subsequent optimizations of the two models of the α site and the six selected models of the β sites yielded the structures of Co(II) exchanged in the corresponding cationic sites.

Our MD simulations of the α (T10T22) and α (T4T24) models of the α site as well as the β T11T4T9(T11T9) and β T14T12T21(T14T21) models of the β sites and subsequent optimizations of selected MD snapshots led to energy stabilizations by 5, 5, 11, and 2 kcal mol^{-1}, respectively, relative to the same models that were not relaxed employing MD simulations but simply optimized by using the structure downloaded from the zeolite structural database.

The optimized structures of the α sites and the best and second-best candidates for the β sites are shown in Figures 2 and 3.

On-going Research / Outlook

In the future, we will further attempt to determine the structure of the β site(s), employing additional experimental methods supported by DFT calculations.

Conclusion

Our study reveals that 40 and 60% of aluminium atoms in the TNU-9 zeolite are isolated single aluminium atoms and aluminium pairs, respectively. The aluminium pairs are present in two types of six-membered rings forming the corresponding α and β (15 and 85%, respectively, of aluminium pairs) sites of bare divalent cations. The α site is located on the TUN straight channel wall and it connects two channel intersections. The suggested near-planar β site is present at the channel intersection.

References

[1] Sklenák, Š., P. C. Andrikopoulos, B. Boekfa, et al. N$_2$O decomposition over Fe-zeolites: Structure of the active sites and the origin of the distinct reactivity of Fe-ferrierite, Fe-ZSM-5, and Fe-beta. A combined periodic DFT and multispectral study. Journal of Catalysis. 2010, 272(2), 262–274. DOI: 10.1016/j.jcat.2010.04.008.

[2] Dědeček, J., Z. Sobalík, and B. Wichterlová. Siting and Distribution of Framework Aluminium Atoms in Silicon-Rich Zeolites and Impact on Catalysis. Catalysis Reviews. 2012, 54(2), 135–223. DOI: 10.1080/01614940.2012.632662.

[3] Sklenák, Š., P. C. Andrikopoulos, S. R. Whittleton, et al. Effect of the Al Siting on the Structure of Co(II) and Cu(II) Cationic Sites in Ferrierite. A Periodic DFT Molecular Dynamics and FTIR Study. The Journal of Physical Chemistry C. 2013, 117(8), 3958–3968. DOI: 10.1021/jp310236d.

[4] Sazama, P., E. Tabor, P. Klein, et al. Al-rich beta zeolites. Distribution of Al atoms in the framework and related protonic and metal-ion species. Journal of Catalysis. 2016, 333, 102–114. DOI: 10.1016/j.jcat.2015.10.010.

[5] Mlekodaj, K., J. Dědeček, V. Pashkova, et al. Al Organization in the SSZ-13 Zeolite. Al Distribution and Extraframework Sites of Divalent Cations. The Journal of Physical Chemistry C. 2018. DOI: 10.1021/acs.jpcc.8b07343.

EFFECT OF Ge/Si SUBSTITUTIONS ON THE LOCAL GEOMETRY OF Si FRAMEWORK SITES IN ZEOLITES: A COMBINED HIGH RESOLUTION ^{29}Si MAS NMR AND DFT/MM STUDY ON ZEOLITE BETA POLYMORPH C (BEC)

Research institution:
The J. Heyrovsky Institute of Physical Chemistry of the Czech Academy of Sciences

Principal investigator:
Štěpán Sklenák

Researchers:
Sarah R. Whittleton, Aurelie Vicente, Christian Fernandez, Somayeh F. Rastegar, Anna V. Fishchuk

Project ID:
OPEN-11-8

Introduction

We employed density functional theory/molecular mechanics (DFT/MM) calculations and ^{29}Si magic-angle spinning (MAS) NMR spectroscopy to investigate the effect of single and multiple Ge/Si substitutions on the ^{29}Si NMR parameters as well as the local geometry of SiO_4 tetrahedra of the nearest (Ge-O-Si) and next-nearest (Ge-O-Si-O-Si) neighbouring Si atoms. The influences of the Ge/Si substitutions are compared with the effects of the corresponding Al/Si substitutions (i.e., Al-O-Si and Al-O-Si-O-Si, respectively). Zeolite Beta polymorph C (BEC), containing double four-membered rings (D4Rs) and exhibiting three distinguishable T sites in the framework, was chosen for this study as a model of germanium containing zeolites.

Zeolites are crystalline microporous aluminosilicates made of corner-sharing TO_4 tetrahedra (T = Si, Al$^-$). They are widely used as molecular sieves and catalysts in industrial chemical processes. Germanium can isomorphically substitute silicon in zeolites (i.e., T = Ge). Many zeolitic structures with framework Ge atoms have been obtained (e.g., BEC, FAU, LTA, MFI, MON, NAT, RHO, SOD) [1]. In addition, a large number of new zeolite topologies with pore sizes ranging from 8-rings to 30-rings, all of them containing double four-membered rings (D4Rs) as structural units, have been synthesized using Ge containing gels.
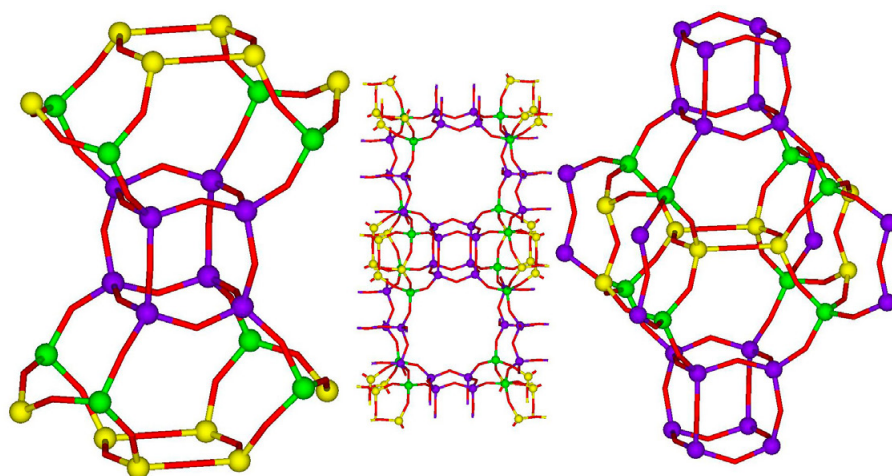

Figure 1.
Structure of the polymorph C beta zeolite. T1 atoms are in violet, T2 atoms in green, T3 atoms in yellow, and oxygen atoms in red.

Results and Methods

Zeolite Beta (BEA) has a three dimensional network of 12-membered ring pores and it is an intergrowth of two polymorphs, A and B. In addition, a polymorph C was also suggested as a hypothetical structure when the structures of polymorphs were solved in 1988 [2]. More than 10 years later, polymorph C (BEC) was prepared in the pure-germanate form (FOS-5) [3], followed by all-silica [4], and germano-silicate forms (ITQ-17) [5, 6]. While polymorphs A and B are the most commonly studied and industrially employed zeolite Beta, BEC is of interest because of its large pore size and linear 12-membered ring channels that intersect along all three crystallographic axes (Figure 1).

A bare zeolite framework model [7–13], which has been successfully employed in previous studies, that includes neither cations nor water molecules is adopted to calculate the local structure around GeO_4, AlO_4^-, and SiO_4 tetrahedra, and to predict the ^{29}Si NMR shieldings. The bare charged framework was found to represent a realistic model to describe the local geometry of AlO_4^- and SiO_4 tetrahedra and predict the ^{27}Al isotropic chemical shifts and the ^{29}Si chemical shifts in aluminosilicates [7–13]. Therefore, we assume that the bare framework model is appropriate to calculate the local structure of GeO_4, AlO_4^-, and SiO_4 tetrahedra and to predict the ^{29}Si NMR shieldings in germanosilicates and germanoaluminosilicates. The DFT method employs the hybrid B3LYP functional. Subsequent to the structure determination, the GIAO NMR method was employed to calculate NMR shielding tensors for the Si atoms of the optimized clusters using the B3LYP functional. The pcS basis sets of Jensen were employed [14].

Our computations give a systematic downshift (Figures 2 and 3) of the ^{29}Si chemical shift of Si by 1–6 ppm and 3–11 ppm for Ge-O-Si and Al-O-Si sequences, respectively.

The majority of the downshifts are 2–3 ppm for Ge and 5–8 ppm for Al. Furthermore, our results reveal that the contributions of two, three, and four Ge atoms as the nearest neighbours to the downshift of Si are not additive, and the calculated downshifts lie in the intervals from 2 to 6 ppm, from 1 to 9 ppm, and from 5 to 11 ppm, respectively. Conversely, the contributions of two, three, and four Al atoms as the nearest neighbours are approximately additive, and the calculated downshifts range from 7 to 18 ppm, from 14 to 23 ppm, and from 20 to 25 ppm, respectively. The downshifts caused by Ge nearest neighbours are less than half compared with the corresponding downshifts caused by Al.

Our calculations show that there is no systematic contribution of T (T = Ge and Al) in T-O-Si-O-Si sequences to the ^{29}Si chemical shift of Si, and not even the direction (sign) of the shift can be predicted without calculating the corresponding sequence. The effect is ± 1 and ± 2 ppm for the majority of the Ge and Al atoms, respectively.

The results of this study provide guidance in interpretations of ^{29}Si MAS NMR spectra of Ge containing zeolites and other Ge containing (alumino)silicate matrixes.
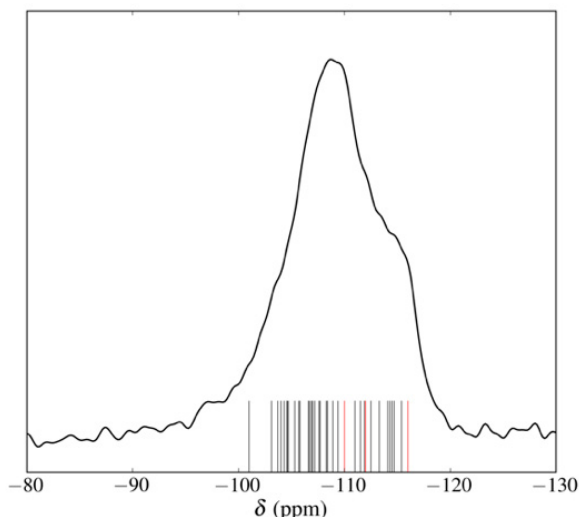

Figure 2.
^{29}Si MAS NMR spectrum
of the BEC-Ge calcined sample with the calculated ^{29}Si
chemical shifts of the Si(T)(4Si,0Ge) atoms (red lines);
Si(T)(3Si,1Ge), Si(T)(2Si,2Ge), Si(T)(1Si,3Ge), and Si(T)
(0Si,4Ge) atoms (black lines) for T = T1, T2, and T3.

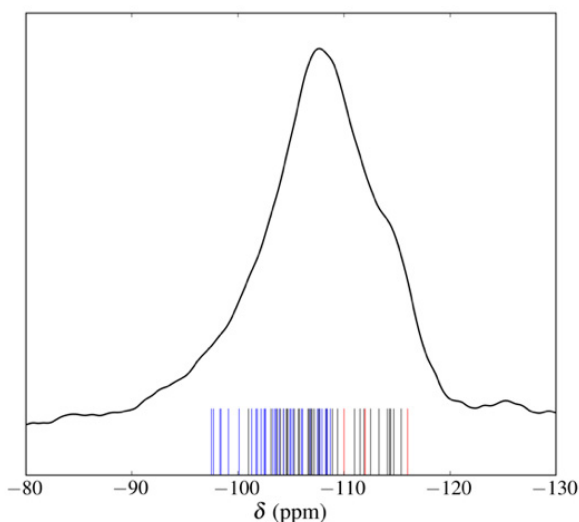*Figure 3.*
^{29}Si MAS NMR spectrum the of the BEC-Ge/Al
calcined sample with the calculated ^{29}Si chemical
shifts of the Si(T)(4Si,0Ge,0Al) atoms (red lines); Si(T)
(3Si,1Ge,0Al), Si(T)(2Si,2Ge,0Al) and Si(T)(1Si,3Ge,0Al)
atoms (black lines); Si(T)(3Si,0Ge,1Al) and Si(T)
(2Si,1Ge,1Al) atoms (blue lines) for T = T1, T2, and T3.

Effect of Ge/Si Substitutions on the Local Geometry of Si
Framework Sites in Zeolites: A Combined High Resolution ^{29}Si
MAS NMR and DFT/MM Study on Zeolite Beta Polymorph

On-going Research / Outlook

In the future, we will further investigate the effects of other hetero T atoms in the zeolite framework on the ^{29}Si chemical shift of nearest neighbours and next-nearest neighbours.

Conclusion

Our computations give a systematic downshift of the ^{29}Si chemical shift of Si by 1–6 ppm for Ge-O-Si sequences. Furthermore, the contributions of two, three, and four Ge atoms as the nearest neighbours to the downshift of Si are not additive, and the calculated downshifts lie in the intervals from 2 to 6 ppm, from 1 to 9 ppm, and from 5 to 11 ppm, respectively. Conversely, the contributions of two, three, and four Al atoms as the nearest neighbours are approximately additive. The downshifts caused by Ge nearest neighbours are less than half compared with the corresponding downshifts caused by Al. Moreover, our calculations show that there are no systematic contributions of Ge and Al as next-nearest neighbours (i.e., Ge-O-Si-O-Si and Al-O-Si-O-Si, respectively) to the ^{29}Si chemical shift of Si, and not even the direction (sign) can be predicted without calculating the corresponding sequence.

References

[1] Database of Zeolite Structures. http://www.iza-structure.org/databases/ (accessed January 31, 2019).

[2] Newsam J. M., M. M. J. Treacy, W. T. Koetsier, C. B. Degruyter, Structural Characterization of Zeolite-Beta, Proceedings of the Royal Society of London Series a-Mathematical Physical and Engineering Sciences. 1988, 420(1859), 375–405. DOI: 10.1098/rspa.1988.0131.

[3] Conradsson T., M. S. Dadachov, X. D. Zou. Synthesis and Structure of (Me$_3$N)$_6$[Ge$_{32}$O$_{64}$].(H$_2$O)$_{4.5}$, a Thermally Stable Novel Zeotype with 3D Interconnected 12-ring Channels. Microporous and Mesoporous Materials. 2000, 41(1-3), 183–191. DOI: 10.1016/s1387-1811(00)00288-2.

[4] Liu Z., T. Ohsuna, O. Terasaki, M. A. Camblor, M. J. Diaz-Cabanas, K. Hiraga. The First Zeolite with Three-Dimensional Intersecting Straight-Channel System of 12-Membered Rings. Journal of the American Chemical Society. 2001, 123(22), 5370–5371. DOI: 10.1021/ja0107778.

[5] Corma A., M. T. Navarro, F. Rey, J. Rius, S. Valencia, Pure Polymorph C of Zeolite Beta Synthesized by Using Framework Isomorphous Substitution as a Structure-Directing Mechanism. Angewandte Chemie-International Edition. 2001, 40(12), 2277–2280. DOI: 10.1002/1521-3773(20010618)40:12<2277:: Aid-anie2277>3.0.Co;2-o.

[6] Corma A., M. T. Navarro, F. Rey, S. Valencia, Synthesis of Pure Polymorph C of Beta Zeolite in a Fluoride-Free System, Chemical Communications. 2001, 1486–1487. DOI: 10.1039/b104114m.

[7] Sklenák, S., J. Dědeček, C. Li, B. Wichterlová, V. Gábová, M. Sierka, J. Sauer. Aluminum Siting in Silicon-Rich Zeolite Frameworks: A Combined High-Resolution–^{27}Al NMR Spectroscopy and Quantum Mechanics/Molecular Mechanics Study of ZSM-5. Angewandte Chemie International Edition. 2007, 46(38), 7286–7289. DOI: 10.1002/anie.200702628.

[8] Sklenák, Š., J. Dědeček, C. Li, F. Gao, B. Jansang, B. Boekfa, B. Wichterlová, and J. Sauer. Aluminum Siting in the ZSM-22 and Theta-1 Zeolites Revisited: A QM/MM Study. Collection of Czechoslovak Chemical Communications. 2008, 73(6-7), 909–920. DOI: 10.1135/cccc20080909.

[9] Sklenák, Š., J. Dědeček, C. Li, B. Wichterlová, V. Gábová, M. Sierka, and J. Sauer. Aluminium siting in the ZSM-5 framework by combination of high resolution 27Al NMR and DFT/MM calculations. Phys. Chem. Chem. Phys. 2009, 11(8), 1237–1247. DOI: 10.1039/B807755J.

[10] Dědeček, J., Š. Sklenák, C. Li, F. Gao, J. Brus, Q. J. Zhu, T. Tatsumi. Effect of Al/Si Substitutions and Silanol Nests on the Local Geometry of Si and Al Framework Sites in Silicone-Rich Zeolites: A Combined High Resolution ^{27}Al and ^{29}Si NMR and Density Functional Theory/Molecular Mechanics Study. The Journal of Physical Chemistry C. 2009, 113(32), 14454-14466. DOI: 10.1021/jp9042232

[11] Dědeček, J., Š. Sklenák, C. Li, B. Wichterlová, V. Gábová, J. Brus, M. Sierka, and J. Sauer. Effect of Al–Si–Al and Al–Si–Si–Al Pairs in the ZSM-5 Zeolite Framework on the ^{27}Al NMR Spectra. A Combined High-Resolution ^{27}Al NMR and DFT/MM Study. The Journal of Physical Chemistry C. 2009, 113(4), 1447–1458. DOI: 10.1021/jp8068333.

[12] Dědeček, J., M. J. Lucero, C. Li, F. Gao, P. Klein, M. Urbanova, Z. Tvaruzkova, P. Sazama, S. Sklenák. Complex Analysis of the Aluminum Siting in the Framework of Silicon-Rich Zeolites. A Case Study on Ferrierites. The Journal of Physical Chemistry C. 2011, 115(22), 11056–11064. DOI: 10.1021/jp200310b.

[13] Klein, P., V. Pashkova, H. M. Thomas, S. R. Whittleton, J. Brus, L. Kobera, J. Dědeček, S. Sklenák. Local Structure of Cationic Sites in Dehydrated Zeolites Inferred from ^{27}Al Magic-Angle Spinning NMR and Density Functional Theory Calculations. A Study on Li-, Na-, and K-Chabazite. The Journal of Physical Chemistry C. 2016, 120(26), 14216–14225. DOI: 10.1021/acs.jpcc.6b04391.

[14] F. Jensen, Basis set convergence of nuclear magnetic shielding constants calculated by density functional methods, The Journal of Chemical Theory and Computation. 2008, 4(5), 719–727. DOI: 10.1021/ct800013z.

Publication

THERMODYNAMIC STABILITY AND ELASTIC PROPERTIES OF Fe-Al-BASED SUPERALLOYS

Research institution:
CEITEC – Central European Institute of Technology, Masaryk University

Principal investigator:
Mojmír Šob

Researchers:
Martin Friák, Petr Šesták, Petr Řehák, Miroslav Černý, Monika Všianská, Jana Pavlů, Ivana Miháliková, Anton Slávik, Martina Mazalová, Vojtěch Kopecký, Nikola Koutná

Project partners:
The Institute of Physics of Materials of the Czech Academy of Sciences, Brno University of Technology

Project ID:
OPEN-10-21

Introduction

Our modern highly industrialized society increasingly requires new structural materials for high-temperature applications in automotive and energy-producing industrial sectors. These new materials will allow (i) for higher operational temperatures in energy-conversion units, and, consequently, (ii) for a higher efficiency, resulting in significant energy savings and lower emissions. Such major advancements will not be possible without a deeper fundamental understanding of structure-property relations spanning from atomistic to microstructural levels. Fe-Al-based superalloys represent a very promising class of materials which can potentially replace expensive Ni-based superalloys used as materials for, e.g. turbine blades in aircraft engines operating at high-temperatures and under high-pressures. To design new Fe-Al-based alloys, a challenging materials-design approach should be adopted to identify suitable combinations of alloying elements.

Results and Methods

Methods

During the last two decades, theoretical calculations regarding atomic configuration and properties of advanced materials became possible using ab initio electronic structure calculations, i.e. fundamental quantum theory (the Schrödinger equation). Here the atomic numbers of constituent atoms and some structural information are employed as the only input data. Such calculations are routinely performed within the framework of the density functional theory in which the complicated many-body interaction of all electrons is replaced by an equivalent but simpler problem of a single electron moving in an effective potential. For a given material, the calculated total energies are used to obtain equilibrium lattice parameters, elastic moduli, relative stabilities of competing crystal structures, energies associated with point and planar defects, alloy heats of formations, etc. In addition, we also obtain information about electronic densities of states and charge densities, which enables us to attain a deeper insight into the structure of matter and interatomic interactions. For internal interfaces and other defects, these calculations are computationally very demanding.

In particular, the disordered phase in Fe-Al superalloys, which is without any long-range periodicity in the distribution of atoms, is very difficult to model using computational codes with periodic boundary conditions (the vast majority of available codes). Therefore, so-called special quasi-random distribution of atoms is needed to simulate the disordered phase, but it is characterized by a higher number of atoms in the computational cell. In the case of our planned calculations of interfaces between the disordered phase and ordered phases, the supercells modelling the interface between the two phases must be indeed very large for the following two reasons. First, the disorder must be present also within the interface plane and this requirement results in the necessity to use a supercell with many atoms within the interface plane. Second, the interfaces, which are periodically repeated infinitely many times by the periodic boundary conditions also in the direction perpendicular to the interface plane, must be separated by a sufficient number of atomic planes so that any interactions between the images are negligible. This requires the use of supercells with many atomic planes also in the direction perpendicular to the computed interface.

Results

We performed an ab initio and atomistic study of the stress-strain response and elastic stability of the ordered Fe_3Al compound with the $D0_3$ structure and a disordered Fe-Al solid solution with 18.75 at.% Al as well as of a nanocomposite consisting of an equal molar amount of both phases under uniaxial loading along the [001] direction. The tensile tests were performed under complex conditions including the effect of lateral stress on the tensile strength and temperature effect. By comparing the behaviour of individual phases with that of the nanocomposite we find that the disordered Fe-Al phase represents the weakest point of the studied nanocomposite in terms of tensile loading. The cleavage plane of the whole nanocomposite is identical to that identified when loading is applied solely to the disordered Fe-Al phase. It also turns out that the mechanical stability is strongly affected by softening of elastic constants C' and/or C_{66} and by corresponding elastic instabilities. Interestingly, we found that uniaxial straining of the ordered Fe_3Al with the $D0_3$ structure leads almost to hydrostatic loading. Furthermore, increasing lateral stress linearly increases the tensile strength. This was also confirmed by molecular dynamics simulations employing Embedded Atom Method (EAM) potential. The molecular dynamics simulations also revealed that the thermal vibrations significantly decrease the tensile strength.

As seen in Figure 1, both Fe_3Al compound and Fe-Al nanocomposite have qualitatively the same type of elastic anisotropy with the <111> directions being the hard ones while the <001> are the soft ones. Elastic anisotropy of the disordered Fe-Al solid solution with 18.75 at.% Al is less pronounced.

A detailed examination of the calculated stress-strain curves and of corresponding structure configurations reveals that Fe_3Al phase does not exhibit any abrupt drop and therefore there is no fracture around the maximum of the stress. On the other hand, the nanocomposite subjected to uniaxial deformation fails due to fracture (there is an abrupt drop in stress). Fracture is located at the cleavage plane with the lowest cleavage stress. This conclusion was confirmed when examining the structure at each strain increment and it has been found that the fracture appears in the disordered phase as it is marked in Figure 2. The location of the plane with the lowest cleavage stress is highlighted by the red colour. Therefore, the disordered phase represents the weakest part of the studied nanocomposite in terms of tensile loading.

Detailed description of all results obtained may be found it the paper [5].

On-going Research / Outlook

There are several very challenging aspects related to the existing Fe-Al-based superalloys, as well as the development of new ones, which we study now and which we want to study in the future. One of the most important problems concerns the effect of different transition-metal solutes or impurities on the thermodynamic stability of Fe-Al-based superalloys. Here we investigated the effect of Ti and Co additives in papers [6–10]. We systematically tested various mechanisms that could explain the exceptionally low magnetic moment measured for a Heusler compound Fe_2AlTi. For the stoichiometric case, none of the mechanisms studied (i.e., trigonal and tetragonal strains, and finite-temperature spin excitations) could account for this effect. Considering Fe-rich and Ti-rich off-stoichiometric configurations with an excess of 6.25 at. % of Fe or Ti atoms, the net magnetization drops to very low values. In the case of Fe_2AlTi, off-stoichiometric alloys with excess Fe are more relevant because the experimental Fe-Al-Ti phase diagram contains only Fe-rich phases above 800°C. For the Fe-rich alloy, the energetically preferred state has a net magnetic moment close to the measured one. Our study demonstrates how sensitively magnetism is affected by off-stoichiometries in the alloy composition. Even relatively small changes of a few percent can cause changes of an order of magnitude in magnetic moments. Therefore, a mandatory requirement when comparing ab initio computed moments with experimental values is to critically assess the stoichiometry of the experimental samples.

We have also used quantum-mechanical calculations to study material properties of four different polymorphs of Fe_2AlCo. Two of them were the full and inverse Heusler structures, but we have also simulated two other structural variants with a very specific distribution of atoms where Co atoms have on average 3 Fe and 3 Co atoms in their second nearest neighbour shell. This atomic arrangement, which does not appear in either the full Heusler or inverse Heusler structure, was suggested by Grover et al. [4] based on their X-ray and Moessbauer data. The lowest formation energy (and thus the highest thermodynamic stability) turns out to be indeed predicted for one of these two polymorphs with this special arrangement of atoms, in particular for that which has one sublattice (occupied only by Fe and Co atoms) as in the inverse Heusler structure. Due to the fact that this thermodynamic preference is based on very small energy differences (only 9 and 37 meV/atom with respect to the lowest-energy polymorph), we predict the occurrence of structural multiplicity at elevated temperatures, in particular chemical disorder at different sublattices, which is indeed seen is experiments. Next, having the results for all four studied polymorphs, we could conclude that the total magnetic moment is clearly correlated with the volume, the states are ferromagnetic in their nature but the local magnetic moments of Fe and Co atoms within different polymorphs can become very complex, and sensitively depend on the chemical composition of the first and second nearest neighbour coordination shells. Lastly, when evaluating the mechanical stability by computing anisotropic single-crystal elastic stiffnesses, we have found that there is a link between thermodynamic and mechanical stability. Thermodynamically more stable compounds tend to have higher value of the bulk modulus and, for example, the full Heusler polymorph of Fe_2AlCo is not mechanically stable with respect to the tetragonal transformation (Bain's path). Further studies, both experimental and theoretical, of this interesting issue would be very desirable.

Conclusion

By comparing the behaviour of individual phases with that of the nanocomposite we find that the disordered Fe-Al phase represents the weakest point of the studied nanocomposite in terms of tensile loading. The cleavage plane of the whole nanocomposite is identical to that identified when loading solely the disordered Fe-Al phase. It also turns out that the strength of the Fe_3Al compound strongly depends on triaxiality of the loading state, i.e., increasing of the lateral stresses significantly increases the tensile strength. This dependence has a linear character and therefore it can be described via a simple formula. For the Fe-Al-based materials studied here, its slope is higher than that of a perfect Fe crystal in the corresponding direction and completely different when compared to a perfect Al crystal. Therefore, the strain response of the Fe-Al alloy and of a nanocomposite cannot be predicted on the basis of the knowledge of the strain response of Fe or Al. Next, we also conclude that there is no brittle-type fracture for uniaxial loading, and the nanocomposite transforms rather continuously and diffusionlessly into a face-centred cubic-like structure, although it fails due to fracture under uniaxial deformation. Finally, our atomistic Embedded Atom Method (EAM) simulations show that temperature significantly affects the mechanical properties compared to those obtained from quasi-static simulations. For example, at room temperature (approx. 300K) the strength decreases to as low as 75% of the zero-Kelvin static lattice value.
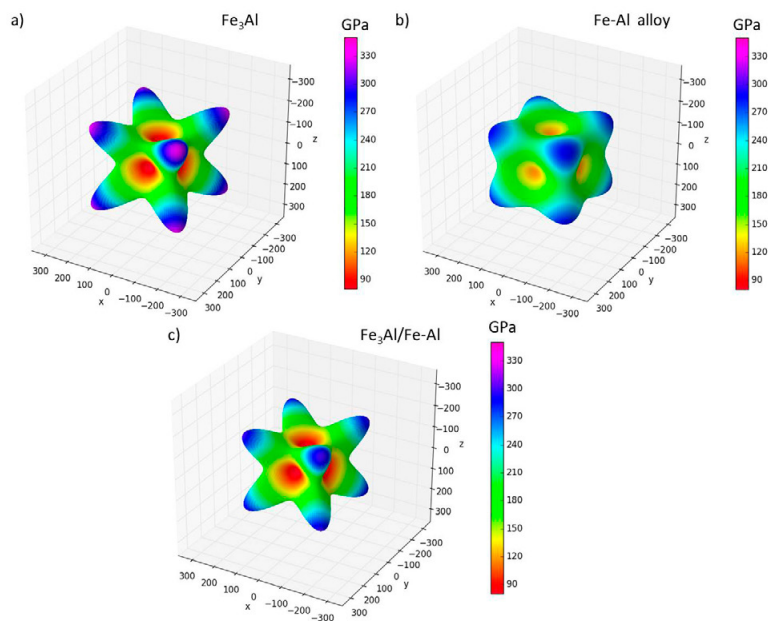

Figure 1.
Directional dependencies of Young's modulus of the ground-state configuration of Fe_3Al compound (a); disordered Fe-Al (b) and the nanocomposite consisting of these two phases (c). All three dependencies were visualized using the SC-EMA software package (freely available at the web page scema.mpie.de) [1-3].
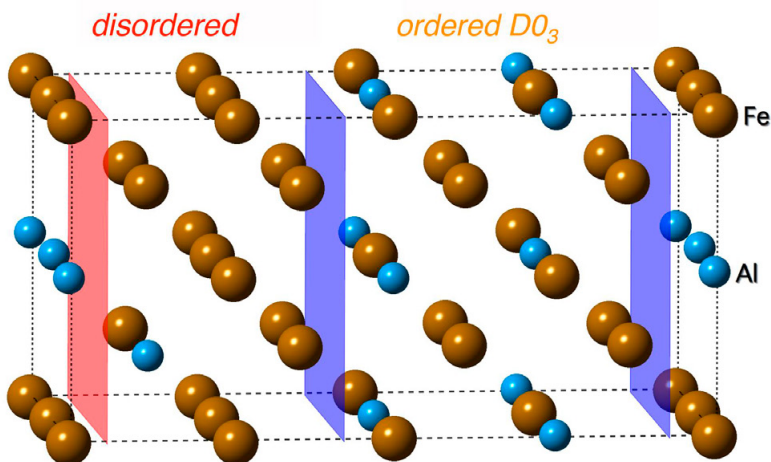

Figure 2.
The location of the cleavage plane in the nanocomposite highlighted by the red plane. The blue planes mark the interfaces between $D0_3$ and disordered phases.

References

[1] Titrian, H., U. Aydin, M. Friák, D. Ma, D. Raabe, J. Neugebauer, J. Self-consistent Scale-bridging Approach to Compute the Elasticity of Multi-phase Polycrystalline Materials. MRS Proceedings. 2013, 1524. DOI: 10.1557/opl.2013.41.

[2] Friák, M., W. A. Counts, D. Ma, B. Sander, D. Holec, D. Raabe, J. Neugebauer. J. Theory-Guided Materials Design of Multi-Phase Ti-Nb Alloys with Bone-Matching Elastic Properties. Materials. 2012, 5(10), 1853–1872. DOI: 10.3390/ma5101853.

[3] Zhu, L.-F., M. Friák, L. Lymperakis, et al. Ab initio study of single-crystalline and polycrystalline elastic properties of Mg-substituted calcite crystals. Journal of the Mechanical Behavior of Biomedical Materials. 2013, 20, 296–304. DOI: 10.1016/j.jmbbm.2013.01.030.

[4] Grover, A. K., R. G. Pillay, V. Nagarajan, P. N. Tandon. Site preference and local environment effects in ferromagnetic ternary alloys. Journal of Magnetism and Magnetic Materials. 1980, 15–18, 699–700. DOI: 10.1016/0304-8853(80)90727-1.

Publications

[5] Šesták, P., M. Friák, D. Holec, M. Všianská, M. Šob. Strength and Brittleness of Interfaces in Fe-Al Superalloy Nanocomposites under Multiaxial Loading: An ab initio and Atomistic Study. Nanomaterials. 2018, 8(11), 873. DOI: 10.3390/nano8110873

[6] Friák, M., A. Slávik, I. Miháliková, D. Holec, M. Všianská, M. Šob, M. Palm, J. Neugebauer. Origin of the low magnetic moment in Fe_2AlTi: An ab initio study. Materials. 2018, 11(9), 1732. DOI: 10.3390/ma11091732.

[7] Friák, M. S. Oweisová, J. Pavlů, D. Holec, M. Šob. An ab initio study of thermodynamic and mechanical stability of Heusler-based Fe_2AlCo polymorphs. Materials. 2018, 11(9). DOI: 10.3390/ma11091543.

[8] Slávik, A., I. Miháliková, M. Friák, M. Všianská, M. Šob. Quantum-mechanical study of magnetic properties of superalloy nanocomposite phase Fe_2AlTi. In Proceedings of the NANOCON 2017 Conference (9th International Conference on Nanomaterials—Research & Application, Brno, Czech Republic, 18–20 October 2017); Tanger Ltd.: Ostrava, Czech Republic, 2018; p. 63–68.

[9] Miháliková, I., M. Friák, A. Slávik, M. Všianská, N. Koutná, D. Holec, M. Šob. First-principles study of interface energies in Fe-Al-based superalloy nanocomposites. In Proceedings of the NANOCON 2017 Conference (9th International Conference on Nanomaterials—Research & Application, Brno, Czech Republic, 18–20 October 2017); Tanger Ltd.: Ostrava, Czech Republic, 2018; p. 69–74.

[10] Miháliková, I., M. Friák, N. Koutná, M. Šob. Magnetic and electronic properties of phases appearing in Fe-Al superalloys: A ab initio study. In Proceedings of the NANOCON 2018 Conference (10th International Conference on Nanomaterials—Research & Application, Brno, Czech Republic, 17–19 October 2018); Tanger Ltd.: Ostrava, Czech Republic, submitted.

Acknowledgement

COMPUTER SIMULATION OF MARTENSITIC TRANSFORMATIONS IN MAGNETIC SHAPE MEMORY ALLOYS

Research institution:
Charles University

Principal investigators:
Martin Zelený,
Jan Zemen

Researchers:
Martin Heczko,
Ladislav Straka,
Oleg Heczko

Project partners:
The Institute of
Physics of the Czech
Academy
of Sciences;
NETME Centre,
Brno University
of Technology

Project IDs:
OPEN-8-28,
OPEN-10-33,
OPEN-11-41

Introduction

Much scientific attention has been paid to Ni-Mn-Ga magnetic shape memory alloys (MSMA) for their engineering potential in sensors, actuators, vibration dampers or other applications [1]. These alloys exhibit interesting properties such as giant magnetic field-induced strain (MFIS), which occurs through the rearrangement of martensite twins in an applied external magnetic field [2]. In comparison with ordinary magnetostrictive materials, MSMAs exposed to an external magnetic field exhibit up to 100 times larger strain [3]. The twin rearrangement takes place via twin boundary motion.

The mobility of twin boundaries primarily depends on martensite structure. While at elevated temperature there is a single austenitic phase derived from stoichiometric Ni_2MnGa with a cubic $L2_1$ structure, various low-temperature martensitic phases occur depending on exact composition [4]. Martensitic phases with orthorhombic or monoclinic structures exhibit modulation of (110) planes in the $[1\bar{1}0]$ direction with a periodicity of ten or fourteen lattice planes (10M or 14M). The third martensitic phase with nonmodulated (NM) tetragonally distorted $L2_1$ structure is typical given large deviations from Ni_2MnGa stoichiometry. In contrast with 10M and 14M martensites with a reported MFIS of 6% or 10%, respectively, MFIS has never been observed in an NM phase.

Understanding the physical mechanisms behind the martensitic transformation and the stability of martensite structures are key issues for magnetic shape memory effect. To gain deeper insight we perform a series of ab initio calculations which reveal the thermodynamic stability of different martensitic phases as well as describe the kinetics of martensitic transformations represented by the energy barrier along transformation paths.

Results and Methods

Using the idea of nanotwinning [6], all known Ni-Mn-Ga martensitic structures can be constructed from monoclinic structures with an alternating sequence of nanotwins comprising of NM structure twinned on (101) lattice planes. A structure with a width of five lattice planes in one orientation and a width of two planes in the other orientation (denoted as $(5\bar{2})_2$) describes the 14M structure. Similarly, the 10M structure can be considered as alternating nanotwins with a width of three and two lattice planes (denoted as $(3\bar{2})_2$). The existence of nanotwins made up of two (101) lattice planes in both 14M and 10M structures indicates that this nanotwin double layer could be the prominent building block of modulated structure. This assumption has been confirmed by our calculations as there is a significant decrease of total energy due to relaxation of Mn and Ga atoms at the nanotwin boundaries within the double layer. Moreover, the $(2\bar{2})_1$ structure consisting solely of oppositely oriented nanotwin double layers, denoted as 4O, exhibits the lowest total energy between all martensitic structures including NM martensite. This newly predicted structure has orthorhombic symmetry with a modulation periodicity of four lattice planes. We propose it to be a new ground state of stoichiometric Ni_2MnGa [11] but so far there is no experimental evidence. However, local sequences of two oppositely oriented double layers, i.e. $(...3\bar{2}3\bar{2}\bar{2}3\bar{2}3...)$ were suggested to occur in 10M martensite forming *a/b* twin boundaries at the mesoscopic scale [12].

Further we investigated the martensitic transformation paths between austenite and other low-symmetry structures of martensite to predict which phase is the most probable to appear. In stoichiometric alloy the transformation paths from austenite to the 4O, 14M or NM martensites exhibit energy barriers, whereas there is no barrier along the transformation paths to 10M martensite (see Figure 1). Therefore the transformation into 10M is always preferred [13]. On the other hand, in off-stoichiometric alloys no barrier was found between austenite and NM martensite. Increasing the concentration of Mn instead of Ga also further stabilizes NM martensite with respect to austenite and modulated martensites.

All ab initio calculations in this work were performed using the Vienna Ab initio Simulation Package (VASP) [7], in which the electron-ion interaction was described by projector augmented-wave potentials [8]. While searching for the minimum energy path between the austenite and martensites, the path was linearly interpolated to ten images and each image was relaxed by the G-SSNEB [9] procedure with respect to the pathway described by the reaction coordinate (RC).

On-going Research / Outlook

The martensitic transformation is associated with characteristic changes in the electronic structure described by the density of states (DOS) [10]. Magneto-optical spectroscopy can serve as a probe of the electronic and magnetic structure in systems with sufficient spin-orbit coupling such as Ni-Mn-Ga. The spectral dependence of the MO Kerr effect is highly sensitive to the induced strain of the lattice and its crystallographic orientation. It provides an indirect view of the DOS. On-going research is focused on ab initio simulations of the ground state electronic structure followed by a linear response calculation of the frequency dependent dielectric tensor. Kerr rotation and Kerr ellipticity are derived from the

off-diagonal elements of the dielectric tensor. We will compare the results for a range of c/a ratios (modelling the transition from austenite to non-modulated martensite), a range of concentrations in off-stoichiometric alloys, and alloys doped by Fe, Co, and Cu. Comparison of these results with the measured MO spectra allows us to track the changes in DOS upon transformation. This will significantly contribute to the fundamental understanding of the martensitic transformation and its link to electronic structure.

Conclusion

Our theoretical findings obtained with help of ab initio calculations demonstrate that the kinetics of the martensitic transformation in Ni-Mn-Ga alloy, represented by the energy barrier along the transformation path, is decisive for the selection of the particular low-symmetry structure of martensite. In further research we will study changes in electronic structure caused by martensitic transformation in off-stoichiometric and doped alloys. For this task we will employ theoretical simulation and experimental measurements of magneto-optical spectra. By combining experimental and theoretical approaches we expect to obtain a deeper understanding of the nature of martensitic transformation in Heusler alloys.
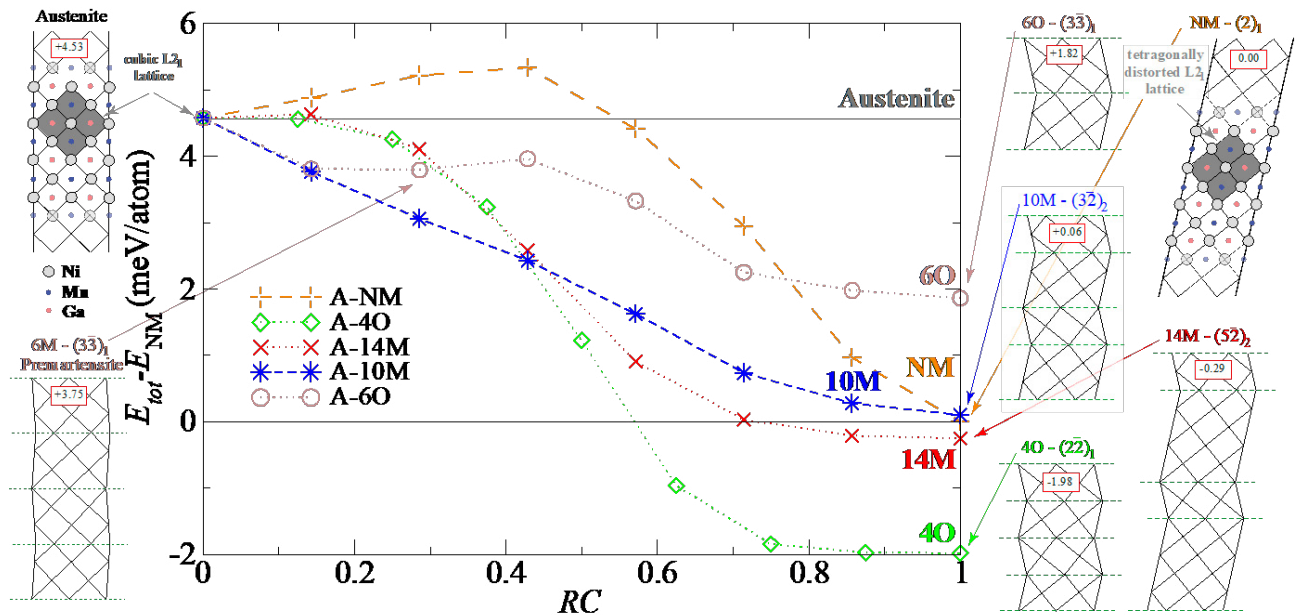

Figure 1.
Calculated minimum energy path of Ni$_2$MnGa along the reaction coordinate RC for the transformation starting from austenite to fully transformed martensite and schematic illustration of the austenite, premartensite 6M and martensite structures: 6O, NM, 10M, 14M, and 4O. Solid grey in the austenite and NM identify the original and tetragonally distorted L2$_1$ cell; the green dashed lines mark nanotwin boundaries; numbers in red boxes correspond to total energy differences in meV/atom. All energies are relative to the total energy of NM martensite. Adapted from [13].

References

[1] Aaltio, I., A. Sozinov, Y. Ge, K. Ullakko, V. K. Lindroos, and S.-P. Hannula. Giant Magnetostrictive Materials. Reference Module in Materials Science and Materials Engineering. Elsevier, 2016, p. 1–14. DOI: 10.1016/B978-0-12-803581-8.01830-0.

[2] Ullakko, K., J. K. Huang, C. Kantner, and R. C. O'Handley. Large magnetic-field- induced strains in Ni_2MnGa single crystals. Applied Physics Letters. 1996, 69(13), 1966–1968. DOI: 10.1063/1.117637.

[3] Madden, J. D. W., N. A. Vandesteeg, P. A. Anquetil, et al. Artificial muscle technology: physical principles and naval prospects. IEEE Journal of Oceanic Engineering. 2004, 29(3), 706–728. DOI: 10.1109/JOE.2004.833135.

[4] Straka, L., A. Sozinov, J. Drahokoupil, V. Kopecký, H. Hänninen, and O. Heczko. Effect of intermartensite transformation on twinning stress in Ni-Mn-Ga 10M martensite. Journal of Applied Physics. 2013, 114(6). DOI: 10.1063/1.4817717.

[5] Söderberg, O., Y. Ge, A. Sozinov, S.-P. Hannula, and V. K. Lindroos. In Handbook of Magnetic Materials, K. H. J. Buschow (ed.). Elsevier, Amsterdam, 2006, 16, p. 1–39. ISBN: 9780444518507

[6] Kaufmann, S., U. K. Rößler, O. Heczko, M. Wuttig, J. Buschbeck, L. Schultz, and S. Fähler. Adaptive Modulations of Martensites. Physical Review Letters. 2010, 104(14). DOI: 10.1103/PhysRevLett.104.145702.

[7] Kresse, G., and J. Furthmüller. Efficient iterative schemes for ab initio total-energy calculations using a plane-wave basis set. Physical Review B. 1996, 54(16), 11169–11186. DOI: 10.1103/PhysRevB.54.11169.

[8] Kresse, G., and D. Joubert. From ultrasoft pseudopotentials to the projector augmented-wave method. Physical Review B. 1999, 59(3), 1758–1775. DOI: 10.1103/PhysRevB.59.1758.

[9] Sheppard, D., P. Xiao, W. Chemelewski, D. D. Johnson, G. Henkelman. A generalized solid-state nudged elastic band method. The Journal of Chemical Physics. 2012, 136(7). DOI: 10.1063/1.3684549.

[10] Entel, P., V. D. Buchelnikov, V. V. Khovailo, A. T. Zayak, W. A. Adeagbo, M. E. Gruner, H. C. Herper, and E. F. Wassermann. Journal of Physics D: Applied Physics. 2006, 39(5), 865–889. DOI: 10.1088/0022-3727/39/5/S13.

Publications

[11] Zelený, M., L. Straka, A. Sozinov, O. Heczko. Ab initio prediction of stable nanotwin double layers and 4O structure in Ni_2MnGa. Physical Review B. 2016, 94(22). DOI: 10.1103/PhysRevB.94.224108.

[12] Straka, L., J. Drahokoupil, P. Veřtát, M. Zelený, J. Kopeček, A. Sozinov, O. Heczko, Low temperature a/b nanotwins in $Ni_{50}Mn_{25+x}Ga_{25-x}$ Heusler alloys. Scientific Reports. 2018, 8(1). DOI: 10.1038/s41598-018-30388-8.

[13] Zelený, M., L. Straka, A. Sozinov, O. Heczko. Transformation Paths from Cubic to Low-Symmetry Structures in Heusler Ni_2MnGa Compound. Scientific Reports. 2018, 8(1). DOI: 10.1038/s41598-018-25598-z.

Physics of Martensitic Transformations for the Functionality enhancement of crystalline materials and nanostructures: www.matfun.eu

05 | LIFE SCIENCES AND BIOLOGY

SIMULATION OF CLOTTING COUPLED WITH BLOOD FLOW

Research institution:	Principal investigator:	Project IDs:
Charles University	Marek Čapek	OPEN-8-39, OPEN-9-30, OPEN-10-24, OPEN-11-44

Introduction

The motivation for the project is the question of whether mathematical modelling can be of direct help in medical decisions when encountering certain situations in the cardio-vascular system. Among these situations, of paramount importance are thrombus development because of atherosclerosis and unwanted coagulation on the surface of prosthetic devices such as artificial implants. Understanding the blood coagulation process could therefore help either the pharmaceutical industry with the design of new anticoagulants or companies producing prosthetic devices with the design of these devices. Properly designed implants will help inhibit coagulation on the artificial surfaces of these implants. A more profound insight into the process of blood coagulation could also help neurosurgeons to decide whether an operation on an aneurysm is necessary and safe, as the blood coagulation process can be set off even in aneurysms where specific blood flow conditions are present. Our aim is to develop a comprehensive but feasible model for coupled blood flow and blood coagulation. The model should be able to describe some of the important rheological and biochemical phenomena. The model development and numerical implementation is based on the current work of M. Čapek in his PhD thesis. The computations based on the model and it's numerical implementation require significant computational resources as it leads to large systems of nonlinear equations.

Results and Methods

Blood clotting is a complex biochemical process. Its primary goal is to stop the loss of blood after blood vessel wall injury. Disbalance in this process can lead to haemorrhage in cases of low coagulation. On the other hand, in the case of hypercoagulability, dysfunction leads to thrombosis, which can cause stroke or infarct. Tens of chemical species take part in the process, and it is vital not to neglected the role of rheological conditions in the blood vessel in the vicinity of the clotting site.

In a mathematical model of the blood coagulation process it is often necessary to relax the requirements of preciseness due to the mentioned complexity, as we still do not possess the computational resources to model the process with the full settings.

The complexity of any model can be roughly estimated by the number of chemical species taking part in the coagulation and by the used rheological model for blood and the emerging clot.

In our first simulation we used the mathematical model of blood coagulation [1], where blood is taken as a Newtonian fluid, and growing a thrombus is traced by a level-set function. The growth rate of the interface depends on both inflow of blood platelets carried by the blood, and the local shear rate. A high shear rate is taken as a trigger of activation of platelets, which then grow into the clot. We modified the tracing of the interface blood-clot by replacing the level-set function with a phase-field function.

We developed distributed code using the finite element library deal.ii [2]. We achieved results comparable with the original work of Weller [1]. We performed quite a large set of runs of code to study the scalability properties of our code, both from the point of view of strong and weak scalability.
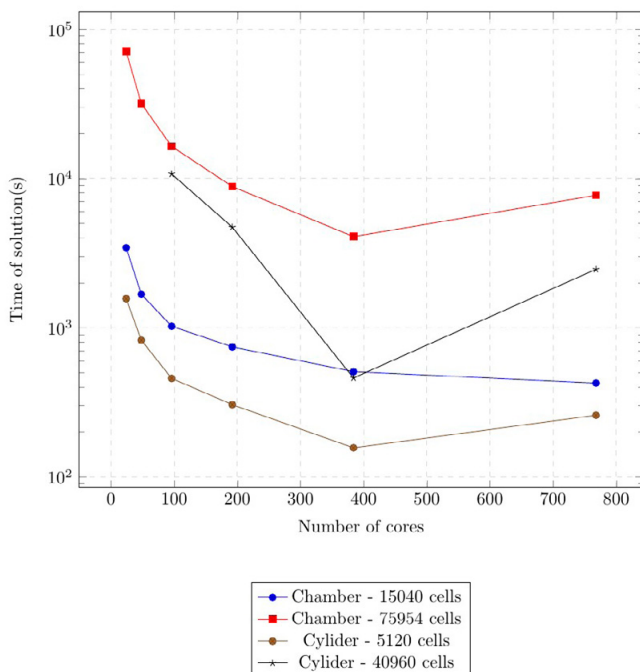

Figure 1.
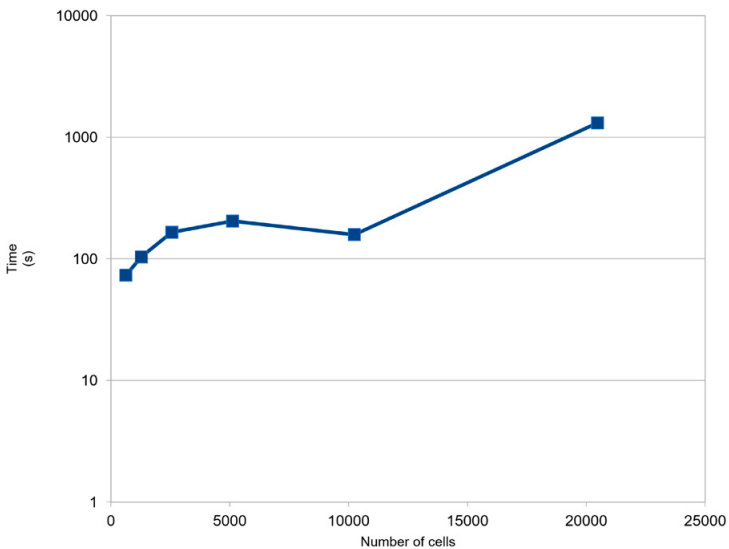Strong scaling – cylinder and chamber geometry

Figure 2.
Weak scaling – cylinder geometry

Figure 1 shows that the computation times decrease with the increase of computational resources up to a certain point, at which the communication overhead of our distributed computations becomes greater than the time to solution of the problem itself.

In the second series of experiments, we increased the number of cores with the number of cells from which the domain is composed. Hence we tried to have a fixed amount of work assigned to a processor. Again Figure 2 demonstrates the deterioration of performance with an increasing number of processors and cells, highlighting the communication overhead of our distributed implementation.

The model [1] is rather simplified, however it does bring new insights to the area of high shear-rate thrombosis.

In our second model we take into account at least the simplified biochemistry of the coagulation process taken from [5]. We want to capture non-Newtonian properties of blood as well, which are well outlined in the model [3, 4]. We have again to discern two domains in our computations – the area of flowing blood, and the area of clot. We utilize the approach from [6], which, simply said, turns on and off the relevant terms in our systems of equations according to the value of a marker function. We chose the phase-field function as a marker function. We can see in Figure 3 and 4, that on arrival of platelets the phase-field (the green structure is the zero value of the phase-field) starts to grow. We note that the activation of platelets is triggered not only by elevated shear-rate, but also by the exposure of specific chemical species in the injured vessel wall. In the model some activating substances also circulate in the flowing blood.

On-going Research / Outlook

We would like to run our simulations for cases of stenosis, where both Newtonian (due to high shear rate, where the flow is quick) and non-Newtonian (due to stasis or recirculation in the areas downstream of the stenosis) features of blood emerge. In such cases we will face the dominant convection. The numeric resolution of fast flows requires specific approaches, which require quite considerable computational power.

Another possibility would be to take into account more thorough biochemistry, as in the case of model [5], we work only with 7 species of transported entities – 2 kinds of platelets and 5 chemical species. As was said, in reality there are tens of species taking part in the coagulation process.

Conclusion

We hope that the achieved results will not only be useful from the theoretical point of view. We mentioned the possibilities for the application of our model in medicine in the Introduction.

The usage of computational facilities of IT4Innovations allows us to perform computations, which could help for this purpose.
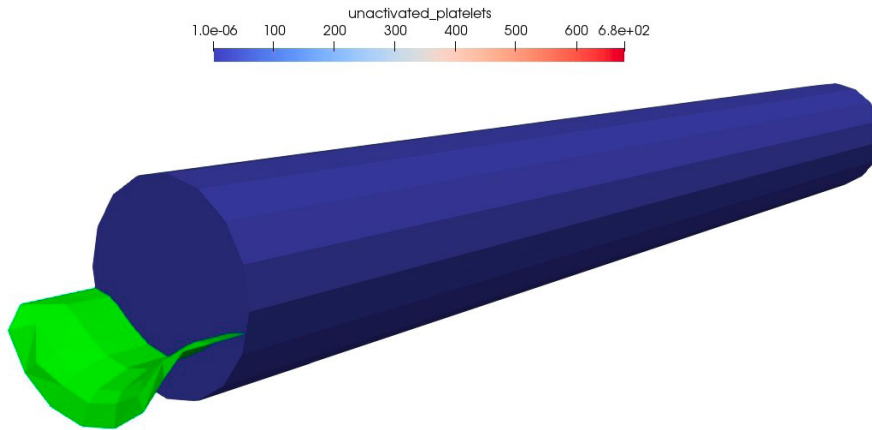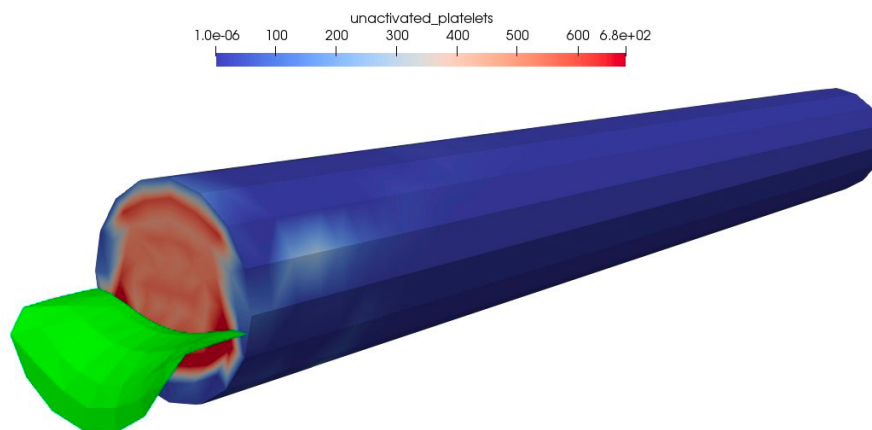
Figure 3.
Start of coagulation

Figure 4.
Development of growing thrombus

References

[1] Weller, F. F. A free boundary problem modeling thrombus growth. Journal of Mathematical Biology. 2010, 61(6), 805–818. DOI: 10.1007/s00285-009-0324-1.

[2] Bangerth, W., R. Hartmann, G. Kanschat. Deal.II–A general-purpose object-oriented finite element library. ACM Transactions on Mathematical Software. 2007, 33(4), 24-es. DOI: 10.1145/1268776.1268779.

[3] Moyers-Gonzalez M., R. G. Owens, J. Fang. A non-homogeneous constitutive model for human blood. Part 1. Model derivation and steady flow. Journal of Fluid Mechanics. 2008, 617. DOI: 10.1017/S002211200800428X.

[4] Owens, R. G. A new microstructure-based constitutive model for human blood. Journal of Non-Newtonian Fluid Mechanics. 2006, 140(1-3), 57–70. DOI: 10.1016/j.jnnfm.2006.01.015.

[5] Storti, F., T.H.S. van Kempen, and F. N. van de Vosse. A continuum model for platelet plug formation and growth. International Journal for Numerical Methods in Biomedical Engineering. 2014, 30(6), 634–658. DOI: 10.1002/cnm.2623.

[6] Li, X., J. Lowengrub, A. Rätz, A. Voigt. Solving pdes in complex geometries. Communications in Mathematical Sciences. 2009, 7(1), 81–107. DOI: 10.4310/CMS.2009.v7.n1.a4.

DATABASE OF METAL-LIGAND COMPLEXES AS MODELS FOR METAL-PROTEIN INTERACTIONS

Research institution:
The Institute
of Organic Chemistry
and Biochemistry
of the Czech Academy
of Sciences

Principal investigator:
Ondrej Gutten

Researcher:
Lubomír Rulíšek

Project partner:
IT4Innovations
National
Supercomputing
Center

Project ID:
OPEN-10-28

Introduction

Transition metals are the wizards of biochemistry and are ubiquitous across species and functions they can provide. Their interactions with proteins, the machinery of life, are crucial not only for understanding the details of the roles they already play in enzymes found throughout all biochemistry, but also for roles they could potentially play in tools and catalysts tweaked to perform desired functions.

Metal-ions provide unique and diverse functions if they can be distinguished properly. Qualitatively, the strength of metal-ion binding is described by the Irving Williams series,

$$Mn^{2+} < Fe^{2+} < Co^{2+} < Ni^{2+} < Cu^{2+} > Zn^{2+}, \qquad (1)$$
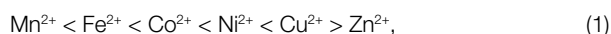
which describes the typical magnitude of stability constants for divalent 3d ions.

Whilst these trends have been being uncovered since the very birth of inorganic chemistry, pairing experimental observations with computationally obtained electronic structure can provide novel insights into both inorganic and computational chemistry. The project attempts to construct a database of metal-ligand complexes as models of protein metal binding sites using methods of computational chemistry. To this end, ten ligands representing amino acid sidechains were selected and combined with the six 3d-metal ions listed above. Several geometries typical for metal-binding sites are considered.

The systematic approach presented in this project puts effort into avoiding multiple sources of potential bias. Moreover, computational chemistry benefits from the comparison of different approaches, ideally on a set of well-organized and heterogeneous data. The output of the project aims to provide a benchmarking data set that could satisfy the diverse requirements of the research community.

Results and Methods

In the preparatory phase, the complexes are generated in a way that systematically examines possible hydrogen bonding patterns while respecting the pre-defined binding geometry of the ligands. Our previous experience shows that this step is required for meaningful interpretation of results.

Structural information is obtained by density functional theory (specifically the BP86 functional [1, 2]) optimization of these structures. Utilization of a pure functional allows for efficient exploitation of the resolution of the identity approximation. BP86 (in conjunction with COSMO for implicit solvation) has been shown to be sufficient for accurate structure optimizations, thus representing an excellent cost/accuracy trade-off [3].

Evaluation of the solvation effect is critical. For this reason DFT is combined with COSMO/RS methodology [4], which takes into account the electronic structure of both the solvent and the solute. The BP86/COSMO-RS protocol for predicting metal-ion selectivity has been previously tested [5]. An argument that model systems can be made relevant for studying selectivity in proteins has also been put forth [6].

We refrain from calculating absolute binding free energies. This quantity is notoriously difficult to compute even for rather simple systems, let alone for protein binding systems for which our systems are only a simple models. Instead, we focus on relative binding free energies, i.e. differences among individual metal-ions, which can be computed with much better accuracy.

The systems are considered to be models of protein binding sites. Hence, constrained optimization was used to enforce tetrahedral arrangement of binding atoms.

Binding sites in proteins vary in exposure to solvent. Solvents of varying polarity (hexane, diethyl-ether, octan-1-ol, water) were used to obtain solvation energies to show the impact of this aspect on selectivity.

Selectivity for a pair of metal-ions is analyzed by building a simple linear regression model. In the initial step, identities of ligands were used as independent variables.

The quality of a regression model is measured by a coefficient of determination, R^2, defined as:

$$R^2 = 1 - \frac{\sum_i e_i^2}{\sum_i (y_i - \bar{y}_i)^2} , \qquad (2)$$

with e_i representing the error of the model and y_i representing the reference values being fitted. Hence, the nominator and denominator in the fraction represent the unexplained and total variance of the data, respectively.

The very simple linear regression model results in a reasonable R^2 value of 0.65 to 0.82 (depending on the metal-ion pair considered). This shows that the identity of a ligand is truly a very strong descriptor for discussing metal-ion selectivity. Thus, it is not surprising that the qualitative concepts of coordination chemistry work very well in most cases.

However, we take interest in the remaining (i.e. the unexplained) variance, which remains significant. Specifically, the interquartile range of metal-ion selectivity in the data set is up to 60 kcal.mol^{-1}, while the median residual error is around 5 kcal.mol^{-1}.

We attempted to use other descriptors (including total charge, presence of hydrogen-bonding patterns, and unspecified cooperative effects between individual pairs of ligands) to build additional linear regression models of the residual errors of the initial model. These models, however, result in $R^2 < 0.1$ (data not shown). In other words, these additional descriptors do not improve our understanding of metal-ion selectivity.

On-going Research / Outlook

The initial intention to construct the database is still ongoing. The focus was shifted from exhaustive construction of all combinations of ligands, metal-ions, and geometries to finding reliable descriptors for explaining the residual variance of metal-ion selectivity. This will require conformational sampling of a few selected systems and correlating the structural details with the variation in selectivity.

Conclusion

The identity of a ligand is a strong predictor for metal-ion selectivity. While this result was expected, there remains a significant variance to be explained. One specific suspect – intramolecular hydrogen bonds – did not prove to affect selectivity in a systematic way.

Cooperative effect of ligands is non-negligible, but not straightforward. Clearly, it is the fine structural details of the complex that are responsible for the variation, and focusing on these aspects with higher resolution is necessary.
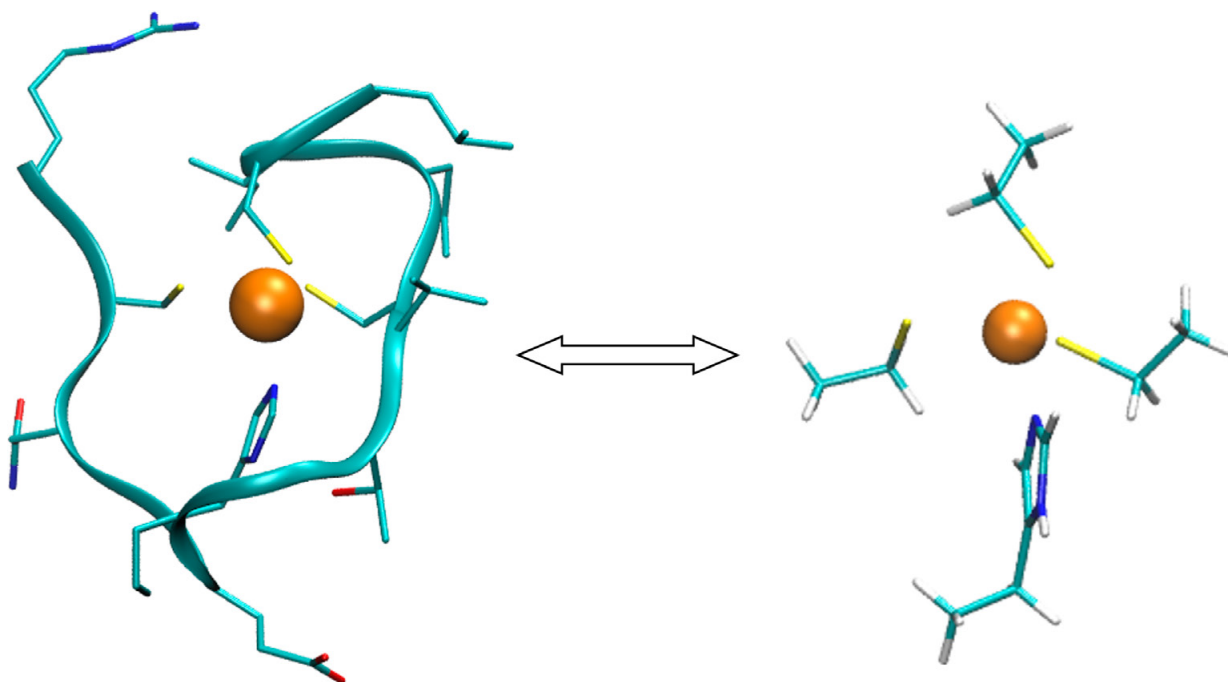

Figure 1.
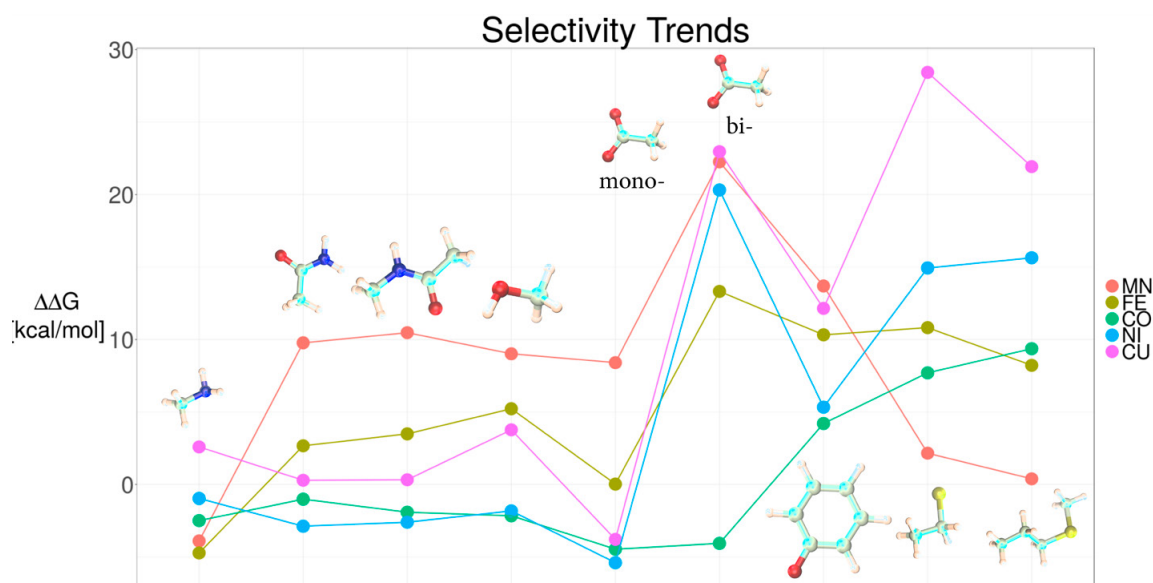An example metallopeptide and corresponding model

Figure 2.
Average contribution to selectivity of each ligand. Zn^{2+} and imidazole are used as a reference.
A positive value indicates that the given ligand is more selective for the given metal ion than an imidazole
ligand for Zn^{2+}.

References

[1] Becke, A. D. Density-functional exchange-energy approximation with correct asymptotic behavior. Physical Review A. 1988, 38, 3098–3100. DOI: 10.1103/PhysReA.38.3098

[2] Perdew, J. P. Density-functional approximation for the correlation energy of the inhomogeneous electron gas. Physical Review B. 1986, 33, 8822–8824. DOI: 10.1103/PhysRevB.33.8822

[3] Narendrapurapu, B. S., N. A. Richardson, A. V. Copan, M. L. Estep, Z. Yang, H. F. Schaefer. Investigating the Effects of Basis Set on Metal–Metal and Metal–Ligand Bond Distances in Stable Transition Metal Carbonyls: Performance of Correlation Consistent Basis Sets with 35 Density Functionals. Journal of Chemical Theory and Computation. 2013, 9(7), 2930–2938. DOI: 10.1021/ct4002398.

[4] Klamt, A. J. Conductor-like Screening Model for Real Solvents: A New Approach to the Quantitative Calculation of Solvation Phenomena. The Journal of Physical Chemistry. 1995, 99(7), 2224–2235. DOI: 10.1021/j100007a062.

[5] Gutten, O., L. Rulíšek. Predicting the Stability Constants of Metal-Ion Complexes from First Principles. Inorganic Chemistry. 2013, 52(18), 10347–10355. DOI: 10.1021/ic401037x.

[6] Gutten, O., L. Rulíšek. How simple is too simple? Computational perspective on importance of second-shell environment for metal-ion selectivity. Physical Chemistry Chemical Physics. 2015, 17(22), 14393–14404. DOI: 10.1039/C4CP04876H.

Publication

IN SILICO DRUG DESIGN

| Research institution:	Principal investigator:	Researchers:	Project partner:	Project ID:
The Institute of Organic Chemistry and Biochemistry of the Czech Academy of Sciences	Pavel Hobza	Diego Elias Honda, Adam Pecina, Martin Lepšík, Saltuk Eyrilmez, Jan Řezáč, Jindřich Fanfrlík	The University of Brasilia	OPEN-12-12

Introduction

We develop a novel scoring function featuring a quantitative semi-empirical quantum mechanical (SQM) description coupled with implicit COSMO solvation. We have already shown that it outperforms widely used scoring functions on various protein-ligand complexes. The accuracy and chemical generality of the SQM/COSMO scoring function make it a perfect tool for computer-aided drug design. In this work, we have extended our study towards biomolecular binding at protein-protein interfaces, which is a crucial prerequisite for understanding of molecular mechanisms of deadly diseases such as cancer.

Results and Methods

We have analyzed two types of protein-protein complex important in cancer. The first was the black-eyed pea Bowman-Birk inhibitor (BTCI) protein complexed with chymotrypsin or trypsin determined by X-ray crystallography (Figure 1). The second was LEDGF/p75 transcriptional coactivator interacting with phosphorylated cellular binding partners as determined by NMR and molecular modelling. In the former case, we used corrected semiempirical quantum-mechanical methods (PM6-D3H4X) developed in our laboratory, which confirmed the importance of Lys26 and Phe53 in the BTCI, Asp186 (trypsin) and Ser195 (chymotrypsin) residues, and quantified side chain contributions of all interacting amino acids (see Figures 2 and 3). In the latter case, we used molecular dynamics to determine the potential binding modes leading to leukaemia.
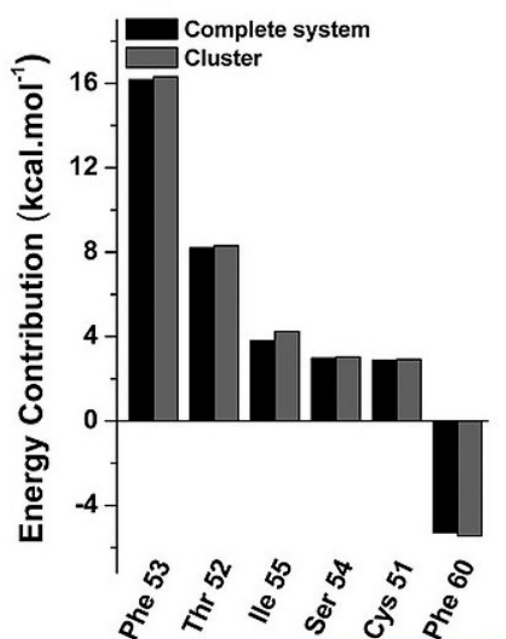
Figure 1.
Crystal structure of trypsin-BTCI-chymotrypsin complex.
Figure adopted from [1].
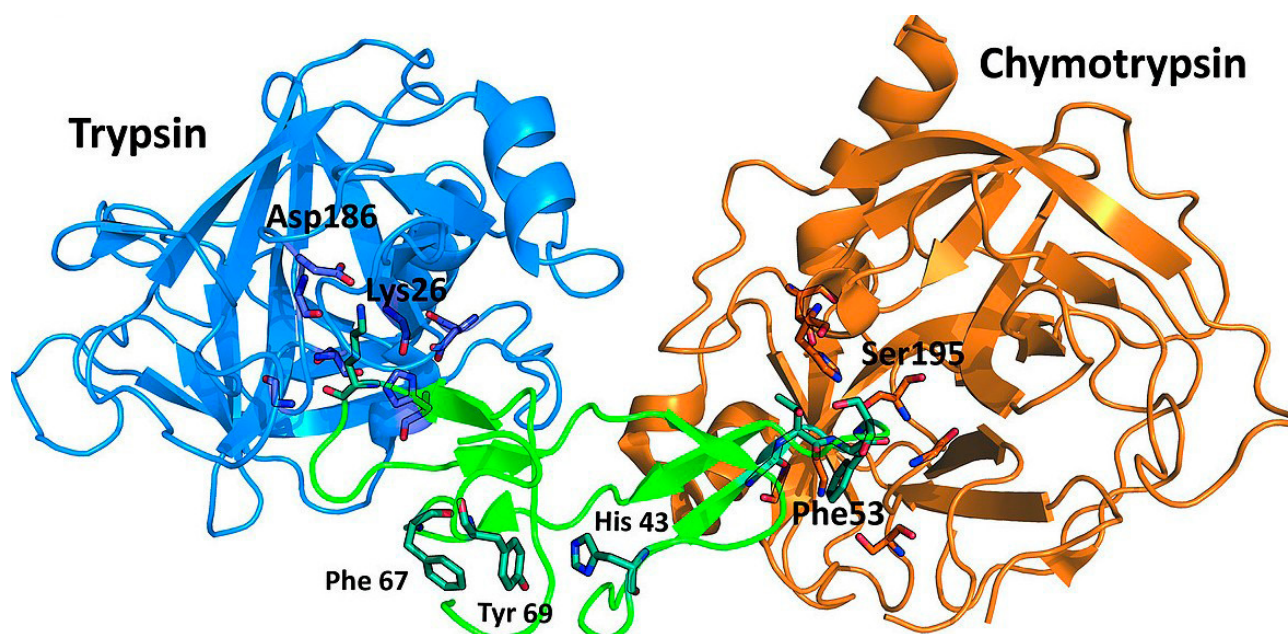
Figure 2.
Amino acid residue side chain contributions to BTCI-chymotripsin interactions computed at the SQM/COSMO level.
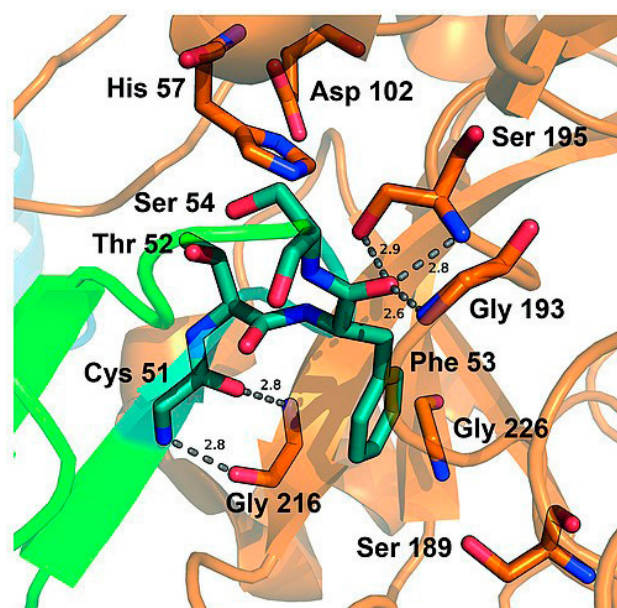*Figure adopted from [1].*

Figure 3.
The substrate specific pocket of the chymotripsin and BTCI binding site. Figure adopted from [1].

On-going Research / Outlook

The SQM/COSMO scoring function has already exhibited superior performance on various protein-ligand complexes. The SQM description enables us to avoid any system-specific parameterizations in the development of our scoring function. The resulting scoring function thus offers generality across the chemical space. In order to demonstrate the generality of the SQM/COSMO scoring function, large-scale applications of the method for diverse protein-ligand complexes and other biomolecular systems are now being set up.

Conclusion

We have developed efficient and accurate computational protocols for evaluating structures, dynamics and energetics at protein-protein interfaces, which extends the capabilities of our SQM/COSMO methodology to targets beyond low-molecular-weight ligands.

Publications

[1] Honda, D. E., J. B. L. Martins, M. M. Ventura, S. M. Eyrilmez, M. Lepšík, P. Hobza, A. Pecina, and S. M. De Freitas. Interface Interactions of the Bowman-Birk Inhibitor BTCI in a Ternary Complex with Trypsin and Chymotrypsin Evaluated by Semiempirical Quantum Mechanical Calculations. European Journal of Organic Chemistry. 2018, 2018(37), 52030–5211. DOI: 10.1002/ejoc.201800754.

[2] Sharma, S., K. Čermáková, J. De Rijck, J. Demeulemeester, Milan M. Fábry, S. El Ashkar, S. Van Belle, M. Lepšík, P. Tesina, V. Duchoslav, P. Novák, M. Hubálek, P. Srb, F. Christ, P. Řezáčová, H. C. Hodges, Z. Debyser, and V. Veverka. Affinity switching of the LEDGF/p75 IBD interactome is governed by kinase-dependent phosphorylation. Proceedings of the National Academy of Sciences. 2018, 115(30), E7053–E7062. DOI: 10.1073/pnas.1803909115.

ExCAPE: BAYESIAN MATRIX FACTORIZATION WITH SIDE INFORMATION FOR PREDICTION OF THE INTERACTIONS BETWEEN CHEMICAL COMPOUNDS AND BIOLOGICAL TARGETS

Research institutions:	Principal investigator:	Researchers:	Project partners:	Project IDs:
Janssen Pharmaceutica NV, IMEC	Vladimir Chupakhin	Thanh Le Van, Tom Vander Aa, Tom Ashby, Vojtěch Cima, Nina Jeliazkova, Hugo Ceulemans	IdeaConsult, IT4Innovations National Supercomputing Center	DD-15-31, OPEN-11-23, OPEN-11-24

Introduction

Prediction of the interactions between chemical compounds and biological targets is a relevant problem for drug design and discovery. If all possible interaction for a given chemical compound is known, then it is easy to guide its optimization because efficacy and possible side effects are known. From the economical point of view this situation is far to reach, as less than 1% of all possible interactions are measured, and one biological end-point on a protein can cost from 50 eurocents to thousands of euros. Various computational approaches were used to fill the chemogenomics matrix (Figure 1), a set of all possible interactions between a set of compounds and a set of proteins [1].
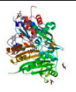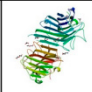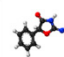

Figure 1.
Chemogenomics matrix: a set of all possible interactions of the chemical compounds with known biological targets. Experimental results cover less than 1% of the matrix, while the purpose of computational models is to fill this matrix, revealing all possible interactions, negative or positive.

There are two main algorithmic ideas for building machine learning models to predict drug-target interaction. The first is to treat each protein target independently. This approach results in separate models for individual targets; hence they are called s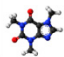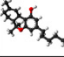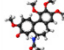ingle-task models. Typical algorithms for this line of direction include Random Forests [2], Support Vector Machines, and XGBoost [3]. Though these methods are simple and can be trained quickly, they ignore the correlations of the targets, which holds potential for overcoming the sparsity of the data. Hence, in the second approach, multi-task learning algorithms, such as matrix factorization [4] and deep learning [5] have been investigated.

In these projects, we study a Bayesian Matrix Factorization method called MACAU [4] and a large-scaled implementation called SMURFF. This model and the SMURFF implementation are attractive for the following reasons: 1) it can deal with large datasets as shown in the results section; 2) it can model uncertainty; 3) the MCMC approximation for the predicted values essentially integrates out of possible hyperparameters, which results in a regularized model without requiring tuning of values for regularizers.

Results and Methods

To evaluate MACAU, we used the ExCAPE database [6]. This dataset consists of 526 distinct target proteins, 955,386 compounds, and 49,316,517 SAR data points (matrix sparsity ~ 90%). Molecule compounds are represented using ECFP6. The dataset was divided into three folds for nested cross validation. The MACAU [4] model implemented in SMURFF has five main hyperparameters, namely the dimension of the latent space (D),
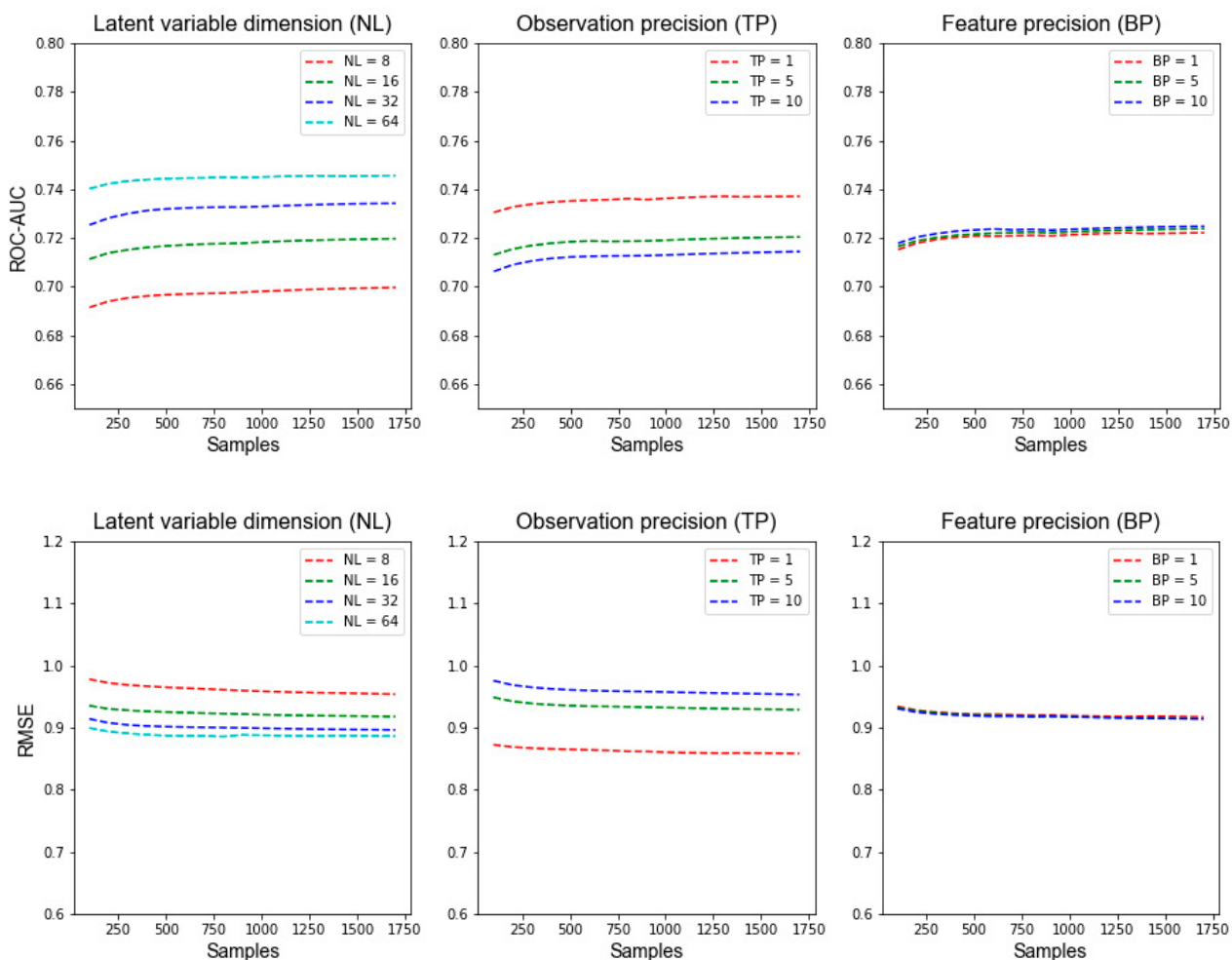
Figure 2.
SMURFF – Hyperparameter tuning using AUC. Each panel shows the average ROC-AUC score of the binarized prediction
values produced by SMURFF. The x-axis is the last number of samples used to make predictions. The y-axis is the average
ROC-AUC per target. We only consider targets that have at least 20 active compounds and 20 inactive compounds.

the precision of the observations (TP), the precision of the compound features (BP), the number of burn-ins, and the number of samples that should be collected from the Gibbs sampling to make predictions. For all experiments, we fixed the number of burn-ins to 200 and ran SMURFF to produce a total of 2,000 samples. Table 1 summarizes the parameters and the considered values.

We ran SMURFF with varying combinations of the hyperparameter values and analysed its performance using ROC-AUC. Figure 2 presents the hyperparameter tuning results using ROC-AUC (A) and RMSE (B). From the figure, we can conclude: 1) SMURFF has an increased performance when we increase the dimension of the latent space D. From the increasing trend of AUC,

we conjecture that the prediction performance will increase up to a certain value and then it will level off. Hence, it is expected that there will be a slightly better result with $D = 128$, for example. However, due to the limit of the storage, we were only able to run experiments with D up to 64; 2) Among the three values of TP, SMURFF has the best performance when TP is equal to 1.0; 3) SMURFF does not significantly change the prediction behaviour when we change BP; 4) SMURFF's performance increases when we increase the number of samples and it tends to plateau when the number of samples is about 700.

SMURFF	
Parameters	Considered values
D	{8, 16, 32, 64}
TP	{1.0, 5.0, 10.0}
BP	{1.0, 5.0, 10.0}
# Samples	{100, 200, …, 1700}

Table 1.
Hyperparameters used in SMURFF

SMURFF was able to finish a run for a parameter setting with a latent dimension size of 64 in 28 hours, and it consumed 1,400 GB of storage on a typical machine on the Salomon cluster.

Conclusion

Our experiments show that the MACAU algorithm and the SMURFF implementation have potential for drug-target interaction prediction problems for large scale datasets. The algorithm can quickly converge, has reasonable errors (RMSE), and the implementation can be applied on large datasets of known compound-target interaction predictions to fill missing interactions.

On-going Research / Outlook

Further research includes but is not limited to improving its performance for highly imbalanced datasets, and to apply it to other applications such as virtual screening, which is relevant for big pharma tasks including finding new compounds active on targets of interest.

References

[1] Lo, Y. C., S. E. Rensi, W. Torng, and R. B. Altman. Machine learning in chemoinformatics and drug discovery. Drug Discovery Today. 2018, 23(8), 1538–1546. DOI: 10.1016/j.drudis.2018.05.010.

[2] Svetnik, V., A. Liaw, C. Tong, J. C. Culberson, R. P. Sheridan, and B. P. Feuston. Random Forest: A Classification and Regression Tool for Compound Classification and QSAR Modeling. Journal of Chemical Information and Computer Sciences. 2003, 43(6), 1947–1958. DOI: 10.1021/ci034160g.

[3] Chen, T., and C. Guestrin. XGBoost: A Scalable Tree Boosting System. In: Proceedings of the 22Nd ACM SIGKDD International Conference on Knowledge Discovery and Data Mining – KDD '16. New York, USA: ACM Press, 2016, p. 785–794. DOI: 10.1145/2939672.2939785.

[4] Simm, J., G. Klambauer, A. Arany, et al. Repurposing High-Throughput Image Assays Enables Biological Activity Prediction for Drug Discovery. Cell Chemical Biology. 2018, 25(5), 611–618.e3. DOI: 10.1016/j.chembiol.2018.01.015.

[5] Unterthiner, T., A. Mayr, G. Klambauer, M. Steijaert, J. K. Wegner, and H. Ceulemans. Deep Learning as an Opportunity in Virtual Screening. NIPS Work. 2014, p. 1–9. Available at http://www.bioinf.jku.at/publications/2014/NIPS2014a.pdf

[6] Sun, J., N. Jeliazkova, V. Chupakhin, et al. ExCAPE-DB: An integrated large scale dataset facilitating Big Data analysis in chemogenomics. Journal of Cheminformatics. 2017, 9(1). DOI: 10.1186/s13321-017-0203-5.

SMURFF – Scalable Matrix Factorization Framework: https://github.com/ExaScience/smurff

THE ROLE OF HYBRIDIZATION IN TRIGGERING ASEXUAL REPRODUCTION IN FISH

Research institutions:
The University
of Ostrava,
IT4Innovations
National
Supercomputing
Center

Principal investigator:
Karel Janko

Researchers:
Martin Mokrejš,
Jan Kočí,
Jan Röslein

Project ID:
OPEN-9-41

Introduction

Sexual reproduction is one of the most common characteristics of eukaryotic organisms and historically one of the most controversial and debated topics in biology [1]. It involves complicated molecular machinery, which, although being highly conserved across taxa [2], has been repeatedly modified in many different ways, leading to the emergence of so-called asexual organisms. Such organisms have attracted considerable attention as excellent models to study the evolutionary dis/advantages of sex [3] and their frequent association with polyploidy also makes them candidate missing links in the formation of polyploid species (rev. in [4]).

Eukaryotic lineages collectively termed as 'asexual' are not an easily definable group as they are scattered throughout the tree of life and employ a wide spectrum of independently arisen cytological mechanisms for gamete production, ranging from completely ameiotic processes (apomixis) to those involving more or less distorted meiotic divisions (automixis) [5, 6]. One common pattern is that such lineages often originated via hybridization of two sexually reproducing species. Although the explanation for the apparent correlation between hybridization and asexuality remains elusive, Ernst [7] and Moritz et al. [8] proposed that unreduced gametes may arise in a hybrid when hybridizing species accumulate a sufficient amount of intergenic incompatibilities to disrupt the cellular regulation of sexual reproduction, yet not too many to seriously compromise hybrid's fertility.

By revealing the speciation history of the fish species Cobitis elongatoides and C. taenia we [9] recently revealed that the process of formation of hybrid asexuals is in fact intertwined with the mechanisms of species formation, which represents a conceptual shift in the understanding of how non-sexual reproductive modes evolve, and what their role is in nature. Specifically, we found that the initial stages of C. elongatoides-taenia species divergence were accompanied by massive gene flow
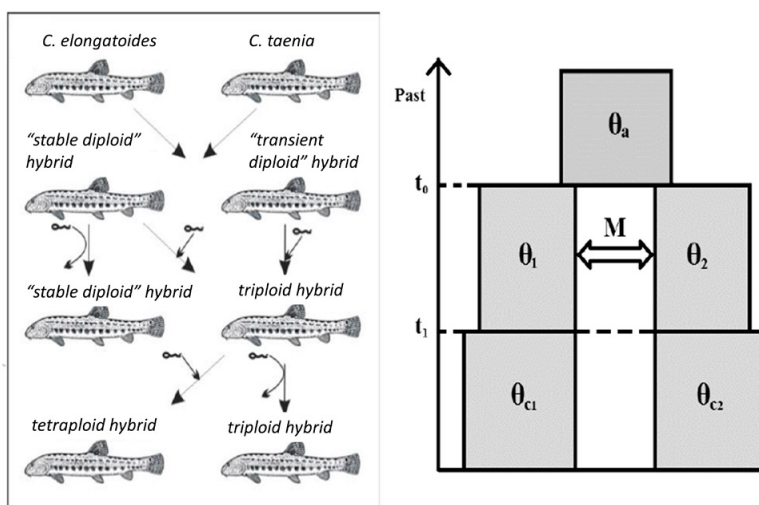
Figure 1.
Left is the scheme of reproductive interactions between two species, C. elongatoides and C. taenia, and their hybrids.
Right: Population divergence model indicating the most-likely scenario of C. elongatoides – C. taenia speciation according to Janko et al. 2018. Both species diverged at t0 (ca 9 Mya) and initially exchanged genes until t1 (ca 1Mya) after which date their genepools became isolated. Population size changes were allowed to change during the simulation. Note that the arrow indicates time, which is supposed to run from the present (down) to the past (up) due to standard assumptions of coalescent simulations.

GenomeScope Profile PE + MP
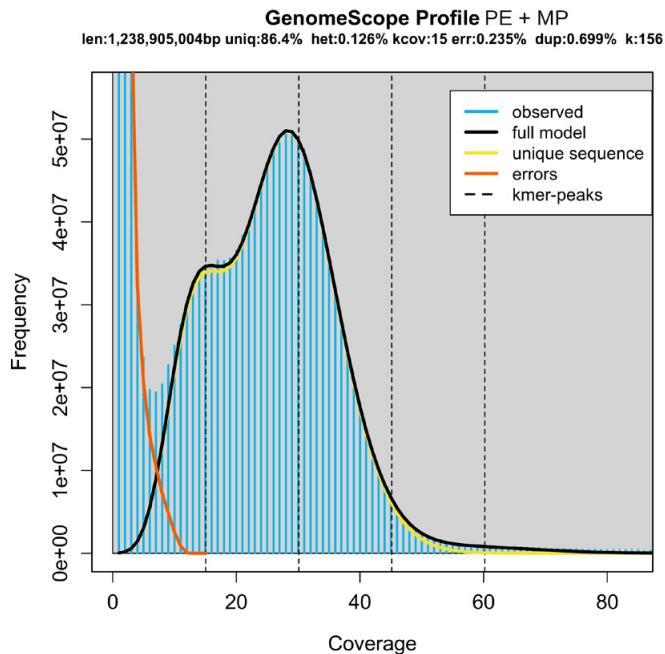len:1,238,905,004bp uniq:86.4% het:0.126% kcov:15 err:0.235% dup:0.699% k:156

Figure 2.
Analysis of observed vs. anticipated k-mers of the size 156 in Illumina paired-end and Nextera Long mate-pair datasets of the Cobitis taenia genome. The sequencing reads were up to 250nt long thanks to the RapidSequencing mode of the Illumina device, which enabled this strict approach.
The left peak at about 15x coverage is formed by k-mers at heterozygotic loci whereas the peak at about 28x coverage is formed by k-mers obtained from homozygotic loci. For the curious, if one were to use 32nt long k-mers for the analysis then the heterozygotic, homozygotic, and tetraploid loci (not visible in this k=156-based chart) would show at coverages 49x, 98x and 196x, respectively (data not shown).

mediated by hybrids with efficient recombination and segregation, but at later stages, the gene flow ceased as all hybrids produced by contemporary species are either clonally reproducing females or sterile males (Figure 1). Hybrid clonality thus appeared as an effective barrier for interspecific gene exchange, which can play the role of primary reproductive isolating mechanisms between new species, even before the emergence of other classical forms of reproductive incompatibility. Interestingly, the ability to produce clonal gametes predisposes hybrid females to establish competitively successful lineages, which are able to spread across the European continent, of which some have attained considerable evolutionary ages spanning over 100,000 generations [10].

Thus, a century after Ernst, it appears that meiotic aberrations leading to hybrid asexuality may represent just another side of the same coin as those leading to hybrid sterility, which is the key factor in species formation.

Because many reasons leading to hybrid sterility are presumably linked with aberrant pairing of homologous chromosome from both hybridizing species, this study investigates the extent to which asexual Cobitis hybrids transmit their genomes clonally en bloc or whether some interactions, such as recombination or gene conversion, exist in these clonal lineages. To do so, we evaluated nucleotide positions that distinguish between both parental species across the genomes, and tested whether clonal hybrids appear as hetero- or homozygotes at such sites, which is indicative of potential chromosomal rearrangements during their evolution.

Results and Methods

The genomic DNA was isolated from a Cobitis taenia diploid female using the classical phenol-chloroform extraction protocol. After isolation, several sequencing libraries were prepared, including classical genomic shot-gun Illumina paired-end sequencing as well as Nextera long mate-pair sequencing. In the first case the DNA was fragmented to ~450bp, whereas in the second case the intended fragment length was ~5kb and ~7kb, using the Covaris ME220 in all cases. Sequencing was performed on an Illumina HiSeq 2500 platform (2 x 250) at Genomics Core Facility - EMBL, resulting in a coverage of ~80X for pair-end reads and a coverage of ~10X for mate-pair libraries. For general operations with FASTQ files, e.g. sequence merging, splitting, de-interleaving, and reformatting, we used BBTools software [11]. For adapter trimming we used Trimmomatic (v. 0.32) and for linker removal splitnextera.sh from the BBTools software bundle. Then PrinSeq [12] was used to remove leading and trailing N's from both ends of the reads, and also from both ends' sequence flanks with PHREDQ <20 in a 20nt window. Illumina error-read correction was performed by tadpole.sh with a k-mer size of 62 (from BBTools). De novo assembly of the genome was performed using ABySS [13]. Subsequently GenomeScope [14] was used to assess the size of the assembly and ploidy of the sample. Eventual contamination of the libraries with DNA from a different organism as well as uniformity of all library preparations was assessed using KAT [15].
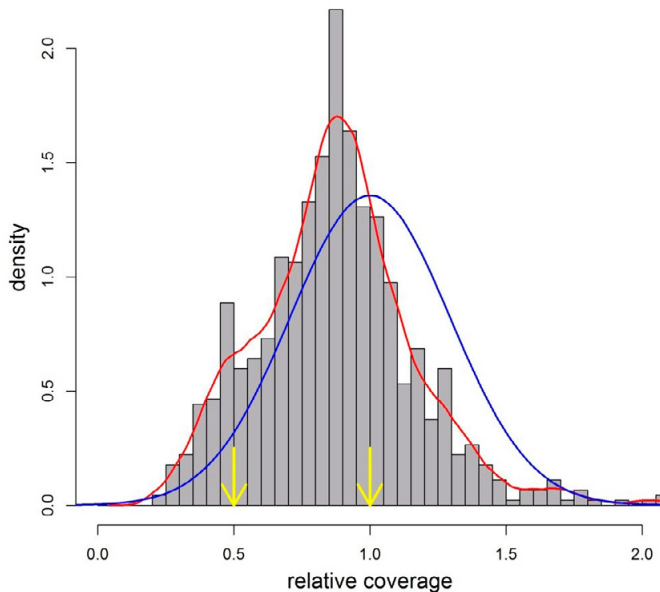
Figure 3.
*Histogram of normalized relative coverage of LOH loci.
Arrows point at biologically meaningful values (0.5
stands for sites subject to hemizygous deletion, 1 for
homozygous sites supposedly originating via gene
conversion, where coverage drop is not expected).
The red line represents the fitted bimodal distribution
with means at 0.5 and 1, while the blue line represents
the estimated unimodal normal distribution centred at
the value 1. The fit of both models was compared with
the LR test and the bimodal distribution fitted the data
significantly better than the unimodal one.*

Based on known genomic sequences, we designed and ordered exome-capture probes to massively sequence a set of ~6000 genes from various fish biotypes. Altogether, we performed the exome-capture sequencing on 46 specimens including parental species as well as their diploid and triploid hybrid lineages according to the protocol described in [9]. Libraries were sequenced on Illumina NextSeq500 (75bp pair-end) and SNP (single-nucleotide differences) called as described in [9].

To detect possible genomic rearrangements in hybrids, we used custom R (R core team 2018) scripts to detect all SNP positions which unambiguously differentiate between both parental species (i.e. the interspecific diagnostic SNPs) and tested whether hybrids appear as heterozygotes on such loci in nuclear genes. For each hybrid and SNP position, we also evaluated its normalized coverage in raw reads and compared it to average coverage at such a position to detect possible deletions (i.e. drops in coverage compared to other individuals).

Counting distinct k-mers in sequencing reads cleaned of adapters and further analysis using genomescope resulted in a genome size estimate of ~1.24Gbp and confirmed diploid nature of the genome. This is well in an agreement with our previous experimental results [16] which showed the genome consists of 50 chromosomes and their cumulative size is 1.3Gbp. The assembly using a k-mer size of 160 resulted in 223,249 fragments ≥ 500nt. The largest contiguous sequence spanned 82,251nt and the largest scaffold spanned 724,617nt. L50 was 4585, LG50 was 6863, N50 was 51,976nt and NG50 was 34706 (Figure 2). The total assembled genome size was 1.074Gnt. A single assembly attempt with back-mapping of original input reads to assess quality required about 56 wallclock hours on 112 CPU cores

and required, depending on the k-mer size, between 800 GB to 1.6 TB of RAM. The use of the SGI UV1 machine based on NUMA architecture providing 3.2 TB of physically available local RAM was hence indispensable. The project utilized in total 690,000 CPU hours. The project utilized about 22 TB of hard disk space, but occasionally needed much more for intermediate files. Using subsequent mapping of exome-capture data onto the available reference, we obtained approximately 50,000 SNP differentiating between both parental species. The 50,000 positions are scattered across the whole 1.3Gbp genome. All hybrids were found as fixed heterozygotes at most of such positions, ultimately proving their F1 origin and generally clonal propagation of their genomes. However, we found that each analysed hybrid possessed between 1–4% of diagnostic positions where it was homozygotic Importantly, these positions were not shared between different hybrid clonal lineages suggesting that such sites do not represent mutations that fixed between species after the origin of clones. Instead, they represent sites where hybrids lost their heterozygosity either by overwriting one parental allele with the other, or by losing it (deletion of one allele). We therefore call such positions 'LOH' (i.e. loss of heterozygosity). Comparisons of relative coverage per LOH position allowed us to distinguish both alternatives. We indeed found that normalized coverage divided by coverage averaged across all individuals at such positions had a clearly bimodal distribution with peaks located at 1 and at 0.5 (Figure 3). This suggests that diploid hybrids had either a 'normal' amount of DNA at their LOH positions, indicating the gene conversion event, or half the amount, indicating the partial loss of one parental chromosome (i.e. hemizygous deletion).

Conclusion

Acquired data unequivocally demonstrated that propagation of inherited genomes is clonal to a high extent, since the vast majority of diagnostic positions remained in a fixed heterozygotic state despite thousands of generations of hybrid evolution. Nonetheless, a non-negligible part of the hybrid's genomes was affected by postformational restructuration. Performed analyses demonstrated that chromosomes of clonal hybrids are subject to occasional hemizygous deletions, but also to gene conversion events that occur through interactions between homologues originating from both hybridizing genomes.

These patterns show that clonal hybrids do not behave as evolutionary 'no-hopers', as traditionally assumed, but that their genomes retain dynamics with a potential of further evolution and that, importantly, investigators of asexual organisms must take into the account the fact that signatures of original hybridisation events might have been considerably modified or overridden by genomic rearrangements during the evolution of naturally occurring asexuals. Such changes are therefore expected not only in asexual taxa with relatively high incidence of pairing of heterospecific homologues [17], but also in taxa, like Cobitis, where classical cytogenetic and population genetic tools have not detected any deviations from clonality.

References

[1] Weismann, A. Amphimixis or the essential meaning of conjugation and sexual reproduction. E. Poulton, S. Schönland, A. Shipley (eds.). Essays upon heredity and kindred biological problems. 1892, Vol. 2., p. 101–222. Oxford: Clarendon Press.

[2] Bernstein, H., and C. Bernstein. Evolutionary Origin of Recombination during Meiosis. BioScience. 2010, 60(7), 498–505. DOI: 10.1525/bio.2010.60.7.5.

[3] Kearney, M., M. K. Fujita, J. Ridenour. Lost sex in the reptiles: constraints and correlations. Schön, I., K. Martens, and P. Dijk (eds.). Lost Sex. Dordrecht Netherlands: Springer. 2009, p. 447–474. DOI: 10.1007/978-90-481-2770-2_21.

[4] Choleva, L., and K. Janko. Rise and persistence of animal polyploidy: evolutionary constraints and potential. Cytogenetic and Genome Research. 2013, 140(2–4), 151–170. DOI:10.1159/000353464.

[5] Stenberg, P., A. Saura. Cytology of Asexual Animals. I. Schön, K. Martens, P. Dijk (eds.). Lost Sex. Dordrecht Netherlands: Springer. 2009, p. 63–74. DOI: 10.1007/978-90-481-2770-2_4.

[6] Stenberg, P., A. Saura. Meiosis and Its Deviations in Polyploid Animals. Cytogenetic and Genome Research. 2013, 140(2–4). DOI: 10.1159/000351731

[7] Ernst, A. Bastardierung als Ursache der Apogamie im Pflanzenreich. Eine Hypothese zur experimentellen Vererbungs- und Abstammungslehre. Nabu Press, 1918. DOI: 10.5962/bhl.title.8212.

[8] Moritz, C., W. M. Brown, L. D. Densmore, et al. Genetic diversity and the dynamics of hybrid parthenogenesis in Cnemidophorus (Teiidae) and Heteronotia (Gekkonidae. In Evolution and Ecology of Unisexual Vertebrates. New York State Museum, Albany, New York. 1989, p. 268–280.

[9] Janko, K., J. Pačes, H. Wilkinson-Herbots, et al. Hybrid asexuality as a primary postzygotic barrier between nascent species: On the interconnection between asexuality, hybridization and speciation. Molecular Ecology. 2018, 27(1), 249–263. DOI:10.1111/mec.14377.

[10] Janko, K., M. A. Culling, P. Rab, P. Kotlik. Ice age cloning-comparison of the Quaternary evolutionary histories of sexual and clonal forms of spiny loaches (Cobitis; Teleostei) using the analysis of mitochondrial DNA variation. Molecular Ecology. 2005, 14(10), 2991–3004. DOI: 10.1111/j.1365-294X.2005.02583.x.

[11] Bushnell, B. BBMap short-read aligner, and other bioinformatics tools. 2015. Available at https://www.researchgate.net/publication/319159625_BBMap_short-read_aligner_and_other_bioinformatics_tools

[12] Schmieder, R., R. Edwards. Quality control and preprocessing of metagenomic datasets. Bioinformatics (Oxford, England). 2011, 27(6), 863–864. DOI: 10.1093/bioinformatics/btr026.

[13] Jackman, S. D., B. P. Vandervalk, H. Mohamadi, et al. ABySS 2.0: Resource-efficient assembly of large genomes using a Bloom filter. Genome Research. 2017, 27(5), 768–777. DOI: 10.1101/gr.214346.116.

[14] Vurture, G. W., F. J. Sedlazeck, M. Nattestad, et al. GenomeScope: fast reference-free genome profiling from short reads. Bioinformatics. 2017, 33(14), 2202–2204. DOI: 10.1093/bioinformatics/btx153.

[15] Mapleson, D., G. Garcia Accinelli, Kettleborough, J. Wright, B. J. Clavijo. KAT: A K-mer analysis toolkit to quality control NGS datasets and genome assemblies. Bioinformatics. 2017, 33(4), 574–576. DOI: 10.1093/bioinformatics/btw663.

[16] Majtánová, Z., L. Choleva, R. Symonová, P. Ráb, J. Kotusz, L. Pekárik, K. Janko. Asexual Reproduction Does Not Apparently Increase the Rate of Chromosomal Evolution: Karyotype Stability in Diploid and Triploid Clonal Hybrid Fish (Cobitis, Cypriniformes, Teleostei). PloS One. 2016, 11(1). DOI: 10.1371/journal.pone.0146872.

[17] Gibbs, H. L., and R. D. Denton. Cryptic sex? Estimates of genome exchange in unisexual mole salamanders (Ambystoma sp.). Molecular Ecology. 2016, 25(12), 2805–2815. DOI:10.1111/mec.13662.

EXPERIMENTAL VALIDATION OF k-WAVE IN ABSORBING FLUID MEDIA

Research institution:	Principal investigator:	Researchers:	Project partner:	Project IDs:
Brno University of Technology	Jiří Jaroš	Elly Martin, Bradley Treeby	University College London	OPEN-9-12, OPEN-10-31

Introduction

The use of ultrasound as a diagnostic imaging tool is well known, particularly during pregnancy where ultrasound is used to create images of the developing baby. In recent years, a growing number of therapeutic applications of ultrasound have also been demonstrated. For example, high-intensity waves can be used to destroy tissue to treat cancer, and low-intensity waves can be used to modulate brain activity [1, 2].

As part of ultrasound therapy, computer models are often used to accurately predict how ultrasound waves travel through the human body, thereby allowing the treatment to be optimised. These models must be carefully validated to ensure that the amplitude and spatial distribution of acoustic pressure can be accurately known at the target location, ensuring that treatments are safe and effective. This process of validation is achieved by comparison of the simulated acoustic pressure with precise experimental measurements of acoustic fields [3, 4].

In this work, the acoustic field in heterogeneous fluid media simulated using the k-Wave acoustic modelling toolbox was validated against experimental measurements of an acoustic field after propagation through liquid filled phantoms. k-Wave is an open source acoustic modelling toolbox which solves a generalised version of the Westervelt equation which accounts for the combined effects of nonlinearity, heterogeneous material properties, and acoustic absorption following a frequency power law [5]. k-Wave is designed and optimised to fully utilise the computational resources offered by the IT4Innovations' Salomon supercomputer.

Results and Methods

The experimental validation setup consisted of a single element spherically focussing piezoceramic ultrasound transducer, with a nominal diameter of 64 mm and a radius of curvature of
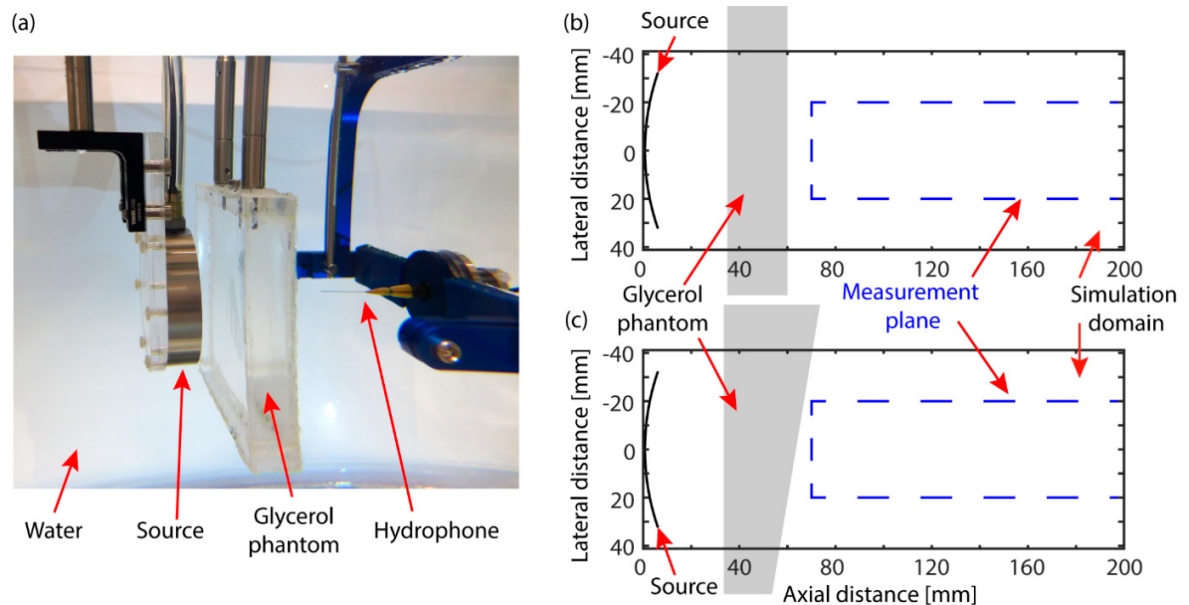

Figure 1.
(a) Measurement setup with planar glycerol phantom. (b) Registered simulation and measurement configuration with planar glycerol phantom. (c) Registered simulation and measurement configuration with wedge glycerol phantom.
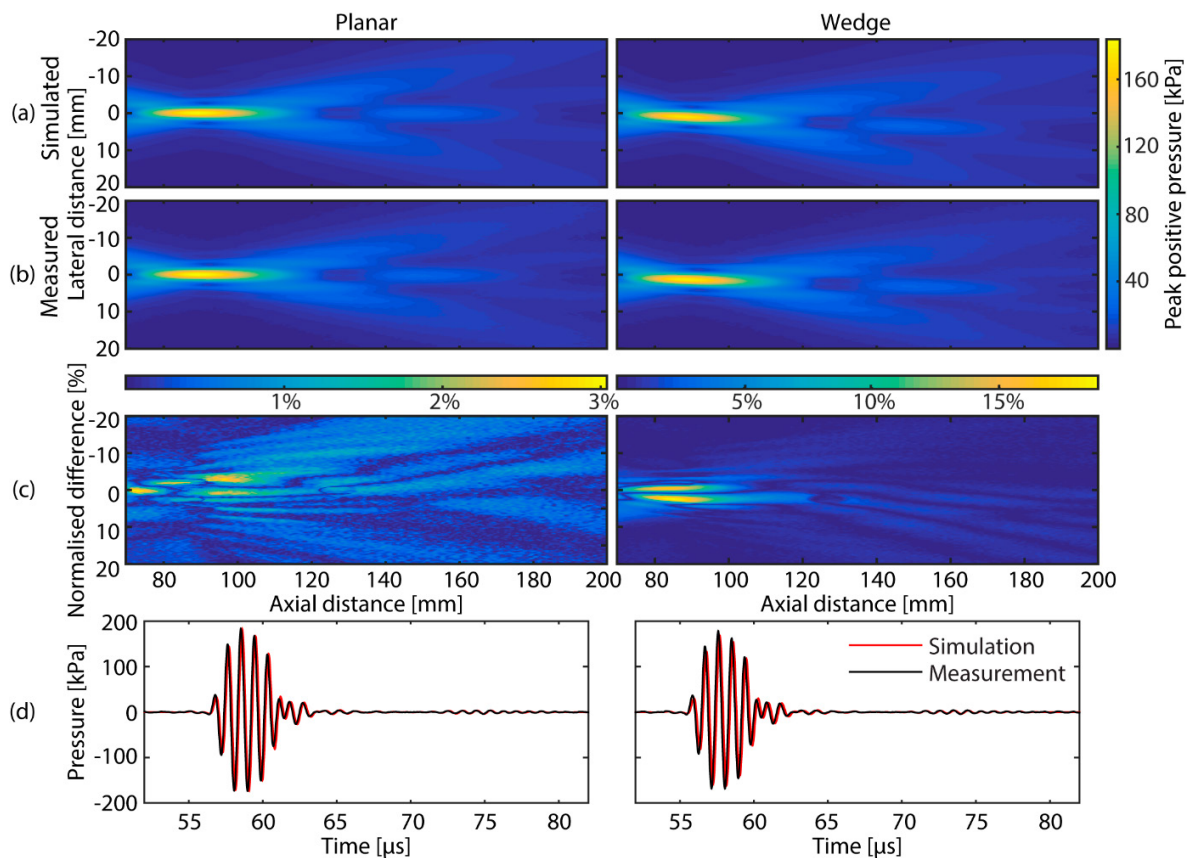
Figure 2.
(a) Simulated peak positive acoustic pressure on the axial-lateral plane. (b) Measured peak positive acoustic pressure on the axial-lateral plane. (c) Absolute difference between simulated and measured peak positive acoustic pressure normalised to the spatial peak of the measured pressure. (d) Simulated and measured pressure waveforms at the location of the spatial peak measured pressure.

98 mm (H151, Sonic Concepts, Bothell, WA, USA). The transducer was driven with a 4-cycle burst at a frequency of 1.1 MHz, by a waveform generator connected to the source via an RF amplifier and impedance matching network. Glycerol was used to introduce fluid heterogeneities into the medium as its sound speed is relatively different from water (1,920 ms^{-1} cf. 1,485 ms^{-1} for water at 21 °C) and its attenuation coefficient (0.45 dB cm^{-1} MHz^{-2}) is comparable to that of soft tissue. The glycerol phantoms were made in-house from laser-cut Perspex housing with acoustically transparent Mylar windows which resulted in a well-known geometry. The acoustic attenuation and sound speed of the glycerol was measured in-house (values as reported above), the density (1,258 kg m^{-3}) and nonlinearity parameter (9.0) were taken from the literature [6]. The source and phantoms were rigidly mounted in a tank of degassed, deionised water using opto-mechanical components to obtain a fixed experimental geometry that could be replicated in simulation as shown in Figure 1. Measurements of acoustic pressure were made on a 130 mm by 40 mm plane using a 0.2 mm PVDF needle hydrophone (Precision Acoustics, Dorchester, UK) mounted on an automated 3-axis translation

stage. Acquisition of waveforms from the hydrophone was performed by a digital oscilloscope controlled via the scanning system software.

For the simulations, a definition of the ultrasound source is required as an input to the model. This was acquired experimentally by acoustic holography. Briefly, the acoustic field generated by the ultrasound transducer at a low drive level was measured on a plane perpendicular to the beam axis in water. The measured pressure signals were propagated back to the location of the source using the MPI version of the k-Wave toolbox running on Salomon. The resulting source pressure signals were then used as the input to the forward simulations, with amplitude scaling applied to match the source pressure levels used in experiments. Forward simulations including the medium heterogeneities were run using the MPI version of k-Wave on 9 nodes using a total of 216 cores on Salomon. The simulations were run on a 2,048 by 864 by 864 grid with a spatial step size of 100 μm and a temporal step size of 20 ns. Input files were in the order of 14 GB, and output files were approximately 300 GB and required approximately 400 GB of RAM. The run

time for each simulation was approximately 12 hours. The simulated pressure was recorded over an axial lateral plane that matched the extent of the measured data. The measured and simulated peak positive acoustic pressure is shown in Figure 2 for media including a planar rectangular slab phantom and a wedge shaped phantom.

The comparison between measured and modelled pressure showed excellent agreement. For the planar glycerol phantom, the geometry of the field agreed closely with only a small difference of 0.2 mm in the position of the focal region. This difference was 0.6 mm for the wedge shaped phantom. The simulated and measured peak focal pressures differed by less than 1% for the planar phantom and by 1.4% for the wedge shaped phantom. As shown in Figure 2(c), the simulated focal waveforms agreed with the measurement in terms of the amplitude, shape, and timing of reflections seen after the main pulse. The larger differences seen with the wedge phantom may be attributed to greater uncertainty in the geometry of the phantom due to the flexibility of the Mylar windows. Glycerol has a lensing effect on the field, so small errors in geometry between measurement and simulation would cause shifts in the focal position. However, the differences in the peak pressures in both cases were within the experimental uncertainty in measured pressure.

Conclusion

When the medium geometry and acoustic properties are well characterised and accurately registered from measurement set-up to simulation domain, excellent agreement can be obtained between simulated and measured acoustic pressure. The results shown here are for a quasi linear field and demonstrate that absorption is correctly modelled in k-Wave under these conditions. This is important for working towards implementing these models for ultrasound treatment planning, and in the short term is of interest to the 1,000s of users of the k-Wave toolbox worldwide.

On-going Research / Outlook

Validation of the k-Wave toolbox is ongoing with a programme of similar measurement and simulation comparisons under increasingly complex conditions planned. There is larger potential for error as the medium properties become more heterogeneous and less well characterised as is the case in biological tissues. Validation experiments will be performed with fields containing a higher degree of nonlinearity, increasingly complex medium geometries, and elastic media, such as bone, which will be important in accurate simulation of transcranial ultrasound propagation.

References

[1] ter Haar G. Therapeutic applications of ultrasound. Progress in Biophysics and Molecular Biology. 2007, 93(1-3), 111–129. DOI: 10.1016/j.pbiomolbio.2006.07.005.

[2] Legon, W., L. Ai, P. Bansal, J. K. Mueller. Neuromodulation with single-element transcranial focused ultrasound in human thalamus. Human Brain Mapping. 2018, 39(5), 1995–2006. DOI: 10.1002/hbm.23981.

[3] Martin, E., B. E. Treeby. Experimental validation of computational models for large-scale nonlinear ultrasound simulations in heterogeneous, absorbing fluid media. In AIP Conference Proceedings 1685, 070007 (2015). DOI: 10.1063/1.4934444.

[4] Martin, E., Y. T. Ling, B. E. Treeby. Simulating Focused Ultrasound Transducers Using Discrete Sources on Regular Cartesian Grids. EEE Transactions on Ultrasonics, Ferroelectrics, and Frequency Control. 2016, 63(10), 1535–1542. DOI: 10.1109/TUFFC.2016.2600862.

[5] Jaroš, J., A. P. Rendell, B. E. Treeby. Full-wave nonlinear ultrasound simulation on distributed clusters with applications in high-intensity focused ultrasound. The International Journal of High Performance Computing Applications. 2015, 30(2), 137–155. DOI: 10.1177/1094342015581024.

[6] Sehgal, M., R. C. Bahn, J. F. Greenleaf. Measurement of the acoustic nonlinearity parameter B/A in human tissues by a thermodynamic method. The Journal of the Acoustical Society of America. 2010, 76(4), 1023–1029. DOI: 10.1121/1.391420.

Publications

Treeby, B. E., F. Lucka, E. Martin, B. T. Cox. Equivalent-Source Acoustic Holography for Projecting Measured Ultrasound Fields Through Complex Media. IEEE Transactions on Ultrasonics, Ferroelectrics, and Frequency Control. 2018, 65(10), 1857–1864. DOI: 10.1109/TUFFC.2018.2861895.

Treeby, B. E., J. Budiský, E. S. Wise, J. Jaroš, B. T. Cox. Rapid calculation of acoustic fields from arbitrary continuous-wave sources. The Journal of the Acoustical Society of America. 2018, 143(1), 529–537. DOI: 10.1121/1.5021245.

Treeby, B. E., F. Vaverka, J. Jaroš. Performance and accuracy analysis of nonlinear k-Wave simulations using local domain decomposition with an 8-GPU server. Proc. Mtgs. Acoust. 2018, 34. DOI: 10.1121/2.0000883.

Martin, E., E. Z. Zhang, J. A. Guggenheim, P. C. Beard, B. E. Treeby. Rapid spatial mapping of focused ultrasound fields using a planar Fabry-Perot sensor. EEE Transactions on Ultrasonics, Ferroelectrics, and Frequency Control. 2017, 64(11), 1711–1722. DOI: 10.1109/TUFFC.2017.2748886.

Robertson, J. L., B. T. Cox, J. Jaroš, B. E. Treeby. Accurate simulation of transcranial ultrasound propagation for ultrasonic neuromodulation and stimulation. The Journal of the Acoustical Society of America. 2017, 141(3), 1726–1738. DOI: 10.1121/1.4976339.

A SOFTWARE TOOL FOR CRANIAL ORTHOSIS DESIGN

Research institution:	Principal investigator:	Researchers:	Project partner:	Project ID:
IT4Innovations National Supercomputing Center	Alena Ješko (Vašatová)	Petr Strakoš, Milan Jaroš, Tomáš Karásek	ING corporation spol. s.r.o	OPEN-9-20

Introduction

Treatment of skull deformities of children by cranial orthosis has been adopted by pediatricians and has been increasingly used since it was first documented in 1981, by [1].

Orthosis can be used to fix positional deformities such as plagiocephaly, brachycephaly, and scaphocephaly. Most of these develop during the first months of a child's life. Their number has increased considerably since pediatricians have internationally recommended the sleeping supine position as a strategy to reduce the prevalence of sudden infant death syndrome. More information can be found in [2, 3].

When manufactured, every orthosis has to be designed individually, which is currently a fully manual task. Our software tool made for designing these orthoses requires very little intervention from a medical technician. This speeds up the production and enables individual parts of the process, from 3D scanning to 3D printing, to be held anywhere in the world without expensive devices concentrated in one place.

To manufacture the orthosis using the method of 3D printing, its digital model has to be represented by a mesh. High-resolution meshes must be used to obtain a high quality product.

To be able to modify the generic model, large systems of linear equations must be solved, which requires the use of efficient and fast solvers.

Results and Methods

During the customisation of the generic cranial orthosis, the model is modified by constrained transformation to the individual patient based on an idealized 3D scan of their head. The scan of the head is cropped afterwards using outlines specified by the medical technician.

The model itself is composed of two parts, a helmet and a locking mechanism. The goal of the transformation is a non-rigid deformation of the orthosis body to fit the cropped scan, and a rigid transformation of the locking mechanism to its specified position. The locking mechanism can only translate and rotate to preserve its functionality.

Furthermore, we also need two auxiliary meshes, so-called cages, which serve as control points for the main transformation and compute rigid body movement of the locking mechanism.

At first, we used the open source 3D graphics and animation software Blender for rapid testing of the proposed methodology. We bound the model mesh with the control cage using the MeshDeform modifier, then we shrank the control cage to the scans using the Shrinkwrap modifier. The MeshDeform modifier automatically deforms the model mesh according to the cage deformation, based on [4].

Although the parallel version of the MeshDeform modifier which we made gives good results, it is still computationally extensive and we have replaced it completely with transformation using radial basis function (RBF), which is computationally less expensive. Transformation by RBF also allows easy incorporation of the rigid parts, which the MeshDeform modifier cannot implicitly do.

RBFs have become a well-established tool to interpolate scattered data [5]. The method requires solving a relatively small system of equations. However, the relativity is caused by comparing the number of control points to the whole mesh. With huge meshes the set of control points becomes large. The implementation of the method is quite simple, even for 3D applications, because no grid-connectivity information is needed. Parallelization of the concept is also straightforward.

The basic principles of RBF could be described in such a way that we are looking for a function that exactly interpolates the displacement of given control points and smoothly interpolates this displacement into the mesh. The displacement function is then represented as a linear combination of polynomial corrections and a linear combination of radially symmetric kernels located at control points.

The choice of the kernel function has a significant influence on the result of the deformation. We use triharmonic [6] or thin plate spline (TPS) [7] kernel functions. To be able to handle rigid transformation, we incorporated techniques from [8], where certain parts of an image are handled as if they are rigid.

For our implementation we used the VTK library to work with 3D geometry and mesh models. To solve large systems of linear equations we use the Intel MKL library. This library offers direct solvers and is optimized for high performance.

Besides the time necessary to obtain the solution of the unknowns from the linear system of equations, another time de-
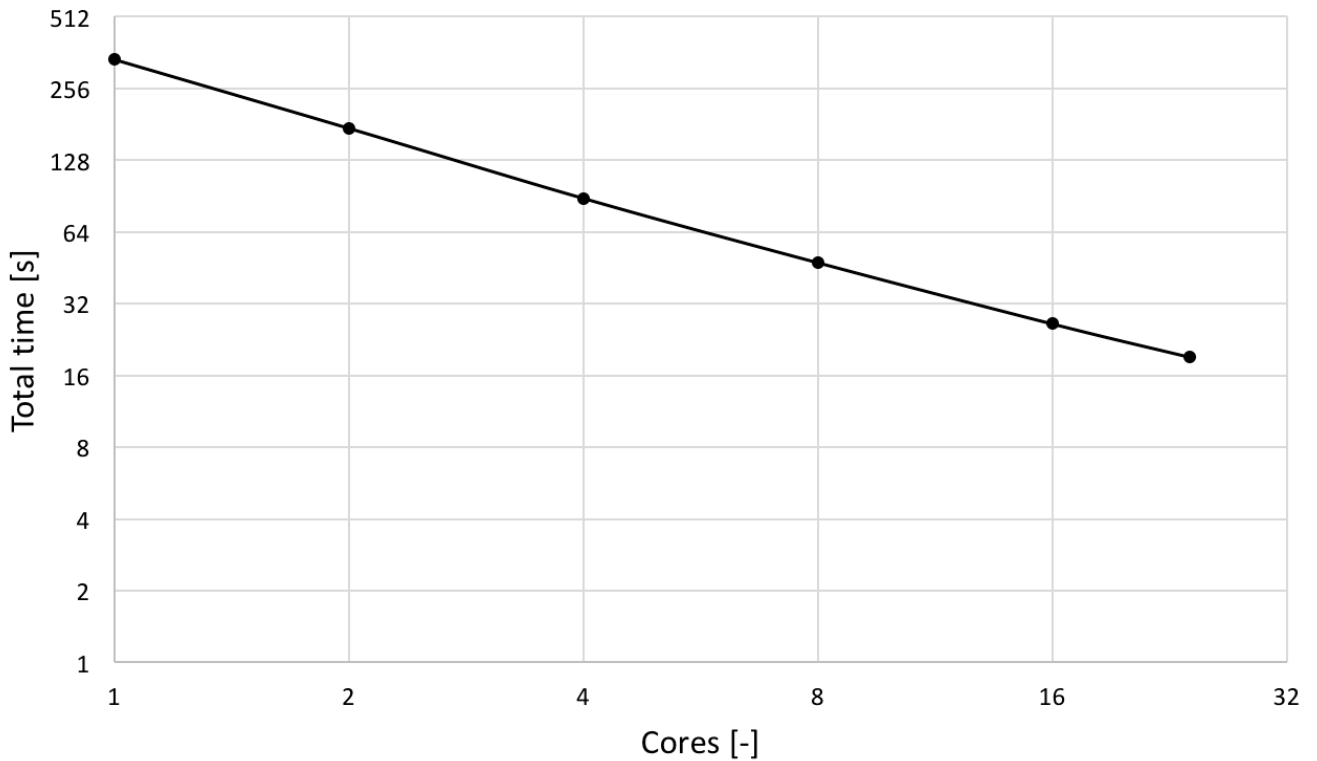
Figure 1.
Total time of the algorithm while utilizing increasing number of CPU cores.

manding operation in the design process is the transformation of the orthosis model to the final shape. The model consists of millions of polygons, therefore to spatially transform each of them we have parallelized the operation by utilizing OpenMP technology. To establish the performance of our implementation we performed measurements focusing on algorithm speed and its possible speed-up by utilizing an OpenMP framework on multiple cores.

In Table 1 we provide time measurements of different parts of the implemented algorithm. As can be seen, the most time consuming part is the transformation of the model to the desired shape and size. Fortunately, this step can easily be parallelized, and more computational resources can be used. The effect of such parallelization is documented in Figure 1.

CPU cores	1	2	4	8	16	24
Shrink [s]	0.80	0.75	0.73	0.72	0.73	0.72
Prepare [s]	85.36	46.44	23.32	12.30	7.96	5.63
Solve [s]	3.94	2.65	2.18	1.96	1.88	1.88
Transform [s]	248.07	124.19	62.29	32.56	15.75	10.87
Total [s]	338.16	174.03	88.51	47.54	26.33	19.09

Table 1.
Computation times within different phases of the algorithm while utilizing OpenMP on 1 to 24 CPU cores.

For the test of the final orthosis design, TPS was used as a kernel function and Bunch-Kaufman factorization of a symmetric matrix using packed storage was used as a solver. Testing was performed on the Salomon supercomputer. The number of vertices of the mesh was 612,546 and the system size was 5452^2. The resulting models can be seen in Figure 2.

Outlook

This work is part of contractual research which aims to automate the whole process, from scanning to 3D printing of the orthosis, and thus is an ongoing task.

Conclusion

We have provided a suitable method based on RBFs for non-rigid transformation of a complex 3D model of a cranial orthosis together with rigid transformation of its specific part that has to preserve the size and the shape. Our method has also been sped up by the OpenMP framework and it can efficiently utilize the available resources of a computer.
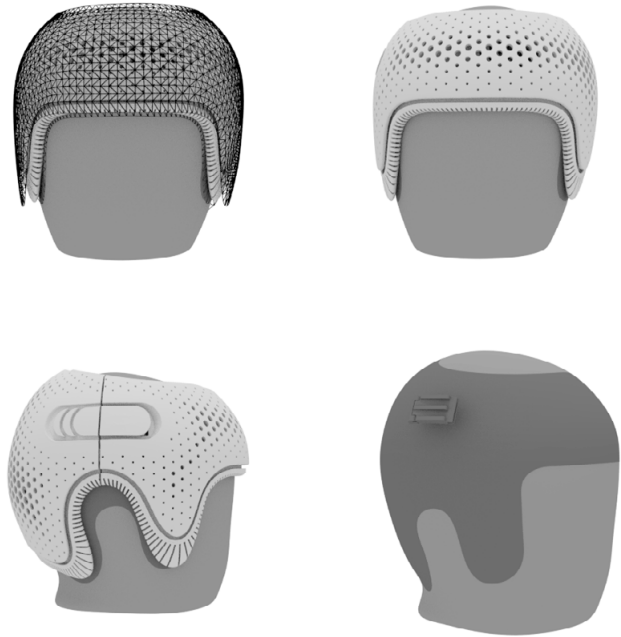
Acknowledgement

Figure 2.
Transformed model of the cranial orthosis to specific size and shape of the head.

References

[1] Clarren, S. K. Plagiocephaly and torticollis: Etiology, natural history, and helmet treatment. The Journal of Pediatrics. 1981, 98(1), 92–95. DOI: 10.1016/S0022-3476(81)80549-5.

[2] Persing, J., H. James, J. Swanson, J. Kattwinkel. Prevention and management of positional skull deformities in infants. PEDIATRICS. 2011, 128(6), 1236–1241. DOI: 10.1542/peds.2011-2220.

[3] Schreen, G., C. G. Matarazzo. Plagiocephaly and brachycephaly treatment with cranial orthosis: a case report. Einstein (São Paulo). 2013, 11(1), 114–118. DOI: 10.1590/S1679-45082013000100021.

[4] Joshi, P., M. Meyer, T. DeRose, B. Green, T. Sanocki. Harmonic coordinates for character articulation. ACM Transactions on Graphics. 2007, 26(3). DOI: 10.1145/1276377.1276466.

[5] de Boer, A., M. S. van der Schoot, H. Bijl. Mesh deformation based on radial basis function interpolation. Computers & Structures. 2007, 85(11–14), 784–795. DOI: 10.1016/j.compstruc.2007.01.013.

[6] Sieger, D., S. Menzel and M. Botsch. High Quality Mesh Morphing Using Triharmonic Radial Basis Functions. Jiao, X. and J.C. Weill, ed. Proceedings of the 21st International Meshing Roundtable. Berlin, Heidelberg: Springer Berlin Heidelberg, 2013, p. 1–15. DOI: 10.1007/978-3-642-33573-0_1.

[7] Modersitzki, J. Numerical Methods for Image Registration. Oxford University Press, 2003. ISBN 9780198528418.

[8] Little, J. A., D. L. G. Hill, D. J. Hawkes. Deformations incorporating rigid structures. Computer Vision and Image Understanding. 1997, 66(2), 223–232. DOI: 10.1006/cviu.1997.0608.

SELECTIVE PLANE ILLUMINATION MICROSCOPY WORKFLOW MANAGER FOR HPC

Research institution:
IT4Innovations National Supercomputing Center

Principal investigator:
Pavel Tomančák

Researchers:
Petr Bainar, Jana Klímová, Jan Kožušznik, Michal Krumnikl, Pavel Moravec, Václav Svatoň

Project partner:
The Max Planck Institute of Molecular Cell Biology and Genetics

Project IDs:
OPEN-12-20, DD-17-31

Introduction

Modern microscopes generate vast amounts of image data that require complex processing. For example, individual acquisitions in Selective Plane Illumination Microscopy (SPIM) can produce several terabytes of images due to very high spatio-temporal resolution. Consequently, processing a typical SPIM dataset on a single computer in a timely manner is often not possible, and employment of high-performance computing (HPC) resources is essential.

Approaches involving HPC clusters often require direct login access to the cluster as well as some expertise in command line operation. Since these two pre-requisites may be unavailable to many researchers, deployment of data processing to remote HPC clusters directly from the graphical user interface (GUI) of a broadly used image analysis platform would substantially lower the entry barrier to this type of parallel processing.

Here we introduce such a solution as a plugin for Fiji ("Fiji Is Just ImageJ"), an open-source platform for biological image analysis [1, 2]. As an application example for the proposed Fiji parallel processing framework we use a complex multi-step processing workflow for large SPIM datasets [3].

Results and Methods

Accessing a remote HPC cluster is often burdened by administrative overhead due to more or less complex security policies enforced by HPC centres. This barrier can be substantially lowered by employing a middleware tool based on the HPC-as-a-Service concept [4]. To facilitate access to HPC from the Fiji environment, we utilize a HEAppE Middleware framework allowing end users to access an HPC system through web services and remotely execute pre-defined tasks. HEAppE is designed to be universal and applicable to various HPC architectures.

We developed a Fiji plugin relying on HEAppE, which enables users to control workflows running on remote HPC resources. As a representative workflow we use a Snakemake-based SPIM data processing pipeline operating on large multi-view SPIM image datasets [3]. The Snakemake workflow engine resolves dependencies between subsequent steps and executes in parallel any tasks appearing to be independent, such as processing of individual time points of a time-lapse acquisition.

The developed plugin can be invoked from the Fiji application menu and enables users to transfer large SPIM data sets to a remote HPC cluster. Moreover, the plugin also features a wizard for pipeline run (job) configuration (Figure 1a) as well as a dashboard for job monitoring and management (Figure 1b). In addition, the plugin provides the user with the option to browse remote resultant data in BigDataViewer [5]. This general approach shall be adopted for any analogous workflow and any HPC infrastructure supporting the HPC as a Service concept.

The test dataset we used was a 90 time-point SPIM acquisition of a Drosophila melanogaster embryo. The dataset consisted of 170 GB of image data.

Using the developed plugin, we transferred the dataset from MPI-CBG in Dresden, Germany to IT4Innovations in Ostrava, Czech Republic and executed the pipeline there on the Salomon supercomputer. Following successful processing, the resultant data were downloaded back to the computer in Dresden.

The data transfer and pipeline execution on Salomon using 90 nodes took 9 hours 37 minutes (see Table 1). For comparison, processing of the same dataset on a common workstation took 23 hours 56 minutes. The results show that despite the data transfer overhead, a significant speedup of SPIM image analysis has been achieved by employing HPC resources.

Data upload	01:40:14 (+/-00:11:13)
Processing	01:41:01 (+/- 00:27:28)
Data download	06:01:12 (+/- 00:17:51)
Total time	**09:22:27 (+/- 00:40:55)**

Table 1.
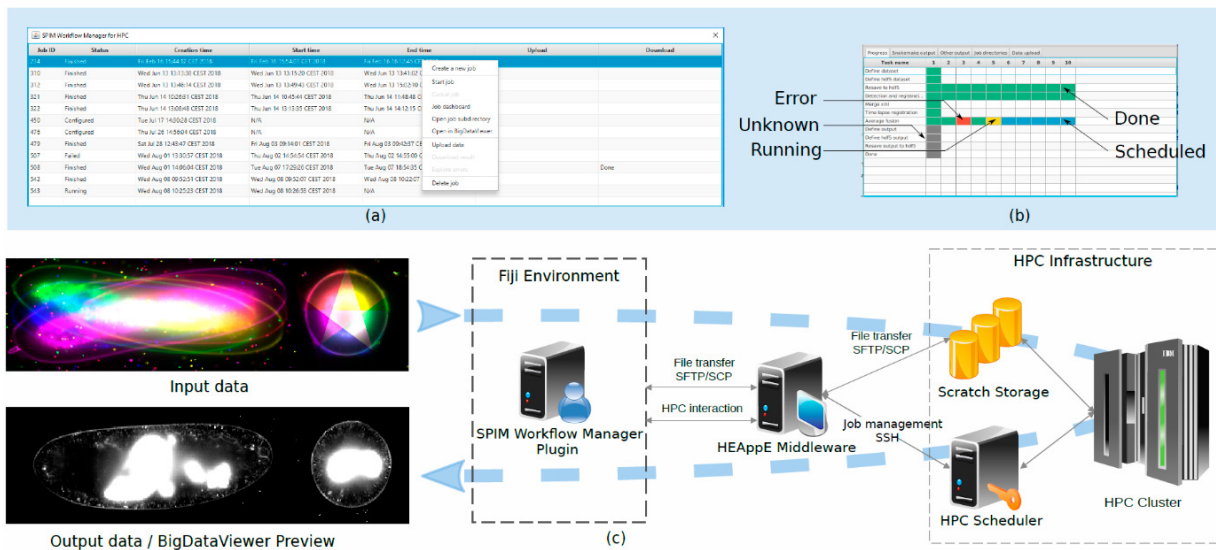*Data transfer and processing on Salomon cluster*

Figure 1.
An overview of SPIM data processing on an HPC cluster: (a) a screenshot of the SPIM Workflow Manager plugin main window with 11 jobs and a context menu; (b) the dashboard for a selected job processing 10 time points of a SPIM recording; (c) an overview of the proposed solution - Left: unregistered and fused SPIM data, Middle: the SPIM data processing workflow in Fiji relying on the HEAppE Middleware framework, Right: an example of an HPC infrastructure.

On-going Research / Outlook

For the future, we will further develop the plugin for Fiji and focus on the data transfer speed.

Conclusion

The developed plugin enables researchers to run computationally intensive tasks on a remote HPC cluster directly from the Fiji environment, significantly enhancing the user experience.

Transferring voluminous data to a remote HPC cluster can be time-consuming, however the imposed overhead is compensated for by the higher processing power offered by the cluster.

Our cluster-mediated data processing approach is applicable to analogous workflows and HPC infrastructures supporting the HPC-as-a-Service concept.

References

[1] Rueden, C., et al. ImageJ2: ImageJ for the next generation of scientific image data. BMC Bioinformatics. 2017, 18(1). DOI: 10.1186/s12859-017-1934-z.

[2] Schindelin, J., I. Arganda-Carreras, E. Frise, et al. Fiji: an open-source platform for biological-image analysis. Nature Methods. 2012, 9(7), 676–682. DOI: 10.1038/nmeth.2019.

[3] Schmied, C., P. Steinbach, T. Pietzsch, S. Preibisch and P. Tomančák. An automated workflow for parallel processing of large multiview SPIM recordings. Bioinformatics. 2016, 32(7), 1112–1114. DOI: 10.1093/bioinformatics/btv706.

[4] Parashar, M., M. Abdelbaky, I. Rodero and A. Devarakonda. Cloud Paradigms and Practices for Computational and Data-Enabled Science and Engineering. Computing in Science & Engineering. 2013, 15(4), 10–18. DOI: 10.1109/MCSE.2013.49.

[5] Pietzsch, T., S. Saalfeld, S. Preibisch and P. Tomančák. BigDataViewer: visualization and processing for large image data sets. Nature Methods. 2015, 12(6), 481–483. DOI: 10.1038/nmeth.3392.

Publications

Krumnikl, M., P. Bainar, J. Klímová, J. Kožusznik, P. Moravec, V. Svatoň, P. Tomančák. SciJava Interface for Parallel Execution in the ImageJ Ecosystem. SAEED, Khalid and Władysław HOMENDA, ed. Computer Information Systems and Industrial Management. Cham: Springer International Publishing, 2018, 2018-09-05, p. 288–299. Lecture Notes in Computer Science. DOI: 10.1007/978-3-319-99954-8_25.

Kožusznik, J., P. Bainar, J. Klímová, M. Krumnikl, P. Moravec, V. Svatoň, P. Tomančák. SPIM Workflow Manager for HPC. Bioimage informatics. 2018 (under review).

Source code: https://github.com/fiji-hpc/hpc-workflow-manager/
Documentation: https://imagej.net/SPIM_Workflow_Manager_For_HPC
HEAppE: http://www.heappe.eu

STRUCTURE AND DYNAMICS OF A RIBOSOME REGULATORY PEPTIDE

Research institution:	Principal investigator:	Project Partner:	Project ID:
The University of Chemistry and Technology in Prague	Michal H. Kolář	The Max Planck Institute for Biophysical Chemistry	Open-12-9

Introduction

Proteins are biomolecules which participate in virtually all processes in cells, ranging from signaling, regulation, catalysis, to structure support, and storage. In all living organisms, the proteins are synthesized by large biomolecular complexes called ribosomes (Figure 1). Ribosomes read the genetic information temporarily stored in a strand of ribonucleic acid (RNA), and translate it into a sequence of amino acids. The amino acids are connected by so called peptide bonds. The ribosomes catalyze the formation of peptide bonds making it possible under conditions common in living matter. Because the catalytic centre is buried deep in the ribosome, all nascent proteins leave the ribosome through a tunnel.

The enormous importance of ribosomes requires precise control of their action. Some regulation mechanisms involve ribosome stalling [1], where the affected ribosome pauses translation, but no protein is released. The stalled ribosomes remain assembled and cannot be recycled. There are many physiological consequences of the stalling: for instance, a large class of antibiotics acts through ribosome stalling [2].

In the genus of marine bacteria *Vibrio*, stalling events regulate how proteins are exported out of the cell. The regulation involves a short peptide called VemP [3]. Recently, the structure of the peptide-ribosome complex has been determined experimentally [4]. VemP is uniquely compact and its structure is well classified. It folds into an α-helix near the catalytic centre which is connected, through an S-shape loop, to another α-helix further along the ribosome tunnel (Figure 1). The inner helix inactivates two nucleobases at the catalytic site, which prevents peptide bond formation.

Using all-atom molecular dynamics (MD) simulations, we studied VemP structure and dynamics on a microsecond time scale. We have attempted to answer what determines the VemP structure. In a broader context, we want to understand, how the tunnel content modulates ribosome function.

Results and Methods

We performed MD simulations of several VemP constructs in an aqueous environment. Namely, we simulated the entire VemP, and the inner and outer helices. Newton's equations of motion were numerically propagated using the GROMACS software package [5], a well established C++ code which uses mixed MPI/OpenMP parallelization and scales up to a few thousand cores [6].
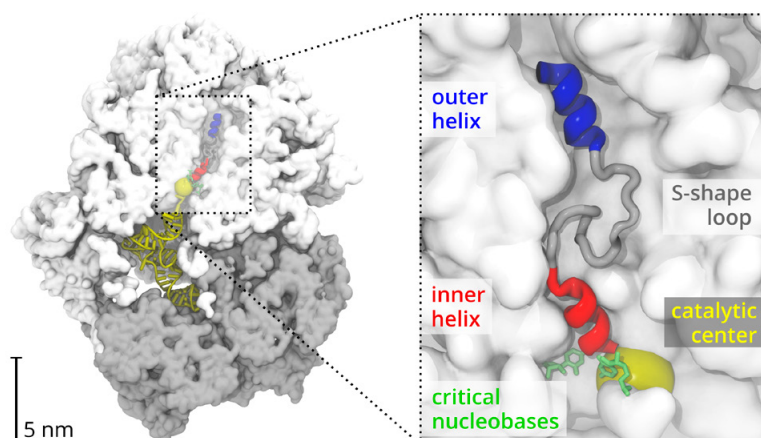

Figure 1.
On the left, a cross-section of a bacterial ribosome is shown with the large ribosomal subunit in white, small ribosomal subunit in grey, and transfer RNA in yellow. On the right, the VemP in the ribosome tunnel features two helical segments. The catalytic centre has the two critical nucleobases highlighted in yellow and green, respectively. Based on PDB 5NWY [4].
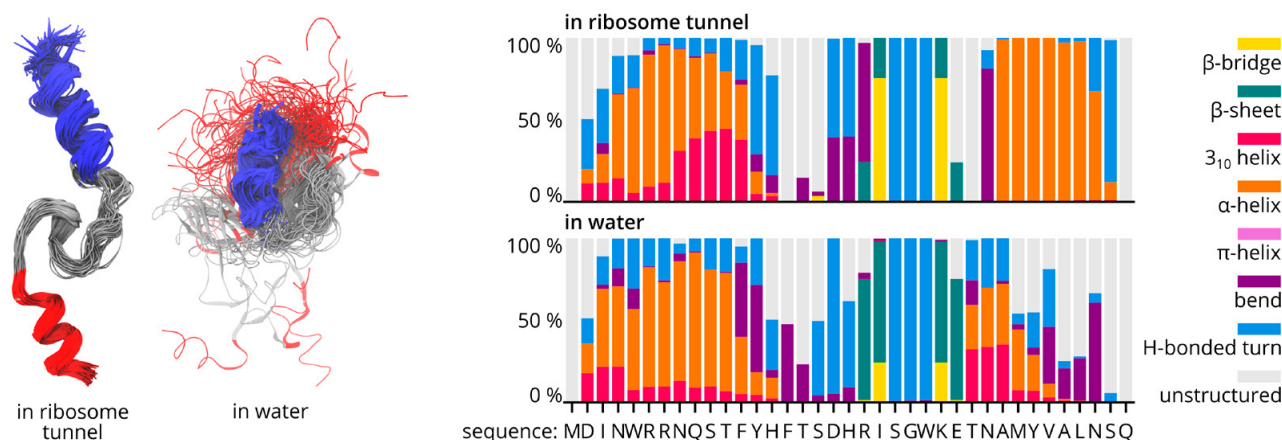
137

Figure 2.
Left: multi-microsecond structural ensembles of the VemP inside and outside the ribosome tunnel.
Right: fractions of various secondary structure motives, as captured by multi-microsecond MD simulations with AMBER parameters.

The peptides were dissolved in a rhombic dodecahedron box filled with explicit water and ions, and simulated at 310 K and 1 bar using periodic boundary conditions. In order to assess, how our conclusions depend on the choice of the empirical potential energy function, two sets of parameters were used to describe the smaller of the systems (inner or outer helix): either the AMBER peptide model with the SPC/E water model, or the CHARMM peptide with the TIP3P water model. For the entire VemP simulations, the AMBER parameters were used. The ensembles of peptide conformations were analyzed and compared with those from the in-ribosome simulations done previously.

Despite the simulations being shorter than the anticipated folding and unfolding times, they suggest that VemP is less stable in water than inside the ribosome tunnel. Starting from the in-ribosome conformation, the entire VemP collapsed down into a more compact conformation within less than 25 ns. The helical character was partially preserved for the outer VemP part, whereas the inner part lost its helicity more notably (red and orange bars in Figure 2). The inner and outer helices, when simulated alone and initiated from the helical structure, lost their helical character and most of the simulation time appeared unstructured. The data for the AMBER and CHARMM sets are qualitatively comparable. Insufficient conformational sampling (i.e. simulation time) prevented us from assessing the quantitative correspondence.

On-going Research / Outlook

Structural information about what happens inside the ribosome tunnel is rather sparse. Traditional biophysical techniques such as X-ray crystallography or cryo-electron microscopy suffer from inherent nascent peptide flexibility. Consequently, the electron density of the tunnel content is often blurred and difficult to interpret. MD simulations may provide a valuable insight into functional motions of the ribosome [7] possibly triggered by the tunnel content.

VemP is able to sense an external mechanical force. The MD simulations (together with the VemP experimental structure) offer a good opportunity to study how VemP responds to such a force, and, most importantly, how the nascent peptides pass through the tunnel. These topics are natural extensions of our current efforts and will be addressed in some of our future simulation projects.

Conclusion

On microsecond time scales, VemP proved stable inside the ribosome tunnel. On the other hand, VemP secondary structure elements are less stable in water, which renders the tunnel walls the structure determining factor. For the inner helix, the tunnel plays a critical role. For the outer helix, the interactions with the tunnel are less important, because the outer helix is somewhat stable even in the water. It agrees with the observation that the tunnel is narrow around the inner helix near the catalytic center, but wider closer to the exit, where the outer helix is located.

References

[1] Wilson, D. N and R. Beckmann. The ribosomal tunnel as a functional environment for nascent polypeptide folding and translational stalling. Current Opinion in Structural Biology. 2011, 21(2), 274–282. DOI: 10.1016/j.sbi.2011.01.007.

[2] Poehlsgaard, J. and S. Douthwaite. The bacterial ribosome as a target for antibiotics. Nature Reviews Microbiology. 2005, 3(11), 870–881. DOI: 10.1038/nrmicro1265.

[3] Ishii, E., et al. Nascent chain-monitored remodeling of the Sec machinery for salinity adaptation of marine bacteria. Proceedings of the National Academy of Sciences. 2015, 112(40), E5513–E5522. DOI: 10.1073/pnas.1513001112.

[4] Su, T., et al. The force-sensing peptide VemP employs extreme compaction and secondary structure formation to induce ribosomal stalling. ELife. 2017, 6. DOI: 10.7554/eLife.25642.

[5] Abraham, M. J., et al. High performance molecular simulations through multi-level parallelism from laptops to supercomputers. SoftwareX. 2015, 1–2, 19–25. DOI: 10.1016/j.softx.2015.06.001.

[6] Kutzner, C., et al. J. Best bang for your buck: GPU nodes for GROMACS biomolecular simulations. Journal of Computational Chemistry. 2015, 36(26), 1990–2008. DOI: 10.1002/jcc.24030.

Publication

[7] Bock, L. V., M. H. Kolář, H. Grubmüller. Molecular simulations of the ribosome and associated translation factors. Current Opinion in Structural Biology. 2018, 49, 27–35. DOI: 10.1016/j.sbi.2017.11.003.

INVESTIGATING PHYSICAL PRINCIPLES OF PROTEIN FOLDING USING QUANTUM-CHEMICAL APPROACHES

Research institution:
The Institute of Organic Chemistry and Biochemistry of the Czech Academy of Sciences

Principal investigators:
Lubomír Rulíšek, Martin Culka

Researchers:
Ondrej Gutten, Jan Řezáč

Project partners:
Jiří Vondrášek, Jakub Galgonek, Jiří Vymětal

Project ID:
OPEN-10-23, OPEN-12-50

Introduction

A full understanding of protein folding is of great interest to the wider scientific community. The majority of current computational studies on protein folding focus on reliable prediction of protein 3D structures based on already resolved protein folds. Alternatively, researchers study the detail of the folding process using empirical force fields, which are in essence trained to reproduce the already known protein folds. Complementary to those empirical approaches, we attempt to derive physico-chemical rules that govern particular primary sequences of amino acids to assume defined 3D structures from the first principles. Consequently, we employ quantum-chemical methods which do not use any information trained on existing experimental protein structures, but rather build on basic physical principles.

Results and Methods

In the first step, we calibrated the quantum mechanical method (dispersion-corrected density functional theory) and solvation model (COSMO-RS) for accurate predictions of conformational energies of medium-sized macrocycles and model tripeptides. It has been shown [1] and argued that an accuracy of 1 kcal.mol^{-1} might be achieved by employing the composite DFT-D3/COSMO-RS protocol (these results were partially obtained at IT4Innovations and acknowledged in the above reference).

The calibrated QM approach is feasible only for reasonably small systems, not only because the geometry optimization and frequency calculation is demanding, but also because we would like to cover the full conformational space of the peptide fragment, which increases with the fragment size. We have chosen tripeptide fragments, firstly because of the reasonable size, and secondly because there are only 8,000 possible combinations of tripeptide sequences, derived from 20 natural amino acids. To better model the situation within the protein chain, we capped the tripeptide on both ends, effectively creating a system with four peptide bonds (Figure 1).
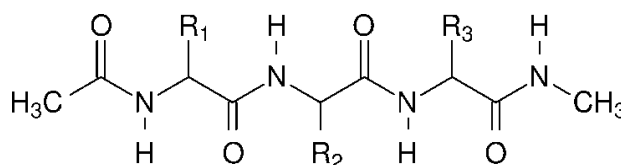

Figure 1.
Model of a capped tripeptide used for atomistic modelling in our research

We surveyed the protein structural database for tripeptide sequences with a strong preference for either a helical or an extended structure. Out of the 8,000 combinations, we chose three sequences which predominantly occur in helices (EAM, KAM and ALA), and three which predominantly occur in extended structure (VIV, VVV and IYI). We extracted the respective conformers from the Top8000 structural database and subjected them to our QM optimization procedure. Additionally, we useded bias-exchange metadynamics to obtain large independent conformer sets for all six tripeptides and treated them in the same way. We evaluated the energies in water, 1-octanol, and hexane to mimic the environment in different parts of the protein. Together, we performed QM geometry optimization and frequency calculation on around 105 conformers, only possible thanks to the IT4Innovations clusters.

The pro-helical conformers had in general lower energy than pro-extended ones (1-5 kcal.mol^{-1}) for all the tripeptides in water, 1-octanol, and hexane. Indeed, when we calculated propensity for the secondary structure using Boltzmann weighting we found out that all the tripeptides from the metadynamics-derived conformer set tend to form helix-like structures. Only the conformers from Top8000 database of the pro-extended tripeptides (VIV, VVV and IYI) retain the tendency to form extended structures in hydrophobic environment of hexane. The environment thus plays a key role in the secondary structure propensity.
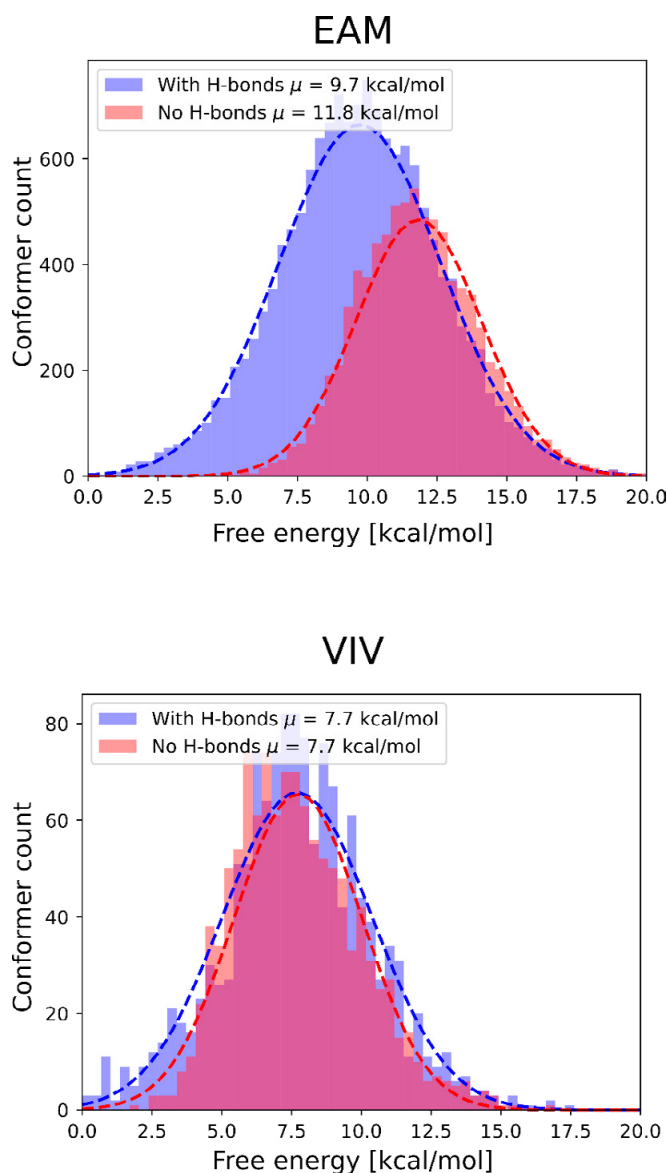
EAM

VIV

Figure 2.
Energy histograms of the conformers of the pro-helical tripeptide
EAM and pro-extended tripeptide VIV from the metadynamics
conformer sets divided into two groups according the presence
of intramolecular hydrogen bonds. Dashed lines represent fits
with a Gaussian function, where μ is the mean value.

We realized that the difference between pro-helical and pro-extended tripeptides cannot lie purely in the structure of their low-energetic conformers, since the compensation energies from the rest of the protein are rather large. We found out that the conformers derived from experimental structures cover a range of energies up to 16 kcal.mol^{-1} wide. We show that the compensation energy of a tripeptide partner in a β-sheet, which stabilizes the extended conformers, can reach up to such values. The difference between pro-helical and pro-extended tripeptides has to thus lie in the comparison of the whole conformer ensembles. Indeed, when we look at the effect of hydrogen bonding on the energetics we see that the pro-helical tripeptides benefit more from the intramolecular hydrogen bonds than the pro-extended conformers (Figure 2). Since the presence of short-range hydrogen bonds is one of the characteristics of the helical structure, we conclude that EAM, KAM and ALA benefit more from helix formation than VIV, VVV and IYI.

To mimic the β-sheet structure, we performed conformational sampling of pro-extended VIV and pro-helical EAM with two partners (FLF and PIW), which represent natural β-sheet partners of these two tripeptides in two crystal structures. To independently compare the behaviour of EAM and VIV, we considered four pairs: VIV-FLF, EAM-FLF, EAM-PIW and VIV-PIW. We calculated interaction free energies for every conformer, and used them to correct the energies of respective conformers of VIV and EAM. We determined that the interaction energies were able to compensate for the relatively high energies (above 5 kcal.mol^{-1} from the global minimum) of the resulting extended conformers. When we plot these conformer energies we see a significant shift of the VIV histogram towards negative values relative to EAM (Figure 3). This means that VIV benefits more from the interaction with both FLF and PIW and thus gains more profit from being part of a β-sheet.
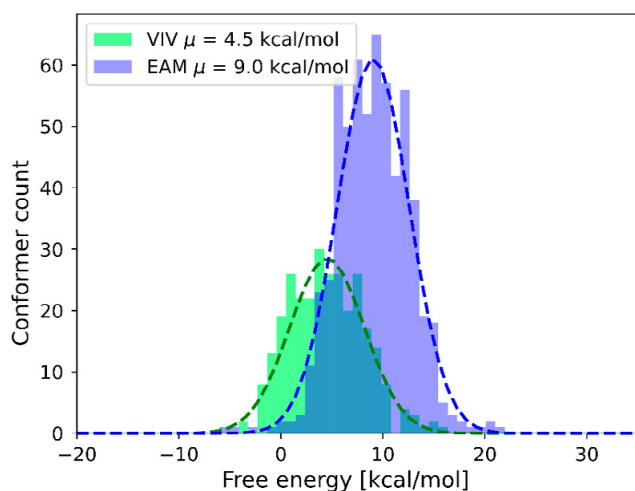
Figure 3.
Histograms of free energies of VIV and EAM tripeptide
conformers relative to the independent VIV and EAM
conformer sets corrected by interaction energies
with a β-sheet-like partner tripeptide FLF in water.
Dashed lines represent fits with a Gaussian function,
where μ is the mean value.

On-going Research / Outlook

Our next research in the area of ab initio protein folding will focus on two aspects. First, since we know the whole conformer ensemble defines the folding tendencies of the tripeptide sequences, we would like to increase the coverage of the conformer space using smaller peptide fragments as building blocks for bigger fragments such as tripeptides. Similar approaches have already been proposed [2], however, they have never been used in conjunction with solvation models, where the conformational space is more diverse. Second, we would like to apply our methodology to tripeptide sequences from several miniproteins such as Trp-Cage or alpha 3D, where the folding mechanism has been studies using molecular dynamics methods [3] and later analyzed using Markov state models [4].

Conclusion

We have developed an accurate and fairly fast methodology to assign free energies to large sets of tripeptide conformers. We applied this approach to peptides with a strong preference for either a helical or an extended secondary structure. We found out that the difference between those tripeptide sequences does not lie in the structure of the low-lying conformers in solution, but rather in the difference in tendencies of the whole conformer ensembles to form either an α-helix or a β-sheet.

References

[1] Řezáč, J., D. Bím, O. Gutten, L. Rulíšek. Toward Accurate Conformational Energies of Smaller Peptides and Medium-Sized Macrocycles: MPCONF196 Benchmark Energy Data Set. Journal of Chemical Theory and Computation. 2018, 14(3), 1254–1266. DOI: 10.1021/acs.jctc.7b01074.

[2] Yu, W., Z. Wu, H. Chen, X. Liu, A. D. Mackerell, and Z. Lin. Comprehensive Conformational Studies of Five Tripeptides and a Deduced Method for Efficient Determinations of Peptide Structures. The Journal of Physical Chemistry B. 2012, 116(7), 2269–2283. DOI: 10.1021/jp207807a.

[3] Lindorff-Larsen, K., S. Piana, R. O. Dror, and D. E. Shaw. How Fast-Folding Proteins Fold. Science. 2011, 334(6055), 517–520. DOI: 10.1126/science.1208351.

[4] Savol, A. J., Chakra S. Chennubhotla. Quantifying the Sources of Kinetic Frustration in Folding Simulations of Small Proteins. Journal of Chemical Theory and Computation. 2014, 10(8), 2964–2974. DOI: 10.1021/ct500361w.

Publications

Řezáč, J., D. Bím, O. Gutten, L. Rulíšek. Toward Accurate Conformational Energies of Smaller Peptides and Medium-Sized Macrocycles: MPCONF196 Benchmark Energy Data Set. Journal of Chemical Theory and Computation. 2018, 14(3), 1254–1266. DOI: 10.1021/acs.jctc.7b01074.

Culka, M, J. Galgonek, J. Vymětal, J. Vondrášek, L. Rulíšek. Towards Ab Initio Protein Folding: Inherent Secondary Structure Propensity of Short Peptides from the Bioinformatics and Quantum-Chemical Perspective. The Journal of Physical Chemistry. Submitted (2018).

MOLECULAR TRANSPORT ACROSS PHOSPHOLIPID MEMBRANE 2

Research institutions:
CEITEC MU,
Masaryk University

Principal investigator:
Robert Vácha

Researchers:
Ivo Kabelka,
Lukáš Sukeník,
Miroslav Jurásek,
Alžběta Türková

Project ID:
OPEN-9-22

Introduction

The inside of a cell is separated from the potentially hostile external environment by a selectively-permeable cytoplasmic membrane. The protective function of the phospholipid membrane can be breached by specific peptides called antimicrobial peptides (AMPs). AMPs are part of the defence system of many organisms, and they could become new therapeutic agents against antibiotic resistant bacteria. The mechanism of AMPs' action is usually direct disruption of plasma membrane or translocation into the bacteria, targeting internal molecules. There are thousands of known AMPs, but molecular understanding and the sequence-to-function relationship is missing [1]. In this project, we elucidated specific properties that allowed peptides to cross biological membranes without significant free energy cost or the need of cellular machinery. Such peptides can be also classified as cell-penetrating peptides and they could be used as therapeutic agents directly, or as carriers for selective and efficient transport of covalently-bound [2, 3] or complexed [4] cargos into target cells.

Results and Methods

We performed both Monte Carlo and Molecular dynamics simulations to determine the free energy landscape of peptides translocating across phospholipid membranes. We used phenomenological coarse-grained models to systematically vary the peptide properties and evaluate their effect. We support the results with all-atom simulations of specific systems. We studied α-helical peptides with different lengths, amphiphilicity, and distribution of hydrophobic content. All peptides showed a similar translocation path consisting of adsorption, tilting, and insertion (see Figure 1).

The peptides were always parallel to the membrane plane in the adsorbed state, and the depth of adsorption was demonstrated to be determined by peptide hydrophobic content. In the tilted state, peptides are partially inserted, with one peptide end in the hydrophobic core. There is a free energy barrier usually associated with the tilted state corresponding to the free energy barrier of the translocation. The inserted state is characterized by the peptide's centre of mass being close to the middle of the bilayer. All peptides, including fully hydrophobic poly-isoleucine peptides, were found to be metastable in the transmembrane orientation in the inserted state, i.e., with peptide ends at opposing leaflets. For the typical free energy profile see Figure 2.

The peptides best at translocating should have a free energy profile as flat as possible, i.e., minimize the difference between the free energy minimum (typically adsorption) and maximum (either the tilted state with a barrier, or solution state). From the calculated free energy profiles we showed the dependence of the profile flatness as a function of peptide length and its hydrophobic content (see Figure 3.) We found that there is an optimal ratio of hydrophilic/hydrophobic content, at which the peptides cross the membrane the easiest, and the optimal length is 4 nm for peptides with charged ends and about 5 nm for peptides with capped ends.

Moreover, we have demonstrated that peptide translocation is dramatically affected by lipid composition. Lipids with positive curvature decrease the translocation barrier and free energy of the inserted state, while peptides with negative curvature, i.e., larger polar heads, increase the free energies.
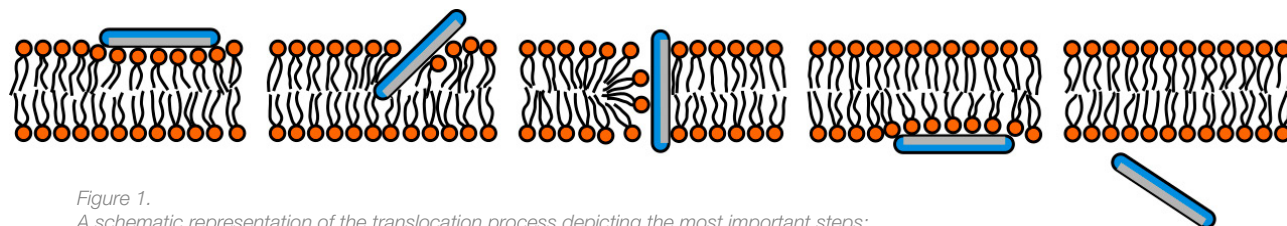

Figure 1.
A schematic representation of the translocation process depicting the most important steps: adsorption to the surface, peptide tilting into the membrane, peptide insertion, its adsorption to the other side of the membrane, and desorption.
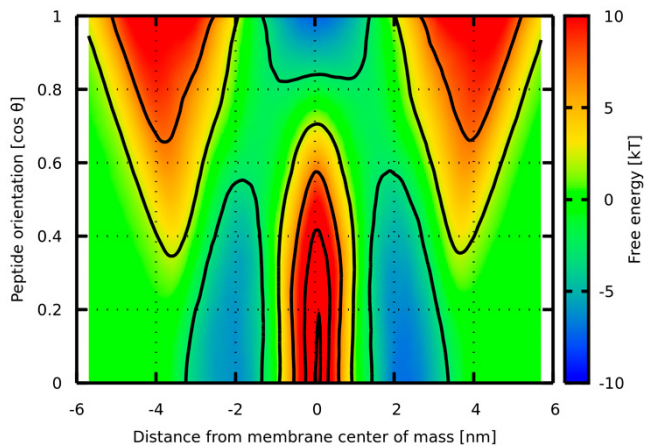
Figure 2.
*A Typical example of the calculated free energy
surface of peptide translocation across a lipid bilayer.
Two important degrees of freedom were selected
for sampling: 1) the peptide distance from the membrane
centre and 2) its orientation with respect to the membrane
normal. The free energy error could be estimated from
the profile asymmetry as the system
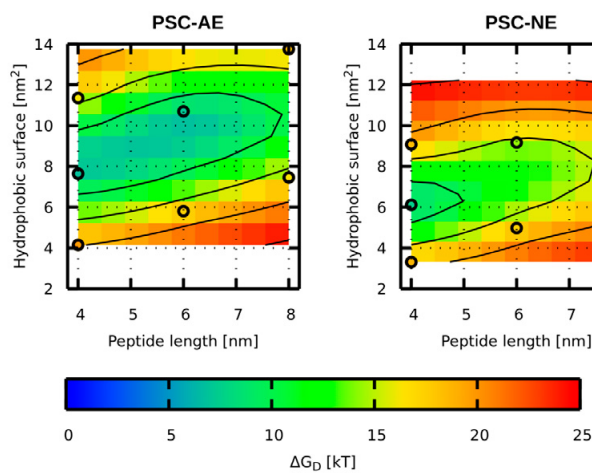is fully symmetric.*

Figure 5. depicts inserted states of poly-isoleucine peptides of different length in their metastable state and preferred orientation.

On-going Research / Outlook

We continue the project with the investigation of specific sequences and their translocation across membranes with various lipid compositions. Several simulations in this direction have already been performed thanks to the support of IT4Innovations.

Conclusion

We are grateful to IT4Innovations, with whose support we were able to perform extensive Monte Carlo and molecular dynamics simulations. This allowed us to determine the optimal hydrophobic content of amphiphilic helical peptides to translocate across phospholipid membranes. The translocation barrier is affected by the chemical nature of peptide ends and lipid composition with negatively curved lipids making the translocation easier. These findings are in agreement with experimental results using fluorescence leakage assays, and provide general guidance to develop new peptides, which could be used as antimicrobial, cell-penetrating, and drug-delivery molecules.
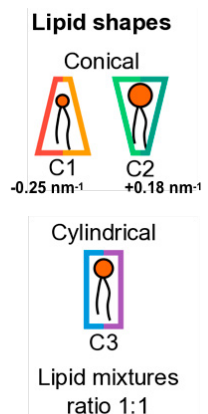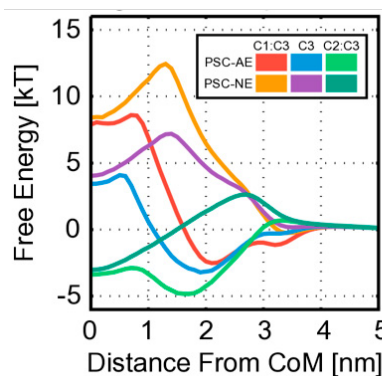

Figure 3.
*The largest free energy differences on the peptide
translocation profiles as a function of peptide length
and hydrophobic content. Two versions of peptide ends
were considered: the peptide with hydrophobic (capped)
ends are displayed in the left figure, and peptides with
naturally charged ends are depicted in the right figure.
Individual data points from the simulations are shown
in circles. The surface is created by interpolation
and contours are drawn every 5 kT.*

Figure 4.
*Calculated free energy profiles of peptide
translocation across the membrane for membranes
of different lipid compositions are on the left. Only half
of the profile is shown for clarity (the second half is
symmetrical). We used lipid mixtures of cylindrical
and conical lipids with a 1:1 ratio. The employed lipids
with their intrinsic curvatures are depicted on the right.
PSC-AE label peptides with hydrophobic ends,
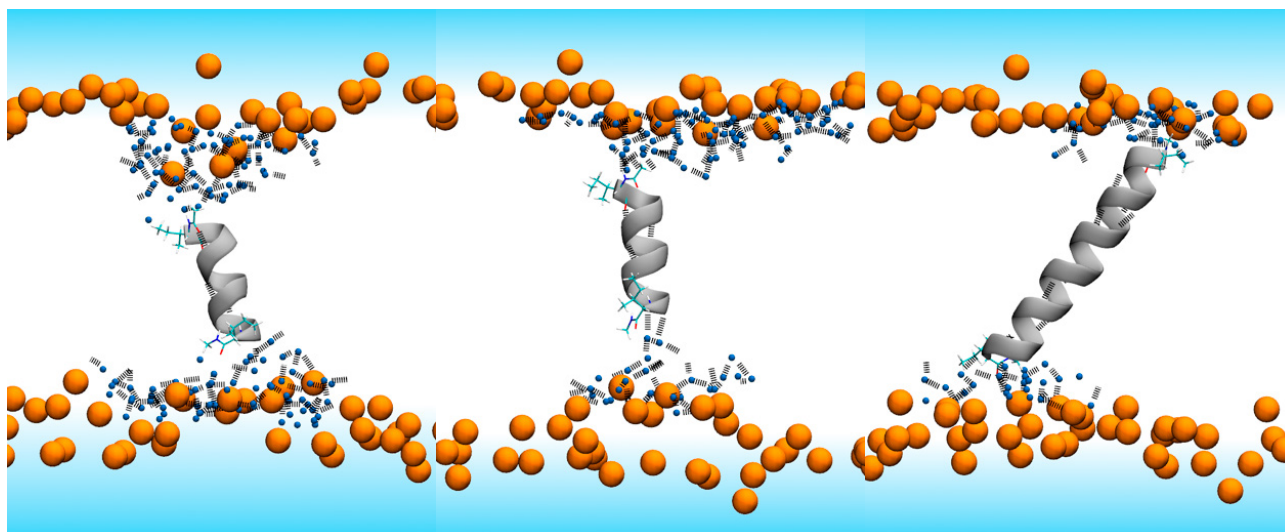while peptides with hydrophilic ends
are labled PSC-NE.*

Figure 5.
Snapshots from the end of 500 ns long simulations of poly-isoleucine peptides with terminal capping in the membrane inserted state. Peptides of a length of 8 (left), 11 (middle), and 21 (right) residues are shown. Lipid phosphates are shown in orange, water oxygens in the peptide proximity are shown in blue, peptide terminal residues are highlighted by sticks, and black dashed lines represent hydrogen bonds. The middle of the membrane is white, while aqueous solution is coloured blue.

References

[1] Scocchi, M., M. Mardirossian, G. Runti, and M. Benincasa, 2016. Non-Membrane Permeabilizing Modes of Action of Antimicrobial Peptides on Bacteria. Current Topics in Medicinal Chemistry. 2015, 16(1), 76–88. DOI: 10.2174/1568026615666150703121009.

[2] Zorko, M., and Ü. Langel. Cell-penetrating peptides: mechanism and kinetics of cargo delivery. Advanced Drug Delivery Reviews. 2005, 57(4), 529–545. DOI: 10.1016/j.addr.2004.10.010.

[3] Bendifallah, N., F. W. Rasmussen, V. Zachar, P. Ebbesen, P. E. Nielsen, and U. Koppelhus. 2006. Evaluation of cell-penetrating peptides (CPPs) as vehicles for intracel- lular delivery of antisense peptide nucleic acid (PNA). Bioconjugate Chemistry. 2006, 17(3), 750–758. DOI: 10.1021/bc050283q.

[4] Crombez, L., G. Aldrian-Herrada, K. Konate, Q. N. Nguyen, G. K. McMaster, R. Brasseur, F. Heitz, and G. Divita, 2009. A new potent secondary amphipathic cell–penetrating peptide for siRNA delivery into mam- malian cells. Molecular Therapy. 2009, 17(1), 95–103. DOI: 10.1038/mt.2008.215.

Publications

Kabelka, I., R. Vácha. Optimal Hydrophobicity and Reorientation of Amphiphilic Peptides Translocating Through Membrane. Biophysical Journal. 2018, 115(6), 1045–1054. DOI: 10.1016/j.bpj.2018.08.012.

Leber, R., M. Pachler, I. Kabelka, I. Svoboda, D. Koller, R. Vácha, K. Lohner, G. Pabst. Synergism of Antimicrobial Frog Peptides Couples to Membrane Intrinsic Curvature Strain. Biophysical Journal. 2018, 114(8), 1945–1954. DOI: 10.1016/j.bpj.2018.03.006.

COMPOUND ACTIVITY PREDICTION USING HIGH-PERFORMANCE MATRIX FACTORIZATION

Research institutions:	Principal investigator:	Researchers:	Project IDs:
IMEC, Aalto University, Janssen Pharmaceutica NV	Tom Vander Aa	Xiangju Qin, Felipe Golib Dzib	OPEN-8-6, OPEN-11-20

Introduction

Exascale computing will provide vast amounts of computing power. In the European H2020 project ExCAPE [1] we have used this computational power to apply large scale machine learning to difficult prediction problems such as pharmaceutical compound activity description. Matrix factorization is a relatively well known and highly demanding machine learning method, which for example Amazon and Netflix use to predict books or movies you might like. In this project we investigated how to apply matrix factorization in drug discovery. We examined how the algorithms and implementations work on large scale system and tested them on realistic industrial data sets. As such this project has brought together HPC and Big Data challenges, through the calculation of complex empirically driven models on large data sets.

Results and Methods

Recommender Systems and Matrix Factorization

Recommender Systems (RS) have become very common in recent years and are useful in various real-life applications. The most popular ones are probably suggestions for movies on Netflix and books from Amazon. However, they can also be used in more unlikely areas, such as drug discovery, where a key problem is the identification of candidate molecules that affect proteins associated with diseases.

In RS one must analyze large and sparse matrices, for example those containing the known movie or book ratings. Matrix Factorization (MF) is a technique that has been successfully used here. As sketched in Figure 1, the idea of this method is to approximate the rating matrix R as a product of two low-rank matrices U and V [2]. Predictions can be made from the approximation U ✕ V which is dense.

Developing SMURFF

While MF is promising, it is very computationally intensive. Hence, we developed SMURFF, a high-performance framework to do matrix factorization on HPC systems. SMURFF was developed during the ExCAPE project. The key application in ExCAPE is chemogenomics: the task of predicting the activity of compounds in the drug discovery phase of the pharmaceutical industry.

Performance Benchmarking

Figure 2 compares the performance of SMURFF with two other popular packages for MF. The X-axis shows the number of cores used. We tested the PyMC3, GraphChi, and SMURFF implementations on a single node with 36 cores, since these implementations do not support multiple nodes, and the "BMF
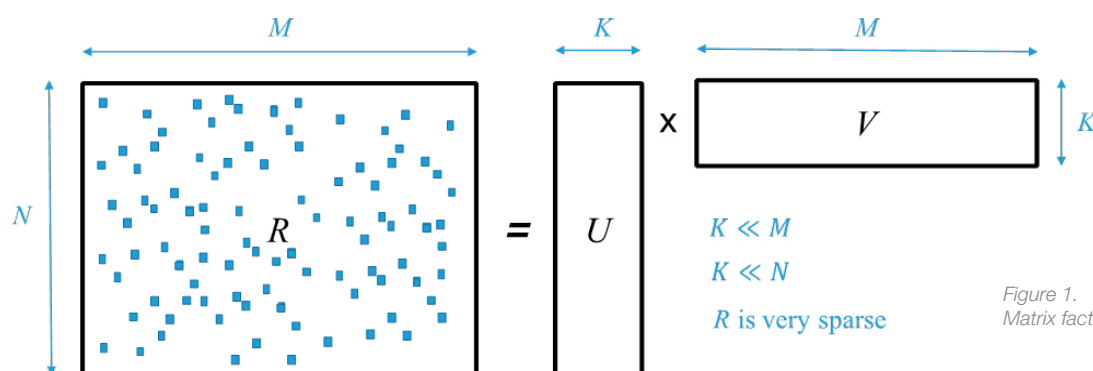

$K \ll M$

$K \ll N$

R is very sparse

Figure 1.
Matrix factorization

with GASPI"-implementation [3] on a system with 128 nodes and 2,048 cores in total, since this version has been optimized for a multi-node supercomputer.

The results show that SMURFF is 15x faster than GraphChi [4], and 1,400x faster than PyMC3 [5]. This is because PyMC3 and GraphChi are very versatile frameworks, easy to use and with many more possibilities than SMURFF. PyMC3, for example, has a high-level Python interface where one can choose many different samplers, from many different distributions. One can even implement custom samplers and distributions in Python. SMURFF on the other hand only supports Gibbs sampling, from Normal distributions. As expected, the BMF-with-GASPI version scales very well, up to 1,000 cores, as shown in [3].

Large Scale Runs

Several large scale SMURFF runs were performed on the Ex-CAPE dataset (v5) using the HyperLoom work-flow framework [6]. We performed a full cross-fold validation to find and verify the best hyperparameters. For example, for the inner fold validation, we explored 37 hyperparameter combinations for 6 folds, resulting in 222 runs of SMURFF.

We did three large-scale runs (inner folds, outer folds, and full dataset) with 703 HyperLoom tasks in total, consuming 180,000 core hours, running on up to 100 nodes in parallel. Out of the 703 tasks, 33 are data preparation, 335 are training tasks, and 335 are prediction tasks on the test set. We produced 335 models with SMURFF. Each model consumed between 508 and 1,700 GB in disk space, for a total disk space used of 221 TB.

On-going Research / Outlook

While the ExCAPE project has finished, SMURFF is still being actively enhanced. We are working on GPU support, investigating the use of FPGAs for the prediction phase, and working on an ultra-scalable algorithm based on posterior propagation.

Conclusion

SMURFF is a multi-core high-performance framework that supports a wide range of Bayesian matrix-factorization algorithms. SMURFF is available as open-source and can be used both on a supercomputer, and on a desktop or laptop machine. The framework has been successfully used to do large scale runs of compound-activity prediction.
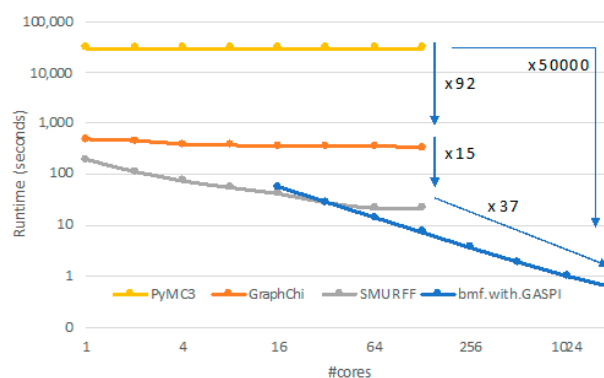

*Figure 2.*
Comparing performance of SMURFF

References

[1] The ExCAPE Consortium. ExCAPE: Exascale Compound Activity Prediction Engine. Available at http://excape-h2020.eu/. Retrieved: June 2017.

[2] Salakhutdinov, R., and A. Mnih. Bayesian probabilistic matrix factorization using Markov chain Monte Carlo. In: Proceedings of the International Conference on Machine Learning. New York, USA: ACM Press. 2008, 25, 880–887. DOI: 10.1145/1390156.1390267.

[3] Vander Aa, T., I. Chakroun, and T. Haber. Distributed Bayesian probabilistic matrix factorization. Procedia Computer Science. 2017, 108, 1030–1039. DOI: 10.1016/j.procs.2017.05.009.

[4] Kyrola, A., G. Blelloch, and C. Guestrin. Graphchi: Large-scale graph computation on just a PC. In: Proceedings of the 10th USENIX Conference on Operating Systems Design and Implementation, ser. OSDI'12. Berkeley, CA, USA: USENIX Association. 2012, p. 31–46. ISBN: 978-1-931971-96-6

[5] Salvatier, J., T. Wiecki, and C. Fonnesbeck. Probabilistic programming in python using PyMC3. PeerJ Computer Science. 2016, 2. DOI: 10.7717/peerj-cs.55.

[6] Cima, V., S. Böhm, J. Martinovic, J. Dvorský, K. Janurová, T. Vander Aa, T. Ashby, V. Chupakhin. HyperLoom: A Platform for Defining and Executing Scientific Pipelines in Distributed Environments. In: Proceedings of the 9th Workshop and 7th Workshop on Parallel Programming and RunTime Management Techniques for Manycore Architectures and Design Tools and Architectures for Multicore Embedded Computing Platforms - PARMA-DITAM '18. New York, USA: ACM Press, 2018, p. 1–6. DOI: 10.1145/3183767.3183768.

Publication

06 | PHYSICS
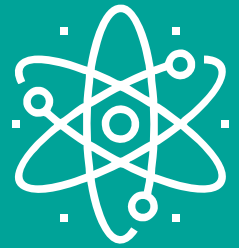
LASER-DRIVEN ION ACCELERATION USING CRYOGENIC HYDROGEN TARGETS

Research institution:	Principal investigator:	Researchers:	Project partners:	Project IDs:
The Czech Technical University in Prague	Martin Matys	Jan Pšikal, Mariana Danielová, Petr Valenta, Sergei Vladimirovich Bulanov	ELI Beamlines (the Institute of Physics of the Czech Academy of Sciences), The Institute of Plasma Physics of the Czech Academy of Sciences	OPEN-10-7, OPEN-12-28

Introduction

Current development of 10 PW laser facilities, such as Extreme Light Infrastructure (ELI) in the Czech Republic, provides new and interesting phenomena in the physics of laser-plasma particle accelerators. This type of accelerator already generates much stronger electric fields in comparison with conventional ones, and may possibly replace them in future in impressive applications, such as proton therapy for the treatment of cancer cells, production of PET (positron emission tomography) medical isotopes, and generation of ultrashort neutron pulses, which are useful in material engineering. The afore mentioned new phenomena, such as relativistic transparency, are enhanced by the production of newly developed targets, such as a cryogenic thin solid-hydrogen ribbon with much lower density than ordinary plastic or metal targets. Therefore, the objective of this project was to study proton acceleration due to the interaction of high-power laser pulse (relevant to ELI) with a hydrogen ribbon of currently realistic thickness, which can be used in experiments in the near future.
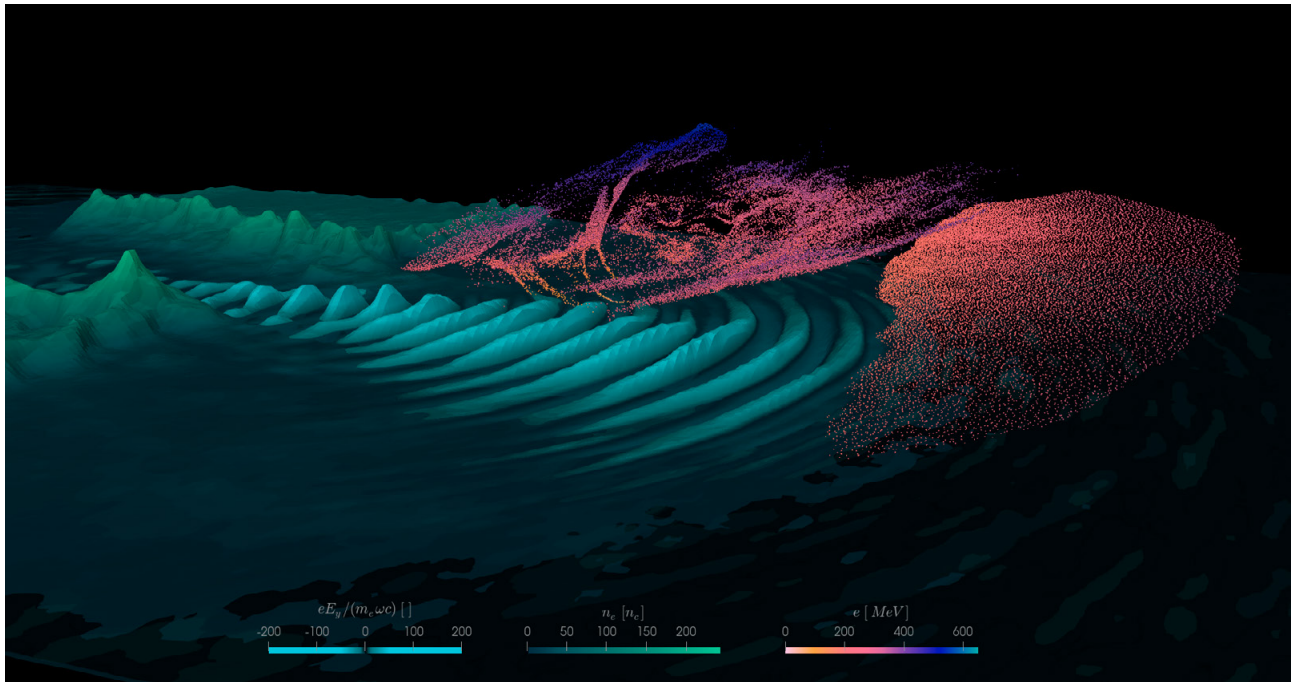

Figure 1.
Laser pulse electric field (light blue), electron density (gray to green) and energy of tracked accelerated protons (purple to blue)
in the 2D simulation. The values of these parameters are visualized by color and by height in the vertical direction.
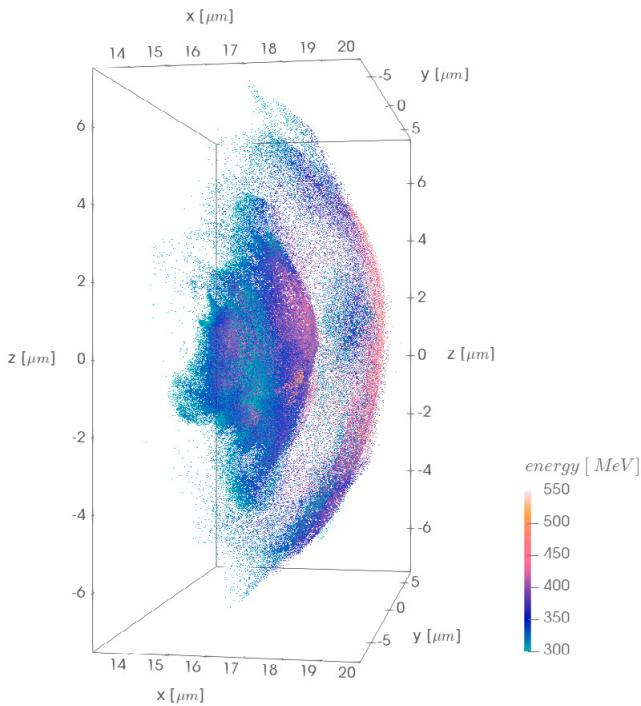
Figure 2.
Positions of tracked accelerated protons with energy
higher than 300 MeV in a 3D simulation

Results and Methods

We studied the interaction of a 10 PW laser with a cryogenic hydrogen target (down to 15 μm) with the help of 2D and 3D particle-in-cell simulations (namely code EPOCH [3]) and a self-implemented particle tracker (created in collaboration with our colleagues from the Institute of Plasma Physics). The combination of high laser intensities and low target densities demonstrated the importance of the RPA mechanism, which dominates TNSA both in the number of accelerated protons and in the maximum energies reached (about 9 times more protons with energy over 10 MeV). After the laser pulse burns through the target, the RIT regime occurs, accelerating protons to energies over 600 MeV. All of these acceleration mechanisms can be seen in Figure 1, where all protons with energy over 300 MeV at the end of the 2D simulation were tracked. Firstly, a cloud of TNSA protons ahead of the laser pulse is visible, then a cloud of RPA protons with higher energies than the previous one, and finally a smaller clump of the most energetic protons is developed above the middle of the figure by the RIT regime. Since 2D simulations can neglect some laser-plasma behaviours and overestimate proton energy [4], more realistic 3D simulations were performed. In comparison to 2D simulations, the laser pulse burned through the target faster, while the temperature of hot electrons was lower. These effects resulted in an increase of energy of protons accelerated by RPA but a reduction in the energy of those accelerated by TNSA [5]. RPA protons with higher energies were then able to overcome slower TNSA protons as is shown in Figure 3; also a group of high-energy protons emerges in the area around position [18,0,0] μm due to the RIT regime.

Data from our simulations were also visualized in collaboration with our colleagues from the Virtual Beamline team at ELI Beamlines, and are used for promotion of laser-plasma physics in the 3D virtual reality web application as it enables people to literally step into the (virtualised) physical interaction and look around, as can be seen in the photos in Figure 3. This immersive approach can also be used for future educational purposes, since different acceleration mechanisms are clearly demonstrated in our data and can be more easily explained inside this 3D virtual reality world than using a 2D screen.
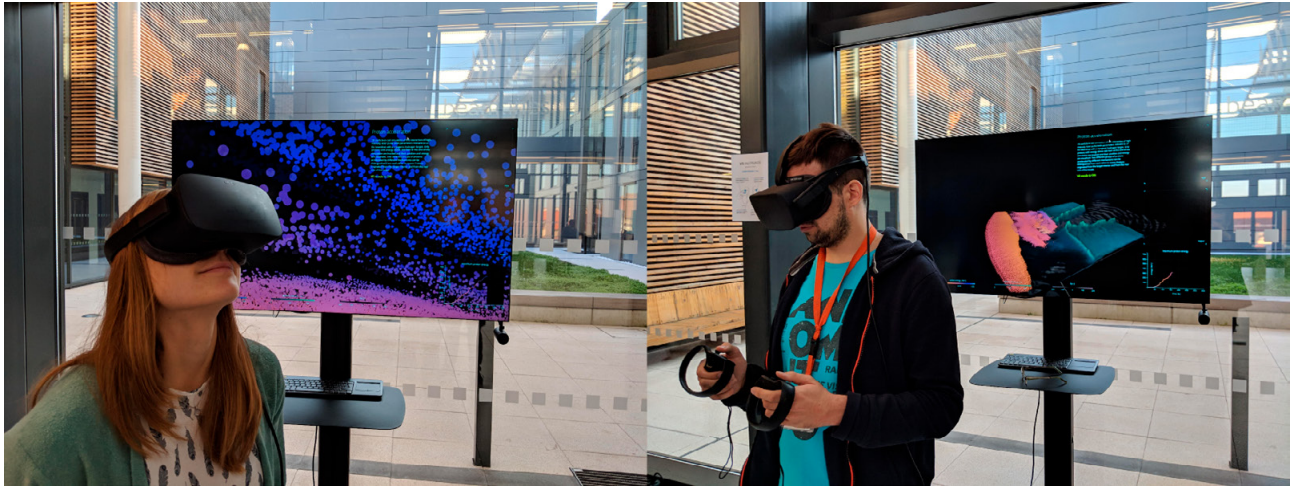
When the laser pulse is interacting with the target, several different ion acceleration mechanisms [1] can be distinguished from each other, as they are acting on different areas of the target. In this work we focused on three main acceleration mechanisms, target normal sheath acceleration (TNSA) acting on the rear side of the target, radiation pressure acceleration (RPA) acting on the front side of the target, and relativistic induced transparency regime (RIT) [2], which takes place after the laser pulse burns through the overdense target and propagates through remaining low density plasma regions. Proper understanding of these acceleration mechanisms and comparison of their efficiency via simulations is important for optimization of target parameters, because the target fabrication and the experimental investigation on multi-petawatt class lasers are currently very costly. Moreover, numerical simulations show the evolution of plasma and acceleration of charged particles with very high temporal resolution which is not accessible by any experimental diagnostics. Our simulations proved the dominance of the RPA mechanism over the TNSA mechanism in our scenario, and the appearance of the RIT regime, which accelerated a relatively small fraction of particles into the highest energy range of several hundreds of MeV.

Figure 3.
Our data visualized in a 3D virtual reality web application

On-going Research / Outlook

Longer 3D simulations with current and lower target thickness are planned.

Conclusion

Our simulations proved the dominance of the RPA mechanism over the TNSA, and occurrence of the very efficient RTI regime in our simulation scenario. The upgrading of the simulation dimension to 3D resulted in enhancement of the RPA acceleration.

References

[1] Macchi, A., M. Borghesi, and M. Passoni. Ion acceleration by superintense laser-plasma interaction. Reviews of Modern Physics. 2013, 85(2), 751–793. DOI: 10.1103/RevModPhys.85.751.

[2] Higginson, A., R. J. Gray, and M. King. Near-100 MeV protons via a laser-driven transparency-enhanced hybrid acceleration scheme. Nature Communications. 2018, 9(1). DOI: 10.1038/s41467-018-03063-9.

[3] Arber, T. D., K. Bennett, C. S. Brady, et al. Contemporary particle-in-cell approach to laser-plasma modelling. Plasma Physics and Controlled Fusion. 2015, 57(11). DOI: 10.1088/0741-3335/57/11/113001.

[4] Stark, D. J., L. Yin, B. J. Albright, and F. Guo. Effects of dimensionality on kinetic simulations of laser-ion acceleration in the transparency regime. Physics of Plasmas. 2017, 24(5). DOI: 10.1063/1.4982741.

[5] Pšikal, J., and M. Matys. Dominance of hole-boring radiation pressure acceleration regime with thin ribbon of ionized solid hydrogen. Plasma Physics and Controlled Fusion. 2018, 60(4). DOI: 10.1088/1361-6587/aaa7fa.

Publications

Pšikal, J., and M. Matys. Dominance of hole-boring radiation pressure acceleration regime with thin ribbon of ionized solid hydrogen. Plasma Physics and Controlled Fusion. 2018, 60(4). DOI: 10.1088/1361-6587/aaa7fa.

Pšikal, J., and M. Matys. Ultra-intense laser interaction with specially-designed targets as a source of energetic protons. In: Proc. SPIE 10241, Research Using Extreme Light: Entering New Frontiers with Petawatt-Class Lasers III. Prague, the Czech Republic, 17 May 2017. DOI: 10.1117/12.2271026.

MOLECULAR DYNAMICS, Rg_2^+/Rg COLLISION

Research institutions:
IT4Innovations
National
Supercomputing
Center,
Laplace – Université
Toulouse III – France

Principal investigator:
Cyril Van de Steen

Project ID:
OPEN-10-3

Introduction

Ion swarm data, such as diffusion coefficient, reduced mobility, and dissociation constant rate, are necessary in chemical electro-hydrodynamic plasma models for optimizing krypton plasma reactors, which are used in different applications such as the biomedical field [1] and space craft propulsion [2]. Measurements of ionic dimer mobility in its parent gas are limited to a small range of reduced electric field and, for diffusion, are not available in the literature. The aim of the presented work is to complete the data missing in the literature.

Results and Methods

Transport coefficients and rate constants calculations of collision processes in low temperature plasma comprise the following steps: 1) effective cross-sections must be calculated for all the relevant collision channels, 2) transport coefficients are then obtained from physical kinetics methods to be further used in macroscopic modeling.

Two channels are considered relevant for the cross-sections calculations. First, the non-reactive scattering (NRS),

$$Kr_2^+ + Kr \rightarrow Kr_2^+ + Kr, \tag{1}$$

has been calculated for a broad range of collision energies within the momentum-transfer approximation together with collision induced dissociation (CID),

$$Kr_2^+ + Kr \rightarrow Kr^+ + 2Kr . \tag{2}$$

Butches of trajectories have been integrated numerically for a sufficiently broad range of the collision energy, E_{coll}, and the impact-parameter, b. 504 trajectories have been integrated for a particular value of b, in total 200-300 different values of b have been considered for each collision energy, $E_{coll} = 0.01 – 100$ eV. Then, inelastic and elastic cross-sections were calculated using the hybrid dynamical method, which consists of quantum treatment of electrons and classical treatment of nuclei. In this work, several sets of DIM (Diatomics-In-Molecule) potential models are used and compared. The DIM approach [3] consists of writing the electronic Hamiltonian as a sum of diatomic and atomic contributions which are represented by accurate ion–neutral and neutral–neutral diatomic potentials. For the ion-neutral interac-
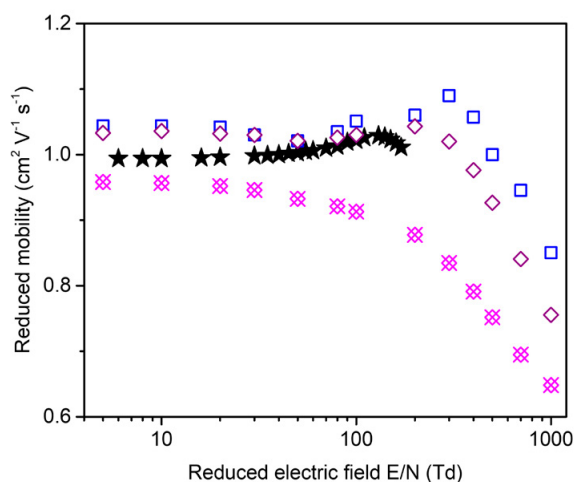

Figure 1.
Standard reduced mobility of Kr_2^+ ions in Kr gas at T = 295 K and P = 760 Torr. Experimental values: [12]. This work: using ion-neutral potentials of Ref. [4]. □ No rovibronic excitation (ΔE=0 eV), ◇ (ΔE=0.024 eV), ※ (ΔE=0.267 eV).

tion, we used Bohommeau et al. and Kalus et al. interaction potentials [4, 5], like in a previous work [6]. For the neutral-neutral interactions, four different interaction potentials were used [7–9], where the fourth potential represents a refitting of the Waldrop neutral potential [8] done by Jäger [9]. Cross-sections, obtained from dynamical calculations were then used in a Monte Carlo code [10] to calculate mobilities over a large range of electric field, and compared with available experimental data. This methodology had already been used in previous studies on other rare-gas ions collisions with their carrier gas (see i.e. [11]).

Figure 1 displays the calculated Kr_2^+/Kr mobilities using the Aziz neutral-neutral potential [7] for Kr/Kr interaction and Bonhommeau potentials [4] for Kr^+/Kr interaction; various rovibronic excitations of the Kr_2^+ ion are considered. This figure shows, as expected, that the Kr_2^+ mobility decreases when vibrational or rotational energies increase. Moreover, we notice that the change of the dimer mobility does not depend much on whether the excitation energy is stored in vibrational or rotational modes.

Furthermore, in order to show the influence of neutral-neutral potential on the mobility, three more neutral–neutral potentials

were used and compared to each other. For example, Figure 2 displays relative deviations of the mobility calculated using the Waldrop neutral-neutral potential [8] as compared to the Aziz one [7]. The observed strong deviations result from the big difference between the repulsive wall in the interaction potential of Aziz and the one of Waldrop (as well as other ab initio potentials). Only deviations between Waldrop and Aziz mobilities are shown here since the others are very close to the one calculated from the Waldrop potential.

On-going Research / Outlook

Now that electronic ground state dimer (Kr_2^+) is investigated, complementary calculations with electronically excited dimers are actually performed within project OPEN–13–2 to observe the influence of the electronic excitations

Conclusion

For electronic ground state ionic krypton dimer collisions with krypton atoms, the hybrid method combined with the Monte Carlo code provides coherent results with experimental values. Dependence on the ionic-neutral potential is attenuated compared to atom-atom collisions, but accurate interatomic potentials (ion-neutral and neutral-neutral) are still crucial to obtain realistic estimates of the reliable mobility and drift coefficient.
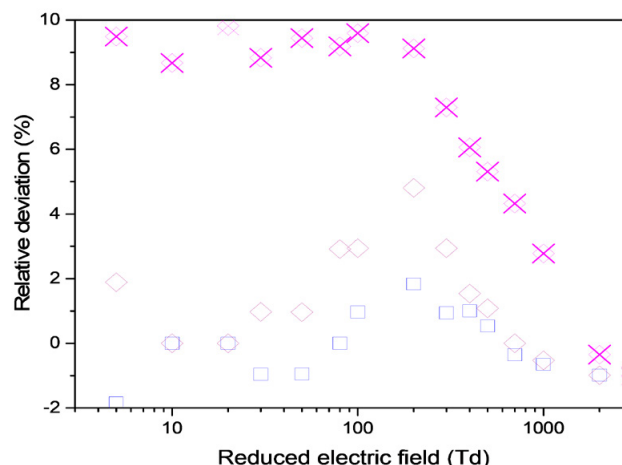

Figure 2.
Relative deviation of reduced mobility of Kr_2^+ ions in Kr gas at T = 295 K and P = 760 Torr, obtained from comparison of neutral potentials of Ref [8] to Ref [7].
☐ *No rovibronic excitation (ΔE=0 eV),* ◇ *(ΔE=0.026 eV),* ✻ *ΔE=0.267 eV).*

References

[1] Machala, Z., K. Hensel, and Y. Akishev. Plasma for Bio-Decontamination, Medicine and Food Security. Dordrecht: Springer Netherlands. New York: Springer, c2012. NATO Science for Peace and Security Series A: Chemistry and Biology. ISBN 978-94-007-2851-6.

[2] NASA - Ion Propulsion. NASA [online]. 2016. Available at: https://www.nasa.gov/centers/glenn/about/fs21grc.html

[3] Ellison, F. O. A Method of Diatomics in Molecules. I. General Theory and Application to H_2O. Journal of the American Chemical Society. 1963, 85(22), 3540-3544. DOI: 10.1021/ja00905a002.

[4] Bonhommeau, D., T. Bouissou, N. Halberstadt and A. Viel. Modelization of the fragmentation dynamics of krypton clusters (Kr_n,n=2–11) following electron impact ionization. The Journal of Chemical Physics. 2006, 124(16), 164308. DOI: 10.1063/1.2186645.

[5] Kalus, R., et al. Modelling of Kr_n^+ clusters (n=2–20). I. Structures and energetics. Chemical Physics. 2003, 294(2), 141-153. DOI: 10.1016/j.chemphys.2003.07.004.

[6] Van de Steen, C. et al. Mobility of Kr^+ ions in Kr for cold plasma modelling. In: Proceedings of the XXXIII International Conference on Phenomena in Ionized Gases. Estoril, Portugal, July 9–14, 2017. Available online at http://icpig2017.tecnico.ulisboa.pt/wp-content/uploads/2017/06/ICPIG2017_proceedings.pdf

[7] Aziz, R. A., and M. J. Slaman. Accurate transport properties and second virial coefficients for krypton based on a state-of-the-art interatomic potential. Chemical Engineering Communications. Accepted 1988, published online 2007, 78(1), 153-165. DOI: 10.1080/00986448908940192.

[8] Waldrop, J. M., B. Song, K. Patkowski, and X. Wang. Accurate ab initio potential for the krypton dimer and transport properties of the low-density krypton gas. The Journal of Chemical Physics. 2015, 142(20), 204307. DOI: 10.1063/1.4921623.

[9] Jäger, B., R. Hellmann, E. Bich, and E. Vogel. State-of-the-art ab initio potential energy curve for the krypton atom pair and thermophysical properties of dilute krypton gas. The Journal of Chemical Physics. 2016, 144(11), 114304. DOI: 10.1063/1.4943959.

[10] Yousfi, M., A. Hennad, and O. Eichwald. Improved Monte Carlo method for ion transport in ion-molecule asymmetric systems at high electric fields. Journal of Applied Physics. 1998, 84(1), 107–114. DOI: 10.1063/1.368007.

[11] Benhenni, M., M. Stachoň, F. X. Gadéa, M. Yousfi, and R. Kalus. Transport and dissociation of neon dimer cations in neon gas: a joint dynamical and Monte Carlo modeling. Journal of Physics B: Atomic, Molecular and Optical Physics. 2016, 49(17), 175205. DOI: 10.1088/0953-4075/49/17/175205.

[12] Helm H, and M. T. Elford. Mobilities and reactions of diatomic rare-gas ions in their parent gases, helium, neon, argon and krypton. Journal of Physics B: Atomic and Molecular Physics. 1978, 11(22), 3939–3950. DOI: 10.1088/0022-3700/11/22/021.

Publication